

**Production of Coated and Free-Standing  
Engineering Components using the HVOF  
(High Velocity Oxy-Fuel) Process**

**Joseph Stokes BA BAI**

**Ph.D**

**2003**

# **Production of Coated and Free-Standing Engineering Components using the HVOF (High Velocity Oxy-Fuel) Process**

by

**Joseph Stokes BA BAI**

A thesis submitted in part fulfilment of the requirement  
for the degree of

**Doctor of Philosophy**

**Supervisor:**

Dr Lisa Looney

Dublin City University

School of Mechanical and Manufacturing Engineering

January 2003

---

# DECLARATION

---

I hereby certify that this material, which I now submit for assessment on the programme of study leading to the award of Doctor of Philosophy, is entirely my own work and has not been taken from the work of others save and to the extent that such work has been cited and acknowledged within the text of my work.

Signed:



I.D. Number: 97970220

Date:

30 Jan. 2003

---

# ACKNOWLEDGMENTS

---

There are many individuals who have assisted me during the present work. I would like to thank you all.

In particular, I would like to acknowledge the contributions of Dr. Lisa Looney of the School of Mechanical and Manufacturing Engineering in Dublin City University, for her supervision, guidance and her constructive suggestions and comments during the course of this investigation.

I would like to thank the academic staff for any help they gave me over the course of my work, especial thanks to Professor Saleem Hashmi (Head of School). I am especially grateful to Michael Tyrrell, Liam Dornican, Keith Hickey, Martin Johnson, Jim Barry, Michael May and Chris Crouch for their technical support, inspiration and discussions throughout this work, and to the secretarial staff for their help. I wish to thank all of my fellow postgraduate students within Dublin City University and elsewhere, for their support and friendship.

I am grateful to both the Irish-American Partnership and the School of Mechanical and Manufacturing Engineering, DCU, without whose funding this project would not have been made possible.

Special thanks are due to my parents and family for their endless support during my studies, without which I may not have got this far. My sincere thanks goes to Ruth Maxwell, for her love, care and encouragement during the last few years, it has been much appreciated.

## **Production Of Coated And Free-Standing Engineering Components Using The HVOF (High Velocity Oxy-Fuel) Process**

**By  
Joseph Stokes BA BAI**

The present study aims to establish the potential of producing various hard metal industrial thick components using the High Velocity Oxy-Fuel (HVOF) thermal spray process, rather than by sintering or casting techniques currently used. It is innovative in that generally research work carried out on this process focuses on coating technologies. In order to spray-form thick tungsten carbide cobalt (WC-Co) components, certain problems have to be overcome. More specifically these problems include minimizing residual stresses (which cause shape distortion in the components), therefore maintaining the integrity of the deposit on a microstructural scale.

Residual stress arises during deposition and, in the present research, was reduced by limiting the rise and fluctuation of the deposition temperature. This was achieved by the utilization of a carbon dioxide cooling system and automated traverse movement of the spray gun, which together enabled continuous deposition at a steady temperature of 500°C, reducing the residual stress by 58% compared to manual spraying. A spraying distance of 200mm and a powder feed rate of 38gmin<sup>-1</sup> exhibited the lowest stress within the deposit using the automated system.

The minimization of the residual stress increased the maximum deposit thickness achieved from 0.6mm to 1.2mm. Higher deposit thicknesses were achieved when the deposition area was reduced. These findings were simulated by the finite element analysis technique. The present research describes the successful production of 9mm thick spray-formed WC-Co components (12mm in diameter). Associative work in this thesis includes the fabricating of larger more complex shaped components, tensile specimens. The tensile specimens were used to measure the stiffness of the deposit (substrate free) and a Young's modulus of 189GPa was measured. Post-heat treatment and measurement of Vicker's hardness and porosity were also investigated. Finally, the economic feasibility of producing WC-Co cylindrical components using spray-forming is briefly discussed.

---

# TABLE OF CONTENTS

---

	Page
<b>Declaration</b>	I
<b>Acknowledgements</b>	II
<b>Abstract</b>	III
<b>Table of Contents</b>	V
<b>List of Figures</b>	XIV
<b>List of Tables</b>	XXVI

---

<b>CHAPTER 1</b>	<b>INTRODUCTION</b>	<b>1</b>
------------------	---------------------	----------

---

---

<b>CHAPTER 2</b>	<b>LITERATURE SURVEY</b>	<b>5</b>
------------------	--------------------------	----------

---

2 1	Introduction	5
2 2	Surface Engineering	7
2 2 1	Solid Surfaces	8
2 2 2	Friction And Wear	9
2 2 3	Surface Protection	11
2 3	Coating Techniques	13

2 4	Thermal Spraying Techniques	15
2 4 1	Flame Heating	16
2 4 2	HVOF Thermal Spray Process	16
2 5	Advantages and Disadvantages of the HVOF System	18
2 6	Thermally Sprayed Coatings	20
2 6 1	Introduction	20
2 6 2	Selected Properties of Coatings	20
2 7	Coating And Forming Materials	28
2 8	Forming	29
2 8 1	Introduction	29
2 8 2	Spray Forming	29
2 9	Spray Process Modelling	31

---

<b>CHAPTER 3</b>	<b>EXPERIMENTAL EQUIPMENT, PROCEDURES AND MEASUREMENT METHODS</b>	<b>32</b>
------------------	---	-----------

---

3.1	Introduction	32
3.2	HVOF Thermal Spraying System	34
3.2.1	Supporting Systems	34
3.2.2	Additional Equipment	34
3.3	Facilities Development	35
3.3.1	System Automation	37
3.3.2	Cooling System	40
3.4	Temperature Measurement Systems	42
3.4.1	Pyroscope	42
3.4.1	Temperature Logging Equipment	44
3.5	HVOF Spraying Procedures	45
3.5.1	Surface Preparation	45
3.5.2	Pre-Heat Treatment	46
3.5.3	Spraying Process	46
3.5.4	Post-heat Treatment	48
3.6	Temperature Measurement	49
3.6.1	Pyrometer Test	49
3.6.2	Thermocouple Temperature Calibration	50
3.6.3	Temperature Dependence On Spraying Distance	52

3.7	Coating Characterisation Equipment	53
3.8	Young's Modulus Measurement	54
	3.8.1 Cantilever Beam Method	54
	3.8.2 Tension Testing Method	59
	3.8.3 Other Determination Techniques	59
3.9	Residual Stress Measurement	60
	3.9.1 The Almen Test Method	60
	3.9.2 Clyne's Analytical Method	64
	3.9.3 X-Ray Diffraction Stress Measurement	68
	3.9.4 The Hole Drilling Method	71
3.10	Coating/Forming Thickness Measurement	73
3.11	Parameter And Process Optimisation	74
	3.11.1 System Automation Control	74
	3.11.2 Young's Modulus And Poisson's Ratio Determination	75
	3.11.3 Spraying Techniques	75
	3.11.4 Forced Cooling	76
	3.11.5 Variation Of Residual Stress With Spraying Distance	77
	3.11.6 Variation Of Residual Stress With Powder Feed Rate	77
	3.11.7 Effect Of Deposit Thickness On Residual Stress On	77
	3.11.8 Effect Of Substrate Thickness On Residual Stress	78
	3.11.9 Effect Of Sample Length And Width On Residual Stress	78
	3.11.10 Effect Of Sample Size On Deposit Thickness	78
	3.11.11 Comparison Of Residual Stress Techniques	78

3.12	Post Treatment Technique	80
	3.12.1 Post-Heat Treatment	80
	3.12.2 Shot Peening	80
3.13	Phase Characterization	81
3.14	Hardness Measurement	82
3.15	Porosity Measurement	84
3.16	Forming Aspect Ratio Relationship	86
3.17	Production Of Thick Formed Components	87
3.18	Production Of A Tensile Specimen	89

---

<b>CHAPTER 4</b>	<b>SPRAY PROCESS MODELLING</b>	<b>91</b>
4.1	Finite Element Analysis	91
4.2	Engineering Problems	93
4.3	Numerical Methods	95
4.4	Steps In The Finite Element Method	96
4.5	Numerical Formulation	97
	4.5.1 Heat Transfer System	97
	4.5.2 Residual Stress Determination	111
4.6	Verification of Results	126
4.7	Capabilities And Organisation Of ANSYS	128
	4.7.1 Creating A Model With ANSYS: Preprocessor	128
	4.7.2 Solution	137
	4.7.3 General Postprocessor	138
4.8	ANSYS Procedure	139

---

<b>CHAPTER 5</b>	<b>RESULTS AND DISCUSSION</b>	<b>140</b>
5 1	Introduction	140
5 2	Temperature Measurement	142
5 2 1	Pyrometer Test	142
5 2 2	Calibration of Remote Temperature Measurement Technique	144
5 2 3	Effect of Spraying Distance and Cooling Temperature	151
5 3	The Automation Of The Process Equipment	157
5 3 1	Linear Traverse Unit	157
5 3 2	Third-Axis Directional Unit	159
5 4	Elastic Properties of Sprayed WC-Co	166
5 5	Stress Distribution Through a Deposit	168
5 6	Optimisation of Spraying Technique and Spraying Parameter	171
5 6 1	Manual Spraying	171
5 6 2	Linear traverse Unit	172
5 6 3	Forced Cooling	172
5 6 4	Variation Of Residual Stress With Spraying Distance	173
5 6 5	Variation Of Residual Stress With Powder Feed Rate	178

5.7	Maximizing Thickness Of The Deposit	180
5.7.1	Effect Of Deposit Thickness On Residual Stress	180
5.7.2	Effect Of Substrate Thickness On Residual Stress	201
5.7.3	Effect Of Sample Length And Width On Residual Stress	206
5.7.4	Effect Of Sample Size On Deposit Thickness	211
5.7.5	Comparison Of Residual Stress Techniques	213
5.8	Post Treatment	216
5.8.1	Post-Heat Treatment	216
5.8.2	Shot Peening Method	220
5.9	Phase Characterization	221
5.10	Hardness Measurement	229
5.11	Porosity Measurement	232
5.12	The Fabrication Of Spray-Formed Engineering Components	234
5.12.1	Forming Die Design	234
5.12.2	Production Of Thick-Formed Components	238
5.12.2	Tensile Specimen	240
5.13	Cost analysis	246

<b>CHAPTER 6</b>	<b>CONCLUSIONS AND RECOMMENDATIONS</b>	<b>251</b>
6 1	Conclusions	251
6 2	Recommendations For Future Work	254
<b>PUBLICATIONS ARISING FROM THIS WORK</b>		<b>255</b>
<b>REFERENCES</b>		<b>256</b>
<b>APPENDICES</b>		<b>A-1</b>
	Appendix 1	A-1
	Appendix 2	A-4
	Appendix 3	A-19
	Appendix 4	A-25
	Appendix 5	A-29
	Appendix 6	A-36
	Appendix 7	A-37

---

# LIST OF FIGURES

---

		PAGE
Figure 1	Brief list of experimental tests carried out in the current research	4
Figure 2	Schematic representation of a metal surface	8
Figure 3	Surface asperities of a nominal smooth surface	9
Figure 4	Three components of surface texture	9
Figure 5	Flow chart of various wear mechanisms	11
Figure 6	Coating deposition technologies	14
Figure 7	Schematic of a Thermal Spray Process	15
Figure 8	Schematic cross-section of Diamond Jet spray gun	17
Figure 9	Schematic of quenching stress	24
Figure 10	Schematic of cooling stresses generated in a coating	25
Figure 11	Effect of coating thickness and tensile residual stress on free edge debonding tensile stresses	27
Figure 12	WC-Co Cylindrical components, manufacture using the HVOF process	30
Figure 13	Schematic of the HVOF thermal spray unit layout	33
Figure 14	Various types of thermal spray automation systems	36
Figure 15	Various planes and directions relevant to the linear traverse unit	37
Figure 16	Schematic of the third-axis directional unit	39
Figure 17	Schematic shows how shifting the substrate up/down facilitates the deposition of large components	40
Figure 18	End view of DJ gun, traverse unit and carbon dioxide cooling system	41
Figure 19	Photo of the optical pyrometer used for temperature measurement and the metallic tube holding the pyrometer sensor	43

Figure 20	Photo of the Pico TC-08 thermocouple device used to measure deposition temperature	44
Figure 21	Schematic of the temperature calibration procedure	51
Figure 22	The Cantilever approach for measuring coating stiffness	55
Figure 23	Strain and stress distribution for coated cantilever beam with applied load P	58
Figure 24	The MAM bending theory for the determination of residual stress	62
Figure 25	Schematic of the cross-section of a thermally sprayed sample	63
Figure 26	Real, calculated and average residual stress distribution in a coated MAM sample, where the substrate has higher stiffness than that of the coating	63
Figure 27	Schematic description of the generation of curvature in a flat bi-material plate as a result of misfit strain	66
Figure 28	Clyne's Method used to determine the distributed residual stress in a thermally sprayed sample	67
Figure 29	Basic features of a typical XRD experiment	69
Figure 30	Schematic of the Vickers indenter and a micrograph of the indentation produce by the Vickers hardness test on a WC-Co specimen	83
Figure 31	Porosity indicated in red by the Buehler Omnimet image analysis system	85
Figure 32	Spray-forming of large components	86
Figure 33	Schematic diagram and photo of die design used in the fabrication of the free-standing WC-Co components	88
Figure 34	Schematic and a photo of die used for fabrication of WC-Co tensile components	90
Figure 35	Finite Element model for temperature distribution through various materials	97

Figure 36	Heat transfer by conduction through a medium	98
Figure 37	Energy balance at a surface with convective heat transfer	100
Figure 38	Heat flow through nodes $i$ and $i+1$ showing (a) heat gained at one side and lost at the other and (b) heat gained at both sides	101
Figure 39	Schematic of the heat transfer system	107
Figure 40	Finite Element model used in the present research	109
Figure 41	Moment in a sample generating a deflection	111
Figure 42	Coated sample subjected to a central displacement	112
Figure 43	Sub-dividing the sample into elements and nodes	113
Figure 44	A solid member of uniform cross-section subjected to a force $F$	114
Figure 45	Internally transmitted forces through an arbitrary element	116
Figure 46	Applying boundary conditions to coarse and fine meshed problems	120
Figure 47	Schematic of the coated sample system used to demonstrate how the finite element technique arrives at a solution	121
Figure 48	Schematic of the graphical contour lines showing the displacements of each node (solid lines) compared to pre-deformed shape (dashed lines)	123
Figure 49	Schematic of the nodal stress contours based on the numerical formulation problem used in the present section	125
Figure 50	Generated moment finite element analysis system	125
Figure 51	Finite element model generation, (a) direct generation, (b) solid modelling approach	129
Figure 52	The relationship between keypoints, lines and areas	130
Figure 53	One-dimensional representation of a problem	131
Figure 54	Various types of two-dimensional elements	132
Figure 55	Simple representation of a two-dimensional element (a), as a series of springs (b) and subjected to a load (c)	133
Figure 56	Schematic of various three-dimensional elements	133

Figure 57	The order of the presented experimental results	141
Figure 58	Graphical results of differing temperatures measured by optical pyrometry and using thermocouples	143
Figure 59	Temperature calibration graph for thermocouple measurement	146
Figure 60	Use of the empirical formula to measure front temperature	147
Figure 61	Mesh generated model used for the heat transfer problem	148
Figure 62	Comparison of finite element and experimental temperature gradient results, from the front (flame temperature) of the sample, through to the back (measured temperature) of the sample	149
Figure 63	Finite element heat transfer result at a flame temperature of 500°C	150
Figure 64	Spraying temperature at various distances with/without cooling	152
Figure 65	Finite element analysis of the temperature gradient found through a sample when CO <sub>2</sub> cooling is involved	153
Figure 66	Graphical representation of the front (flame surrounded by cooling) temperature versus the back temperature	154
Figure 67	Graphical representation of the finite element analysis front (flame shrouded by cooling) temperature plotted against the back temperature for various substrate thicknesses	156
Figure 68	Calibration of traverse unit	158
Figure 69	Effect of traverse speed on the motion of the forcer	158
Figure 70	Deposit with ten passes and 0mm vertical increment	160
Figure 71	Deposit with twenty passes set at a 10mm and 7.5mm vertical increment	161
Figure 72	Deposit with twenty passes and 5mm vertical increment	162
Figure 73	Deposit with twenty passes set at a 2mm and 1mm vertical increment	163

Figure 74	Three samples showing the difference between spray deposits produced using the third-axis traverse unit at various height increments	164
Figure 75	Scanning electron microscope micrographs of the end view of samples produced using the third-axis traverse unit, (a) 0mm increment, (b) 5mm increment and (c) 10mm increment	165
Figure 76	The cantilever test results presented in an excel sheet	167
Figure 77	An example of a deflected sample	169
Figure 78	Average and distributed residual stress through a WC-Co deposit found using the MAM test	170
Figure 79	Distributed residual stress through a WC-Co deposit calculated using Clyne's Analytical Method	170
Figure 80	Differences in stress ranges as a function of spraying techniques	173
Figure 81	Maximum stress change as a function of spraying distance carried out at various powder feed rates	175
Figure 82	Deformed residual stress samples deposited at a spraying distance of 150mm at various powder feed rates	175
Figure 83	Residual stress samples sprayed at 180 and 200mm	177
Figure 84	Residual stress samples sprayed at 250mm	177
Figure 85	Scanning electron microscope surface images of WC-Co formed at various powder feed rates, showing the presence of unmelted particles and voids. A = Voids, B = Solid particles	179
Figure 86	Residual stress in a 0.2 and 0.6mm thick deposit of WC-Co plus substrate	183
Figure 87	Residual stress in a 1 and 2mm thick deposit of WC-Co plus substrate	184
Figure 88	Residual stress in a 2.5 and 3mm thick deposit of WC-Co plus substrate	185

Figure 89	Deformed and cracked sample due to excessive residual stress	186
Figure 90	Change in the shape of the deposit as the deposit thickness increased from 1mm to 2mm	187
Figure 91	Maximum stress change as a function of deposit thickness	188
Figure 92	Stress distribution for a 1.2mm thick WC-Co deposit	189
Figure 93	Various sized spray formed components	190
Figure 94	Residual stress development in thinner deposits	193
Figure 95	Pre-heating and spraying temperature	194
Figure 96	Temperature development in thick deposits	194
Figure 97	Resultant deflection for a 0.2mm deposit on a 0.075mm substrate	197
Figure 98	The finite element distribution through a 0.2mm deposit on a 0.075mm substrate	198
Figure 99	Finite element and experimental stress analysis of a 0.2mm thick deposit	199
Figure 100	Finite element and experimental stress analysis of a 1mm (a) and 2mm (b) thick deposit	200
Figure 101	The effect of substrate thickness on stress	203
Figure 102	Predicted dependence on specimen width/length ratio of the critical curvature at a bifurcation instability	208
Figure 103	Effect of increasing the substrate length on residual stress calculated using the finite element technique	210
Figure 104	Higher deposit thickness as a function of residual stress	212
Figure 105	A typical X-ray diffraction measurement profile	213
Figure 106	Stresses relieved with the hole drilling method	214
Figure 107	Time-temperature curve showing the post-heat treatment used on the WC-Co samples	217
Figure 108	Time-temperature curve showing all three cycles, pre-heat, spraying and post-heat treatment used on the WC-Co samples	217

Figure 109	Graph showing the relationship between residual stress and post-heat treatment	219
Figure 110	Through thickness residual stress distribution for non-treated and a shot peened sample	220
Figure 111	Images of the resulting microstructures after various polishing techniques	223
Figure 112	X-ray diffraction pattern for the starting powder Diamalloy 2003 WC-12%Co	224
Figure 113	Top image shows crystalline WC particles embedded in an amorphous matrix. Bottom images shows the nucleation of elemental tungsten due to the oxidation during spraying and post-heat treatment	225
Figure 114	X-ray diffraction patterns for HVOF sprayed WC-12%Co	226
Figure 115	X-ray diffraction patterns for HVOF sprayed Diamalloy 2003 WC-12%Co, post-heated at 690°C and 890°C	227
Figure 116	X-ray diffraction patterns for WC-Co coating heat-treated at 1350°C	228
Figure 117	The variation hardness with deposit thickness	230
Figure 118	Relationship of hardness on post heat temperature	231
Figure 119	Relationship of porosity on deposit thickness	233
Figure 120	Schematic of uneven distribution of the as-sprayed aluminium releasing layer	237
Figure 121	Thick WC-Co spray formed components, deposited before the split die technique was used	238
Figure 122	Free-standing WC-Co spray-formed components	239
Figure 123	Split tensile forming die and the location of the releasing layer	241
Figure 124	Thermally sprayed tensile specimens	242
Figure 125	Finite element result for the tensile specimen	244

Figure 126	Tensile stress strain curve for the WC-Co material	245
Figure 127	The distribution of costs in the production of a cylindrical component	249
Figure A1	Computer aided drawing of the traverse unit framework	A-4
Figure A2	Schematic diagram of the forcer of the linear motor	A-6
Figure A3	Schematic of the forcer and its interaction with the platen	A-7
Figure A4	Schematic of flux paths and teeth (pole face) position, steps 1 and 2 of a linear step motor	A-9
Figure A5	Schematic of flux paths and teeth position, steps 3 and 4 of a linear step motor	A-10
Figure A6	Schematic of the LX drive	A-11
Figure A7	Platen arrangement for spraying distance control	A-12
Figure A8	Control panel for the operation of the third-axis unit	A-18
Figure A9	Position of neutral axis	A-23
Figure A10	Sagittal Method	A-24
Figure A11	Schematic diagram of the orientation of the measured lattice planes with respect to specimen structure	A-26
Figure A12	Plane stress elastic model of a flat specimen	A-27
Figure A13	Milling Guide RS-200	A-30
Figure A14	Rosette strain gauge orientation	A-31
Figure A15	Computer Aided Drawing of the tensile specimen shape used to produce WC-Co samples	A-36
Figure A16	Schematic of the steady-state heat transfer problem to be analysed	A-38
Figure A17	Schematic of residual stress due to applied deflection	A-60

---

# LIST OF TABLES

---

		PAGE
Table 1	Benefits of using HVOF coatings	19
Table 2	Various Diamond Jet HVOF coating hardness results	21
Table 3	Various Diamond Jet HVOF coating porosity results	22
Table 4	Tungsten carbide cobalt powder data	28
Table 5	Spray parameters suggested by Sulzer METCO for the deposition of tungsten carbide cobalt	47
Table 6	Physical properties characterising and disturbing various engineering systems	94
Table 7	Heat transfer parameters found from experimental data	108
Table 8	Parameters used in the heat transfer finite element analysis	109
Table 9	The effect of substrate thickness on stress	203
Table 10	The effect of substrate thickness on stress experimentally and using the finite element technique	205
Table 11	The effect of sample length on stress	207
Table 12	The effect of sample width on stress	208
Table 13	Comparison of residual stress measurement techniques	215
Table 14	The effect of changing the substrate material on stress	235
Table 15	Effect of different releasing layer techniques on the formation of thick components	236
Table 16	HVOF spray-forming versus sinter-forming of a WC-Co component	250
Table A1	Values and signs for $\gamma$	A-34

---

# INTRODUCTION

---

Thermal spraying is one of the most versatile hard facing techniques available for the application of coating materials used to protect components from abrasive wear, adhesive wear, erosive wear or surface fatigue and corrosion (such as that caused by oxidation or seawater) [1,2,3]. The coatings may also increase heat resistance, when a material with a low thermal conductivity is deposited onto a base material. In thermal spraying the initial coating material (materials in the form of rod, wire, or powder) is heated, generally to a molten state and projected onto a receiving surface, known as a substrate. A variety of engineering problems have been solved using thermal spraying applications and as research continues the application of this coating technique may be used in engineering areas otherwise not considered [4,5]. Presently, hydraulic pump seals and valves are some of the components in the oil industry that require thermally sprayed coatings to protect the components surface against hostile environments [6]. The uses of thermal spraying ranges across many manufacturing processes, from the automotive [7,8], through to the space exploration industry [9]. Metals, carbides and cermets are the most widely used coating materials, however the spraying of polymers has been researched also [10,11]. Within the thermal spray technique are various types of processes, one of which is the High Velocity Oxy-Fuel (HVOF) process used in the current research.

The HVOF process is one of the most popular thermal spraying technologies and has been widely adopted by many industries due to its flexibility and the superior quality of coatings produced. The HVOF process is a relatively new thermal spray process (the Sulzer METCO Diamond Jet HVOF was developed in 1988), offering coatings with higher bond strengths, and hardness together with lower porosity, compared to its other thermal spray counterparts [12]. Industrial use of the process is growing according to Parker et al. [13], especially in the aeronautical industry, both

in the commercial and in the defence airline industries [14]. Focus is starting to move towards the deposition of thermal barrier coatings (TBCs) such as in the case of  $ZrO_2 + 8 \text{ wt. } \% Y_2O_3$  TBC on a CoNiCrAlY base material [15]. HVOF thermally sprayed coatings are used in a wide range of other applications such as the gas turbine, petroleum [16], chemical, paper/pulp [17], automotive [18,19] and manufacturing industries [20]. Tungsten carbide-cobalt (WC-Co) is the coating material under review in the report, has a many applications in the above mentioned industries [20,21,22], due to its impressive mechanical properties. The coating application of the WC-Co material is very popular, however the spray-forming of this material has not been widely documented [23]. The report will explore the aspects of depositing WC-Co coatings using the HVOF process and then investigate the possibilities of spray-forming tungsten carbide-cobalt components.

Forming of free standing components by thermal spraying is not a new idea but, to date, work has focused more on the technique of Vacuum Plasma Spraying (VPS) rather than the HVOF thermal spray system [24]. Forming with the VPS system has been carried out on various types of materials from metals to composites [25], but the formed thickness is generally low [26] due to the high internal stresses resulting from plasma spray processes as compared to the HVOF process [27].  $Al_2O_3$  components have however been formed to a thickness of 2.5mm [28]. A thickness of 3mm alumina and 5% calcia stabilized zirconia has been sprayed using a plasma system, but this was only achieved by the use of reinforcing pins [29]. Study of forming with the HVOF process has not been extensive as most of the HVOF research has been concentrated on coatings.

Previous research at the Materials Processing Research Centre (MPRC) has shown that the HVOF thermal spray process has also the potential to form components [30]. At present such small tungsten carbide-cobalt (WC-Co) components, as those considered in this study, are often manufactured using an expensive powder processing route such as sinter-forming. It is proposed that thermal spraying may pose an attractive alternative, for some applications such as cutting tool inserts.

Challenges do exist in using HVOF thermal spraying for the purpose of forming such a hard material, as it is very difficult to spray to a thickness greater than approximately 0.6mm [31]. This is because cracking or deformation of the component results as thickness increases, due to internal stresses building-up. This study explores the possibility of spraying high thickness WC-Co components by controlling the build-up of this residual stress within the component.

The remainder of the report is divided into a number of sections. Chapter two is a review of literature relevant to the study. A wide ranging literature survey identified International Thermal Spraying conferences (as outlined in Appendix 1), as being particularly important. The large quantity of mainly peer reviewed research published in these proceedings covers all aspects of thermal spraying, and is a rich resource. This is supplemented by journal publications and industry data. While information sourced from industry does not carry the same academic weight as journal publications, it is relevant and useful. The chapter focuses initially on various wear modes that effect engineering surfaces in service and how coatings protect these surfaces. Various thermal spraying techniques are examined, in terms of their function and performance with reference to internationally published research. The effect of thermal spraying parameters on the coatings' performance is investigated in terms of microstructure and mechanical properties. The chapter introduces sinter-forming and spray forming techniques and concludes with an introduction into finite element analysis; a technique which is later used to simulate heat transfer and residual stress within coatings.

The experimental equipment involved in the HVOF Diamond Jet process is presented in chapter three, along with its associated procedures. The facility includes auxilliary equipment used to optimise the process for repeatability and control. The chapter also includes a description of equipment used for measurement of coating and formed component properties.

The finite element modelling of the spray process, specifically heat transfer and residual stress development is presented in chapter four. The chapter describes the finite element analysis technique and procedures used in the research.

In chapter five the experimental results and discussion are presented. The results show the temperature calibration technique, the benefit of using a linear traverse unit and a carbon dioxide cooling system to reduce residual stress during coating build up and the forming/production of thick components with the process. Post-heat treatment of the components is discussed as a method to reduce the residual stress within the material. The effect of post-heat treatment on phase development is identified. Mechanical properties such as hardness, porosity and stiffness of the formed components are addressed, to ascertain their dependence on forming thickness. Results of numerical analysis by way of finite element techniques are also discussed, in terms of heat transfer and residual stress development within the sprayed components. Figure 1, shows a list of the experimental test results observed in the research.

<p><b>Optimization of Spraying Parameters:</b></p> <ul style="list-style-type: none"> <li>• Spraying Temperature</li> <li>• Spraying Distance</li> <li>• Post-heat Treatment</li> </ul>	<p><b>Material Physical Characterization:</b></p> <ul style="list-style-type: none"> <li>• Phase Development</li> </ul>
<p><b>Residual Stress Analysis:</b></p> <ul style="list-style-type: none"> <li>• Clyne's Test Method</li> <li>• XRD Diffraction</li> <li>• Hole Drilling Method</li> </ul>	<p><b>Mechanical Properties:</b></p> <ul style="list-style-type: none"> <li>• Hardness</li> <li>• Porosity</li> <li>• Young's Modulus</li> </ul>
<p><b>Finite Element Modelling:</b></p> <ul style="list-style-type: none"> <li>• Heat Transfer</li> <li>• Residual Stress Development</li> </ul>	

Figure 1, Brief list of experimental tests carried out in the current research.

Finally, chapter six summarises conclusions from the results found within the present research, and presents recommendations for future research. The future research includes expanding the current study to produce coatings and spray-formed components from other base materials other than tungsten carbide cobalt by the HVOF process.

---

# LITERATURE SURVEY

---

## 2.1 INTRODUCTION

Serviceable engineering components not only rely on their bulk material properties but also on the design and characteristics of their surface. This is especially true in wear resistant components, as their surface must perform many engineering functions in a variety of complex environments. The behaviour of a material is therefore greatly dependent on the surface of a material, surface contact area and the environment under which the material must operate. The surface of a metallic material is made up of a matrix of individual grains, which vary in size and bond strength depending on the means by which the material was manufactured and on the elements used to form those grains.

The surface of these components may require treatment, to enhance the surface characteristics. Surface treatments that cause microstructure changes in the bulk material include heating and cooling/quenching through induction, flame, laser, and electron beam techniques, or mechanical treatments (one example is cold working). Surface treatments that alter the chemistry of a surface include carburizing, nitriding, carbonitriding, nitrocarburizing, boriding, siliconizing, chromizing and aluminizing.

Hard facing is another form of surface treatment, where the bulk material's surface is given a protective layer of another material having more superior properties than those of the bulk material. An example of this is coating a turbine pump seal joint with a corrosive resistive material, to prevent salty water from eroding the pump. Each method of hard facing, examples of which are coating deposition, cladding or welding, causes particular physical and chemical effects on the bulk material, some

beneficial, some detrimental. For example stresses which may exist in the protective material can create problems, however careful monitoring and research may limit these effects, to hopefully produce quality, serviceable engineering components. The following sections will describe the concept of surface engineering and the effects engineering environments have on these surfaces. Hard facing techniques are described in detail especially with regard to coating deposition technologies, with particular emphasis on thermal spray techniques, including the HVOF (High Velocity Oxy-Fuel) process, that used in the current research.

As described earlier, the production of free-standing components was initially conceived in the MPRC group by Helali, et al. [30], where thin shelled components were fabricated using the HVOF facility. Low residual stress generation was found for thin components, however the stress was found to increase as component thickness increased. The present research will look at coating stainless steel or aluminium with tungsten carbide cobalt using the HVOF thermal spraying process. The aim of the research is to reduce the residual stresses within these coatings through optimisation of the HVOF process. Once this has been accomplished the same optimisation will be utilized to reduce stress generation in formed tungsten carbide cobalt components.

## 2.2 SURFACE ENGINEERING

The surface characteristics of engineering materials have a significant effect on the serviceability and life of a component, thus cannot be neglected in design. As described by [32], “Surface engineering can be defined as the branch of science that deals with methods for achieving the desired surface requirements and their behaviour in service for engineering components”. The surface of any component may be selected on the basis of texture and colour, but engineering components generally demand a lot more than this. Engineering components must perform certain functions completely and effectively, under various conditions in aggressive environments.

Engineering environments are normally complex, combining loading with chemical and physical degradation to the surface of the component. Surface wear damage is a phenomenon which effects how a component will last in service. An example of a component working in an aggressive environment is a cutting tool used in machining processes. The tool experiences high loads, high speeds and friction and, as a consequence, high temperatures: These factors lead to surface wear of the component. Lubrication in tribological applications reduces friction and wear, however conventional liquid lubricants fail under extreme conditions, namely low pressure, oxidative or corrosive environments, high speeds and high loads. Surface coatings can help deal with these circumstances. Improving the tool surface, not only improves the life of the tool, but also improves the surface finish of the machined part. Obviously it is important to understand the physical and chemical make up of the applied surfaces, in order to design quality components which yield high service lives.

### 2.2.1 Solid Surfaces

A metal may look clean and polished, however the surface microlayers as shown in figure 2, have been formed due to external factors including machining, temperature and oxide formation. Depending on the manufacturing process involved in producing a material, a zone of work-hardened material will occupy the base of these additional layers. Above this worked layer is an amorphous or microcrystalline structure, called the 'Beilby' layer, which is a result of melting and surface flow during machining of the molecular layers. An oxide layer sits on top of the Beilby layer, due to the oxygen available from the external environment, and surface oxidation mechanisms. A layer of adsorbates occupies the outer region and this is made up of water vapour or hydrocarbons from the environment that may have condensed and physically or chemically adsorbed onto the surface.

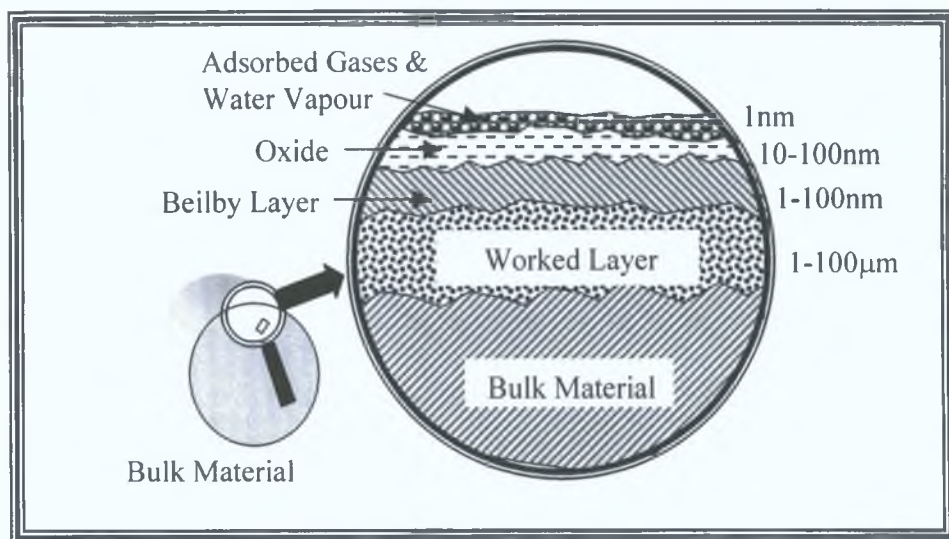


Figure 2, Schematic representation of a metal surface, adapted from [33].

The surface shape or topology depends upon the process used for forming, be it moulding, casting, or cutting and abrading. As shown in figure 3 this is often seen microscopically as a series of asperities rather than the flat surface seen macroscopically. The geometrical texture may be characterized by its surface profile as shown in figure 4, and results from three different components of surface texture (roughness, waviness and error of form).

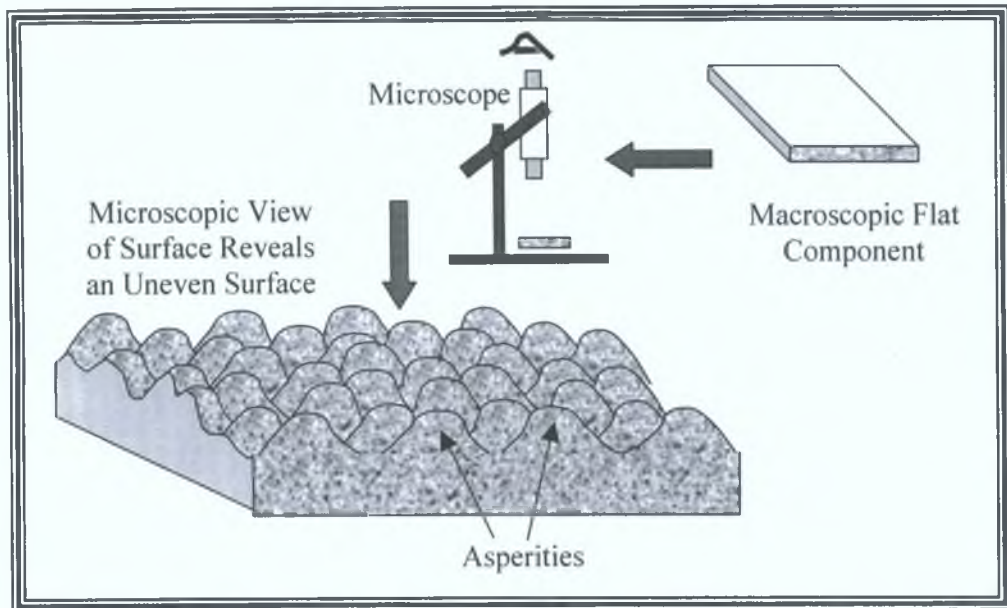


Figure 3, Surface asperities of a nominal smooth surface.

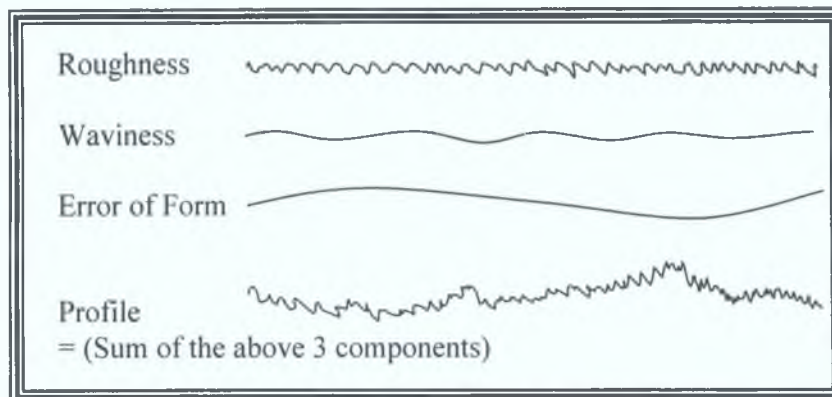


Figure 4, Three components of surface texture.

### 2.2.2 Friction And Wear

Friction and wear occur where two surfaces undergo sliding or rolling under load. Friction is a serious cause of energy dissipation, where wear is the main cause of material wastage. Suitable materials are selected for mating bodies and/or solid/liquid lubrication, is used to control friction and hence reduce the wear rate at which the mating surface degrades. In order to make the best choice of material for

certain conditions, a deeper understanding of these two processes (friction and wear) is necessary.

Friction is the resistance to relative motion of contacting bodies. The degree of friction is expressed as a coefficient of friction  $\mu$ , which is expressed as the ratio of force required to initiate or sustain relative motion, to the normal force that presses the two bodies together. Two modes of friction may occur; sliding or rolling friction. The friction between sliding surfaces (*sliding friction*) is due to the combined effects of adhesion between flat surfaces, ploughing by wear particles and hard asperities, and asperity deformation. Rolling friction is a complex phenomenon because of its dependence on so many factors, including inconsistent sliding (called *slip*) during rolling, and energy losses during mixed elastic and plastic deformations. Rolling friction may be classified into two types, one in which large tangential forces are transmitted (one example, the traction drives and driving wheels of an automobile), and another in which small tangential forces are transmitted, often referred to as *free rolling*.

Wear is a process of removal of material from one or both of two solid surfaces in solid state contact, occurring when two solid surfaces are in sliding or rolling motion together according to Bhushan et al. [33]. The rate of removal is generally slow, but steady and continuous. Figure 5 shows the five main categories of wear and the specific wear mechanisms that occur in each category. Each specific mode of wear looks different to the next, and may be distinguished relatively easily. Further information on these various wear types may be found in my additional report [34].

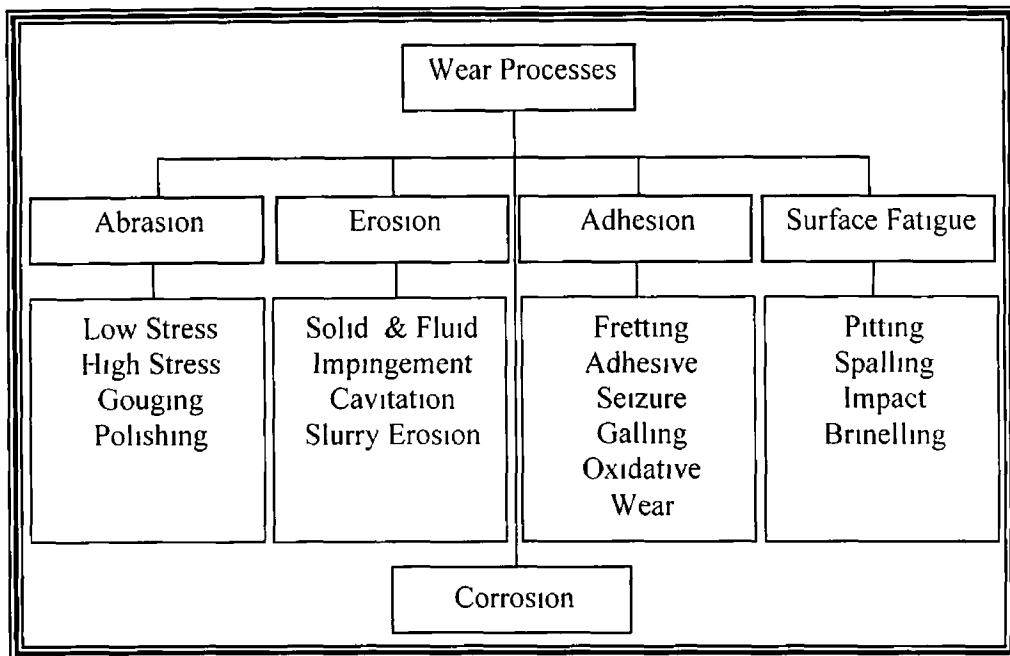


Figure 5, Flow chart of various wear mechanisms

### 2 2 3 Surface Protection

Much tribological research, involves the minimization of friction and wear experienced by materials in service. Effective lubrication between moving surfaces considerably reduces friction and therefore wear. Another approach is to surface harden components.

Ando et al [35], found that nitriding steel with an ammonia and nitrogen-hydrogen flame mixture, causes an increase in surface hardness. Diffusion methods such as carburizing, carbonitriding, nitrocarburizing, boriding and aluminizing, are also used to harden materials, however this process is time consuming [33].

A variety of bulk materials, (ferrous and non-ferrous metals, alloys, ceramics and cermets), can be modified by alloying, mixing, compositing, and coating to achieve

adequate resistance to wear corrosion and friction. Ceramics and cermets appear to be ideal wear-resistant materials, and suit many tribological applications provided that their strength and toughness are acceptable. Coating less wear resistant component materials with that of a high resistant material, offers an ideal method of surface protection.

## 2.3 COATING TECHNIQUES

If a material is added or deposited onto the surface of another material (or the same material), it is known as a coating. Coatings are frequently applied to the surface of materials to serve one or more of the following purposes:

- 1 To protect the surface from the environment that may produce corrosion or other deteriorative reactions
- 2 To improve the surface's appearance

There are many coating deposition techniques available, and choosing the best process depends on the functional requirements, (size, shape, and metallurgy of the substrate), adaptability of the coating material to the technique intended, level of adhesion required, and availability and cost of the equipment. Figure 6 shows commonly used coating deposition techniques, with these techniques being divided into metallics and non-metallics. Metallic coating deposition can be considered under three categories, hard facing being the technique most important to this research. Further information on these various deposition techniques may be found in my additional report [34]. The thermal spraying technique will be presented in more detail in the following section.

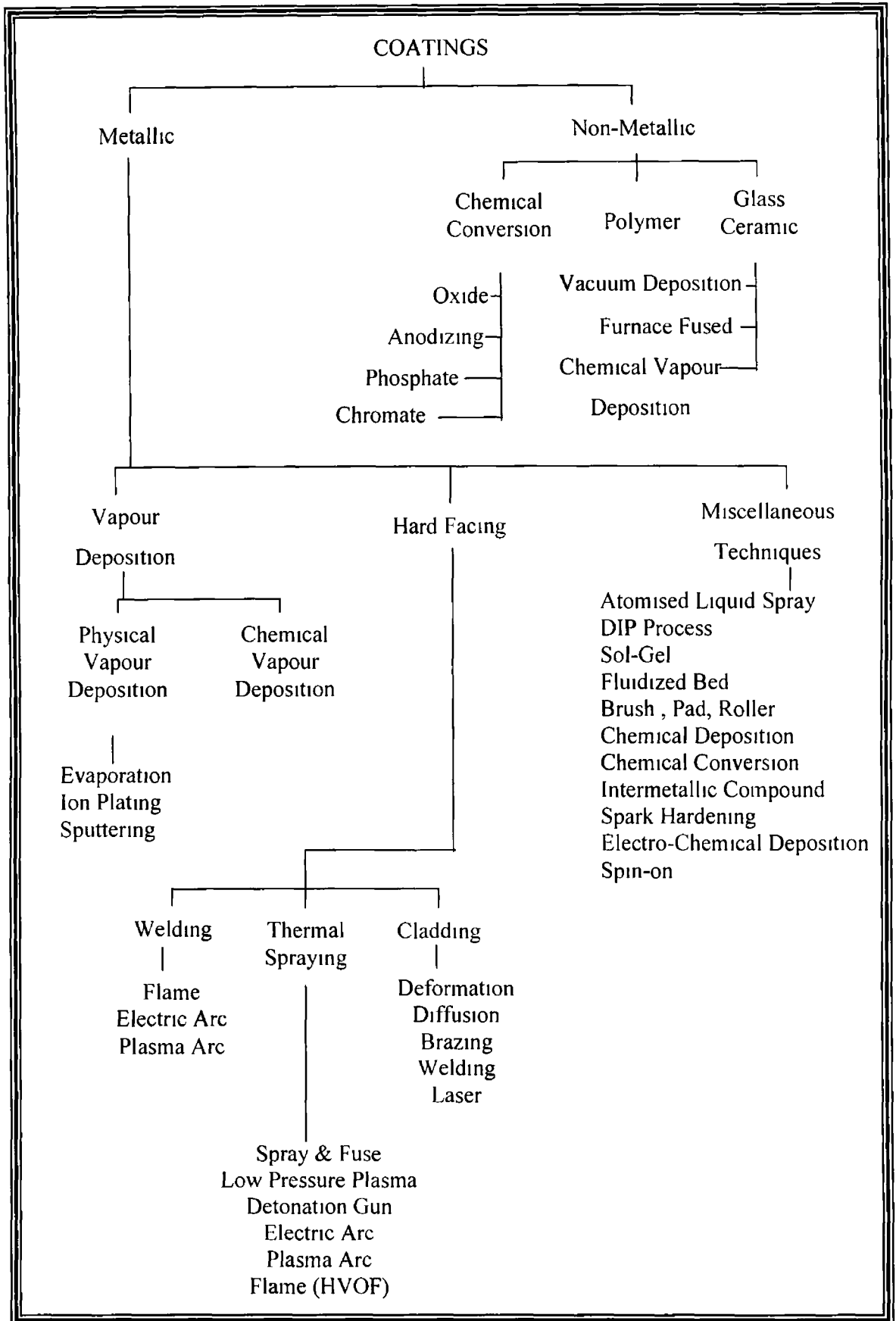


Figure 6, Coating deposition technologies, adapted from [33]

## 2.4 THERMAL SPRAY TECHNIQUES

In the early nineteen hundreds, a young Swiss inventor named Dr. Max Schoop invented thermally spraying, after watching his son playing with his toy cannon. Dr. Schoop noticed that the hot lead shots that were projected out of the cannon, stuck to almost any surface, the result of which gave him the idea that if metal could be melted and projected in a spray like manner, then a surface could be built up with that material. The technology continued (for further information please refer to my additional report [34]), until in 1988 METCO introduced the Diamond Jet HVOF (High Velocity Oxy-Fuel) system, the process under investigation in the current research.

Thermal spraying is a process where by a coating material is fed to a heating zone to become molten, and is propelled from there to a base material (substrate), as shown in figure 7. The thermal energy used to melt the coating material, may be divided into two categories: electrical and flame heating. Refer to my additional report for further information [34].

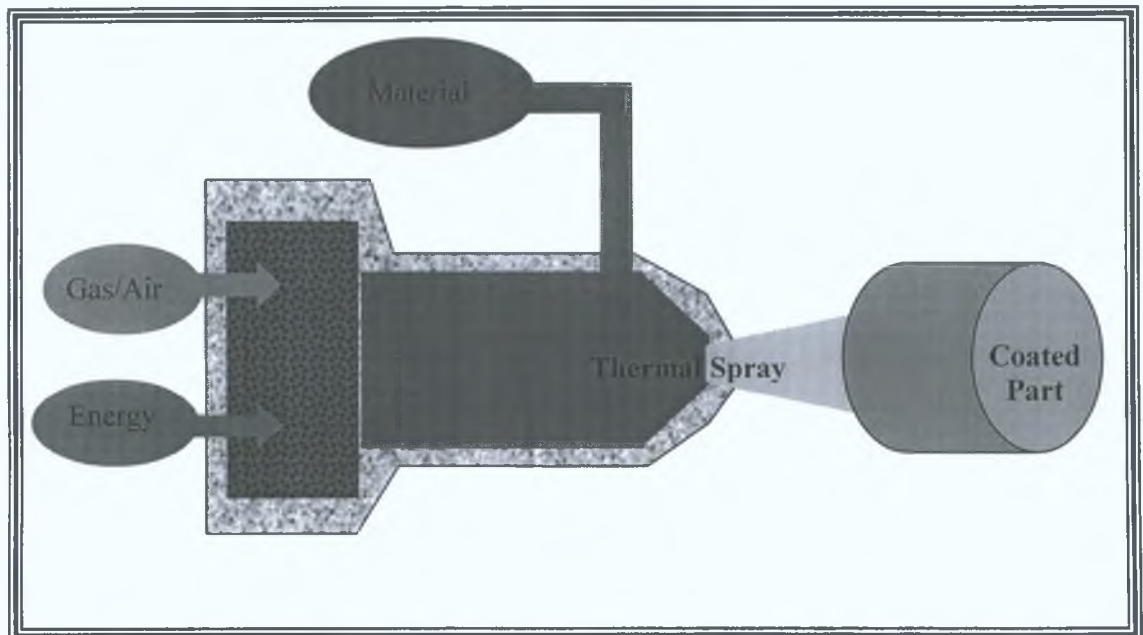


Figure 7, Schematic of a Thermal Spray Process.

### 2.4.1 Flame Heating

In flame heating processes, the deposition material is passed through an intense combustion flame, where the material becomes molten. The gas stream providing the combustion, expands rapidly due to the explosive heating effect, thus propels the molten particles out of the combustion chamber, onto the receiving substrate. There are three main processes where combustion is used to melt the coating material:

- 1 Flame Spraying Process
- 2 Spray and Fuse Process
- 3 HVOF Thermal Spray Process

Further information on these processes may be found in my additional report [34].

### 2.4.2 HVOF Thermal Spray Process

The HVOF (High Velocity Oxy-Fuel) thermal spray process is a form of the flame spraying process, but utilising only powder as the coating material rather than wire or rod. The Diamond Jet HVOF thermal spraying is a flame deposition technique whereby powder material is melted by the use of combustion of oxygen and a fuel gas and is propelled at a high velocity by the use of compressed air, towards a surface as shown in figure 8. In the combustion zone, the powder material enters the flame, where it becomes molten or semi-molten, depending on the melting temperature and the feed rate of the material. The flame temperature for the HVOF process is between 2300 - 3000°C [36]. The molten or semi-molten particles are then propelled out of the gun nozzle at supersonic velocities of over 1350m/s towards the substrate or forming die. Further information on the HVOF gun design and process characteristics may be found in my additional report [34].

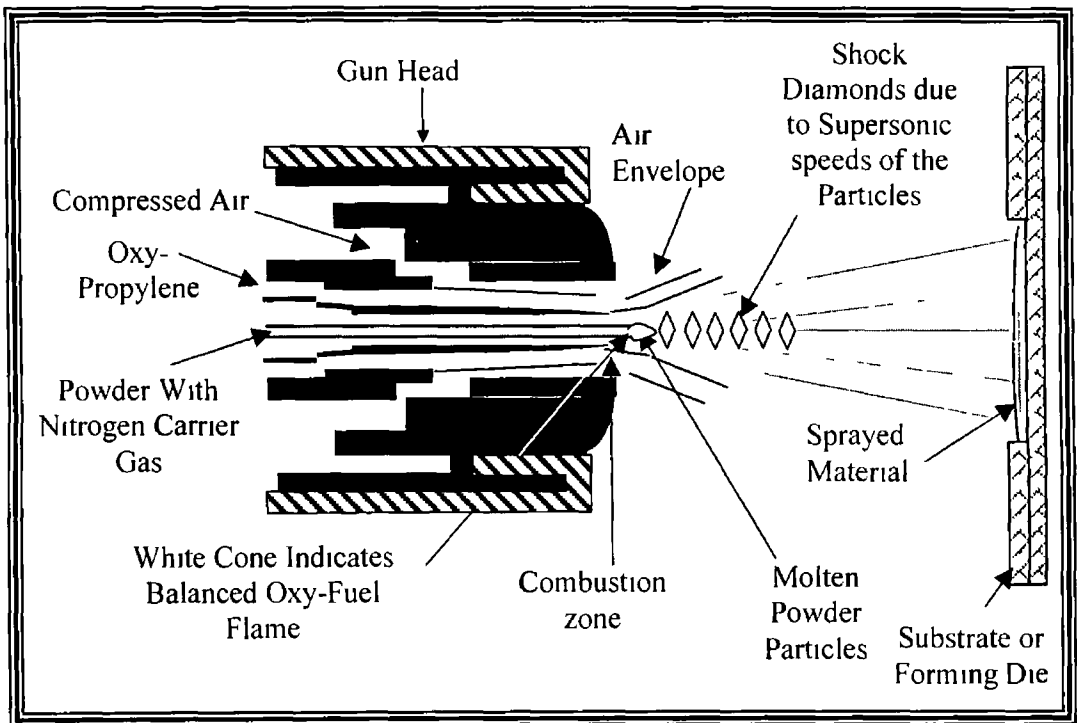


Figure 8, Schematic cross-section of Diamond Jet spray gun

## 2.5 ADVANTAGES AND DISADVANTAGES OF THE HVOF SYSTEM

Particle velocity is very important in thermal spray processes; higher velocity results in higher bond strengths, lower porosity, as the particle has less time to cool down at high velocities, thus impacts a substrate in a semi-molten state. The HVOF process is designed around producing these high velocities, and this contributes the advantages that HVOF has over other thermal spray processes in terms of particle condition [37,38] including:

- More uniform and efficient particle heating, due to the high turbulence experienced by the particles within the combustion chamber
- Much shorter exposure time in flight due to the high particle velocities
- Lower surface oxidation due to short particle exposure time compared to other thermal spraying techniques
- Reduced mixing with ambient air once jet and particles leave the gun
- Lower ultimate particle temperatures compared to other processes such as plasma or arc guns, as these processes operate at temperatures of 16000 and 6000°C as opposed to 3000°C in the HVOF (oxygen/propylene mixture) process

Table 1 summarises the reasons the HVOF process produces such high quality coatings. The powder material selection for the HVOF DJ process may be found in the following report [34].

Table 1, Benefits of using HVOF coatings.

<b><u>Coating Benefit</u></b>	<b><u>Main Reasons for this Benefit</u></b>
Higher density (Lower Porosity)	Higher Impact Energy
Improved Corrosion Barrier	Less Porosity
Higher Hardness Ratings	Better Bonding, Less Degradation
Improved Wear Resistance	Harder, Tougher Coating
Higher Bond and Cohesive Strengths	Improved Particle Bonding
Lower Oxide Content	Less In-flight Exposure Time to Air
Fewer Un-melted Particle Content	Better Particle Heating
Greater Chemistry and Phase Retention	Reduced Time at Higher Temperatures
Thicker Coatings (per pass & total)	Less Residual Stress
Smoother As-sprayed Surfaces	Higher Impact Energies

## 2 6 THERMALLY SPRAYED COATINGS

### 2 6 1 Introduction

Generally, any material which does not decompose, vaporize, sublime, or dissociate on heating, can be thermally sprayed. Consequently a large class of metallic and non-metallic materials (metals, alloys, ceramics, cermets, and polymers) can be deposited by thermal spraying. A thermally sprayed coating is a deposit, produced by a process in which molten or semi-molten particles are applied by impact onto a substrate. Coatings have distinct characteristics which differentiate them from bulk material formed by other manufacturing routes. Further information on the deposition, build up, structure and the properties of a deposit, may be found in my additional report [34]. Properties of the deposit which are important in this report are, hardness, elastic modulus, porosity and residual stress, therefore these will be examined in the following section.

### 2 6 2 Selected Properties of Coatings

One of the advantages of thermal spraying is the ability to produce coating properties to suit the application required. Materials may be sprayed to create a hard or soft, dense or porous coating, thus reporting on the various coating properties produced by thermal spray processes can be difficult. The HVOF process presents the highest results when compared to other thermal spraying processes, producing low roughness, high bond strengths, higher hardness, lower porosity, low oxide content and higher thickness [27-33]. The overall result is a coating with reproducible coating characteristics and high wear resistance.

#### (1) Hardness

Thermal spray coatings generally include voids and oxides within the coating structure, thus macro-hardness levels are less than those of the equivalent material in its wrought or cast form. Oxides often increase hardness, however they reduce the

internal strength of the coating, therefore reducing the coating's performance. There are two tests by which hardness is measured, macro and micro hardness tests.

Macro-hardness tests are carried out to determine the resistance of the total coating deposit to point penetration, measured with either the Brinell or Rockwell hardness test. Many standards and reports outline how these tests are carried out [39-41].

Micro-hardness is carried out at extremely low loads of 50 to 100 grams on individual particles using what is known as a Knoop hardness test. A Vickers (standard diamond pyramid) hardness test is often used to determine the hardness for tungsten carbide coatings, using a 300 gram load, and the values are expressed in  $DPH_{300}$ . There are many standards that outline micro-hardness tests to evaluate the hardness of a coating, including the standard ISO 4516 [42]. Table 2 shows the hardness values measured for various Diamond Jet HVOF coatings.

Table 2, Various Diamond Jet HVOF coating hardness results [31].

Coating Material	Hardness ( $DPH_{300}$ )
Diamalloy 1005 Nickel/Chromium Molybdenum Base Superalloy	350 - 450
Diamalloy 2003 Tungsten Carbide- Cobalt	1015 - 1035
Diamalloy 3001 Cobalt Based Alloy	600 - 650
Diamalloy 3006 Chromium Carbide / Nickel Chromium	550 - 700

## (2) Elastic Modulus

The elastic moduli and the stresses at the material failure (ultimate stress for metals and alloys or fracture stress for brittle materials) are intrinsic properties of a material. The reduction of porosity in a coating greatly influences the elastic modulus of the coating [43]. Measuring the elastic modulus for a coating is difficult as has the substrate attached, however production of free-standing spray formed components

lead to more accurate measurements. Depending on the thermal spraying process utilized, elastic moduli results for tungsten carbide-cobalt vary from 152 to 214GPa (performed using a tensile test on a free standing ring) [43].

### (3) Porosity

Porosity or voids in the coating microstructure is an important issue in thermal spraying, as it is owing to this physical property that many coating mechanical properties (such as bond strength) differ from those of their counterpart bulk materials [43]. Depending on the thermal spraying process utilized, porosity may vary between 0.1 and 15 of the volumes percent. Optimisation of the spraying parameters reduces the high porosity however, certain thermal spraying processes offer lower void content than others. The HVOF process exhibits the lowest porosity of all known thermal spraying techniques, as the high particle impact velocity, compresses most air pockets out of the microstructure[27,33]. Table 3 shows porosity results for various Diamond Jet HVOF coatings.

Table 3, Various Diamond Jet HVOF coating porosity results [31].

Coating Material	Porosity (%)
Diamalloy 1005 Nickel/Chromium Molybdenum Base Superalloy	1
Diamalloy 2003 Tungsten Carbide- Cobalt	< 0.5
Diamalloy 3001 Cobalt Based Alloy	1.5
Diamalloy 3006 Chromium Carbide / Nickel Chromium	1

### (4) Residual Stress

Residual stress is one of the major problems in thermal spraying, especially in the development of thick coatings [44-46]. In the HVOF thermal spray system, individual molten or semi-molten particles impinge a substrate or pre-existing

molten material at speeds of up to 1350m/s [47]. Despite their low mass, the effect of particles striking a surface at this speed causes certain deformations to the pre-existing material (be it substrate or previous deposit) [48]. The impingement of each particle incurs stress fields, which depend upon the solid state of this pre-existing material.

In addition to the mechanical effects of impact, temperature effects are also relevant to stress development. These include the effects of both local and global temperature changes. Each particle is heated in the combustion chamber of the HVOF gun, and is projected towards a receiving substrate or forming die. On impacting the substrate, the particles deform into lamella that cool down to their melting point and solidify. The combustion temperature of the HVOF process approaches 3000°C [20], however the deposition temperature at the substrate is much lower. For the powder material Tungsten Carbide 12%wt Cobalt (WC-Co) it is, for example approximately 500°C [49]. Therefore the temperature decrease experienced by the particles is immense. This leads to the formation of quenching stresses in the individual lamella. These stresses are only alleviated by the introduction of micro-cracks in the material, or debonding from the substrate.

According to Pawlowski [43], as many as 5 to 15 lamellae may exist in a single pass of spray (depending on initial powder particle size). As the lamellae solidify they contract, but are constrained by each other and the substrate, thus generating high tensile stresses in the individual lamella as shown in figure 9. This tensile quenching stress in the lamella is unavoidable, and may be estimated by the expression for thermal stress, leading to equation 3 below.

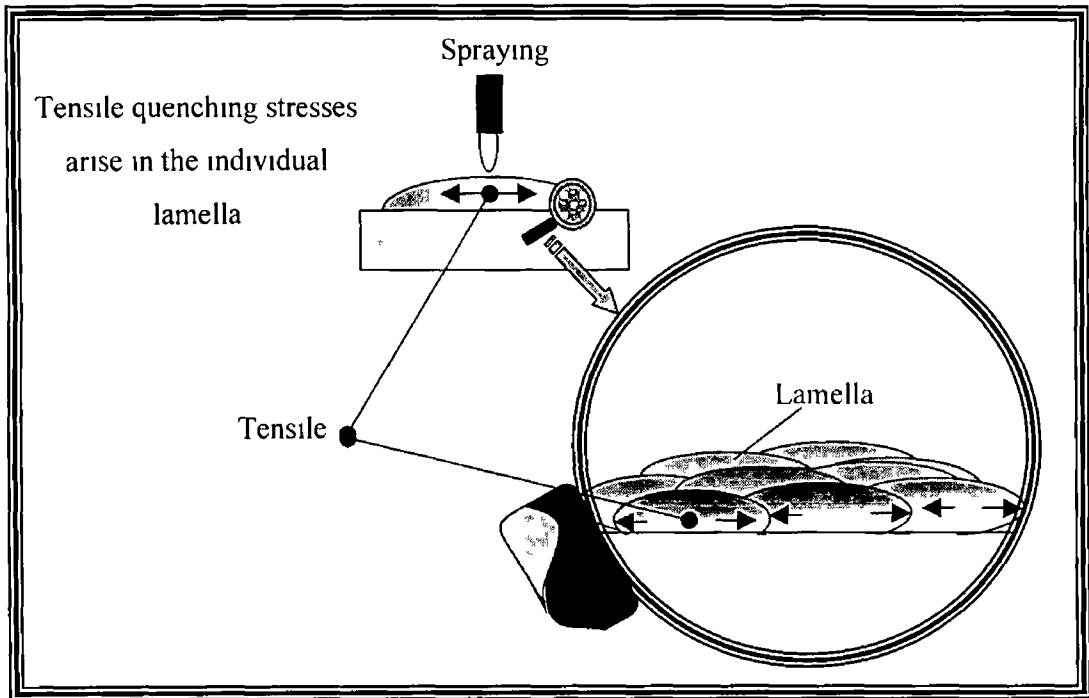


Figure 9, Schematic of quenching stress

The quenching stress is as follows

$$\sigma_q = E_c \varepsilon \quad \text{Equation 1}$$

and the thermal strain is given by

$$\varepsilon = \frac{\Delta L}{L} = \alpha_c \Delta T \quad \text{Equation 2}$$

therefore

$$\sigma_q = \alpha_c (T_L - T_s) E_c \quad \text{Equation 3}$$

Where,

$\sigma_q$  = quenching stress

$E_c$  = elastic modulus of the coating

$\varepsilon$  = thermal strain

$\Delta L$  = change in length due to the increase / decrease in temperature

$L_o$  = original length

$\alpha_c$  = coefficient of thermal expansion of the coating

$\Delta T$  = change in temperature

$T_L$  = the temperature of the individual lamella material at impact with substrate

$T_s$  = the temperature of the substrate

When deposition is ceased or interrupted, cooling stresses 'generate', due mainly to the mismatch in the thermal expansion coefficients of the substrate and the coating;  $\alpha_s$  and  $\alpha_c$  respectively. Whether the cooling stress in the coating is tensile or compressive depends upon the relative values of these expansion coefficients. If, as the temperature decreases, the coating contracts to a greater extent than the substrate ( $\alpha_c > \alpha_s$ ), a tensile stress is generated in the coating. This may lead to adhesion loss and cracking of the coating or formed material [50]. If the coefficients are equal, then no cooling stress will develop. However, if the coating contracts by a smaller amount than the substrate ( $\alpha_c < \alpha_s$ ), the resulting cooling stress will be compressive as shown in figure 10.

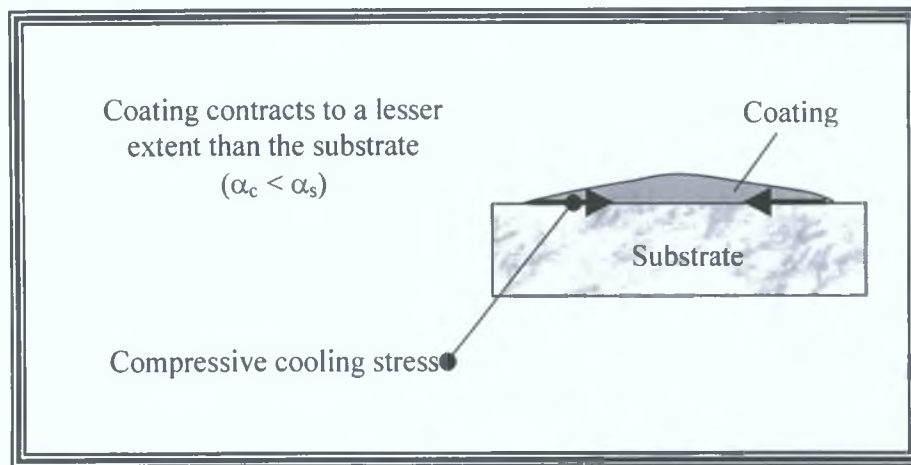


Figure 10, Schematic of cooling stresses generated in a coating.

The cooling stress is superimposed upon the tensile quenching stress with the result that, as summarised in Pawlowski [43], the nature of the overall residual stress may be determined by the following criteria:

- a)  $\alpha_c < \alpha_s$  stresses in the coating may be either tensile or compressive
- b)  $\alpha_c = \alpha_s$  stresses in the coating are tensile
- c)  $\alpha_c > \alpha_s$  stresses in the coating are tensile

The possibility of either tensile or compressive stress when  $\alpha_c < \alpha_s$  arises because a tensile stress will remain in the deposited material if the magnitude of the compressive cooling stress is less than that of the tensile quenching stress and when the coating is applied at a temperature higher than that of the substrate temperature [51]. However, if the cooling stress is greater, then the resultant is compressive. The implication of this is that high tensile quenching stresses can be negated by the compressive cooling stresses, through appropriate selection of the deposited material and substrate, however the compressive stress dominates as coating/forming thickness increases. The generation of residual stress due to increasing deposit thickness reduces the bond strength of the material, according to Greving et al. [51]. This reduction in bond strength, is attributed to the relationship between the residual stress and the 'free edge effects' in the deposit [51]. In-plane tensile stresses, acting in the same direction as the residual stresses in the deposit, cause free edge debonding of laminate plates, causing a peel-back mechanism between the deposit and the base material [52].

A free body diagram of the deposit containing residual stress is shown with the edge effect in figure 11. The residual stress in the deposit produces a tensile stress at the edge, where the deposit tries to separate from the base material, as shown in figure 11 (a). Figure 11 (b) shows a tensile residual stress in the x-direction for a thin coating. The edge effect is a stress distribution in the y-direction with tension at the edge compression away from the edge. The shape of the  $\sigma_y$  stress distribution satisfies equilibrium of the free body diagram. Two important characteristics of the  $\sigma_y$  stress distribution exist, the first is a moment equilibrium about point 2 of the free body diagram in figure 11, which requires that the  $\sigma_y$  stress distribution be tensile at the free edge. The second important characteristic is that if the coating is thicker, the moment caused by the residual stress in the deposit is larger, as shown in figure 11 (c). Therefore, the  $\sigma_y$  stress distribution must increase to balance this larger moment, the results is a higher tensile  $\sigma_y$  stress at the edge. The conclusion is that the thicker the coating, the higher the tensile edge stresses, hence this will increase the tendency for debonding.

Post heat treatment using a furnace, is generally used to change a deposit materials' phase composition, however this process is also used to stress relieve (reduce thermal stresses generated during the thermal spraying process) components to a stress free state.

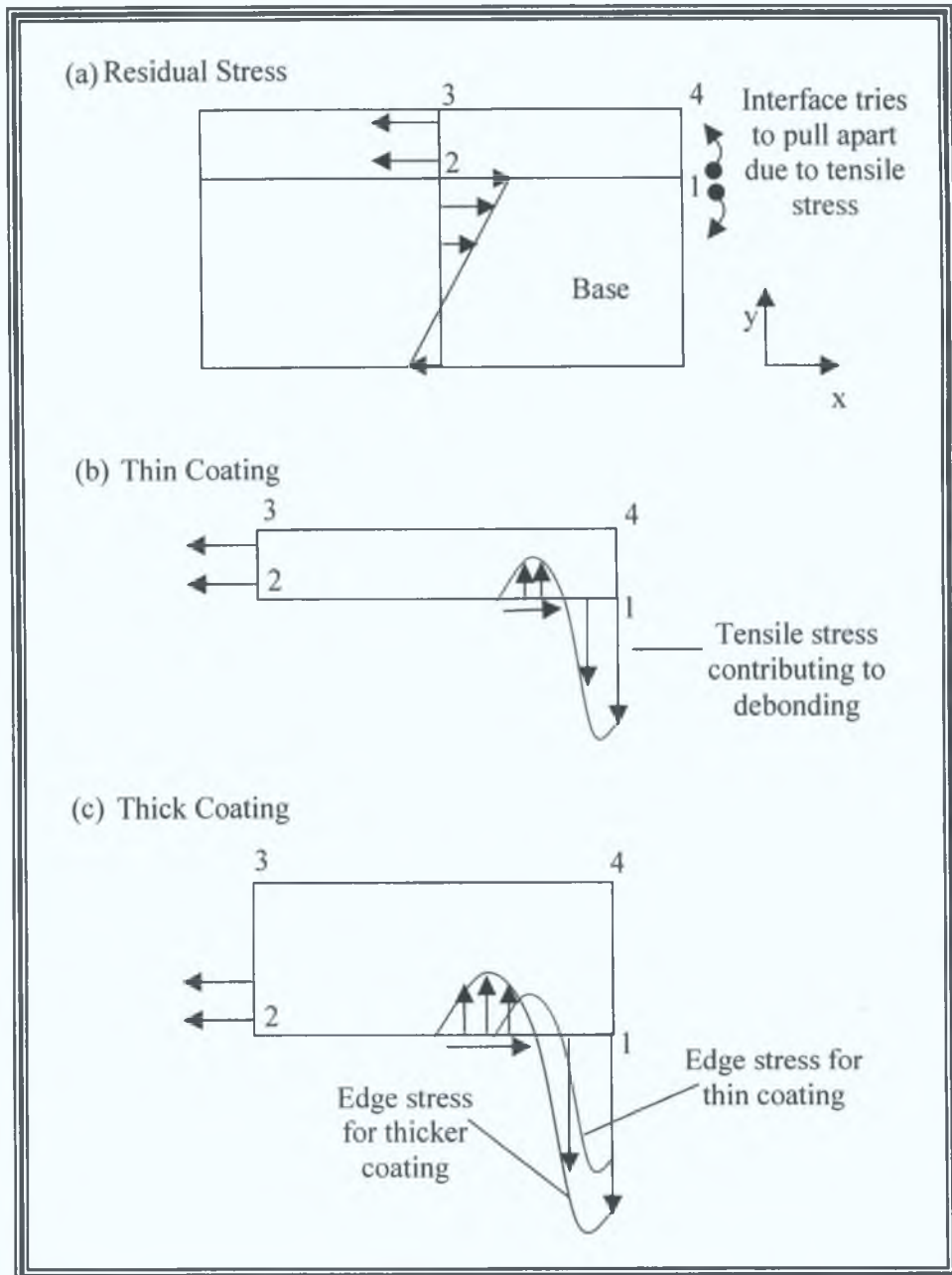


Figure 11, Effect of coating thickness and tensile residual stress on free edge debonding tensile stresses, adapted from [51].

## 2.7 COATING AND FORMING MATERIALS

METCO have characterized nineteen out of thirty one powder materials suitable for deposition by their HVOF Diamond Jet System [53]. Over the history of the HVOF research in the Dublin City University Materials Processing Research Centre, four of the Sulzer METCO powder materials have been examined: Nickel Chromium Alloy, Stainless Steel, a Tool Steel Match and Tungsten Carbide-Cobalt. As the Diamalloy 2003 tungsten carbide-cobalt material is used in the current study to fabricate both thick engineering coatings and formed components, this material is addressed in the following section.

Details of the Tungsten Carbide-12%Cobalt powder (Diamalloy 2003) are given in table 4. This powder is a fine cast and crushed carbide-cobalt powder. Diamalloy 2003 meets the Aerospace Material Specification ASM 7879 and is recommended for applications which require a fine as-sprayed surface. Typical applications in the gas turbine industry include the coating of aircraft flap tracks, expansion joints, compressor air seals, fan duct segments and stiffeners, and mid span supports [21]. Other applications include servomotor shafts, cam followers and cylinder liners. In order to understand how the tungsten carbide-cobalt behaves during the thermal spraying cycle, it is necessary to investigate the production route of this powder. Further information on the production of tungsten carbide-cobalt and its resulting thermally sprayed microstructure may be found in my additional report [34].

Table 4, Tungsten carbide cobalt powder data [53].

Product	Powder Type	Average Particle Size
Diamalloy 2003	W <sub>2</sub> C/WC (Tungsten Carbide) -Balance Co (Cobalt) -12%	14µm

## 2.8 FORMING

### 2.8.1 Introduction

Forming is an old art, examples of formed jewellery made of gold date back to 3000BC [54]. The primary objective of metal forming is to produce a desired shape change and therefore in this process, it must be recognised that material properties affect the process, and processing alters the material properties [55]. Further information on metal injection molding (MIM), powder casting methods, and the conventional sinterforming are all addressed in my additional report [34].

### 2.8.2 Spray Forming

Spray forming is one of numerous methods of producing engineering components. It involves heating a powder material to its melting temperature and impinging the individual particles or the atomised material onto a flat substrate. Rapid solidification begins as the particle is in flight until it becomes in contact with the substrate or pre-deposited material. This technique generally used in production is called the Osprey process (see report [34] for more details).

Spray forming can be accomplished with many different thermal spray technologies yielding a range of materials with different properties. Monolithic materials, composite materials, and multi-layer materials have all been fabricated and their properties are comparable cast versions of the parent material [35]. However, success has been limited to low thickness components. The HVOF technique is generally used as a coating process, but previously has been employed to spray-form industrial components due to the process flexibility and superior deposit properties (high bond strength and low porosity). Tensile properties of stainless steel 316L sprayed using the HVOF system were compared to wrought and cast 316L samples by Voggenreiter, et al. [56] and it was found that the HVOF spray deposits yielded the highest strengths of the three. Thin walled near net shaped components, have been successively produced by previous research groups [57], including in the

Dublin City University's Materials Processing Research Centre (MPRC) as shown in figure 12, [30].

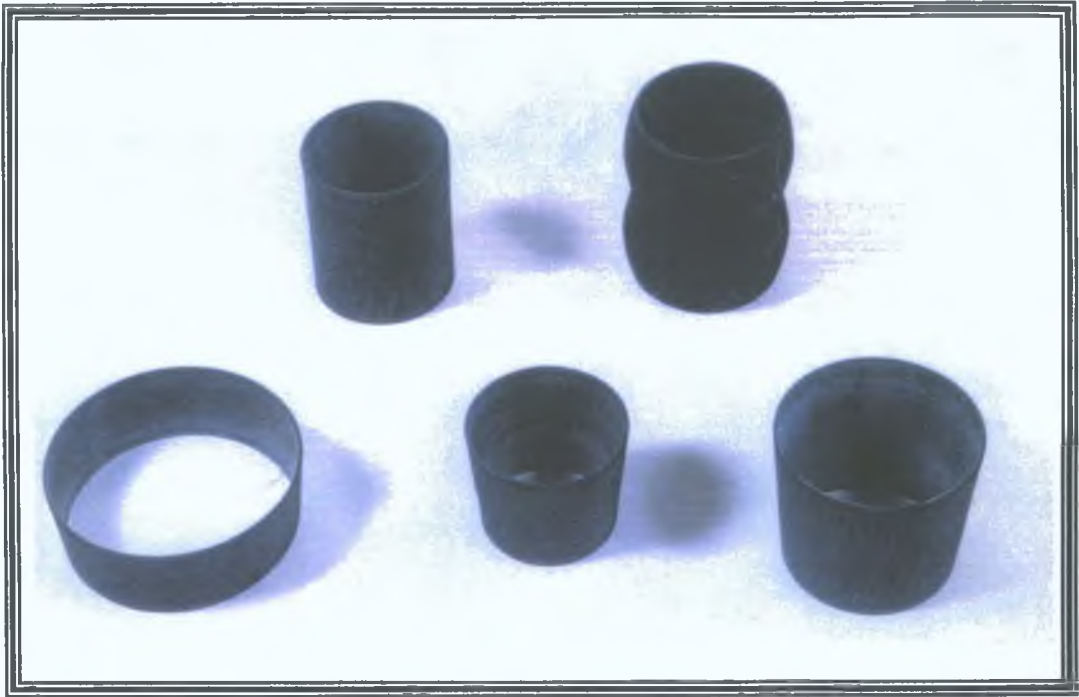


Figure 12, WC-Co Cylindrical components, manufacture using the HVOF process [49].

This report shows that the Diamond Jet HVOF process has the potential to fabricate thick complex shaped components such as cutting tool inserts or possibly larger components by controlling its parameters. The research has optimized the spraying parameters, to increase thickness, reduce residual stress, increase hardness and decrease porosity. This was done by spraying a tungsten carbide-cobalt deposit onto a forming die, then releasing the deposit to produce a free-standing component. Therefore while optimization of the spraying parameters involve producing 'coatings', these 'coatings' were later transformed into formed components. The spray formed components was then compared to sintered tungsten carbide-cobalt components mechanical and physical properties.

## 2.9 SPRAY PROCESS MODELLING

Due to the recent advances in thermal spraying technology, considerable research emphasis has been placed on the development of models capable of predicting what happens at various stages during the process. In order to gain a deeper knowledge of the mechanisms involved in thermal spraying, it is necessary to isolate the factors affecting these constitutive properties (for example residual stress generation) and in doing so quantify the effect of the individual factors. Further information on the various types of modelling carried out in the thermal spray area may be found in my report [34].

Finite Element Analysis (FEA) is a useful tool, used to predict an outcome of a particular engineering situation, however it is only useful if it is validated by experimental results. It is important to remember that numerical techniques will never yield the exact result of an engineering problem, hence the user must always question his/her theoretical results no matter how close they come to the experimental results. This statement will be addressed in more detail later in the report.

---

# EXPERIMENTAL EQUIPMENT AND PROCEDURES

---

## 3.1 INTRODUCTION

In the present research, a HVOF thermal spraying facility was used to produce coatings and to investigate the possibility of producing free-standing engineering components. The facility consists of three main units:

1. Spraying system
2. Support system
3. Controlling system

These systems are integrated together for the production of coatings, or thermally spray-formed engineering components. The spraying system equipment was supplied by Sulzer METCO, the developers of the Diamond Jet (DJ) HVOF system, whereas the support and controlling systems were purchased from individual companies. Figure 13 shows a schematic diagram of the layout of the complete facility.

In addition to the process equipment used, equipment used to measure various characteristics of the coating/forming material are also presented, along with the procedure used to conduct these measurements.

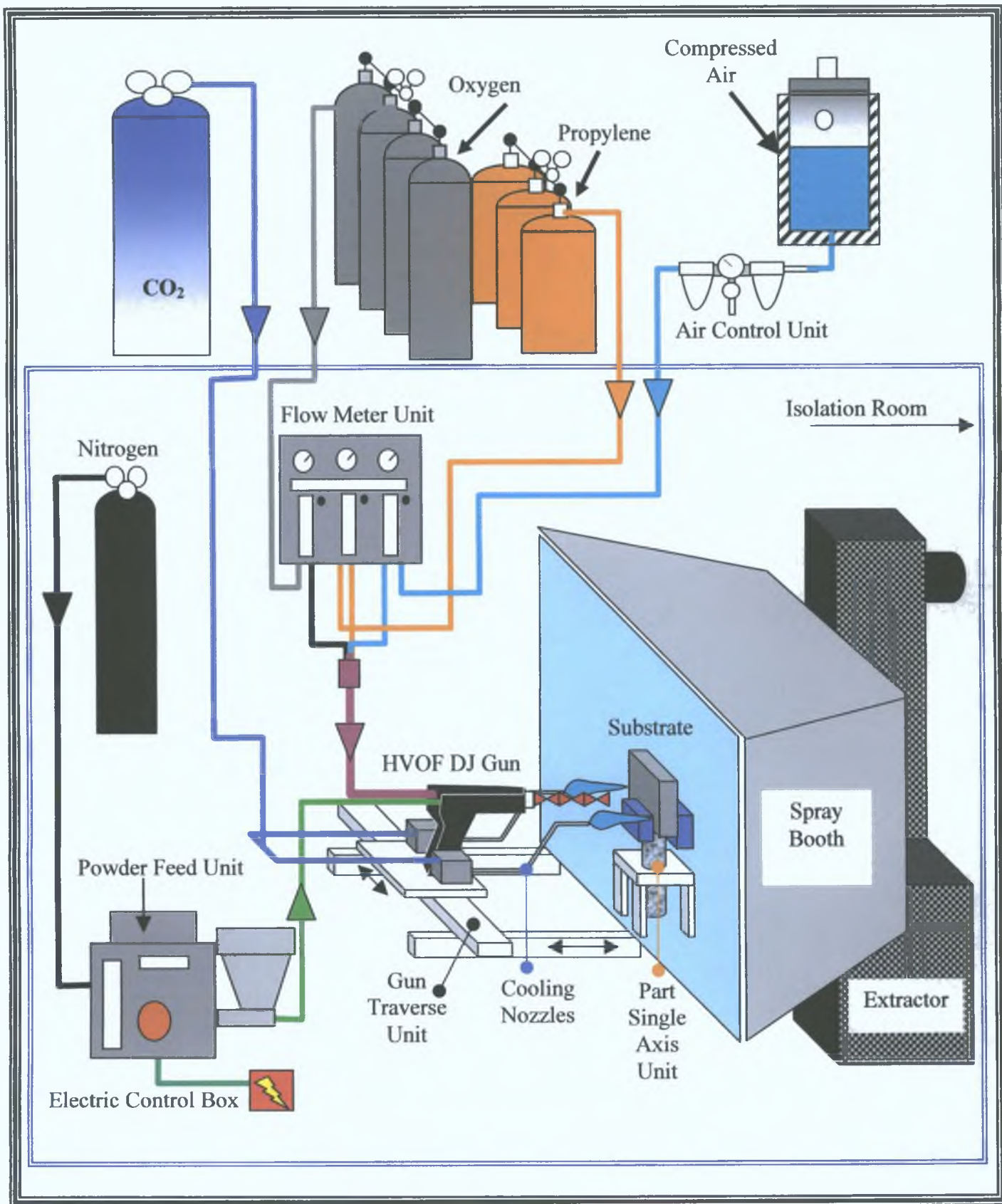


Figure 13, Schematic of the HVOF thermal spray unit layout.

## 3.2 HVOF THERMAL SPRAYING SYSTEM

The objective of the HVOF process is to transfer kinetic and thermal energy to powder particles, with high efficiency. This energy is achieved by a combination of gases to combust and propel these particles. The HVOF thermal spraying system consists of a gas supply unit, flow meter unit, powder feed unit, and a Diamond Jet (DJ) gun, all supplied by Sulzer METCO. Description of these units and their working principles are presented in my additional report [34].

### 3.2.1 Supporting Systems

Thermal spraying equipment should be operated in a safe and workable environment. Safety for the operator is very important, therefore proper functioning facilities must be in place before the commencement of spraying. In addition powder materials are very often hazardous, therefore personal safety equipment must be worn. Under the heading of supporting systems, the following are discussed in my additional report [34]: the spray booth and exhaust system, facility isolation, electrical power supply, and safety equipment.

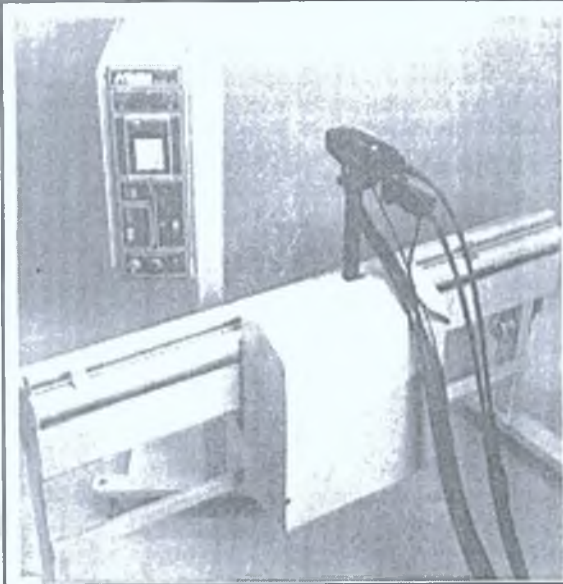
### 3.2.2 Additional Equipment

A clean substrate surface is of prime importance for good quality coatings, and there are many methods of preparing substrates surfaces, one method been grit blasting. Grit blasting (using a Ventublast Mammouth, see report [34] for more details) can often be used as an dry particle erosion device and as a shot peening operation, which normally induces residual stress in a component, however this was also used to reduce thermal stresses (those generated during deposition) within a coating. After spraying, post-heat treatment relieves internal stresses in the coatings and spray formed components, hence in this case a furnace (provided by Lenton Thermal Designs, see report [34] for more details) is used.

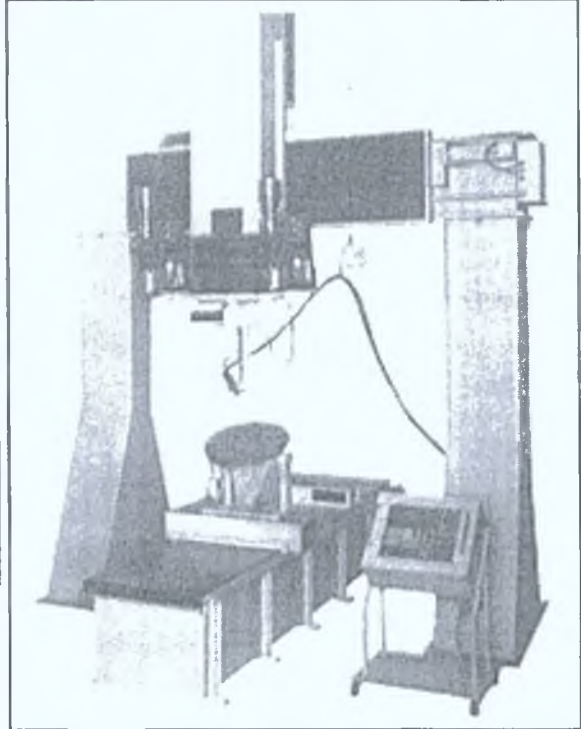
### 3.3 FACILITIES DEVELOPMENT

At the onset of the current research, modifications to the existing system were required to upgrade the facility for repeatability, process control and accurate measurement (distance, temperature and residual stress). Previously to the research presented here, thermal spraying at the Materials Processing Research Centre was carried out manually (the gun was hand held, hence spraying distances were estimated), which lead to some variability in spraying distances (and in turn spraying temperature). There are many thermal spray automation systems available, as shown in figure 14. Some of these automated systems move in one or two directions (traverse units), or in the case of multidirectional deposition, robotic systems are used to move the gun/torch [58]. In the case of coating cylindrical components, either a lathe or a turntable is used to move the component. In all of these cases, traverse and rotational speeds must be calculated to yield quality coatings [59]. In the present research, a specially designed system of controlling the spraying distance was implemented as part of the present work, and comprises of a linear traverse unit. In order to produce large deposit components, a part single-axis unit was designed.

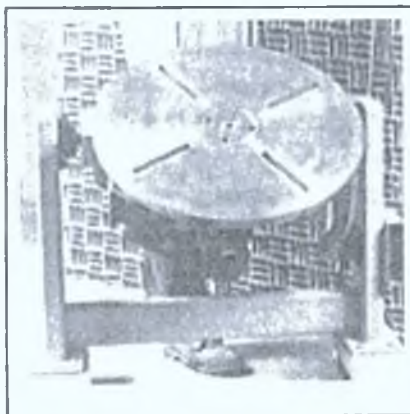
In an effort to reduce residual stress, interruption to spraying was previously the only method of controlling spraying temperature to a set value. The result was the formation of almost distinct layers in the sprayed microstructure, which formed a brittle coating or component. Therefore forced cooling, by the use of a carbon dioxide cooling system, was required to constrain the spraying temperature. Temperature was previously measured by an optical pyrometer, which proved unsatisfactory because the measurement it recorded for spraying temperature was affected by the flame of the spray gun. Thus a system incorporating thermocouples was utilised in the present work. Each of these system developments are described in the following sections.



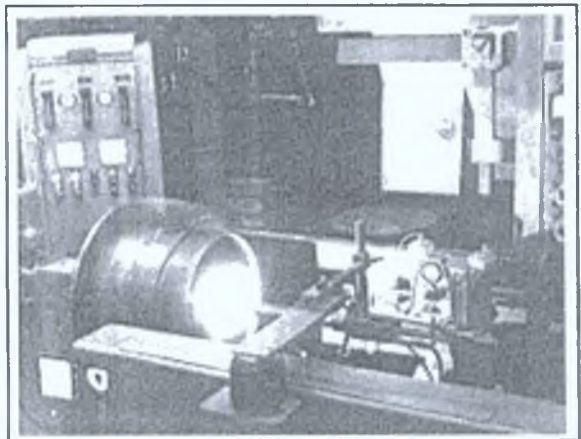
Two Axis Gun Traverse Unit



Multi-Axis Gun Manipulator



Turntable



Spray Lathe

Figure 14, Various types of thermal spray automation systems, adapted from [58].

### 3.3.1 System Automation

#### (A) Gun Traverse Unit

Manual operation of a thermal spraying process, causes an increase in residual stress in the deposited material, as will be shown later. Hence to overcome such a problem, a semi-automated process for traversing the spray gun was required. To traverse the spray gun back and forth, a LX-L20 Series Linear Stepper Motor (LX stands for Linear X-direction), developed by the Parker-Hannifin Compumotor Division, which operates using electrical magnetic principles was utilised. The stationary element is referred to as the platen, and the moving element on which the gun is mounted, is called the forcer, figure 15. Using a specially written computational program, traverse distance, speed and accelerations may be controlled to accomplish an ideal path of motion of the gun during spraying. The traverse unit itself operates in the x-direction, however the y and z-directions may also be adjusted prior to deposition.

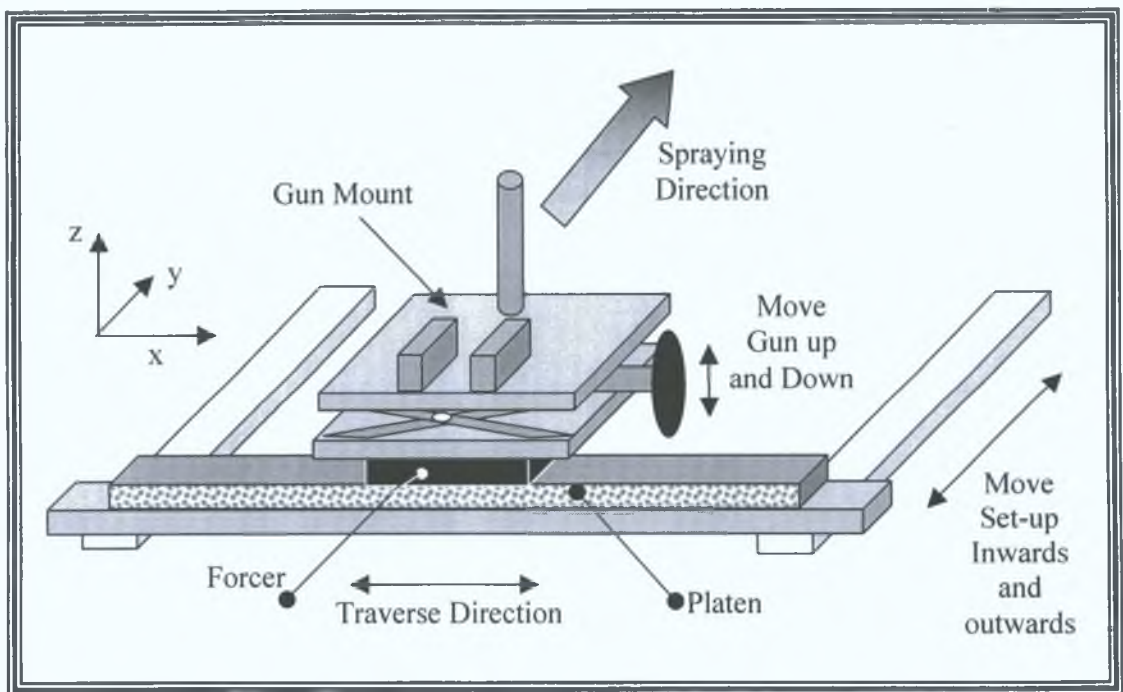


Figure 15, Various planes and directions relevant to the linear traverse unit.

Depending on the component to be fabricated, a single axis (X-plane) in which the gun would traverse from left to right, was deemed appropriate for the HVOF process. A second axis (Y-plane) allows the gun mount, forcer and platen to be fixed at various spraying distances, however this adjustment of distance is set before deposition. An adjustable platform was designed to give various heights in the Y-plane, which could be changed manually to align the guns' nozzle opening to that of the receiving substrate. A third axis (Z-plane) seemed less important, due to the complexity of the automation movement and also due to the geometry of the components to be fabricated.

The specification of the horizontal (X-plane) traversing unit stepper motor (described later), depended on some considerations such as the load characteristics, performance requirements and coupling techniques. The equipment comprised of a forcer and platen unit which was purchased from the Compumotor Division, this was mounted on an aluminium frame, the working principle and computational programming of the individual parts of the Gun Traverse Unit is described in Appendix 2.

### (B) Third-Axis Directional Unit

In order to produce larger coatings/components an added feature was required along with the gun traverse unit. A third-axis directional unit was designed and manufactured by Lyons [60], as shown in figure 16. A stepper motor is connected to a lead screw at one end, while the component clamp and adjoining structure is connected at the other end of the screw thread. For support, two guide bars are aligned at either side of the lead screw. When the motor rotates the lead screw, a fixed (fixed to the under part of the spray booth, as shown in figure 16) drive mechanism works against the lead screw, moving the full mechanism (and in turn the component clamp) either up or down depending on the rotational direction of the stepper motor. One pass of the HVOF DJ gun deposit can produce a spray deposit of up to 12mm wide (depending on the spraying distance used and the powder feed rate). In this width only about 60% of the deposit has a high concentration of

material. When the gun traverse unit makes one pass, a signal (using the travel limits) is sent to the third-axis unit control system, to shift the component either up or down by a specific distance. Hence when the gun deposits the second layer, the deposit builds up the low density areas of the coating, as shown in figure 17. The working principle and computational programming of the Single Axis Unit is described in Appendix 2.

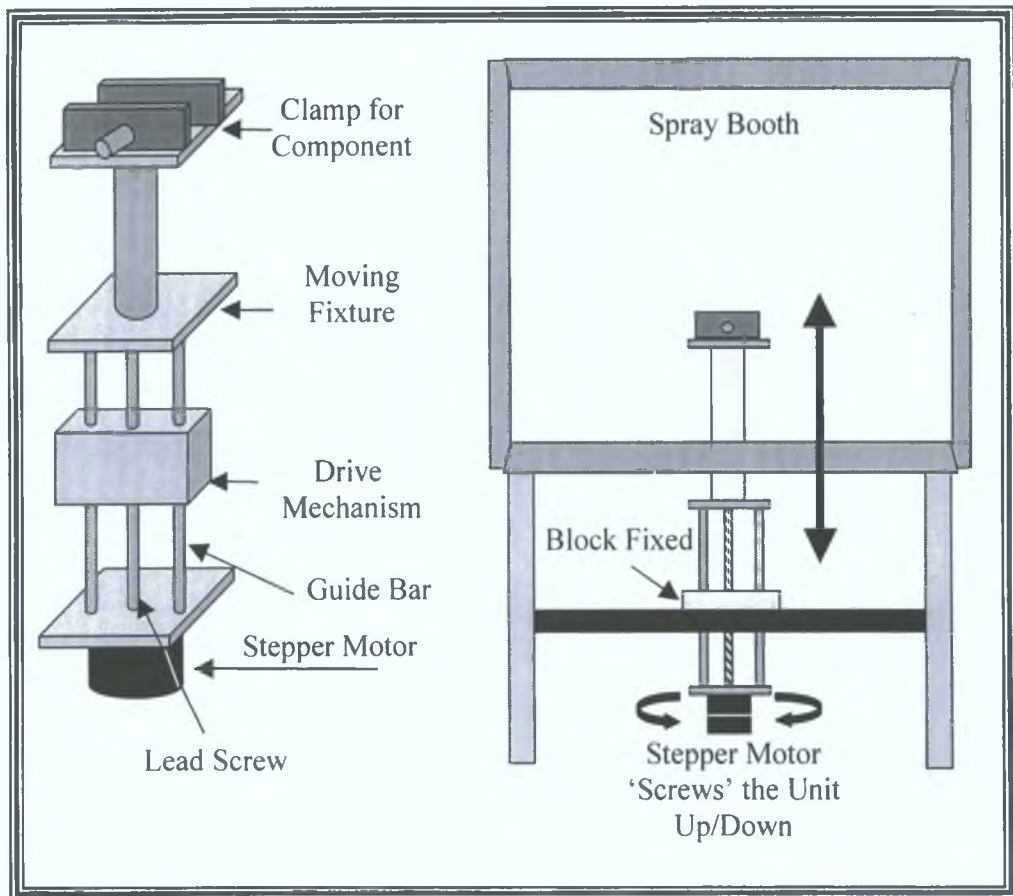


Figure 16, Schematic of the third-axis directional unit, adapted from [60].

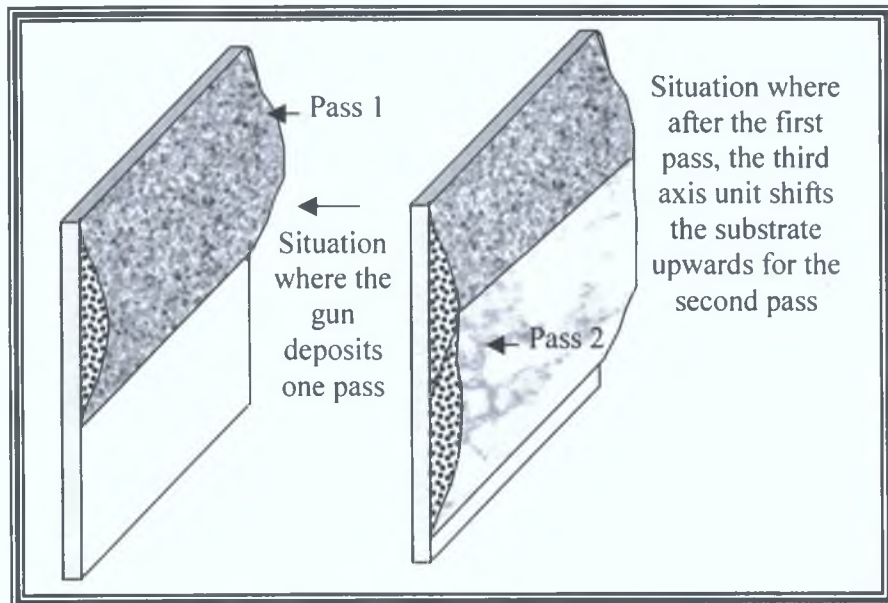


Figure 17, Schematic shows how shifting the substrate up/down facilitates the deposition of large components.

### 3.3.2 Cooling System

It was hoped that the introduction of a carbon dioxide cooling system into the HVOF system would allow continuous spraying, thus producing a uniform microstructure. This proposal was based upon the work carried out by the B.O.C. Gases Company (U.K.) [62,63]. The Materials Processing Research Centre HVOF system was adapted to include a Carbon Dioxide cooling system. Attached to the gun mount, are two carbon dioxide cooling solenoid consoles and nozzles, as shown in figure 18. Pressure from the gas cylinder feeds the liquid carbon dioxide through the nozzles onto the die, triggered by a switch connected to the CO<sub>2</sub> consoles. As deposition occurs the carbon dioxide cools (liquid carbon dioxide operates at  $-78^{\circ}\text{C}$ ) the sprayed region, thus reducing and controlling the substrate temperature during spraying.

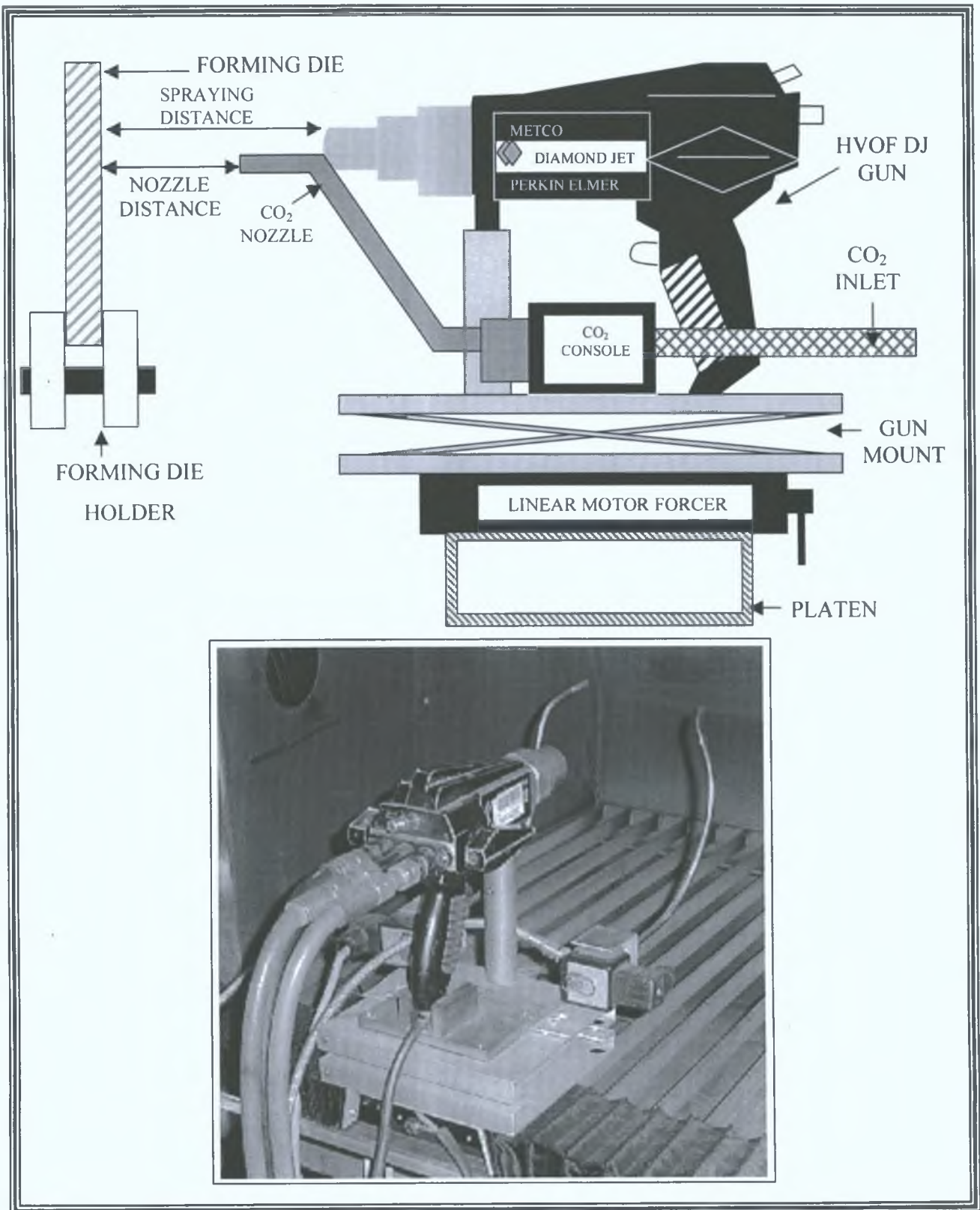


Figure 18, End view of DJ gun, traverse unit and carbon dioxide cooling system.

### 3.4 TEMPERATURE MEASUREMMENT SYSTEMS

Continuous temperature measurement is essential to monitor the deposited material temperature while spraying. Two systems of measurement were investigated, one an optical method such as the pyroscope, and secondly a method using a series of thermocouples, connected to a Pico TC-08 thermocouple converter.

#### 3.4.1 Pyroscope

The optical pyrometer or optical fibre thermometer used in the present study, as shown in figure 19, is made by Accufibre and is of the type Model 10 (modified low temperature), which measures temperatures in the range of 200 to 1000°C. The pyrometer operates on the principle that all substances at temperatures above absolute zero emit radiant energy, due to the atomic and molecular agitation associated with the temperatures of these substances. As temperature increases the rate of emission of the radiation per unit area increases. The optical pyrometer 'collects' the radiant energy from the work piece from a range of a few millimeters to several meters (approximately 4 meters), thus is practical when direct contact or close proximity sensors are impractical. In the case of thermal spraying, radiation emitted from the hot molten particles and from the flame influences the measurement of temperature from a forming core. To avoid this influence, a metallic tube was developed by Helali [49] to 'house' the pyrometer, consisting of two shields, with a small hole in each shield, so that only the radiant energy of the forming core reached the sensor as shown in figure 19. Internally the housing tube was painted black to absorb the radiation from the sprayed materials and the flame.

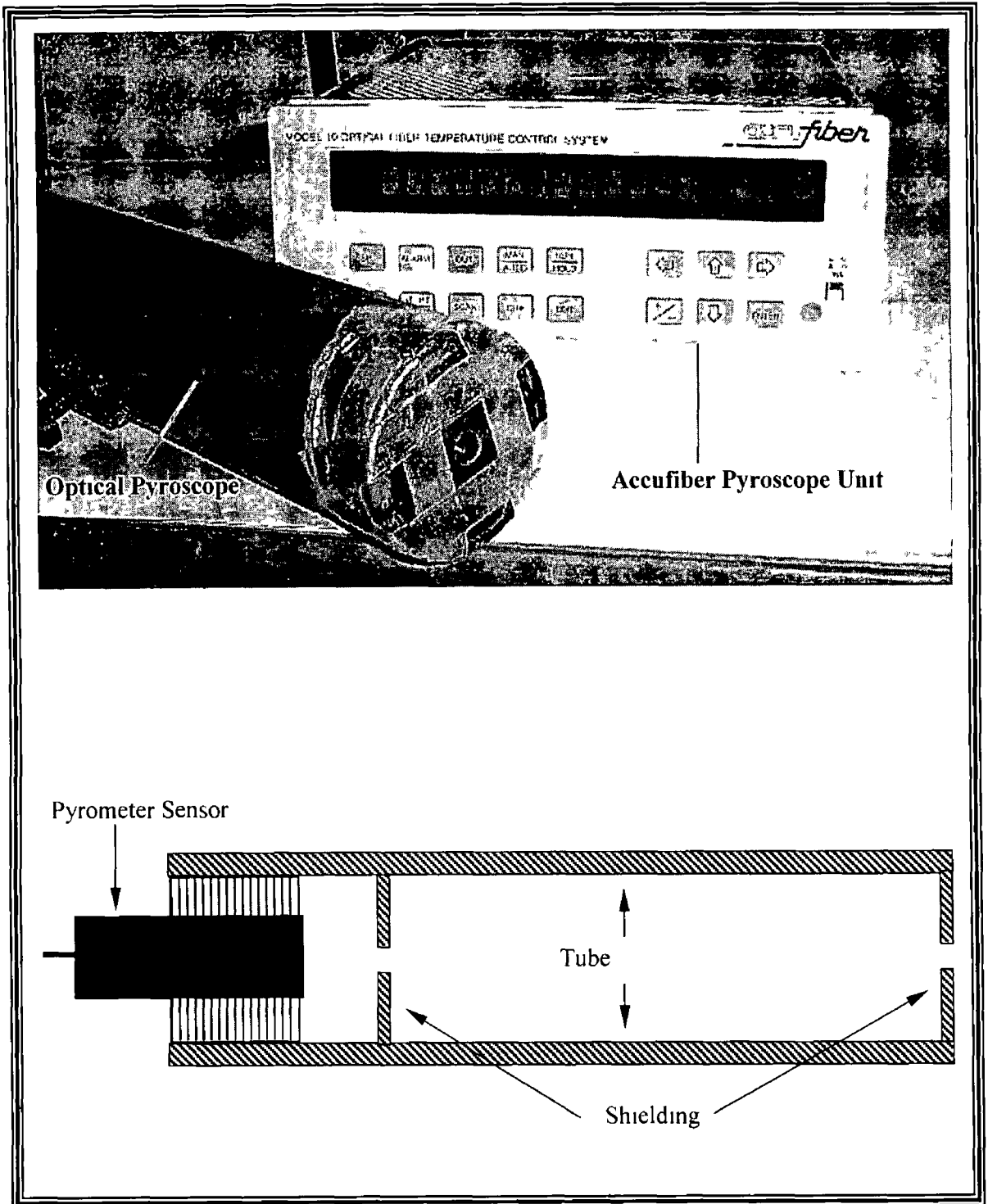


Figure 19, Photo of the optical pyrometer used for temperature measurement and the metallic tube holding the pyrometer sensor

### 3.4.2 Temperature Logging Equipment

The temperature logging equipment used in the study is known as Pico TC-08 Thermocouple to PC Converter (figure 20), developed by Pico Technology Limited. The Pico TC-08, eight-channel thermocouple to personal computer converter can measure temperatures in the range of  $-270$  to  $1800^{\circ}\text{C}$ , and works for a wide range of thermocouple types and probes. The converter is attached to the serial port of a computer and a specific program allows eight individual temperatures to be measured at intervals in the range of 1 millisecond to several hours. The results are both tabulated and plotted for the operators' convenience. The type of thermocouple presently used is the K-type, with an overall range of  $-220$  to  $1300^{\circ}\text{C}$ , and an accuracy of  $0.5^{\circ}\text{C}$ . The thermocouples were fixed at various positions onto the substrate for temperature measurement.

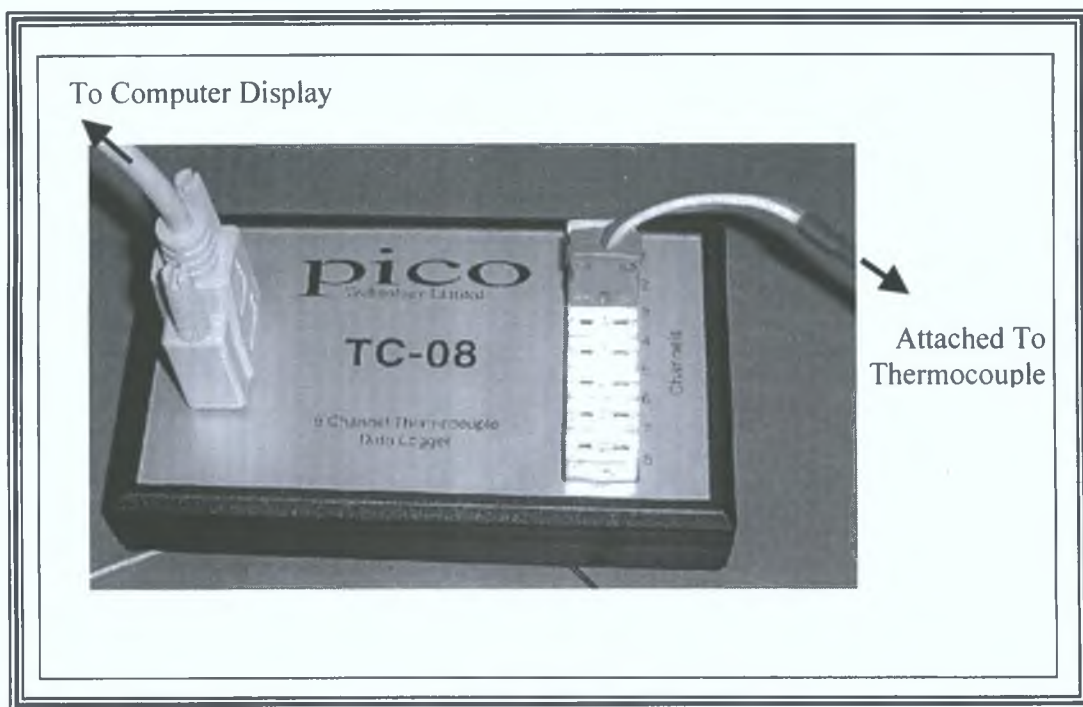


Figure 20, Photo of the Pico TC-08 thermocouple device used to measure deposition temperature.

### 3.5 HVOF SPRAYING PROCEDURES

The entire HVOF thermal spraying process used to produce WC-Co coatings and the spray-formed components is described in the following sections: surface preparation, pre-heat treatment, spraying process and the post-heat treatment.

#### 3.5.1 Surface Preparation

##### (1) Adhesive Applications

The substrate surface finish and integrity is crucial for the application of thermally sprayed coatings, [64, 65]. Although surface cleanliness is impossible to achieve in the scientific sense, nevertheless adequate surface treatment has proved to provide sufficient bond strengths between the deposit material and the receiving substrate [66]. Cleaning is generally carried out by eroding the surface by a harder material, that is with the grit (sand) blasting unit, see report [34].

##### (2) Non-Adhesive Applications

Adhesion of the deposit to the substrate may not always be required, such as where forming a component is the purpose of spraying. In this situation the substrate acts more as a die, than a supporting product. To effectively produced spray-formed components, it is essential that the deposit adheres somehow to the substrate, but is however easily removed afterwards.

One technique to achieve this is by placing an interlayer or, what is known as a releasing layer, in between the substrate and the deposit. The releasing layer may be thermally sprayed onto the substrate surface, or applied to the surface using other means. Surface preparation would then be carried out before deposition to allow adhesion of the deposit to the releasing layer. After deposition this layer would be removed by melting it away in a furnace. Another method, introduced in the present study, is to cover the internal surfaces of a forming die with aluminium foil, and again this foil can be melted away during post-heat treatment.

Previous tests carried out by Helalı et al [30], show that aluminium acts as an ideal releasing layer in the production of WC-Co components, as its melting temperature can be incorporated into the post-heat treatment of the produced material. Helalı et al [30] found that a layer of thickness 75 $\mu$ m is sufficient to ensure adhesion of the deposit to the releasing layer and that melting the aluminium at 650°C, will release the formed component from the substrate.

### 3.5.2 Pre-Heat Treatment

Moisture build up on the substrate surface may be removed by exposing the surface to a high temperature, a process known as pre-heat treating. Thermal stresses occur when there is a difference in the thermal expansion coefficient between the substrate and the deposited material. Pre-heating the substrate may reduce or elevate thermal stresses, dependent on the exposure temperature. The pre-heat temperature for a steel substrate is usually within the range of 90 to 150°C [33], but tests have shown [30], that a pre-heat temperature of 450°C reduces greater amounts of residual stress built up in WC-Co coatings, compared to temperatures below 150°C. The pre-heat temperature should be such, that the rate of expansion of the substrate and rate of contraction of the impacting must be minimised in order to control the build up of residual stress [43]. Pre-heating is carried out by igniting the gun (with a flint lighter), and heating the substrate with the guns' flame, up to the desired pre-heat temperature prior to deposition.

### 3.5.3 Spraying Process

Spraying of a material depends on the thermal spraying process used and the type of material being sprayed. In the case of the HVOF thermal spraying process, Sulzer METCO have outlined recommended spraying parameters for the deposition of Diamalloy 2003, WC-Co as shown in table 5 [31]. In terms of coating quality, optimisation of these parameters is essential.

Table 5, Spray parameters suggested by Sulzer METCO for the deposition of tungsten carbide cobalt [31].

	Tungsten Carbide-Cobalt
<b>Spray Parameters</b>	
• Oxygen pressure (Bar)	10.3
• Oxygen flow (SLPM†)	265.0
• Propylene pressure (Bar)	6.9
• Propylene flow (SLPM†)	73.0
• Air pressure (Bar)	5.2
• Air flow (SLPM†)	325.0
• Nitrogen pressure (Bar)	12.1
• Nitrogen Flow (SLPM†)	325
Spray distance (mm)	200
Powder feed rate (gmin <sup>-1</sup> )	38
SLPM† = Standard Litres Per Minute	

All safety clothing and ventilation must be in place before spraying starts. The WC-Co powder is poured into the hopper of the powder feed assembly. The required nozzles for the spraying of WC-Co are cleaned and inserted into the HVOF gun prior to spraying. The oxygen bottles are opened and set to the pressure shown in table 5, then its gas flow rate is adjusted at the gas flow meter. The compressed air is then turned on, and set to the pressure and flow rate shown in table 5, for lighting.

Propylene is then finally set to its parameters. The gun is then ignited and set up for spraying the WC-Co by varying the air flow rate to 325 SLPM.

Nitrogen is allowed to flow through the powder feed unit and is also adjusted to its parameters according to table 5. The powder is fed to the gun by switching on the feed button on the gun. The flow rate of powder is then adjusted to  $38\text{gmin}^{-1}$ .

The spraying distance is controlled by the use of the linear motor, which also controls the traverse speed of the deposit. The spraying temperature maybe controlled, by using the carbon dioxide cooling system. After deposition, the substrate and adjoining spray material are ready for post-heat treatment.

#### 3.5.4 Post-heat Treatment

Post-heat treatment of WC-Co components is used for two reasons; one to release the component from the die and second to reduce the residual stress that had built up during spraying. The post-heat treatment is carried out in the furnace under a nitrogen atmosphere.

As previously described, the aluminium releasing layer is melted away in order to remove a WC-Co component away from the forming die. Heating the die assembly above the melting temperature of the aluminium ( $\approx 650^{\circ}\text{C}$ ) for a sufficient length of time (eighty minutes according to Helali [49]), dissipates all the aluminium away from the die and the spray-form component [30].

Post-heat treatment has been proved as an effective stress relief process, where tungsten carbide-cobalt coatings or spray-formed components are elevated to temperatures of  $650^{\circ}\text{C}$  [30, 67.68].

## 3.6 TEMPERATURE MEASUREMENT

Tests carried out by Helali [49] showed that the reliability of temperature readings measured by the optical pyrometer was unsatisfactory. Temperature values were inaccurate by as much as 25%, compared with readings measured using K-type thermocouples. Therefore it will be important to either increase the accuracy of the pyrometer or else to introduce a more reliable method of measurement.

### 3.6.1 Pyrometer Test

The pyrometer, which works on an optical measurement principle, was set up for temperature calibration. Two tests were carried out; one measurement of a heated metal and secondly measurement of spraying temperature.

#### (1) Measurement of a Heated Solid

Two K-type thermocouples were attached to one side of a solid stainless steel block. The block was then placed into a furnace and raised to a temperature of 1000°C. After heating, the block was removed from the furnace and placed in front of the optical pyrometer (with the thermocouples facing the pyrometer) for temperature measurement. Temperature values were recorded every second as the block cooled by both devices (pyrometer and thermocouple TC-08 device).

#### (2) Spraying Temperature Measurement

The Diamond Jet HVOF gun was set up to spray tungsten carbide cobalt onto a stainless steel substrate at a distance of 200mm. Again a thermocouple was attached to the stainless steel just under the deposition zone, to acquire an approximate spraying temperature, and the pyrometer was focused onto the deposition zone at a distance of 200mm. Temperatures measured by both the pyrometer and the thermocouple were then compared and analysed.

### 3.6.2 Thermocouple Temperature Calibration

Thermocouples are an efficient method of temperature measurement, however measuring the temperature during deposition poses problems, as the deposit coats the tip of the thermocouple, hence records incorrect readings. It is proposed as part of the current research that the spraying temperature can be measured by extrapolation from the temperature measured at the back of the substrate. The advantage of determining a relationship between the temperatures across gradients of different materials is that it allows temperature measurement to be made from the back of the die which, through a calibration curve, give actual spraying temperatures in the front-side of the die.

Based on the spray parameters given in [31], the Diamond Jet HVOF gun was fixed at a spraying distance of 200mm from the gun nozzle and the forming die. Two thermocouples were fixed onto the back and two onto the front-side of a forming die to establish a temperature gradient across the substrate/die and various thicknesses of deposit material as shown in figure 21. The temperature gradient was found by heating the front-side of the forming die with the flame of the gun, and measuring the temperature difference between the front and the back of the die and applied coatings. The temperature gradients were determined for:

1. The forming die itself
2. The die with an aluminium releasing layer
3. The die, releasing layer and two thicknesses of WC-Co forming material

The temperature of the die and relevant coatings was allowed to stabilise (around ten seconds) at each individual temperature, before values were recorded.

Using this method, spraying temperatures at various spraying distances were measured, for both normal spraying, and spraying with forced cooling (using the carbon dioxide cooling system).

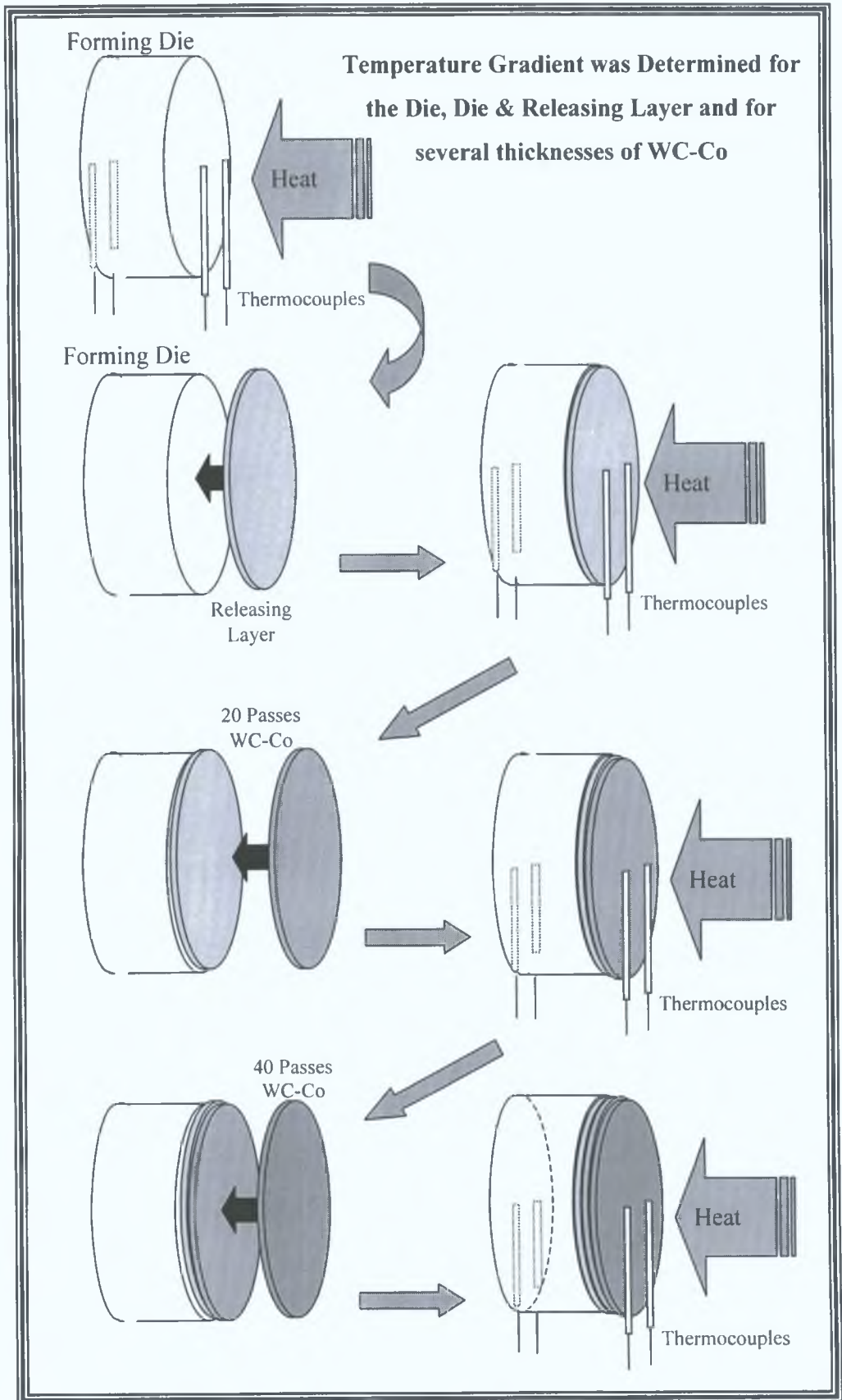


Figure 21, Schematic of the temperature calibration procedure.

### 3.6.3 Temperature Dependence On Spraying Distance

This section investigated whether deposition temperature was a function of spraying distance. If one measures the temperature of the HVOF flame, they will find that the temperature decreases with increased distance from the HVOF gun's head, hence the particles decrease in temperature as they move from the gun's nozzle [69].

With the use of the linear traverse unit (allowing for exact spraying distances), thermal spraying was carried out on stainless steel substrates at spraying distances from 125 to 260mm (at intervals of 10mm). WC-Co was sprayed at each distance, with and without forced cooling (using the carbon dioxide cooling system), to measure the resulting spraying temperature. At each distance the temperature at the back of the substrate (using three thermocouples) was measured during deposition. Using the temperature calibration procedure outlined in the previous section, a spraying temperature was determined for each spray distance. The test was carried out three times at each distance.

### 3.7 COATING CHARACTERISATION EQUIPMENT

Observation of a specimen visually either macro- or microscopically, enable the detection of large defects (adhesion failure, cracks and so on). There are numerous optical techniques available, including the Optical Microscope (OM), Scanning Electron Microscope (SEM) and X-ray Diffraction (XRD). Further information on the operation of these optical techniques may be found in my additional report [34].

The full coating microstructure description contains such information as; chemical composition (at the macro and microstructure scale), grain morphology and its orientation, defects (such as voids or second phases) and coating thicknesses. Mechanical properties such as microhardness, tensile strength, fracture strength, elastic modulus, toughness, porosity, and wear resistance can all be identified using optical techniques [70]. The report focuses on the relationship between residual stress and deposition thickness and measurement of these two parameters depend on the use of characterisation equipment such as optical techniques.

Microstructural characterisation using an optical microscope has now become a standard test in a coating/formed component's development (post deposition). However, prior to microscopic observation, the sprayed piece must be prepared metallographically. Observation of the longitudinal or traverse section of the coating (perpendicular to the coating surface) provides information about the surface of the substrate and about the changes that occurred in the microstructure through the deposit. Care has to be taken to ensure the proper grinding and polishing procedure is chosen. Blemishes resulting from poor preparation include scratches, deformation, smearing, edge rounding, pull-out, cracks, contamination, embedded abrasive, lapping tracks and staining, according to Glancy (1994) [71]. Extensive details on the grinding, polishing and etching procedures are provided in my report [34].

### 3.8 YOUNG'S MODULUS MEASUREMENT

The elastic moduli of a coating and the stresses at which material failure occurs are very important in the determination of a coating's reliability. According to Pawlowski [69], Young's modulus is influenced by porosity, hence post-heat treatment which may reduce porosity can thus increase stiffness. Young's modulus determination of a coating is difficult, as in general the coating is attached to a substrate, however there are many methods using bending theory used to calculate these properties. In residual stress determination an elastic modulus ( $E_c$ ) and Poisson's ratio ( $\nu_c$ ) for a coating is required, hence determination of these properties is crucial at this point of the report.

#### 3.8.1 Cantilever Beam Method

There are other methods of measuring the stiffness and Poisson's ratio of the coating. Rybicki, et al. [202, 203] describes a cantilever beam method for measuring both of these properties. Figure 22 shows the experimental set up used to determine the Young's modulus and Poisson's ratio, for thermally sprayed coatings. Two biaxial strain gauges are placed on the coating surface, and two placed directly opposite on the substrate side. A force is applied to the end of the substrate, thus the strain is measured to yield the two properties using the 'Laminate Plate Theory'.

The laminate plate theory is used in the cantilever beam method, to relate the unknown  $E_c$  (coating stiffness) and  $\nu_c$  (coating Poisson's ratio), to the loading of the gauge sections. This theory assumes a linear strain distribution through the thickness of the coated cantilever beam, and plane stress conditions. Figure 23 shows a schematic of the strain (a) and stress (b) distribution respectively, for a coated cantilever with applied load.

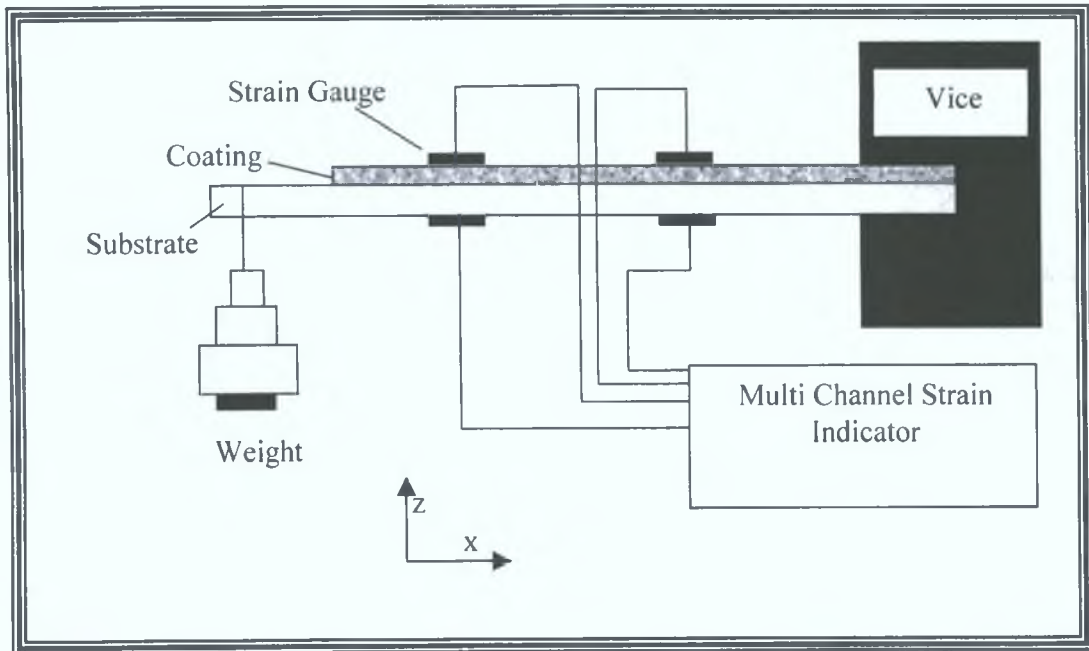


Figure 22, The Cantilever approach for measuring coating stiffness.

The difference in mechanical properties between the coating and substrate introduces stress discontinuity at the interface. The equilibrium equations for the coated beam are as follows [72,73], where the stresses ( $\sigma_x$  in the x-direction,  $\sigma_y$  in the y-direction) are related to the forces ( $F_x$  in the x-direction,  $F_y$  in the y-direction) and moments ( $M_x$  in the x-direction,  $M_y$  in the y-direction) by:

$$0 = F_x = \iint \sigma_x \, dzdy \quad \bar{M}_x = M_x = \iint \sigma_z \, zdzdy \quad \text{Equation 4}$$

$$0 = F_y = \iint \sigma_y \, dzdy \quad 0 = M_y = \iint \sigma_y \, zdzdy \quad \text{Equation 5}$$

For the coated beam,

$$F_x = w(\sigma_{xSI} + \sigma_{xSG}) \frac{t_s}{2} + w(\sigma_{xCI} + \sigma_{xCG}) \frac{t_c}{2} \quad \text{Equation 6}$$

$$M_X = w \left[ \sigma_{XSG} \frac{t_s^2}{2} + (\sigma_{XSI} - \sigma_{XSG}) \frac{t_s^2}{3} \right] \\ + w \left[ \sigma_{XCI} (t_c) \left( \frac{t_s}{2} + \frac{t_c}{6} \right) + \sigma_{XCG} (t_c) \left( \frac{t_s}{2} + \frac{t_c}{3} \right) \right] \quad \text{Equation 7}$$

$$F_Y = w(\sigma_{YSI} + \sigma_{YSG}) \frac{t_s}{2} + w(\sigma_{YCI} + \sigma_{YCG}) \frac{t_c}{2} \quad \text{Equation 8}$$

$$M_Y = w \left[ \sigma_{YSG} \frac{t_s^2}{2} + (\sigma_{YSI} - \sigma_{YSG}) \frac{t_s^2}{3} \right] \\ + w \left[ \sigma_{YCI} (t_c) \left( \frac{t_s}{2} + \frac{t_c}{6} \right) + \sigma_{YCG} (t_c) \left( \frac{t_s}{2} + \frac{t_c}{3} \right) \right] \quad \text{Equation 9}$$

where  $w$  is the width of both the coating and substrate,  $\bar{M}$  is the applied bending moment at gauge location,  $P$  the applied load,  $t_s$  and  $t_c$  are the thickness of the substrate and coating respectively,  $\epsilon_{XCG}$  and  $\epsilon_{YCG}$  are the longitudinal and respective traverse strain gauge readings on the coating,  $\epsilon_{XSG}$  and  $\epsilon_{YSG}$  are the longitudinal and respective traverse strain gauge reading on the substrate,  $\epsilon_{XCI}$  and  $\epsilon_{YCI}$  are the longitudinal and respective traverse strain at the coating interface,  $\epsilon_{XSI}$  and  $\epsilon_{YSI}$  are the longitudinal and respective traverse strain at the substrate interface,  $\sigma_{XCG}$  and  $\sigma_{YCG}$  are the longitudinal and respective traverse stress gage reading on the coating,  $\sigma_{XSG}$  and  $\sigma_{YSG}$  are the longitudinal and respective traverse stress gage reading on the substrate,  $\sigma_{XCI}$  and  $\sigma_{YCI}$  are the longitudinal and respective traverse stress at the coating interface,  $\sigma_{XSI}$  and  $\sigma_{YSI}$  are the longitudinal and respective traverse stress at the substrate interface.

The surface stresses,  $\sigma_{CG}$  and  $\sigma_{SG}$ , are related to the strains and the mechanical properties of the coating and substrate from the following:

$$\sigma_{XCG} = \frac{E_c}{(1-\nu_c^2)} (\epsilon_{XCG} + \nu_c \epsilon_{YCG}) \quad \text{Equation 10}$$

$$\sigma_{XSG} = \frac{E_s}{(1-\nu_s^2)} (\epsilon_{XSG} + \nu_s \epsilon_{YSG}) \quad \text{Equation 11}$$

where  $\nu_s$  and  $\nu_c$  are the Poisson's ratio for the substrate and coating respectively,  $E_s$  and  $E_c$  are the Young's modulus for the substrate and coating respectively, the surface strains,  $\epsilon_{XCG}$ ,  $\epsilon_{YCG}$ ,  $\epsilon_{XSG}$  and  $\epsilon_{YSG}$ , are measured with the strain gages. The interface stresses can be calculated from:

$$\sigma_{XCI} = \frac{E_c}{(1-\nu_c^2)} (\epsilon_{XCI} + \nu_c \epsilon_{YCI}) \quad \text{Equation 12}$$

$$\sigma_{XSI} = \frac{E_s}{(1-\nu_s^2)} (\epsilon_{XSI} + \nu_s \epsilon_{YSI}) \quad \text{Equation 13}$$

where the interface strains,  $\epsilon_{XCI}$ ,  $\epsilon_{YCI}$ ,  $\epsilon_{XSI}$  and  $\epsilon_{YSI}$ , can be found from the assumption of a linear strain distribution from the surface strains. Test were carried out on coated (WC-Co) aluminium and stainless steel substrates, then two of the four equilibrium equations were used to solve the stiffness and Poisson's ratio of the coating.

The least squares method minimizes a function composed of four equilibrium equations. The function  $\phi(E_c, \nu_c)$  is based on minimizing the maximum stress difference.  $M_P$  is the applied force  $P$  times the distance between the load location and the gauge location.

$$\phi(E_c, \nu_c) = \frac{(H + T_c)^2}{36} [F_x^2 + F_y^2] + [M_X + M_P] + [M_Y]^2 \quad \text{Equation 14}$$

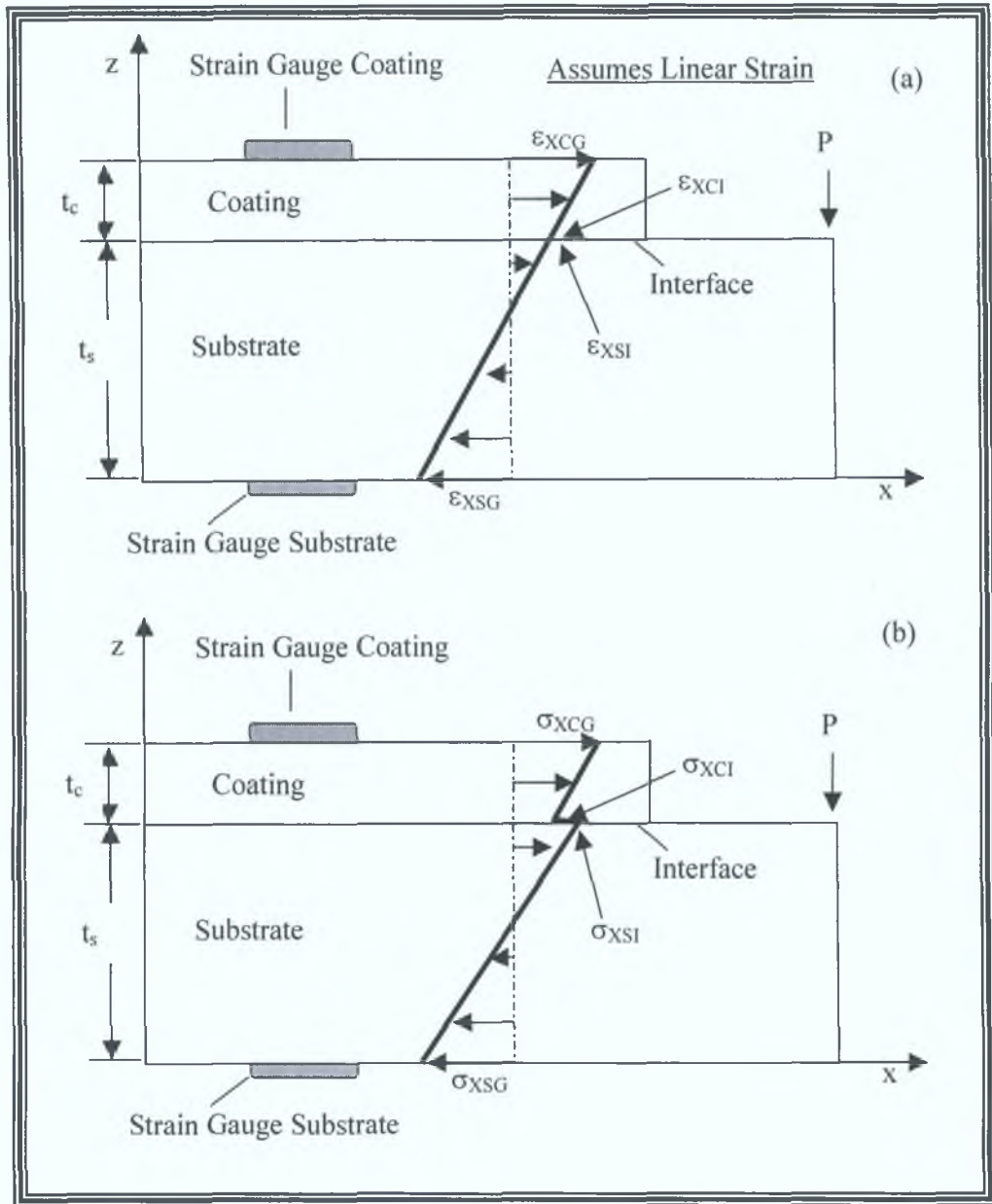


Figure 23, Strain and stress distribution for coated cantilever beam with applied load  $P$ .

### 3.8.2 Tension Testing Method

As the current research strives to produce free-standing WC-Co components, the research also endeavours to produce free-standing WC-Co tensile specimens, and together with the standard ASTM E8M [74]. The production of free-standing tensile specimens is described in a later section and successful specimens were subjected to a tensile load, to measure the Young's modulus of the material.

### 3.8.3 Other Determination Techniques

There are other techniques used to measure the stiffness of a coating, such as the three/four point bend test, indentation and the curved specimen deflection tests, however neither of these tests were used in the current research. In the three/four point experimental test the coated or free-standing sample is placed on two knife edges and force is applied through a third knife edge (three point test) or two knife edges (four point test). The bend test can be monitored acoustically to detect the crack formation (especially for brittle ceramic coatings) [75]. The elastic modulus is found from the applied load and the deflection measured when the deposit fails.

The indentation test and a curved specimen deflection test, are two Young's modulus measurement techniques, used to determine this parameter in both the perpendicular and parallel directions respectively [76]. The indentation test involves, drawing a diamond hemispherical indenter with known radius across the coating surface. After scratching under various loads, the depth of scar is measured by a stylus (used to measure surface roughness). The radius of contact between the indenter and the coating surface, together with Hertz's contact theory, calculates the Young's modulus perpendicular to the coating plane [76]. The measurement process for Young's modulus parallel to the coating plane, involves spraying a cylindrical stand-alone component. The component is compressed in the radial direction where the load is measured. Using this technique, the Young's modulus is measured in accordance to the deflection of a curved beam theory.

### 3.9 RESIDUAL STRESS MEASUREMENT

Residual stress creates the most difficulty in the production of thick spray formed components. It is important to be able to measure the residual stress within a deposit in order to control and reduce its build up by varying the spray parameters. Residual stress in thermally sprayed coatings may be measured by many techniques including a simple method using the modified 'Almen' test, similar to that outlined in SAEJ443 [77], Clyne's Method and the X-ray diffraction and hole drilling methods [78].

#### 3.9.1 The Almen Test Method

John O. Almen developed this technique primarily for measuring shot peening intensity. It was observed that shot peening a substrate generated induced stresses, which could be measured by the resulting substrate curvature. Further tests have shown that the same procedure may be used to measure residual stress in thermally sprayed coatings, known as the 'Modified Almen Method' (MAM) [79]. The free body diagram in figure 24, illustrates the bending theory used to determine the residual stress of the coating. The forces acting on the coating and the substrate, are denoted by  $F_c$  and  $F_s$  respectively;  $M_c$  and  $M_s$  are the corresponding bending moments.  $E_s$ ,  $A_s$  and  $h_s$  are the properties Young's modulus, area and height of the substrate respectively, and similarly  $E_c$ ,  $A_c$  and  $h_c$  are the properties for the coating. The coefficient of expansion for the coating and substrate are given as  $\alpha_c$  and  $\alpha_s$ .  $R_c$  and  $R_s$  are the resulting bending radius values for the coating and the substrate respectively. The bending theory and numerical formulation is described in Appendix 3 [80].

Once all of the dimensions and parameters are known (including the Young's modulus of the coating), the average stress in a coating may be found using equation 15:

$$\therefore \sigma_{\text{Average}} = \frac{F}{A_c} = \left[ \frac{\left[ -\frac{h_c}{2R_c} - \frac{h_s}{2R_s} + (\alpha_s - \alpha_c)\Delta T \right] \left[ \frac{E_c E_s h_c A_s}{E_c h_c + E_s h_s} \right]}{A_c} \right]$$

Equation 15

However one may be interested in the stress distribution across the coating and substrate, and may have to rely on the more simplistic approach of applying beam theory. Using this the stress at any point in the coating may be found by the following expression:

$$\sigma_{xc} = -\frac{E_c y}{R}$$

Equation 16

The negative sign indicates that a positive bending moment produces a negative curvature. The position relative to the neutral axis (that is  $y$ ), is positive if working above the neutral axis and negative if below, with reference to figure 25. Figure 26 shows the expected differences between the average coating stress, the measured distributed stress and the real distribution [209] in a thermally sprayed sample.

Due to the high temperatures experienced by thermal sprayed materials, the Young's modulus for a coating differs to that of material produced by other manufacturing techniques. Hence, selection of an appropriate coating Young's modulus value for equations 15 and 16, is vital to establish a stress distribution through the coating.

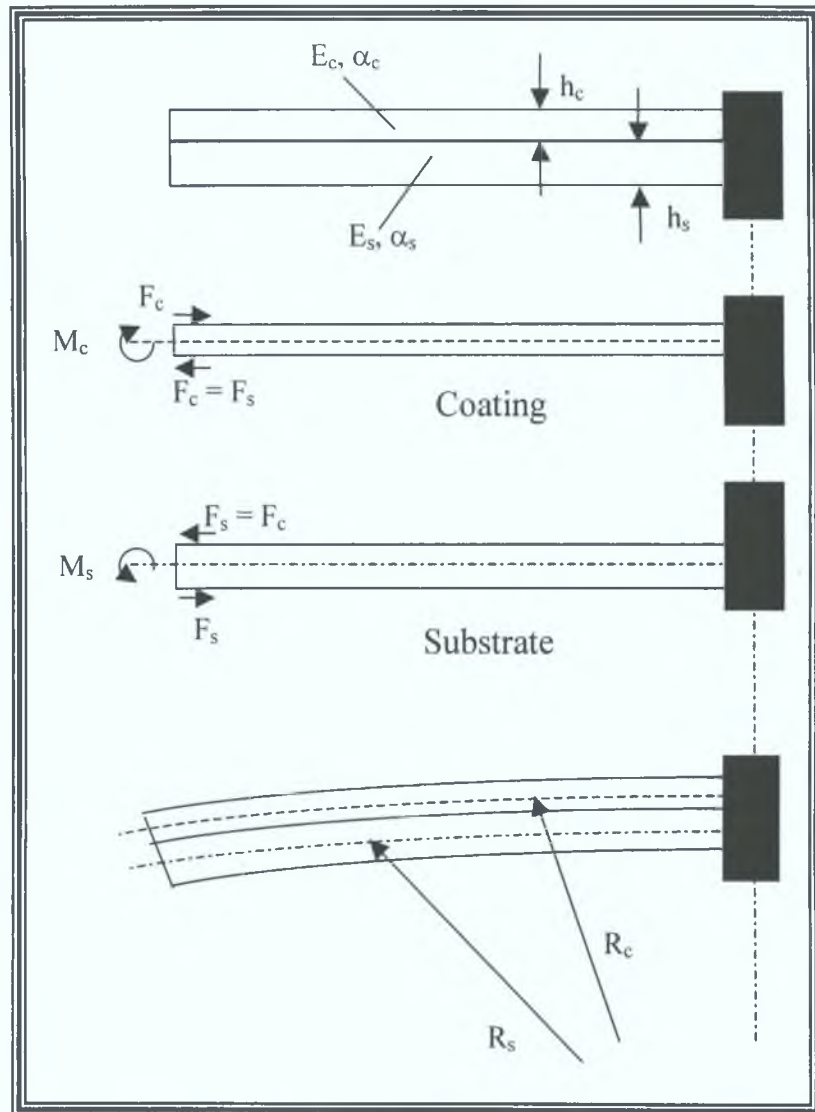


Figure 24, The MAM bending theory for the determination of residual stress.

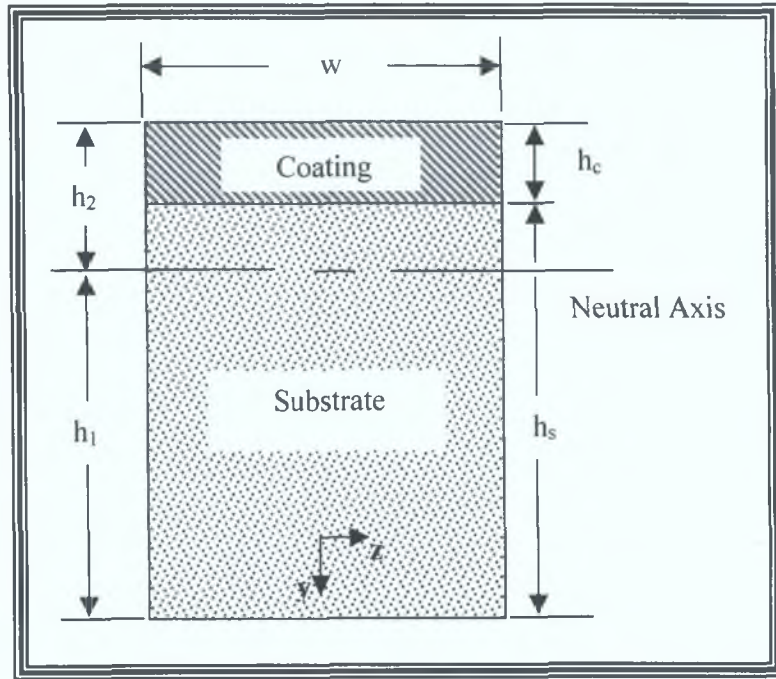


Figure 25, Schematic of the cross-section of a thermally sprayed sample.

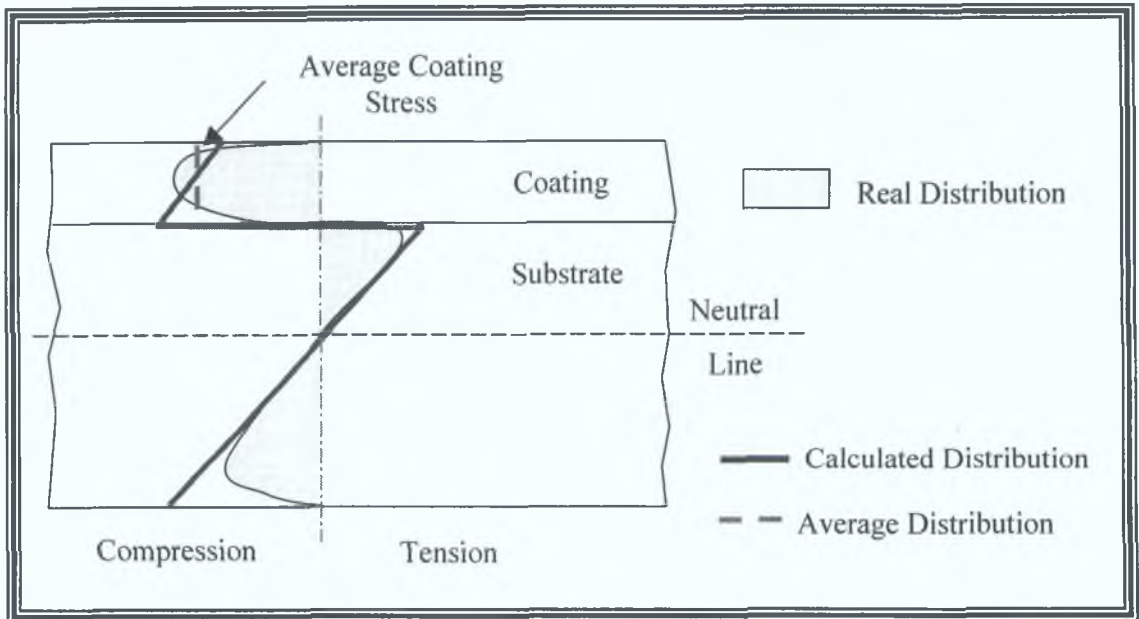


Figure 26, Real, calculated and average residual stress distribution in a coated MAM sample, where the substrate has higher stiffness than that of the coating, adapted from [79].

### 3.9.2 Clyne's Analytical Method

A closer look at the Modified Almen test Method reveals that this method does not account for 'Misfit Strain'. The main interest in this thesis lies in the stress levels, which are generated within the surface coating (and the substrate). It is useful therefore to consider the situation in terms of misfit strains, that is, relative differences between the stress-free dimensions of various layers. The simplest system is composed of just two layers, the coating and the substrate, but it may be appropriate (particularly for thick coatings) to consider the coating as being deposited as a series of layers. A further general point is that it can be very instructive to note how the system will adopt a curvature as a result of the imposition of a misfit strain. This can be useful, not only in helping to understand the mechanics of stress generation, but also for using curvature monitoring to measure residual stress levels.

Tsui and Clyne [82] used an analytical method which considers a pair of plates bonded together with a misfit strain  $\Delta\varepsilon$  in the  $x$ -direction as shown in figure 27. The resultant stress distribution, for thick deposits, was derived by Clyne [83]. The stress distributions are readily found for the simple misfit strain case, using the following expressions [83]:

$$\text{[Stress at the Top of the Deposit]} \quad \sigma_c \Big|_{y=h_c} = -\Delta\varepsilon \left( \frac{E'_c h_s E'_s}{h_c E'_c + h_s E'_s} \right) + E'_c \kappa (h_c - \delta)$$

Equation 17

$$\text{[Stress at the Bottom of the Deposit]} \quad \sigma_c \Big|_{y=0} = -\Delta\varepsilon \left( \frac{E'_c h_s E'_s}{h_c E'_c + h_s E'_s} \right) + E'_c \kappa \delta$$

Equation 18

$$\text{[Stress at the Top of the Substrate]} \quad \sigma_s \Big|_{y=0} = \Delta\varepsilon \left( \frac{E'_c h_s E'_s}{h_c E'_c + h_s E'_s} \right) - E'_s \kappa \delta$$

Equation 19

$$\text{[Stress at the Bottom of the Substrate]} \quad \sigma_s \Big|_{y=-h_s} = \Delta\varepsilon \left( \frac{E'_c h_s E'_s}{h_c E'_c + h_s E'_s} \right) - E'_s \kappa (h_s + \delta)$$

Equation 20

Where  $\sigma_c$  and  $\sigma_s$  are the respective stresses in the coating and substrate.  $\Delta\varepsilon$  is given as:

$$\Delta\varepsilon = (\alpha_s - \alpha_c)\Delta T$$

Equation 21

Where  $\alpha_c$  and  $\alpha_s$  are the respective coefficients of thermal expansions for the substrate and coating, and  $\Delta T$  is the difference in temperature.  $E'_c$  and  $E'_s$  are given as follows:

$$E'_c = \frac{E_c}{(1-\nu_c)}$$

Equation 22

$$E'_s = \frac{E_s}{(1-\nu_s)}$$

Equation 23

Where  $E_c$  and  $E_s$  are the respective coating and substrate stiffnesses.  $\kappa$  is the curvature of the beam (given as  $\frac{1}{R}$ , where  $R$  is found in a similar way to that shown in the MAM test) and  $\delta$  is the overall deflection of the beam.

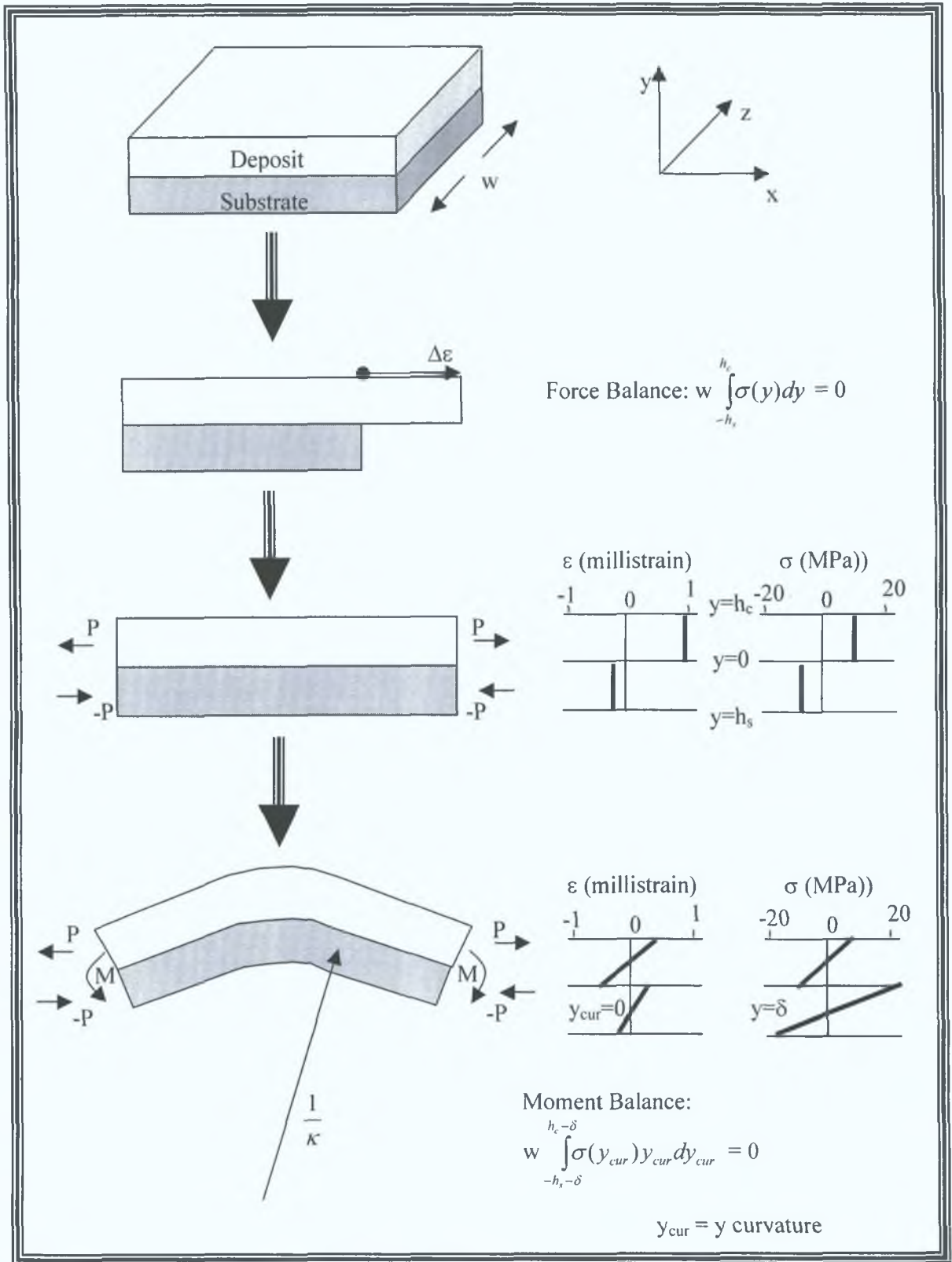


Figure 27, Schematic description of the generation of curvature in a flat bi-material plate as a result of misfit strain, adapted from [82]

Clyne's method was used to measure residual stress as it proved to be a quick method of analysis compared with other techniques such as the hole drilling and X-Ray diffraction. In the method, strips (20mm wide  $\times$  80mm long  $\times$  0.075mm thick) of 316L stainless steel, were first lightly sanded to enable adhesion of the coating to the steel strip (grit blasting was not carried out as this would have induced residual stress), then the strips were fixed onto a mount by clamping bolts. The strip was pre-heated to 450°C and then the WC-Co material subsequently deposited to the desired thickness, as shown in figure 28 [84]. Following deposition, the distributed stresses were deduced by measuring the resulting deflection of the sample and using equations 17 to 20.

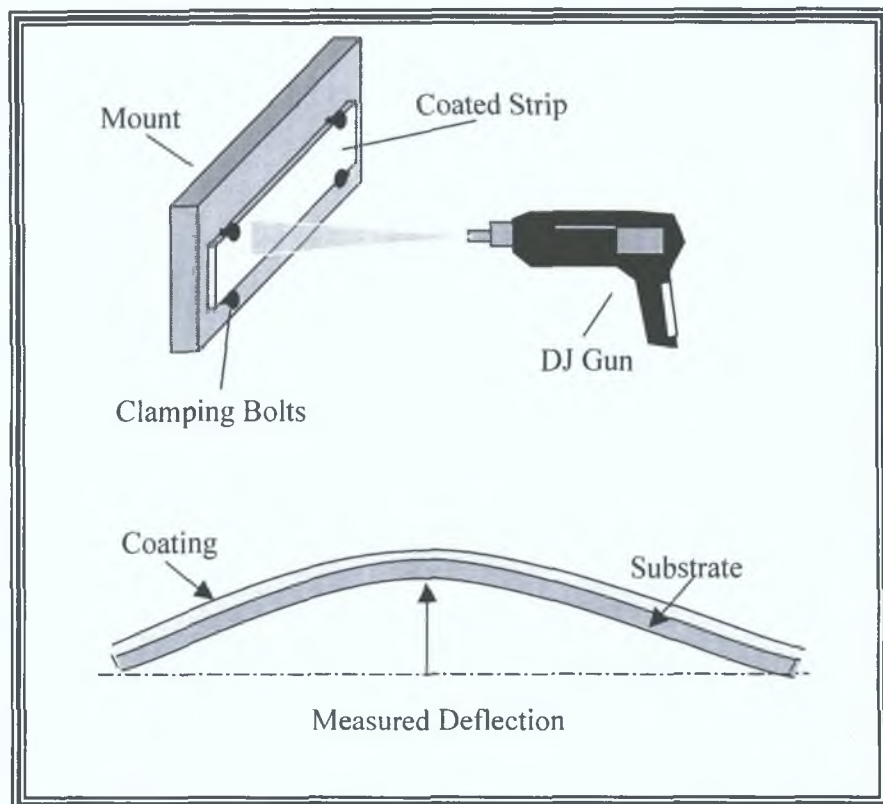


Figure 28, Clyne's Method used to determine the distributed residual stress in a thermally sprayed sample.

### 3.9.3 X-Ray Diffraction Stress Measurement

X-ray Diffraction (XRD) offers unparalleled accuracy in the measurement of atomic spacing, therefore it is an ideal choice in the determination of strain states in thin films. Figure 29 shows the basic features of this non-destructive XRD experiment, where the diffraction angle  $2\theta$  is the angle between the incident and diffracted X-rays. In a typical experiment the diffracted intensity is measured as a function of  $2\theta$  and the orientation of the specimen, which yields the diffraction pattern. Crystals consist of planes of atoms that are spaced a distance  $d$  apart and changes in the  $d$ -spacing (figure 29) are calculated using Bragg's Law. If a monochromatic x-ray beam impinges upon a sample with an ordered lattice spacing  $d$ , constructive interference occurs at an angle (diffraction angle). The condition for constructive interference from planes with spacing  $d$ , is given by Bragg's Law:

$$n\lambda = 2d \sin\theta \qquad \text{Equation 24}$$

where  $n$  is an integer value,  $\lambda$  is the wavelength of the X-ray beam (typically of the range 0.7 to  $2\text{\AA}$ ) and  $\theta$  is the angle between the atomic planes and the incident (and diffracted) X-ray beam. Changes in strain, and thus the  $d$ -spacing, translate into changes in the diffraction angle measured by the detectors. The diffraction pattern is recorded on a photographic film. When the film is removed from the camera, flattened and processed, it shows the diffraction lines and the holes for the incident and transmitted beams. This diffraction pattern forms the basis in the determination of stress within a coating.

For the diffraction to be observed, the detector must be positioned so as to receive the diffractive ray at an angle of  $2\theta$ , and the crystal must be orientated so that the normal to the diffracting plane is co-planar with the incident and diffracted X-rays. Slits collimate the incident X-rays, which impinge on the specimen at an angle  $\theta$  and afterwards the X-ray passes through receiving slits, towards the detector.

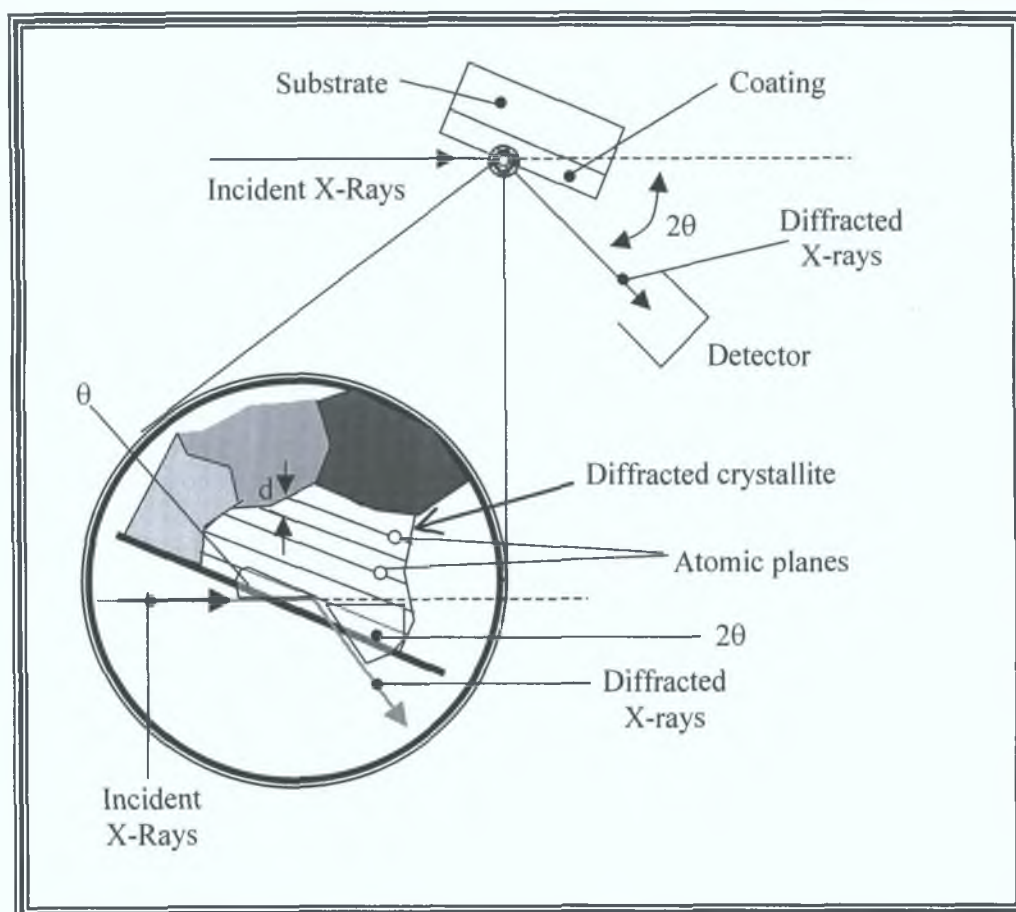


Figure 29, Basic features of a typical XRD experiment.

Since atomic spacings are accurately measured with XRD, it can be used as a method of characterising homogeneous and inhomogeneous strains [85]. The strain in the crystal lattice is measured and the residual stress producing the strain is calculated, assuming a linear elastic distortion of the crystal lattice [86.87]. To determine the stress, the strain in the crystal lattice must be measured for at least two precisely known orientations relative to the sample surface. Therefore, X-ray diffraction residual stress measurement is applicable to materials that are crystalline, relatively fine grained, and produce diffraction from any orientation of the sample surface.

The diffractometer used in the current study (Siemens Diffrac-500 XRD) has a diffraction scanning range from  $-110$  to  $+165$  degrees for  $2\theta$ . Generally the machine is set up according to the parameters detailed with the equipment and initially a broad scan is carried out to find a chosen peak with the highest intensity (highest  $2\theta$  angle). The sample is placed on a holder and is allowed to rotate at any angle  $\psi$ . The process involves measuring various values of strain ( $\epsilon_{\phi\psi}$ ) in multiple  $\psi$  directions, where  $\psi$  is chosen so that the corresponding  $\sin^2\psi$  are equally spaced. The result is given as a graph of  $\sin^2\psi$  (*intensity*) against  $\epsilon_{\phi\psi}$  (*Two Theta*). From the graph, the slope of the line which best fits the measured points is calculated. The residual stress in the coating is given by measuring the slope for two or more different angles of  $\psi$ , and substituting into the following equation, derived (see Appendix 4) from the assumption that the principal stresses exist in the plane of the surface [88]:

$$\sigma_{\phi} = \frac{E}{1 + \nu} (\text{Slope of Graph}) \quad \text{Equation 25}$$

Where  $\sigma_{\phi}$  is the stress result,  $E$  is the Young's modulus of the coating/deposit and  $\nu$  is the Poisson's ratio of the coating.

### 3.9.4 The Hole Drilling Method

Residual stress may also be measured using another method, known as the hole drilling method. This method is “semi-destructive” as localised damage is done to the coating surface. The strain gauge rosettes used in the study were the CEA-06-062UM-120 precision strain gages, which are constructed of self-temperature-compensated foil on a flexible polyimide carrier and incorporate a centering target for use with a precision milling guide. Their characteristics are:

- Resistance in Ohms at 24 °C =  $120.0 \pm 0.4\%$
- Gage factor at 24 °C =  $2.07 \pm 1.0\%$
- Temperature range from  $-100$  °C to 350 °C
- Strain limits = 3%

The rosette strain gauge measures strain in three directions,  $0^\circ$ ,  $45^\circ$  and  $90^\circ$  (or another type at  $0^\circ$ ,  $60^\circ$  and  $120^\circ$ ), as described in ASTM E1561 [89] while the central region is cut away. The rosettes (rectangular shape  $12.2 \times 9.6 \text{ mm}^2$ ) have the grid center line diameter of 5.13 mm and the length of each strain gage is 1.57 mm. The gauge and the surface of the coating was thoroughly prepared before the gauge is attached. Preparation to the surface entailed rubbing fine emery paper to remove any surface contamination. An adhesive was then used to bond the gauge to the surface. The test is carried out by connecting the strain gauge to a strain-recording instrument (P-3500). The hole is drilled through the coating/deposit via the central region of the strain gauge to relax the residual stress in the material being measured [90].

The RS-200 Milling Guide (MicroMeasurements, USA) is one high precision instrument for residual stress analysis by the hole drilling method and was the unit used in the current study. A carbide precision cutter, powered by a high-speed air turbine unit (speeds of 300000 revolutions per minute at clean air pressures of 3atm), was used to mill the hole. Milling was carried out until the depth of the milled hole was equal to a distance of 0.4 of the mean gauge circle diameter (D), to ensure total

relaxation of residual stress, or through the thickness, where the total thickness is less than 1.2 D.

Residual stress is calculated using Kirsch's Theory [91]. In order to accurately measure the strain, certain hypothesis must be launched:

- The milled hole must be concentric with the rosette
- The coating should be isotropic, and a linear elastic material
- The tension perpendicular to the surface can be assumed to be negligible
- The main tension direction is constant along its depth
- The internal tensions do not exceed one third of the yield strength

The equations specified by ASTM E837-95 [92], used to calculate the residual stress in the material are shown below (Appendix 5). The strain values  $\varepsilon_1$ ,  $\varepsilon_2$  and  $\varepsilon_3$  relate to the measured strains from the rosette gauge.

$$\sigma_{\min}, \sigma_{\max} = \frac{\varepsilon_3 + \varepsilon_1}{4A} \pm \frac{\sqrt{(\varepsilon_3 - \varepsilon_1)^2 + (\varepsilon_3 + \varepsilon_1 - 2\varepsilon_2)^2}}{4B} \quad \text{Equation 26}$$

Where

$$A = - \frac{1 + \nu}{2E} \cdot \bar{a} \quad \text{Equation 27}$$

$$B = - \frac{1}{2E} \cdot \bar{b} \quad \text{Equation 28}$$

and

$$\tan 2\nu = \frac{\varepsilon_3 + \varepsilon_1 - 2\varepsilon_2}{\varepsilon_3 - \varepsilon_1} \quad \text{Equation 29}$$

E and  $\nu$  are the Young's modulus and Poisson's ratio respectively for the material (coating in this case).  $\bar{a}$  and  $\bar{b}$  are constants for the blind holes according to the data supplied by the gauge manufacturer.

### 3.10 COATING/FORMING THICKNESS MEASUREMENT

Coating/spray-formed thicknesses measurement is an important procedure in the present research and the equipment utilised depended on whether the thickness is of the order of micron or of the millimetre range. The following methods have been used in the current work;

- Fischerscope Multi Thickness Measuring Instrument
- Dial Gauge Measurement
- Microscopic Measurement

Further information on these methods may be found in my additional report [34].

### 3.11 PARAMETER AND PROCESS OPTIMISATION

As spray forming is a development of coating technology, previous research is therefore very important to the success in forming components. Based on the research carried out on the HVOF process in the Materials Processing Research Centre (MPRC), it was felt at the onset of this study that further improvement in spraying conditions was required. The following text outlines the various parameters (such as spraying distance control) requiring development, and the procedure involved in the implementation of that development.

#### 3.11.1 System Automation Control

The linear traverse unit was tested for various traverse speeds and accelerations to find the optimum parameters to produce quality coatings. Tests were carried out at traverse speeds suggested by Irons [59], to measure the benefits of keeping pass thicknesses low and traverse speeds reasonably high. This was carried out by loading the mount on the traverse unit, with the HVOF Diamond Jet gun and Carbon Dioxide cooling nozzles. Different velocities were then keyed into the LX program, and the resultant speed was calculated by timing the travel of the assembly over a distance of 500mm. The optimum speed and acceleration depended on; pass deposition thickness, spraying temperature, motion of the unit (whether it had a smooth or jolting motion) and residual stress build up per pass.

Similar to the linear traverse unit, control of the third-axis directional unit was required to find the optimum height step between each pass to reduced the gaussian profile of the coating with support from publications such as Figueroa et al. [93] and Fasching et al. [94]. The optimum speed and displacement depended on; pass deposition thickness, spraying temperature and the distance between deposit peaks.

### 3.11.2 Young's Modulus And Poisson's Ratio Determination

As all of the residual stress determination techniques depend on using the Young's modulus and Poisson ratio for the WC-Co material, hence these properties were established using the 'Cantilever Bean Method' as previously described. The acquired properties were then used in the following sections on residual stress determination.

### 3.11.3 Spraying Techniques

In the previous research carried out by Helali [49], where conical thin shaped components were produced, the DJ spray gun was fixed to a mount at the required distance from the lathe (onto which the conical shaped substrates were attached), this enabled the spraying distances to be measured accurately. Following this research Tan [61] investigated the coating and repair of components by spraying manually (as a traverse unit did not exist in the facility at the time).

Hence the current research measures residual stress as a function of spraying technique (manually and controlled). The spraying distance was controlled by moving the traverse unit in and out a set distance from the substrate material. Initially strips of stainless steel were used for residual stress measurement using the Clyne's Method as described earlier. Based on the spray parameters shown in table 5. thermal spraying was carried out at a spraying distance of 200mm and a powder feed rate  $38\text{gmin}^{-1}$ , while varying the various spraying techniques such as manual spraying and spraying with automated linear traverse of the gun. Five residual stress tests were carried out for each spray technique.

Manual spraying was carried out by estimating a spraying distance (from the HVOF gun from the substrate) of 200mm, as carried out by Tan [61]. Twenty passes of Diamalloy 2003 WC-Co were applied to each of the five steel strips. The resulting

deflection of each strip was measured to calculate the distributed residual stress in the specimens.

The HVOF gun was then placed onto the linear traverse unit, at an exact spraying distance of 200mm. Again twenty passes of WC-Co were applied onto five steel strips, to determine the distributed residual stress build up in each of the coatings.

#### 3.11.4 Forced Cooling

It has been observed [49,61] that whilst spraying time increases, the spraying temperature increases, therefore interruption to spraying is required, in order to achieve a constant spray temperature. In those studies compressed air was used to control the temperature drift, but this only delayed the drift for short periods. As spraying at a constant temperature is very important, research into another method of temperature control was needed to increase the efficiency of the DCU system. Forced cooling helps control the spraying temperature, hence reducing the effect of mismatch in thermal expansion coefficients between the coating and the substrate, therefore reducing residual stress build-up.

Carbon dioxide has been reported [62] as a more efficient system of controlling deposition temperature, hence residual stress was measured as a function of forced cooling. Spraying was carried out at an exact spraying distance of 200mm (using the linear traverse unit), with the use of the carbon dioxide cooling system. Twenty passes of Diamalloy 2003 WC-Co were applied to five steel strips. The resulting deflection of each strip was measured using the Clyne's Method to calculate the distributed residual stress in the specimens.

### 3.11.5 Variation Of Residual Stress With Spraying Distance

Once spraying distance was controlled and forced cooling had been implemented, determination of the ideal spraying distance for the deposition of WC-Co was necessary. The method of selection of an ideal distance was by way of residual stress determination using Clyne's Method. Mounted steel strips were deposited with five passes of WC-Co at various distances from 150 to 250mm (at intervals of 10mm). Three tests were carried out at each spraying distance. The stress distribution at each of these distances, was calculated and the maximum stress within the coating was displayed graphically as a function of spraying distance.

### 3.11.6 Variation Of Residual Stress With Powder Feed Rate

Previously in the MPRC, Helali [49] and Tan [61] found two ideal powder feed rates both 45 and 38gmin<sup>-1</sup> respectively, for the WC-Co material. It is expected that the effect of manual spraying could have led to this difference in results. Hence a corrected value of powder feed rate needs to be determined. The method of determination was similar to that in the last section, by way of residual stress determination. Again mounted steel strips were deposited with five passes of WC-Co using forced cooling, at various powder feed rates and the maximum residual stress in the coating was measured for each of the tests. Three tests were carried out at each feed rate.

### 3.11.7 Effect Of Residual Stress On Deposit Thickness

Mounted steel strips were pre-heated and then sprayed with WC-Co up to various thicknesses (by varying the number of passes with the gun), with the use of the linear traverse unit and the Carbon Dioxide cooling. The deposition was carried out at a spraying distance of 200mm and a powder feed rate of 38gmin<sup>-1</sup>, as these were found to be the optimum parameters in the previous sections. Resulting deflections in the steel strips were measured and the distributed residual stress was determined through the coating.

### 3.11.8 Effect Of Residual Stress On Substrate Thickness

WC-Co was deposited onto six 1mm thick substrates. Two deposit thicknesses were applied (0.2mm and 1mm), with the use of the linear traverse unit at a spraying distance of 200mm and the carbon dioxide cooling. Resulting deflections in the steel strips were measured and the distributed residual stress was determined through the coating.

### 3.11.9 Effect Of Residual Stress On Sample Length And Width

Mounted steel strips were pre-heated and then sprayed with WC-Co up to various lengths (100, 80 and 40mm) and widths (20 and 10mm) of samples with the use of the third-axis unit, and carbon dioxide cooling. The deposition was again carried out at a spraying temperature of 200mm and a powder feed rate of  $38\text{gmin}^{-1}$ . Resulting deflections in the steel strips, were converted into the maximum coating residual stress values, to measure the effect the length and width of a coated sample had on residual stress.

### 3.11.10 Effect Of Sample Size On Thickness

The length and width of the stainless steel strips were reduced while increasing the deposit thickness, to produce a maximum deposit thickness. Each sample was pre-heated and then sprayed with WC-Co at a spraying temperature of 200mm and a powder feed rate of  $38\text{gmin}^{-1}$ . The deflections in the steel strips, were converted into stress change values (residual stress).

### 3.11.11 Comparison Of Residual Stress Techniques

Ten samples used to determine the maximum residual stress in the coating by Clyne's Method were selected, ranging from a compressive stress of 50 to 200MPa. Five of these coated samples were metallgraphically polished using the Buehler

Motopol 2000 specimen preparation unit (see report [34]) and the residual stress was measured using the Siemens Diffrac-500 X-ray diffraction system. The residual stress was measured for the final five coated samples using the RS-200 Milling Guide (hole-drilling technique). Clyne's Method of residual stress determination was compared to the X-ray diffraction and the hole-drilling techniques.

## 3 12 POST TREATMENT TECHNIQUE

### 3 12 1 Post-Heat Treatment

Ten coated steel strips used for residual stress determination were placed into the Type EF 10/8 Lenton Thermal Design furnace (see report [34]) at 650°C for 80 minutes (and varying temperatures and times after that) in a nitrogen atmosphere to stress relieve the samples. Each strip had a different measured coating residual stress result (measured using Clyne's Method). This experiment was carried out to verify work carried out by Helali [49], which stated that post heat treating coatings at 650°C for 80 minutes would reduce the sample to a stress free state. The stress was determined by measuring the resulting deflection after post-heat treatment and calculating the maximum residual stress in the coating using Clyne's Method.

Some coatings (two at each temperature) were subjected to further post-heat treatments at 690, 890 and 1320°C using the Lenton Eurotherm Controller 902P furnace, for one and two hours. These samples were then ground and polished using the Buehler Motopol 2000 specimen preparation unit, and examined by the Siemens Diffrac-500 X-ray diffraction system for elemental and phase changes within the coatings microstructure as described in the next section.

### 3 12 2 Shot Peening Method

The shot peening method was used to reduce the tensile stress at the surface of the WC-Co deposit. Silicon carbide shots, 1mm in diameter impacted a 0.2mm thick deposit on a 0.075mm substrate at 90° for two minutes, using the Ventublast Mammoth sandblaster. The resultant deflection was converted into a residual stress distribution through the thickness of the sample. The stress distribution for the shot peened material was compared to the material's stress distribution before peening.

### 3.13 PHASE CHARACTERISATION

Materials composed of any element, can be successfully studied with X-ray Diffraction (XRD) [95]. XRD has already been described as a residual stress measurement method, but one of its most important uses is in phase identification. The identification was done by comparing the measured d-spacings in the diffraction pattern and, to a lesser extent, their integrated intensities with known standards in the JCPDS (Joint Committee on Powder Diffraction Standards, 1986) Powder Diffraction software, attached to the Siemens Diffrac-500 X-ray diffraction system. For specimens containing several phases, the proportion of each phase was determined from the integrated intensities in the diffraction pattern. Each of the polished post-heat treated samples in the previous section were examined by the Siemens Diffrac-500 X-ray diffraction system.

### 3.14 HARDNESS MEASUREMENT

Three methods of measuring the hardness of a material are generally used, such as static indentation, dynamic indentation and the scratch method. In the static test (test carried out in the current research) a ball, diamond cone or a pyramid shaped indenter is forced into the material. Hardness tests carried out at loads of 200 grammes and greater, are known as the Vickers hardness test, whereas the Knoop test is carried out at lower loads of less than 200 grammes [96].

The hardness of the WC-Co deposit was measured by the Vickers test method using the Leitz Miniload hardness tester. The scatter of hardness results at loads of 300 grammes, tend to be less than with lower loads [97], hence a 300 gramme load was applied with a pyramid shaped indenter (figure 30 A). The indentation was observed using a microscope at a magnitude of 50X and the indentation width was measured (figure 30 C). The force  $F$  applied to cause the indentation is measured, along with the arithmetic mean of the two separately measured diagonals  $d$  (in millimetres), given in equation 30.

$$d = \frac{d' + d''}{2} \quad \text{Equation 30}$$

The calculation of Vickers hardness (values expressed in  $DPH_{300}$ ) was calculated as follows [98]:

$$HV = 1.854 \times 10^6 \frac{0.102 \times F}{d^2} \quad \text{Equation 31}$$

Samples must be larger than the minimum distances shown in figure 112 B, there must be greater than half the mean diagonal length ( $d$ ) between the edge of the indentation and the side of the sample. The thickness of the tested material must be greater than one and a half times the mean diagonal length ( $d$ ). Various samples were tested for hardness, to measure the effect of WC-Co deposit thickness and post-heat treatment, on hardness. Three samples were used to determine the relationship between thickness and hardness. Hardness results were measured every millimetre

from a thickness of 1 up to 8mm. The samples post-heat treated at 690, 890 and 1320°C using the Lenton Eurotherm Controller 902P furnace for one and two hours, were then tested for hardness to investigate if phase changes in the microstructure increased or decreased hardness.

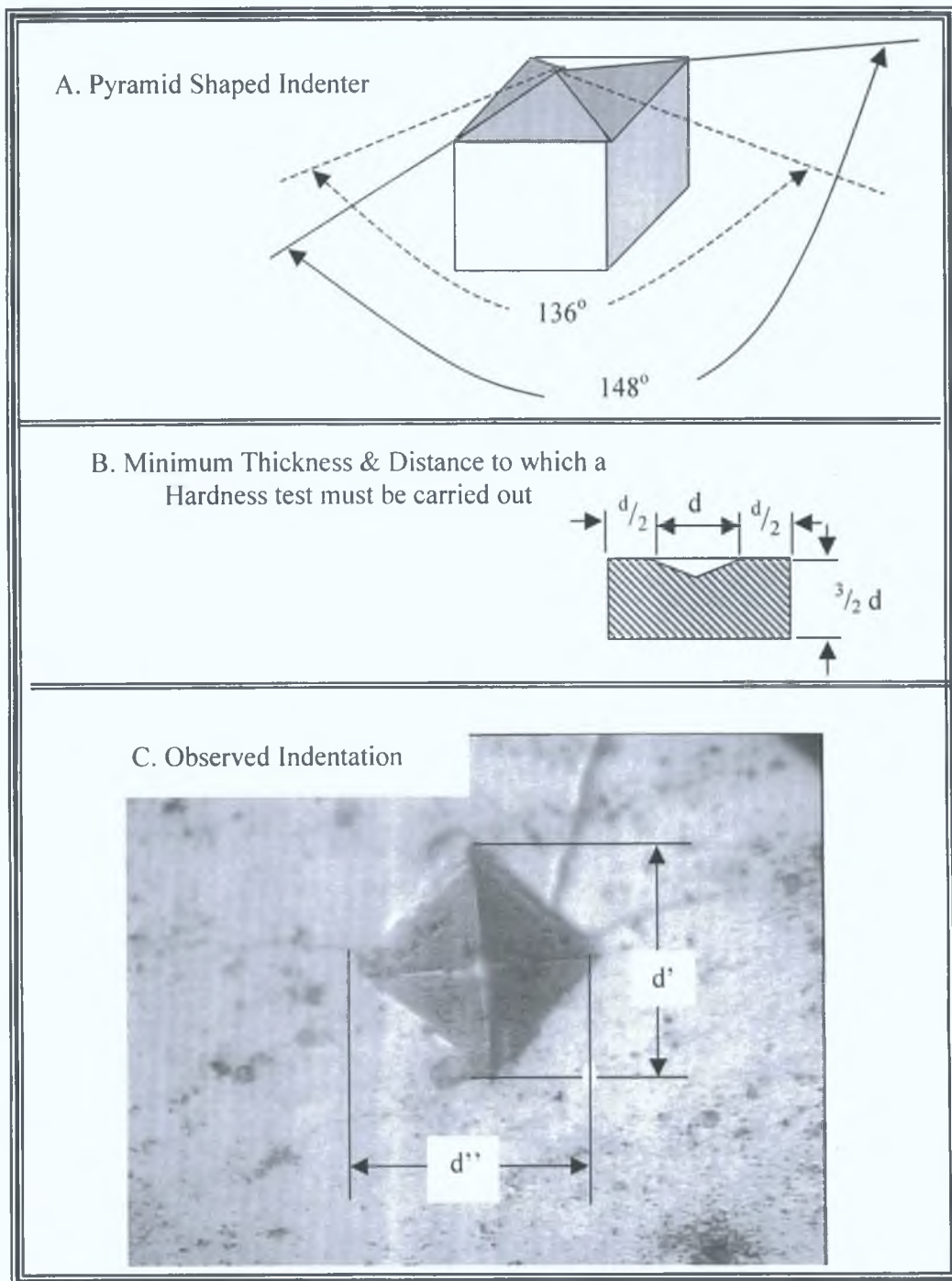


Figure 30, Schematic of the Vickers indenter and a micrograph of the indentation produce by the Vickers hardness test on a WC-Co specimen.

### 3.15 POROSITY MEASUREMENT

Porosity can be described as either isolated voids (closed porosity) or pores (open porosity). Porosity is often measured using an indirect observation method using either an optical microscope, scanning electron microscope, or by the X-ray scattering technique. Samples must first be mounted and polished before measurement commences. The porosity is measured by comparing the amount of porosity in a micrograph of the sample being measured, to that of a micrograph of a known porosity. Another method is to measure the area of porosity and comparing it as a percentage of the total view field area. Visual measurement (by eye) of the area can lead to inaccuracies in results, therefore there are personal computer based support systems to aid the analysis.

The 'Reichert MEF2 Optical Microscope', along with the Buehler Omnimet image analysis system, was used to determine porosity values in the Materials Processing Research Centre. The computer analysis system determines the pore area size in the view field by converting the pore areas (grey-level areas) into a background colour such as red while the rest of the microstructure remains in its original colour (figure 31). The area of one feature can be numerically related to the total area of the picture, as the program counts the number of one colour type pixels (red) and sets that as a ratio of the total number of pixels in the picture (total area).

Various coated samples were sectioned, ground and polished to reveal the coating microstructure. Three samples were used to determine the relationship between deposit thickness and porosity. Porosity results were measured every millimetre from a thickness of 1 up to 8mm. The samples post-heat treated at 690, 890 and 1320°C using the Lenton Eurotherm Controller 902P furnace for one and two hours, were then tested for porosity to investigate if porosity increased or decreased with post-heat treatment.

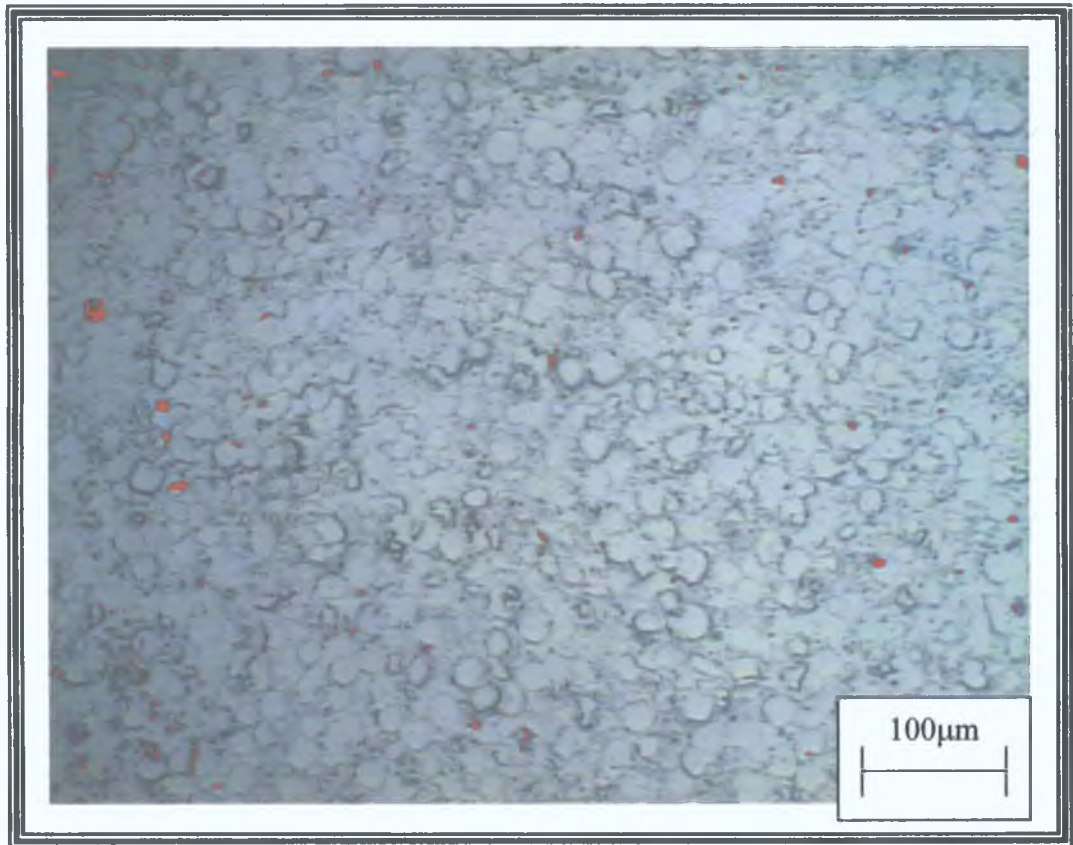


Figure 31, Porosity indicated in red by the Buehler Omnimet image analysis system.

### 3.16 FORMING ASPECT RATIO RELATIONSHIP

Residual stress will be shown in the current research to reduce coating and spray-forming thicknesses. Higher thicknesses were only achieved in the previous sections, if the aspect ratio (component height to diameter ratio) is high. The experiment described investigated producing spray-formed components which were both large (wide and long) and thick, and the maximum aspect ratio (component height to diameter ratio) achieved was measured.

The forming die comprising of a solid 316L stainless steel plate (varying in width and length depending on the test), as shown in figure 32. An aluminium releasing layer was deposited using the HVOF system to a thickness of  $75\mu\text{m}$ , as suggested by Helali [49]. The forming die was then pre-heated, to reduce the effect of mismatch in thermal expansion between the forming die and the formed material. Spraying of the components was carried out with forced cooling. The forming die with deposit was immediately placed into a pre-heated furnace for post-heat treatment after deposition. After post-heat treatment the die with deposit was allowed to cool slowly, and separation of the formed component occurred.

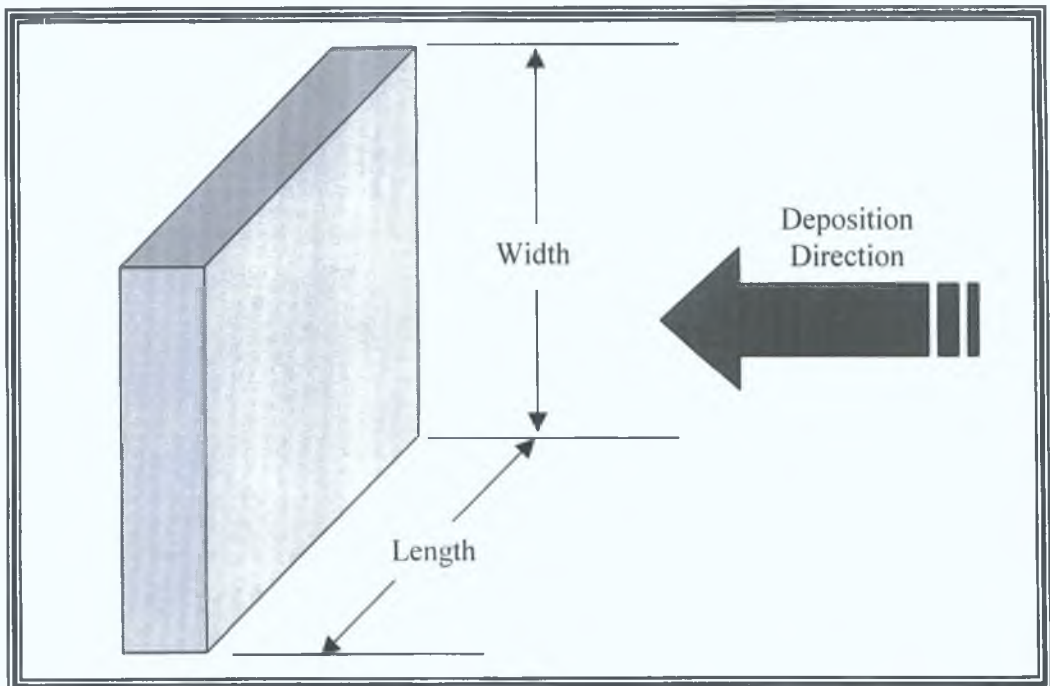


Figure 32, Spray-forming of large components.

### 3.17 PRODUCTION OF THICK FORMED COMPONENTS

The use of the gun and third axis traverse units, not only increase deposition thickness but also reduces surface roughness [94], hence the deposition of near-net shapes (shapes that require little or no finishing) is a possibility with the HVOF process. Once the spray process had been optimised and the coating properties established, the next stage was to produce thick spray-formed components.

A forming die, comprising of three 316L stainless steel plates was used, as shown in figure 33. The base plate supports the actual forming material whilst spraying. The central plate acts as a forming plate, where the deposit fills up the hollow void, to produce the component. A masking plate was used at the front of the assembly, to separate the deposited material inside the forming die from that deposited at its edge.

An aluminium releasing layer was used to enable the removal of the deposited component from the die, post-deposition. Two methods of applying the layer were used. One method was by depositing an aluminium coating using the HVOF system to a thickness of 75 $\mu\text{m}$ , as suggested by Helali [49]. The second method involved lining the internal surface of the die with an aluminium foil layer of thickness 100 $\mu\text{m}$ .

The forming die was pre-heated, to reduce the effect of mismatch in thermal expansion between the forming die and the formed material. Spraying of the components was carried out with forced cooling. Once the desired forming thickness was achieved, the forming die with deposit was immediately placed into a pre-heated furnace at post-treated for over an hour. After post-heat treatment the die with deposit was allowed to cool slowly, and separation of the formed component occurred.

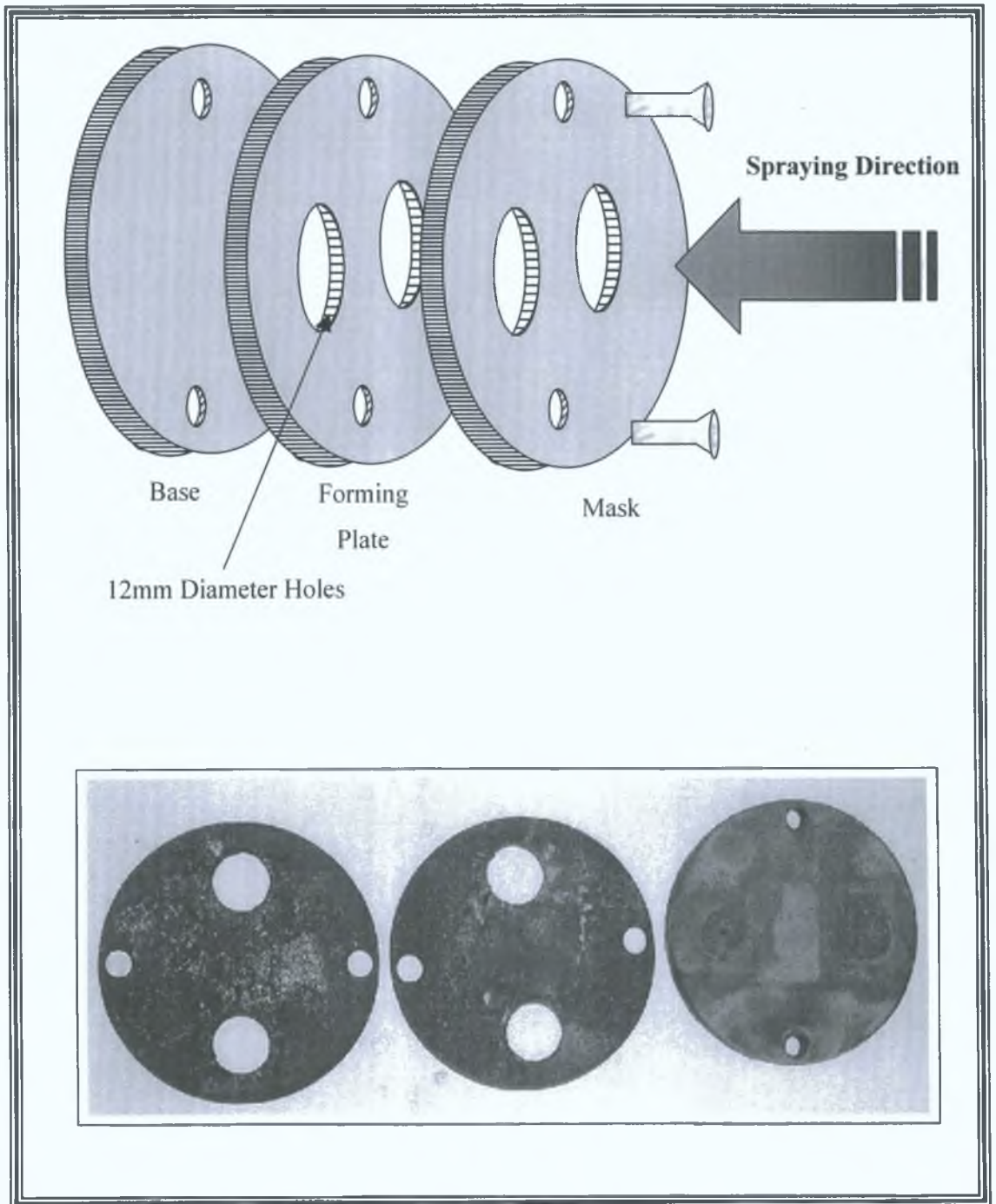


Figure 33, Schematic diagram and photo of die design used in the fabrication of the free-standing WC-Co components.

### 3.18 PRODUCTION OF A TENSILE SPECIMEN

Previously the 'Cantilever Test' was described as the method used to determining the Young's modulus of the WC-Co material. The test is acceptable however the influence of the attached substrate was questioned, as the substrate properties may influence the measurement of the deposits stiffness. The following experiment describes the production of a free-standing WC-Co tensile specimen.

A forming die assembly, similar to that for the cylindrical components was designed to produce tungsten carbide cobalt spray-formed tensile specimens, based on the dimensions required for sinter-formed specimens, outlined in ASTM E8M-96 [74], ASTM B823 [99] and MPIF [100], as shown in Appendix 6.

The forming die comprised of three 316L stainless steel plates, as shown in figure 34. The base plate supported the actual forming material whilst spraying. The central plate acted as the forming plate, where the deposit fills up the hollow void, to produce the specimen. A masking plate was used just as in the previous experiment at the front of the assembly. An aluminium releasing layer (lining the internal surface of the die with an aluminium foil layer of thickness 100 $\mu$ m) was used to enable the removal of the deposited component from the die, post-deposition. The forming die was pre-heated and spraying of the components was carried out with forced cooling. Once the desired forming thickness was achieved, the forming die with deposit was immediately placed into a pre-heated furnace at 675°C for over an hour. After post-heat treatment the die with deposit was allowed to cool slowly, and separation of the formed component occurred. The samples were then tensile tested with the Hounsfield H20K-W tension/compression tester (using a 20kN load cell), to measure the tungsten carbide-cobalt stiffness. The rate of displacement was set at the machines minimum 0.54 mm.min<sup>-1</sup>. The data was transferred to an Excel spreadsheet where the stress-strain relationship was graphically presented. From the stress-strain graph a Young's modulus for WC-Co was determined.

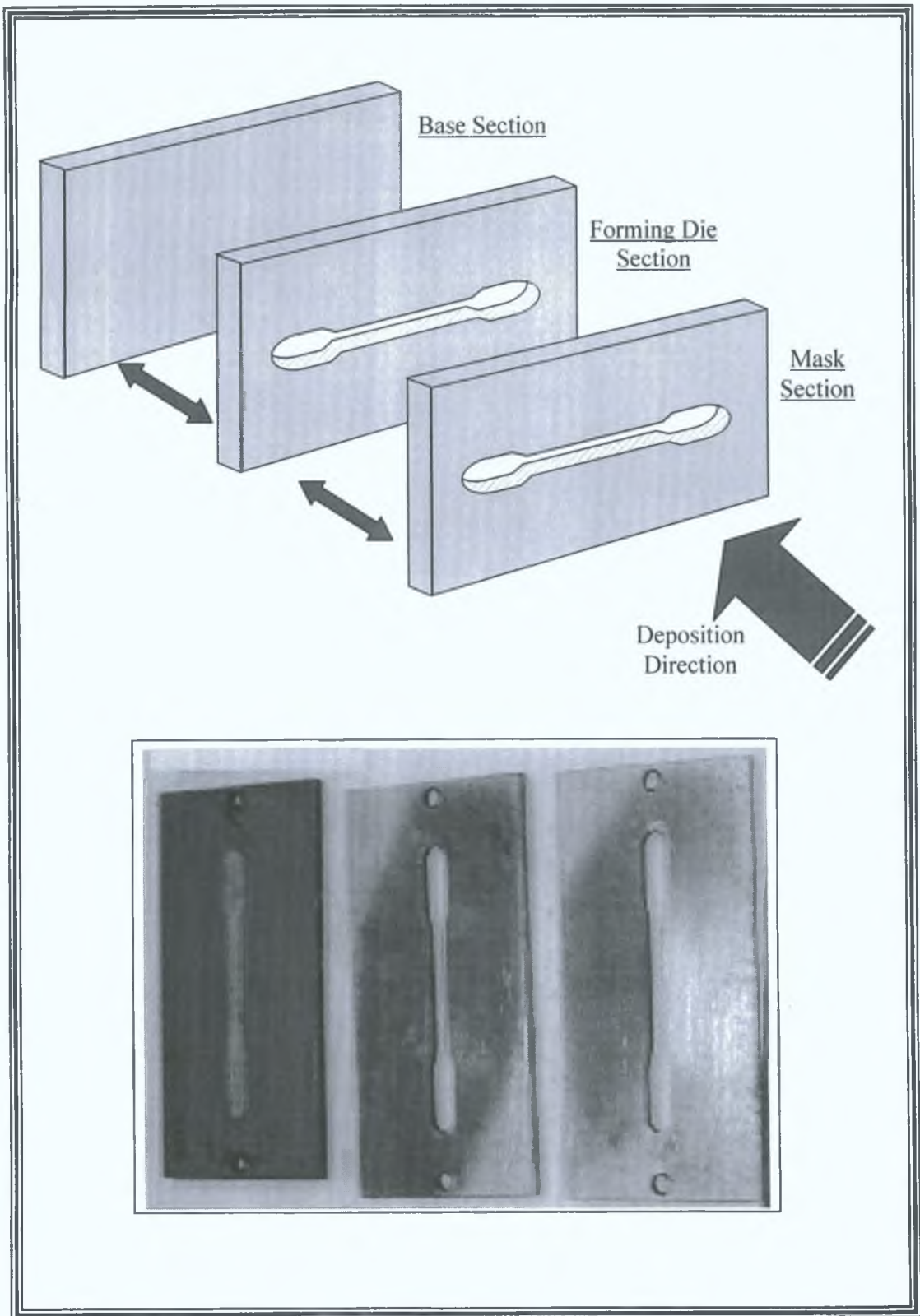


Figure 34, Schematic and a photo of die used for fabrication of WC-Co tensile components.

---

# MODELLING OF SPRAY DEPOSIT

---

## 4.1 FINITE ELEMENT ANALYSIS

The finite element method is a numerical procedure, that can be used to obtain solutions to a large class of engineering systems, including stress analysis, heat transfer, fluid flow and electromagnetism. In thermal spraying, finite element analysis is used either to validate or predict experimental results, through numerical formulation. Residual stress is a major problem in thermal spraying where high thickness coatings are required, due to the rapid solidification and cooling of sprayed droplets during cooling. Experimental analysis may help the researcher understand where these stresses arise in a component, hence lead to the prevention of such outcomes. Finite element analysis may support experimental findings and predict results for more complex situations. In general most of the analyses of residual stress, consist of analytical models of the behaviour of molten droplets striking the substrate surface, similar to that detailed by Fukanuma et al. [101], nevertheless finite element analysis similar to that shown here has also been documented [102,103]. In this research finite element analysis of heat transfer and residual stress in the coated sample is carried out and compared to experimental data generated during the current research. There are many finite element method software programs available to yield various engineering solutions, however the ANSYS finite element program was used in the current research, as it is widely available within the university. Hence the followings sections are specific to the ANSYS program.

The origin of the modern finite element method may be traced back to the early 1900s, when some investigators approximated and modelled elastic continua using discrete equivalent elastic bars. The ANSYS finite element method program was released in

1971 for the first time. ANSYS is a comprehensive general purpose finite element computer program, which contains over 100,000 lines of code [104]. ANSYS is capable of performing static, dynamic, heat transfer, fluid flow, and electromagnetism analyses. The current version of ANSYS has multiple windows incorporating a Graphical User Interface (GUI), pull-down menus, dialog boxes, and a tool bar. The objective of this section is to introduce the basic concepts in finite element formulation, including numerical formulation. The following topics are addressed:

- Engineering Problems
- Numerical Methods
- Steps in the Finite Element Method
- Numerical Formulation of systems specific to this research
- Verification of Results

## 4 2 ENGINEERING PROBLEMS

Engineering problems can be described in general as being mathematical models of physical situations [105]. The mathematical models generally comprise of numerous differential equations with sets of corresponding initial and boundary conditions. The differential equations are derived by applying fundamental laws and principles of nature to an engineering system. These equations represent the balance of mass, force, or energy and when possible, the solution of these equations renders a detailed behaviour of a system under a given set of conditions.

Analytical solutions show the exact behaviour of a system at any point within the system. An analytical solution may be composed of two parts: firstly a homogenous part and secondly a particular part. In any engineering system, there are two sets of parameters that influence the way a system behaves. Firstly, there are those parameters that provide information regarding the natural behaviour of a given system and always appear in the homogeneous part of the solution. Examples of these parameters include thermal conductivity, modulus of elasticity, and viscosity properties of a material, as shown in table 6. On the other hand, there are parameters that produce disturbances in a system and they appear in the particular part of the solution. Examples of disturbing parameters include temperature difference across a medium, external forces, moments, and pressure difference in a fluid flow, as shown in table 6.

Table 6, Physical properties characterising and disturbing various engineering systems.

<b>Engineering Problem</b>	<b>Parameters that Characterise a Problem</b>	<b>Parameters that Disturb a Problem</b>
Heat Transfer	<ul style="list-style-type: none"> <li>• Thermal Conductivity</li> </ul>	<ul style="list-style-type: none"> <li>• Heat Input</li> <li>• Temperature Difference</li> </ul>
Solid Mechanics	<ul style="list-style-type: none"> <li>• Modulus of Elasticity</li> <li>• Modulus of Rigidity</li> <li>• Second Moment of Area</li> <li>• Polar Moment of Inertia</li> </ul>	<ul style="list-style-type: none"> <li>• External Forces</li> <li>• Moments</li> <li>• Support Excitation</li> </ul>
Fluid Flow	<ul style="list-style-type: none"> <li>• Viscosity</li> <li>• Relative Roughness</li> <li>• Solid Permeability</li> </ul>	<ul style="list-style-type: none"> <li>• Pressure Difference</li> <li>• Rate of Flow</li> </ul>
Electrical Networks	<ul style="list-style-type: none"> <li>• Resistance</li> <li>• Permeability</li> </ul>	<ul style="list-style-type: none"> <li>• Voltage Difference</li> </ul>

### 4.3 NUMERICAL METHODS

Many practical engineering problems can only be solved approximately. This inability to obtain an exact solution may be attributed to either the complex nature of the governing differential equations or the difficulties that arise from dealing with initial and boundary conditions [105]. To deal with such problems, numerical approximations are used. In contrast to analytical solutions, which show the exact behaviour of a system at any point within the system, numerical solutions approximate exact solutions only at discrete points. The first step in the numerical procedure is to discretize (divide) a system into small subsystems known as elements, where their shape is described by discrete points known as nodes.

There are two types of numerical methods, finite difference methods and finite element methods. With finite difference methods, the differential equation is written at each discrete point (node), and the derivatives are replaced by difference equations, this approach results in a set of simultaneous linear equations [106]. Finite difference methods are easy to understand in simple systems, however they become difficult to apply to systems with complex geometries or with complex boundary conditions, an example of this would be a system involving non-isotropic material properties.

The finite element method use integral formulations, rather than difference equations, to create a system of algebraic equations. Moreover, an approximate continuous function is assumed to represent the solution for each element. The complete solution is generated by connecting or assembling the individual solutions, allowing for continuity at the inter-elemental boundaries.

#### 4.4 STEPS IN THE FINITE ELEMENT METHOD

The basics steps involved in any finite element analysis consist of the following:

##### Preprocessor Phase

- Create and discretize the solution domain into finite elements, that is the system is sub-divided into elements and nodes
- Assume a shape function to represent the physical behaviour of an element.
- Develop equations for an element
- Arrange and assemble the elements to present the entire system. Construct the global stiffness matrix
- Apply boundary conditions, initial conditions and loads

##### Solution Phase

- Solve a set of linear or non-linear algebraic equations simultaneously to obtain nodal results, such as displacement values at different nodes or temperature values at different nodes in a heat transfer system

##### Postprocessor Phase

- Obtain other important information including stress values, heat fluxes and so on

## 4.5 NUMERICAL FORMULATION

The following examples illustrate the simplified one-dimensional direct formulation steps used to analyse both heat transfer and residual stress systems experienced in the current research, with reference to Fagan [105] and Moaveni [106]

## 4.5.1 Heat Transfer System

A sample consists of a stainless steel substrate, coated with aluminium (releasing layer), on which a coating of tungsten carbide-cobalt is placed. The following describes the determination of the temperature distribution through the three materials, when a heat source is placed near the tungsten carbide-cobalt surface.

Preprocessing Phase

*Discretize the solution domain into finite elements*

The system is represented by six nodes (discrete points) and five elements (sub-systems) as shown in figure 35.

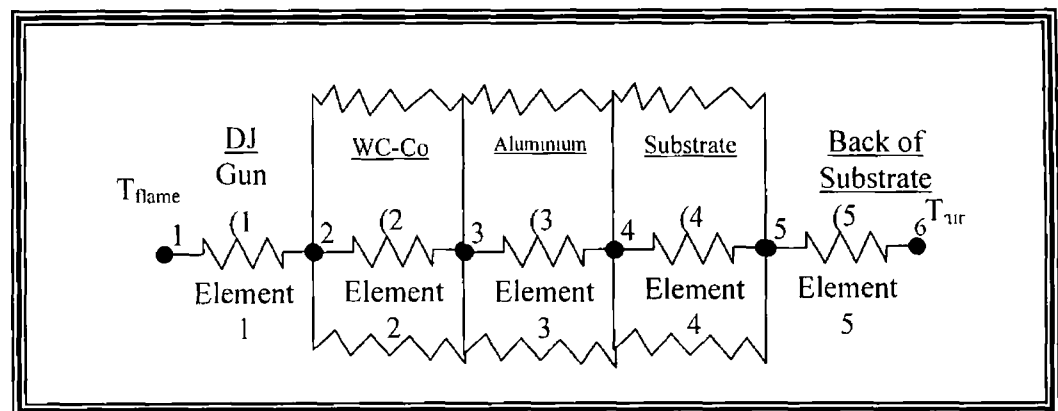


Figure 35, Finite Element model for temperature distribution through various materials

*Assume a solution that approximates the behaviour of an element*

In this situation, there are two modes of heat transfer (conduction and convection), both of which must be understood before formulation of the conductance matrix and the thermal load matrix. It must be noted that the solution ignores the fact that heat loss will be experienced around the sides of the sample, hence an approximation of the real solution will be found.

The steady state thermal behaviour of the elements (2), (3), and (4) may be modelled using Fourier's Law. When there is a temperature gradient in a medium, conduction heat transfer occurs, as shown in figure 36. The energy is transported from the high-temperature region to the low-temperature region by molecular activity.

The heat transfer rate is given by Fourier's Law

$$q_x = -kA \frac{\partial T}{\partial X} \quad \text{Equation 32}$$

$q_x$  is the X-component of the heat transfer rate,  $k$  is the thermal conductivity of the medium,  $A$  is the area, and  $\frac{\partial T}{\partial X}$  is the temperature gradient. The minus sign is due to the fact that heat flows in the direction of decreasing temperature.

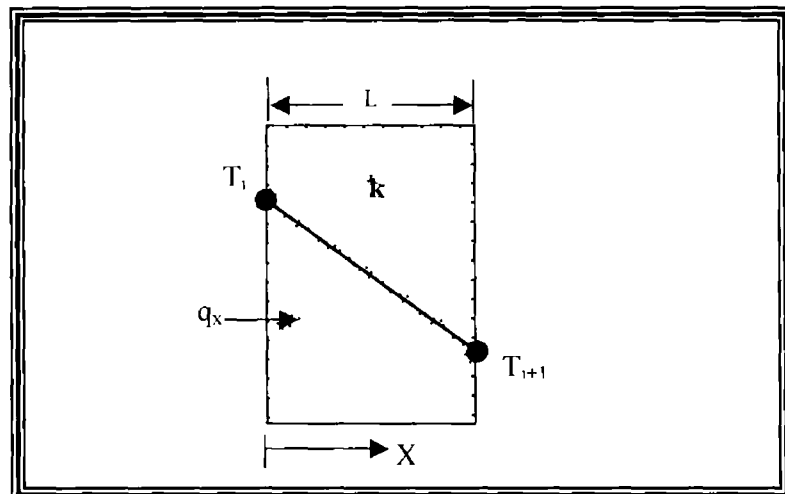


Figure 36 Heat transfer by conduction through a medium

Equation 32 can be written in terms of the spacing between the nodes (length of the element)  $L$  and the respective temperatures of the nodes  $i$  and  $i+1$ ,  $T_i$  and  $T_{i+1}$  by the following [107]:

$$q = \frac{kA(T_i - T_{i+1})}{L} \quad \text{Equation 33}$$

The steady state behaviour of elements (1) and (5) may be modelled using Newton's Law of Cooling. Convection heat transfer occurs when a fluid in motion comes into contact with a surface whose temperature differs from the moving fluid. The overall heat transfer rate between the fluid and the surface is governed by Newton's Law of Cooling [108], by the following equation:

$$q = hA(T_f - T_s) \quad \text{Equation 34}$$

where  $h$  is the heat transfer coefficient ( $W/m^2K$ ),  $T_s$  is the surface temperature, and  $T_f$  represents the temperature of the moving fluid (gas). According to Holman [108], under steady state conduction, the application of energy balance to a surface requires that the energy transferred to a surface by conduction must be equal to the energy transferred by convection. Hence,

$$-kA \frac{\partial T}{\partial X} = hA[T_f - T_s] \quad \text{Equation 35}$$

as shown in figure 37.

$h$  (for convection) is given by:

$$h = \frac{k}{L} \quad \text{Equation 36}$$

therefore

$$kA \frac{\partial T}{\partial X} = \frac{kA}{L} (\Delta T) \quad \text{Equation 37}$$

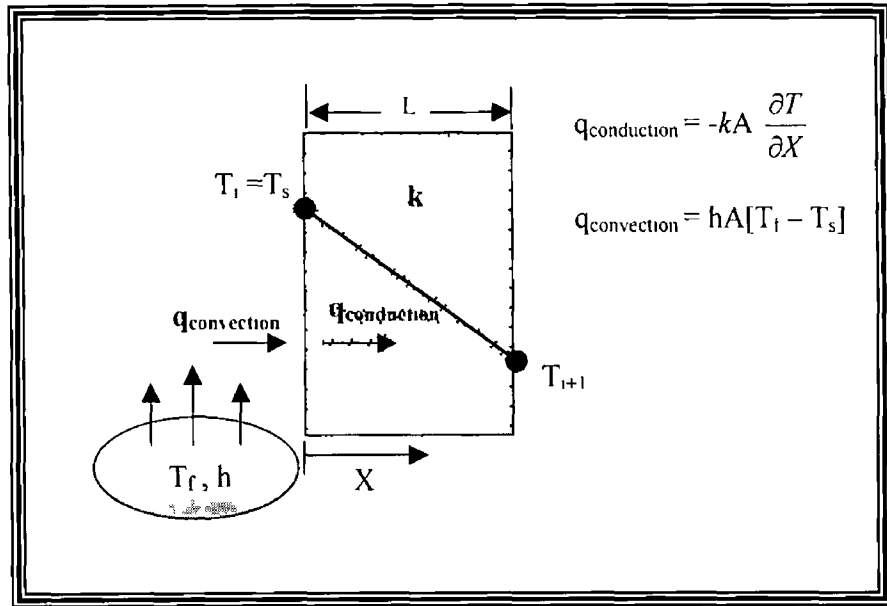


Figure 37 Energy balance at a surface with convective heat transfer

*Develop equations for an element*

The heat flow through nodes  $i$  and  $i+1$  is depicted in figure 38. As each element in the coated substrate system has two nodes and has associated temperatures with each node, two equations can be created for each element. These equations must involve nodal temperatures and the element's thermal conductivity based on Fourier's law. Under steady state conditions, the application of the conservation of energy requires that the sum of  $q_i$  and  $q_{i+1}$  into an element be zero, that is the energy flowing out of node  $i+1$  must be equal to the energy flowing into node  $i$ . There exists two situations encountered at an elemental position. One, the element may experience a heat gain at one side and a heat loss at the other (figure 38 a), or secondly the element may experience a heat gain at both sides (figure 38 b). Note that the sum of  $q_i$  and  $q_{i+1}$  is zero regardless of which representation of figure 38, is selected. The following analysis

is based on the representation shown in figure 38 (b). The heat transfer rates,  $q_i$  and  $q_{i+1}$ , and the nodal temperatures (discrete points),  $T_i$  and  $T_{i+1}$ , for an element (sub-system) are related according to the equations:

$$q_i = \frac{kA}{L}(T_i - T_{i+1}) \quad \text{Equation 38}$$

$$q_{i+1} = \frac{kA}{L}(T_{i+1} - T_i) \quad \text{Equation 39}$$

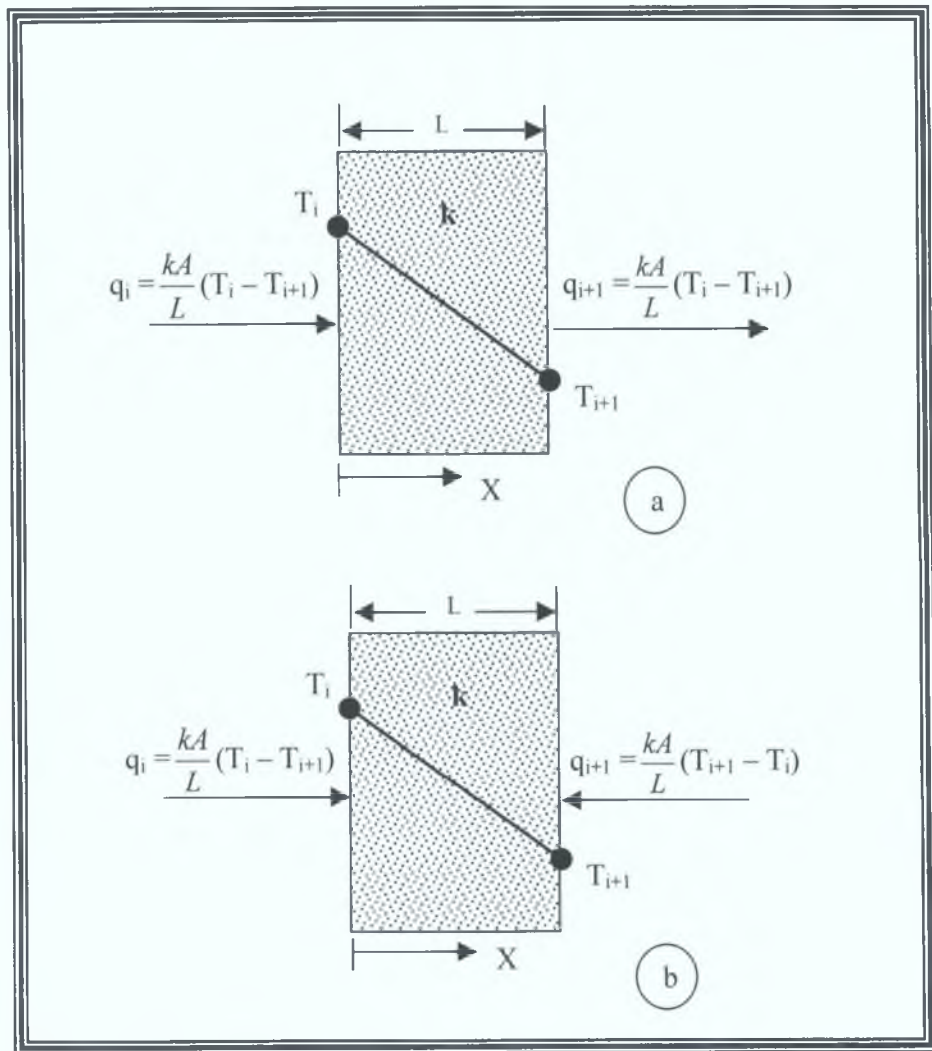


Figure 38. Heat flow through nodes  $i$  and  $i+1$  showing (a) heat gained at one side and lost at the other and (b) heat gained at both sides.

The elemental description given by equations 38 and 39 may be expressed in matrix form as follows:

$$\begin{Bmatrix} q_i \\ q_{i+1} \end{Bmatrix} = \frac{kA}{L} \begin{bmatrix} 1 & -1 \\ -1 & 1 \end{bmatrix} \begin{Bmatrix} T_i \\ T_{i+1} \end{Bmatrix} \quad \text{Equation 40}$$

The thermal conductance matrix for the element shown in figure 38 (b), is given as:

$$[\mathbf{K}]^{(e)} = \frac{kA}{L} \begin{bmatrix} 1 & -1 \\ -1 & 1 \end{bmatrix} \quad \text{Equation 41}$$

*Assemble the elements to present the entire system.*

Using equation 41 the position matrix for the first element is given by:

$$[\mathbf{K}]^{(1)} = \mathbf{A} \begin{bmatrix} \frac{k_1}{L_1} & -\frac{k_1}{L_1} \\ -\frac{k_1}{L_1} & \frac{k_1}{L_1} \end{bmatrix} \quad \text{Equation 42}$$

and its position in the global conductance matrix (overall matrix to describe the total system) is given by:

$$[\mathbf{K}]^{(G)} = \mathbf{A} \begin{bmatrix} \frac{k_1}{L_1} & -\frac{k_1}{L_1} & 0 & 0 & 0 & 0 \\ -\frac{k_1}{L_1} & \frac{k_1}{L_1} & 0 & 0 & 0 & 0 \\ 0 & 0 & 0 & 0 & 0 & 0 \\ 0 & 0 & 0 & 0 & 0 & 0 \\ 0 & 0 & 0 & 0 & 0 & 0 \\ 0 & 0 & 0 & 0 & 0 & 0 \end{bmatrix} \begin{matrix} T_1 \\ T_2 \\ T_3 \\ T_4 \\ T_5 \\ T_6 \end{matrix} \quad \text{Equation 43}$$

Similar to element 1, the elemental position matrices together with their position in the global conductance matrix for elements 2, 3, 4 and 5 are given as follows

$$[\mathbf{K}]^{(2)} = A \begin{bmatrix} \frac{k_2}{L_2} & -\frac{k_2}{L_2} \\ -\frac{k_2}{L_2} & \frac{k_2}{L_2} \end{bmatrix} \quad \text{and} \quad [\mathbf{K}]^{(2c)} = A \begin{bmatrix} 0 & 0 & 0 & 0 & 0 & 0 \\ 0 & \frac{k_2}{L_2} & -\frac{k_2}{L_2} & 0 & 0 & 0 \\ 0 & -\frac{k_2}{L_2} & \frac{k_2}{L_2} & 0 & 0 & 0 \\ 0 & 0 & 0 & 0 & 0 & 0 \\ 0 & 0 & 0 & 0 & 0 & 0 \\ 0 & 0 & 0 & 0 & 0 & 0 \end{bmatrix} \begin{matrix} T_1 \\ T_2 \\ T_3 \\ T_4 \\ T_5 \\ T_6 \end{matrix}$$

Equation 44

$$[\mathbf{K}]^{(3)} = A \begin{bmatrix} \frac{k_3}{L_3} & -\frac{k_3}{L_3} \\ -\frac{k_3}{L_3} & \frac{k_3}{L_3} \end{bmatrix} \quad \text{and} \quad [\mathbf{K}]^{(3c)} = A \begin{bmatrix} 0 & 0 & 0 & 0 & 0 & 0 \\ 0 & 0 & \frac{k_3}{L_3} & -\frac{k_3}{L_3} & 0 & 0 \\ 0 & 0 & -\frac{k_3}{L_3} & \frac{k_3}{L_3} & 0 & 0 \\ 0 & 0 & 0 & 0 & 0 & 0 \\ 0 & 0 & 0 & 0 & 0 & 0 \\ 0 & 0 & 0 & 0 & 0 & 0 \end{bmatrix} \begin{matrix} T_1 \\ T_2 \\ T_3 \\ T_4 \\ T_5 \\ T_6 \end{matrix}$$

Equation 45

$$[\mathbf{K}]^{(4)} = A \begin{bmatrix} \frac{k_4}{L_4} & -\frac{k_4}{L_4} \\ -\frac{k_4}{L_4} & \frac{k_4}{L_4} \end{bmatrix} \quad \text{and} \quad [\mathbf{K}]^{(4c)} = A \begin{bmatrix} 0 & 0 & 0 & 0 & 0 & 0 \\ 0 & 0 & 0 & 0 & 0 & 0 \\ 0 & 0 & 0 & \frac{k_4}{L_4} & -\frac{k_4}{L_4} & 0 \\ 0 & 0 & 0 & -\frac{k_4}{L_4} & \frac{k_4}{L_4} & 0 \\ 0 & 0 & 0 & 0 & 0 & 0 \\ 0 & 0 & 0 & 0 & 0 & 0 \end{bmatrix} \begin{matrix} T_1 \\ T_2 \\ T_3 \\ T_4 \\ T_5 \\ T_6 \end{matrix}$$

Equation 46

$$[\mathbf{K}]^{(s)} = \mathbf{A} \begin{bmatrix} \frac{k_5}{L_5} & -\frac{k_5}{L_5} \\ -\frac{k_5}{L_5} & \frac{k_5}{L_5} \end{bmatrix} \quad \text{and} \quad [\mathbf{K}]^{(5G)} = \mathbf{A} \begin{bmatrix} 0 & 0 & 0 & 0 & 0 & 0 \\ 0 & 0 & 0 & 0 & 0 & 0 \\ 0 & 0 & 0 & 0 & 0 & 0 \\ 0 & 0 & 0 & 0 & 0 & 0 \\ 0 & 0 & 0 & 0 & \frac{k_5}{L_5} & -\frac{k_5}{L_5} \\ 0 & 0 & 0 & 0 & -\frac{k_5}{L_5} & \frac{k_5}{L_5} \end{bmatrix} \begin{matrix} T_1 \\ T_2 \\ T_3 \\ T_4 \\ T_5 \\ T_6 \end{matrix}$$

Equation 47

The overall global conductance matrix (matrix for the system) is given as the sum of each elemental position:

$$[\mathbf{K}]^{(G)} = [\mathbf{K}]^{(1G)} + [\mathbf{K}]^{(2G)} + [\mathbf{K}]^{(3G)} + [\mathbf{K}]^{(4G)} + [\mathbf{K}]^{(5G)} \quad \text{Equation 48}$$

Hence the overall global conductance matrix for the coated substrate system shown in figure 35 is given as follows:

$$[\mathbf{K}]^{(G)} = \mathbf{A} \begin{bmatrix} \frac{k_1}{L_1} & -\frac{k_1}{L_1} & 0 & 0 & 0 & 0 \\ -\frac{k_1}{L_1} & \frac{k_1}{L_1} + \frac{k_2}{L_2} & -\frac{k_2}{L_2} & 0 & 0 & 0 \\ 0 & -\frac{k_2}{L_2} & \frac{k_2}{L_2} + \frac{k_3}{L_3} & -\frac{k_3}{L_3} & 0 & 0 \\ 0 & 0 & -\frac{k_3}{L_3} & \frac{k_3}{L_3} + \frac{k_4}{L_4} & -\frac{k_4}{L_4} & 0 \\ 0 & 0 & 0 & -\frac{k_4}{L_4} & \frac{k_4}{L_4} + \frac{k_5}{L_5} & -\frac{k_5}{L_5} \\ 0 & 0 & 0 & 0 & -\frac{k_5}{L_5} & \frac{k_5}{L_5} \end{bmatrix} \quad \text{Equation 49}$$

*Apply Boundary Conditions and Thermal Loads*

Finite element formulation of heat transfer systems, always lead to an equation of the form [108]:

$$[K]\{T\} = \{q\} \quad \text{Equation 50}$$

$$[\text{Conductance Matrix}]\{\text{Temperature Matrix}\} = \{\text{Heat Flow Matrix}\} \quad \text{Equation 51}$$

In this system, the WC-Co coating is exposed to a known flame temperature  $T_1 = 500^\circ\text{C}$  (first boundary condition), and the air temperature behind the substrate  $T_6 = 50^\circ\text{C}$  (second boundary condition). In the case the overall matrix equation is represented as follows:

$$A \begin{bmatrix} \frac{k_1}{L_1} & -\frac{k_1}{L_1} & 0 & 0 & 0 & 0 \\ -\frac{k_1}{L_1} & \frac{k_1}{L_1} + \frac{k_2}{L_2} & -\frac{k_2}{L_2} & 0 & 0 & 0 \\ 0 & -\frac{k_2}{L_2} & \frac{k_2}{L_2} + \frac{k_3}{L_3} & -\frac{k_3}{L_3} & 0 & 0 \\ 0 & 0 & -\frac{k_3}{L_3} & \frac{k_3}{L_3} + \frac{k_4}{L_4} & -\frac{k_4}{L_4} & 0 \\ 0 & 0 & 0 & -\frac{k_4}{L_4} & \frac{k_4}{L_4} + \frac{k_5}{L_5} & -\frac{k_5}{L_5} \\ 0 & 0 & 0 & 0 & -\frac{k_5}{L_5} & \frac{k_5}{L_5} \end{bmatrix} \begin{Bmatrix} T_1 \\ T_2 \\ T_3 \\ T_4 \\ T_5 \\ T_6 \end{Bmatrix} = \begin{Bmatrix} 500^\circ\text{C} \\ 0 \\ 0 \\ 0 \\ 0 \\ 50^\circ\text{C} \end{Bmatrix}$$

Equation 52

As matrices are a representation of a series of simultaneous equations, the equation for the first row and the final row should read as follows:

$$T_1 = 500^\circ\text{C} \quad \text{Equation 53}$$

$$T_6 = 50^\circ\text{C} \quad \text{Equation 54}$$

Therefore rows 1 and 6 are adjusted (by removing the  $\frac{k}{L}$  constants) in the global conductance matrix, to yield the results shown equations 53 and 54 as follows

$$A \begin{bmatrix} \frac{1}{A} & 0 & 0 & 0 & 0 & 0 \\ -\frac{k_1}{L_1} & \frac{k_1}{L_1} + \frac{k_2}{L_2} & -\frac{k_2}{L_2} & 0 & 0 & 0 \\ 0 & -\frac{k_2}{L_2} & \frac{k_2}{L_2} + \frac{k_3}{L_3} & -\frac{k_3}{L_3} & 0 & 0 \\ 0 & 0 & -\frac{k_3}{L_3} & \frac{k_3}{L_3} + \frac{k_4}{L_4} & -\frac{k_4}{L_4} & 0 \\ 0 & 0 & 0 & -\frac{k_4}{L_4} & \frac{k_4}{L_4} + \frac{k_5}{L_5} & -\frac{k_5}{L_5} \\ 0 & 0 & 0 & 0 & 0 & \frac{1}{A} \end{bmatrix} \begin{Bmatrix} T_1 \\ T_2 \\ T_3 \\ T_4 \\ T_5 \\ T_6 \end{Bmatrix} = \begin{Bmatrix} 500^\circ C \\ 0 \\ 0 \\ 0 \\ 0 \\ 50^\circ C \end{Bmatrix}$$

Equation 55

Row two is as follows when multiplied out

$$-\frac{Ak_1}{L_1} T_1 + \frac{Ak_1}{L_1} T_2 + \frac{Ak_2}{L_2} T_2 - \frac{Ak_2}{L_2} T_3 = 0 \quad \text{Equation 56}$$

By equation 53

$$\frac{Ak_1}{L_1} T_2 + \frac{Ak_2}{L_2} T_2 - \frac{Ak_2}{L_2} T_3 = A \frac{k_1}{L_1} 500 \quad \text{Equation 57}$$

Similarly row five reduces to the following

$$-\frac{Ak_4}{L_4} T_4 + \frac{Ak_4}{L_4} T_5 + \frac{k_5}{L_5} T_5 = A \frac{k_5}{L_5} 50 \quad \text{Equation 58}$$

Ignoring the equations involved in row 1 and 6, and incorporating the known boundary conditions into rows 2 and 5 of the heat transfer system, equation 55 is reduced to:

$$A \begin{bmatrix} \frac{k_1}{L_1} + \frac{k_2}{L_2} & -\frac{k_2}{L_2} & 0 & 0 \\ -\frac{k_2}{L_2} & \frac{k_2}{L_2} + \frac{k_3}{L_3} & -\frac{k_3}{L_3} & 0 \\ 0 & -\frac{k_3}{L_3} & \frac{k_3}{L_3} + \frac{k_4}{L_4} & -\frac{k_4}{L_4} \\ 0 & 0 & -\frac{k_4}{L_4} & \frac{k_4}{L_4} + \frac{k_5}{L_5} \end{bmatrix} \cdot \begin{Bmatrix} T_2 \\ T_3 \\ T_4 \\ T_5 \end{Bmatrix} = \begin{Bmatrix} \frac{k_1}{L_1} 500 \\ 0 \\ 0 \\ \frac{k_5}{L_5} 50 \end{Bmatrix} \quad \text{Equation 59}$$

Substituting the conductivity  $k$  values, length  $L$  (taken as the heat effected zone distance for the flame or the thickness of the material) and exposure area ( $A$ ) values (latter two taken from the experimental data in the current research, see figure 39), into equation 59, results in the calculation of the various elemental temperatures ( $T_{2-5}$ ). The data shown in table 7 represents a real heat transfer situation:

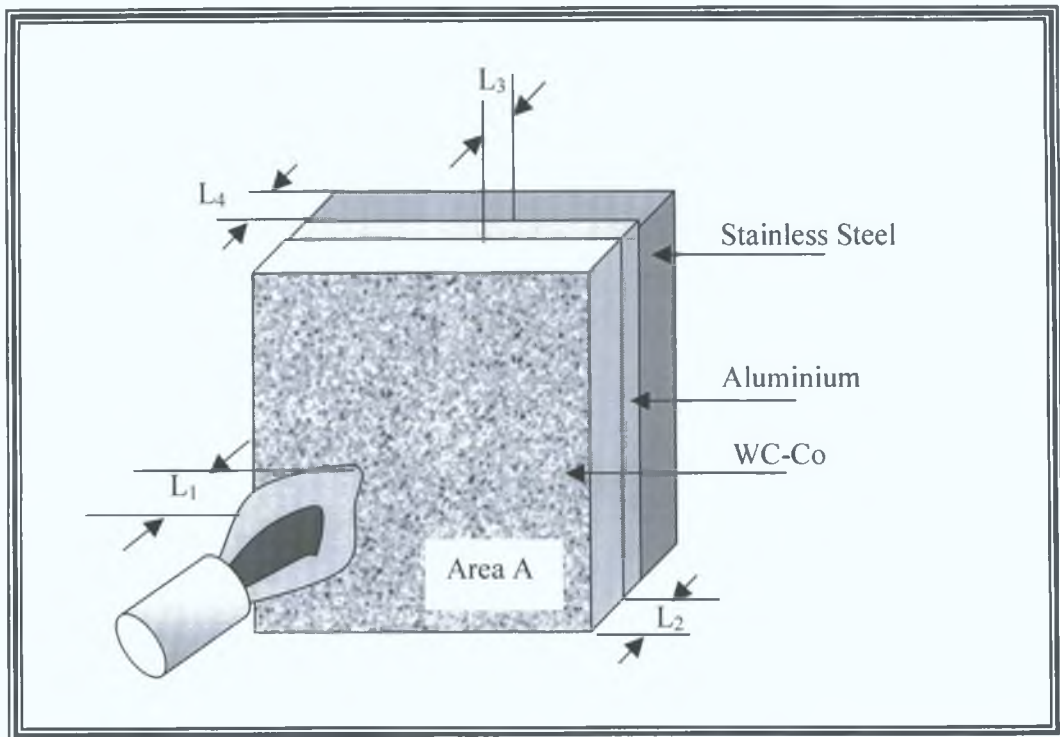


Figure 39, Schematic of the heat transfer system.

Table 7, Heat transfer parameters found from experimental data.

Item	Conductivity $k$ (W/mK)	Length $L$ (m) x $10^{-3}$	$k/L$ (W/m <sup>2</sup> K)	Area $A$ (m <sup>2</sup> ) x $10^{-3}$
(1) Flame (500°C)	0.058 Ref. [108]	20	3.0	1.6
(2) WC-Co	90 Ref. [33]	2	45000	1.6
(3) Aluminium	125 Ref. [109]	0.75	166666.7	1.6
(4) Stainless Steel	25 Ref. [109]	6	4166.7	1.6
(5) Air Behind Substrate (50°C)	0.03 Ref. [108]	20	1.5	1.6

According to table 7;

$$A \cdot \begin{bmatrix} 3 + 45000 & -45000 & 0 & 0 \\ -45000 & 45000 + 166666.7 & -166666.7 & 0 \\ 0 & -166666.7 & -166666.7 + 4166.7 & -4166.7 \\ 0 & 0 & -4166.7 & 4166.7 + 1.5 \end{bmatrix} \cdot \begin{Bmatrix} T_2 \\ T_3 \\ T_4 \\ T_5 \end{Bmatrix} = \begin{Bmatrix} 3(500) \\ 0 \\ 0 \\ 1.5(50) \end{Bmatrix} \quad \text{Equation 60}$$

Simplifying, the following result is obtained;

$$A \cdot \begin{bmatrix} 45003 & -45000 & 0 & 0 \\ -45000 & 211666.7 & -166666.7 & 0 \\ 0 & -166666.7 & 170833.4 & -4166.7 \\ 0 & 0 & -4166.7 & 4168.2 \end{bmatrix} \cdot \begin{Bmatrix} T_2 \\ T_3 \\ T_4 \\ T_5 \end{Bmatrix} = \begin{Bmatrix} 1500 \\ 0 \\ 0 \\ 75 \end{Bmatrix} \quad \text{Equation 61}$$

In the present research, convection from the flame at the front and convection with the air at the back of the sample was ignored. Experimental data provided temperatures both at the front and back of the sample, hence convection was not required. The system use is shown in figure 40.

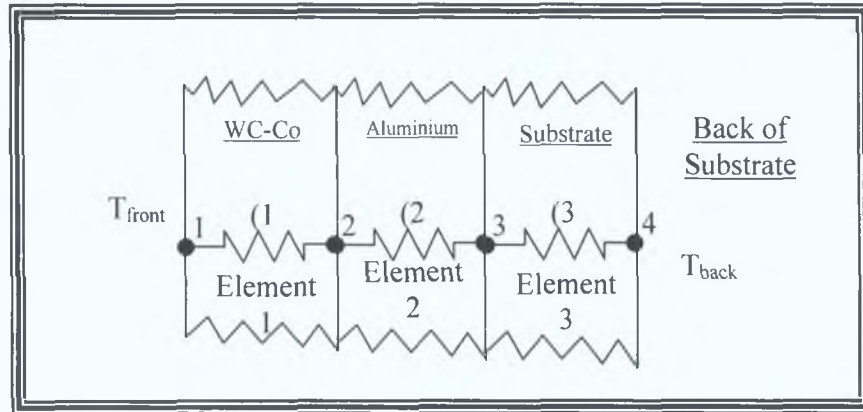


Figure 40, Finite Element model used in the present research.

Equation 52 in this case is reduced to:

$$A \begin{bmatrix} \frac{k_1}{L_1} & -\frac{k_1}{L_1} & 0 & 0 \\ -\frac{k_1}{L_1} & \frac{k_1}{L_1} + \frac{k_2}{L_2} & -\frac{k_2}{L_2} & 0 \\ 0 & -\frac{k_2}{L_2} & \frac{k_2}{L_2} + \frac{k_3}{L_3} & -\frac{k_3}{L_3} \\ 0 & 0 & -\frac{k_3}{L_3} & \frac{k_3}{L_3} \end{bmatrix} \cdot \begin{Bmatrix} T_1 \\ T_2 \\ T_3 \\ T_4 \end{Bmatrix} = \begin{Bmatrix} 500 \\ 0 \\ 0 \\ 0 \end{Bmatrix} \quad \text{Equation 62}$$

Where 500 is the only known front temperature. Substituting the conductivity  $k$  values, length  $L$  (taken as the heat effected zone distance for the flame or the thickness of the material) and exposure area ( $A$ ) values (from table 8) into equation 62, results in the calculation of the various elemental temperatures ( $T_{2-4}$ ).

Table 8, Parameters used in the heat transfer finite element analysis

Item	Conductivity $k$ (W/mK)	Length $L$ (m) x $10^3$	$k/L$ (W/m <sup>2</sup> K)	Area $A$ (m <sup>2</sup> ) x $10^3$
(1) WC-Co	90 Ref [33]	2	45000	1.6
(2) Aluminium	125 Ref [109]	0.75	166666.7	1.6
(3) Stainless Steel	25 Ref [109]	6	4166.7	1.6

$$A \begin{bmatrix} 45000 & -45000 & 0 & 0 \\ -45000 & 211666.7 & -166666.7 & 0 \\ 0 & -166666.7 & 170833.4 & -4166.7 \\ 0 & 0 & -4166.7 & 4166.7 \end{bmatrix} \begin{Bmatrix} T_1 \\ T_2 \\ T_3 \\ T_4 \end{Bmatrix} = \begin{Bmatrix} 500 \\ 0 \\ 0 \\ 0 \end{Bmatrix} \quad \text{Equation 63}$$

Solution Phase

*Solve a system of algebraic equations simultaneously*

Solving the previous matrix (equation 63) yields the temperature distribution across the sample

$$\begin{Bmatrix} T_1 \\ T_2 \\ T_3 \\ T_4 \end{Bmatrix} = \begin{Bmatrix} 500 \\ 499.99 \\ 499.98 \\ 499.98 \end{Bmatrix} \text{ } ^\circ\text{C} \quad \text{Equation 64}$$

The results show that the spraying temperature (front temperature) of 500°C, is reflected in a temperature of 357.8°C, across the substrate (back temperature)

Postprocessing Phase

*Obtain other Information*

The solution (equation 64) may be represented as a temperature contour of the thermal gradient through the sample

#### 4.5.2 Residual Stress Determination

A substrate material (stainless steel) is coated with WC-Co to a certain thickness. During deposition, stresses (quenching of lamella and cooling of coating) generate, generating a moment at the ends of the sample, causing the sample to deflect, as shown in figure 41.

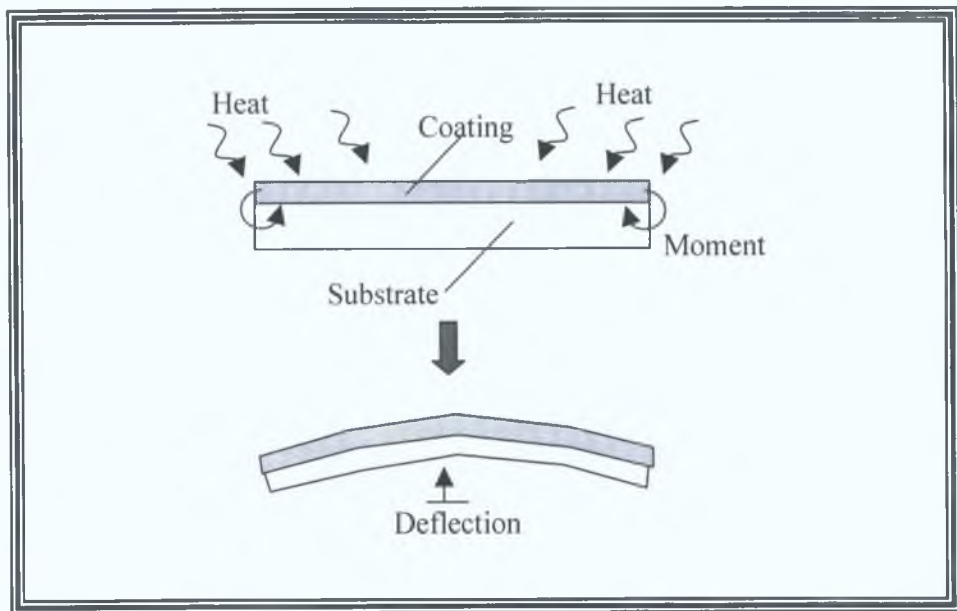


Figure 41, Moment in a sample generating a deflection.

As explained in an earlier section, the simulation of both the quenching and cooling stresses in one system is quite difficult, hence the method of simulation used in the present study relied on the deformation of the final sample post-spraying. To demonstrate the numerical formulation for this system, two simple approximation methods were analysed. One method was to apply various temperatures to a coated sample of known thickness and then measure the stress through the tungsten carbide-cobalt deposit when the resulting deflection measured in the finite element analysis, equalled that found experimentally in the Clyne's Method. In this case the applied temperature in the finite element system generated a thermal load in the centre of the beam, and caused the beam to deflect, similar to that used by Steffens et al. [102]. Appendix 7 shows the procedure used to simulate this system.

Similarly this system was simulated by applying a known deflection to the sample (Appendix 7) and compared to the latter. The system was simulated by locking both ends of the sample while subjecting the centre of the sample to a ‘thermal load’  $P$  (to generate the deflection), as shown in figure 42. The load and in turn deflection creates an internal stress in the deposit causing permanent bending in the sample. The elastic modulus for each material is given as  $E_s$  (substrate) and  $E_c$  (coating). The sample has a width  $W$ , length  $L$ , and thicknesses of  $t_s$  (substrate), and  $t_c$  (coating). The numerical formulation for the latter system will be described in the following section.

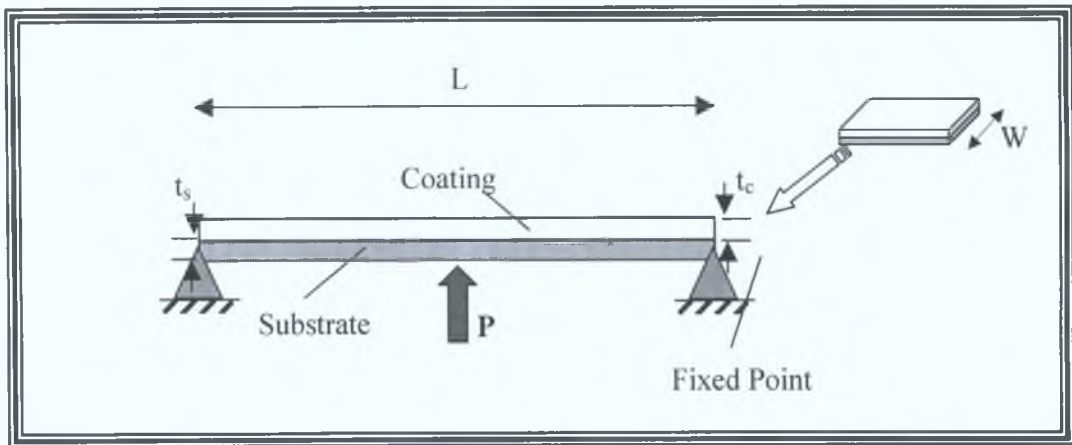


Figure 42, Coated sample subjected to a central displacement.

### Preprocessing Phase

*Discretize the solution domain into finite elements.*

In order to highlight the basic steps in the finite element analysis, the coated sample is discretized into simple parts. The sample has been divided into four individual segments called elements, with each segment having a uniform cross-section as shown in figure 43. Each element is represented as an elastic beam with nodes top and bottom of the element and in turn each element is joined to another element by connecting one node to the next. The accuracy of the results may be increased, by increasing the number of additional nodes and elements.

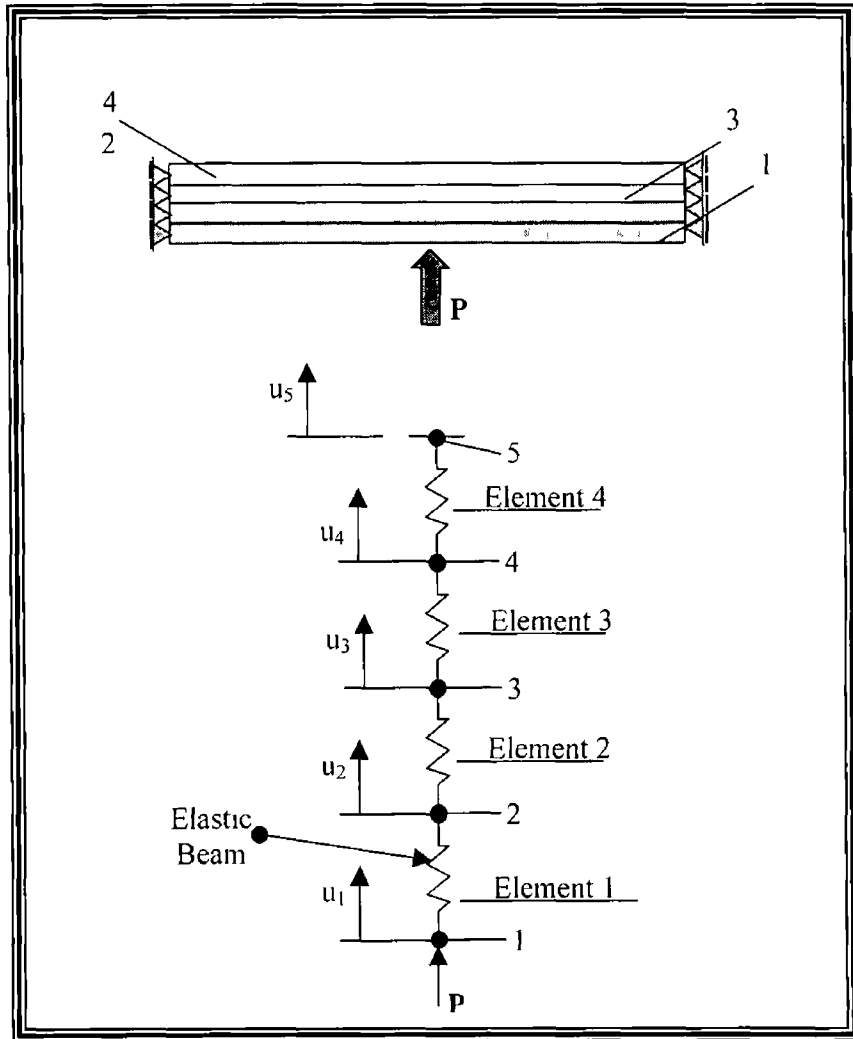


Figure 43, Sub-dividing the sample into elements and nodes

*Assume a solution that approximates the behaviour of an element*

In order to study the behaviour of a typical element, figure 44 shows a solid member with a uniform cross-section  $A$  of a length  $l$  subjected to a force  $F$

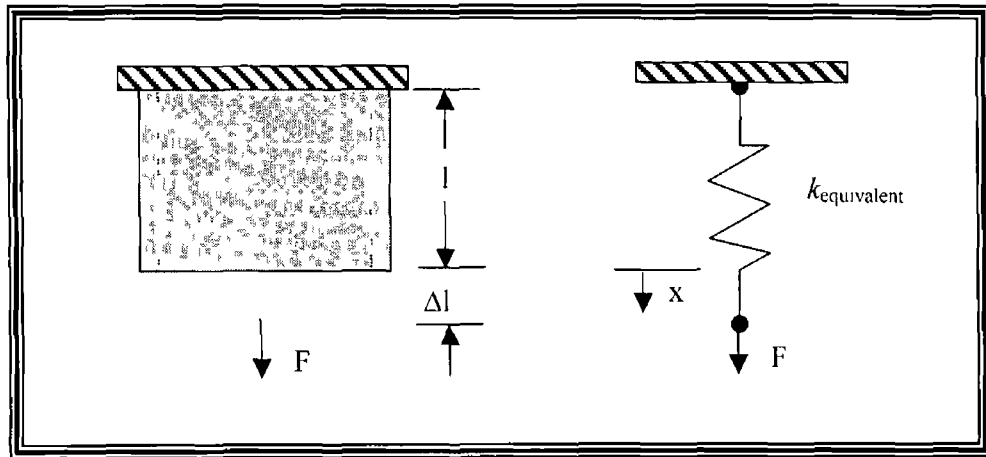


Figure 44, A solid member of uniform cross-section subjected to a force F

The average stress  $\sigma$  in the member is given by

$$\sigma = \frac{F}{A} \quad \text{Equation 65}$$

The average normal strain  $\epsilon$  of the member is defined as the change in length  $\Delta l$  per unit length  $l$  of the member

$$\epsilon = \frac{\Delta l}{l} \quad \text{Equation 66}$$

Over the elastic region, the stress and strain are related by Hooke's Law, according to the following equation,

$$\sigma = E\epsilon \quad \text{Equation 67}$$

where  $E$  is the modulus of elasticity of the material. Combining these equations results in

$$F = \left( \frac{AE}{l} \right) \Delta l \quad \text{Equation 68}$$

Equation 68 is similar to the equation for a linear spring,  $F = kx$ . Therefore, a centrally loaded member of uniform cross-section may be modelled as a spring with equivalent stiffness of

$$k_{eq} = \frac{AE}{l} \quad \text{Equation 69}$$

The coated sample is modelled as a series of centrally loaded members with equal cross-sections. Thus, the sample is represented by a model consisting of four elastic springs (elements) in series, and the elastic behaviour of each element is modelled by an equivalent linear spring according to the equation:

$$f = k_{eq}(u_{i+1} - u_i) = \frac{AE}{l}(u_{i+1} - u_i) \quad \text{Equation 70}$$

$u_i$  and  $u_{i+1}$  are the displacements of the member at nodes  $i$  and  $i+1$  respectively, and  $l$  is the length of the element.

*Develop equations for an element.*

As each element has two nodes, and with each node there is an associated displacement, then the system requires two equations for each element. These equations must involve nodal displacements and the element's stiffness. The elemental relationship between the internally transmitting forces ( $f_i$  and  $f_{i+1}$ ), and the end displacements ( $u_i$  and  $u_{i+1}$ ) is shown in figure 45.

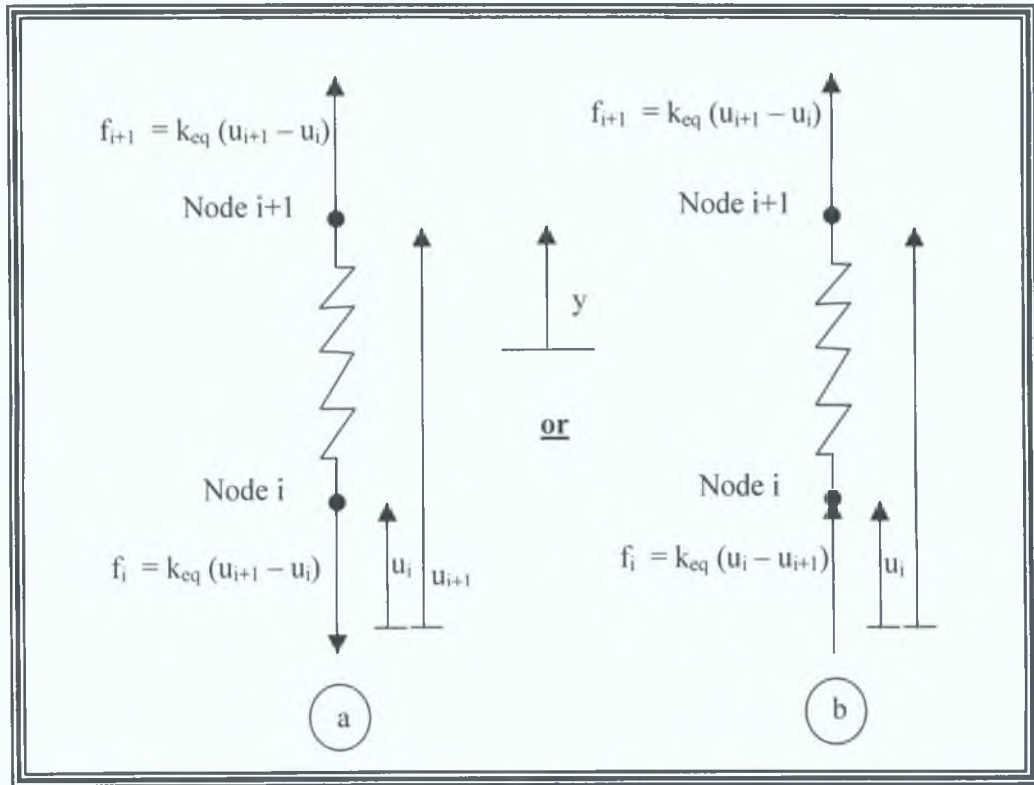


Figure 45, Internally transmitted forces through an arbitrary element.

Static equilibrium conditions require that the sum of  $f_i$  and  $f_{i+1}$  be equal to zero. In figure 45, there are two ways (tension or two forces acting in the same directions) to represent the transmission of forces acting on a member. The representation shown in figure 45 (b), will be observed, so that the directions of  $f_i$  and  $f_{i+1}$  are in the same direction as  $y$ . Thus the transmitted forces at nodes  $i$  and  $i+1$  are as follows:

$$f_i = k_{eq} (u_i - u_{i+1}) \quad \text{Equation 71}$$

$$f_{i+1} = k_{eq} (u_{i+1} - u_i) \quad \text{Equation 72}$$

Equations 72 may be expressed in matrix form as follows:

$$\begin{Bmatrix} f_i \\ f_{i+1} \end{Bmatrix} = \begin{bmatrix} k_{eq} & -k_{eq} \\ -k_{eq} & k_{eq} \end{bmatrix} \begin{Bmatrix} u_i \\ u_{i+1} \end{Bmatrix} \quad \text{Equation 73}$$

*Assemble the elements to present the entire system*

Applying the elemental description given in equation 73, to all elements, and assembling them will lead to the formation of an elemental matrix

$$[\mathbf{K}]^{(1)} = \begin{bmatrix} k_1 & -k_1 \\ -k_1 & k_1 \end{bmatrix} \quad \text{Equation 74}$$

and its position in the global stiffness matrix is given by

$$[\mathbf{K}]^{(1G)} = \begin{bmatrix} k_1 & -k_1 & 0 & 0 & 0 \\ -k_1 & k_1 & 0 & 0 & 0 \\ 0 & 0 & 0 & 0 & 0 \\ 0 & 0 & 0 & 0 & 0 \\ 0 & 0 & 0 & 0 & 0 \end{bmatrix} \quad \text{Equation 75}$$

The nodal displacement matrix is shown alongside the position of element 1 in the global stiffness matrix to observe its contribution of a node to its neighbouring elements. Similarly for elements 2, 3 and 4, the following equations apply

$$[\mathbf{K}]^{(2)} = \begin{bmatrix} k_2 & -k_2 \\ -k_2 & k_2 \end{bmatrix} \quad \text{and} \quad [\mathbf{K}]^{(2G)} = \begin{bmatrix} 0 & 0 & 0 & 0 & 0 \\ 0 & k_2 & -k_2 & 0 & 0 \\ 0 & -k_2 & k_2 & 0 & 0 \\ 0 & 0 & 0 & 0 & 0 \\ 0 & 0 & 0 & 0 & 0 \end{bmatrix} \quad \text{Equation 76}$$

$$[\mathbf{K}]^{(3)} = \begin{bmatrix} k_3 & -k_3 \\ -k_3 & k_3 \end{bmatrix} \quad \text{and} \quad [\mathbf{K}]^{(3G)} = \begin{bmatrix} 0 & 0 & 0 & 0 & 0 \\ 0 & 0 & 0 & 0 & 0 \\ 0 & 0 & k_3 & -k_3 & 0 \\ 0 & 0 & -k_3 & k_3 & 0 \\ 0 & 0 & 0 & 0 & 0 \end{bmatrix}$$

Equation 77

$$[\mathbf{K}]^{(4)} = \begin{bmatrix} k_4 & -k_4 \\ -k_4 & k_4 \end{bmatrix} \quad \text{and} \quad [\mathbf{K}]^{(4G)} = \begin{bmatrix} 0 & 0 & 0 & 0 & 0 \\ 0 & 0 & 0 & 0 & 0 \\ 0 & 0 & 0 & 0 & 0 \\ 0 & 0 & 0 & k_4 & -k_4 \\ 0 & 0 & 0 & -k_4 & k_4 \end{bmatrix}$$

Equation 78

The final (overall) global stiffness matrix is obtained by assembling, or adding together each element's position in the global stiffness matrix:

$$[\mathbf{K}]^{(G)} = [\mathbf{K}]^{(1G)} + [\mathbf{K}]^{(2G)} + [\mathbf{K}]^{(3G)} + [\mathbf{K}]^{(4G)} \quad \text{Equation 79}$$

$$[\mathbf{K}]^{(G)} = \begin{bmatrix} k_1 & -k_1 & 0 & 0 & 0 \\ -k_1 & k_1 + k_2 & -k_2 & 0 & 0 \\ 0 & -k_2 & k_2 + k_3 & -k_3 & 0 \\ 0 & 0 & -k_3 & k_3 + k_4 & -k_4 \\ 0 & 0 & 0 & -k_4 & k_4 \end{bmatrix} \quad \text{Equation 80}$$

#### *Apply Boundary Conditions and Loads*

In this system, the sample is held at both ends while a load  $P$  is applied to the centre of the sample. Applying this condition (adopting equation 73) results in the following set of linear equations:

$$\begin{bmatrix} k_1 & -k_1 & 0 & 0 & 0 \\ -k_1 & k_1 + k_2 & -k_2 & 0 & 0 \\ 0 & -k_2 & k_2 + k_3 & -k_3 & 0 \\ 0 & 0 & -k_3 & k_3 + k_4 & -k_4 \\ 0 & 0 & 0 & -k_4 & k_4 \end{bmatrix} \cdot \begin{Bmatrix} u_1 \\ u_2 \\ u_3 \\ u_4 \\ u_5 \end{Bmatrix} = \begin{Bmatrix} P \\ 0 \\ 0 \\ 0 \\ 0 \end{Bmatrix} \quad \text{Equation 81}$$

In solid mechanics systems, the finite element formulation always lead to a general equation of the form [106]:

$$[K = \text{Stiffness matrix}] \{u = \text{Displacement matrix}\} = \{F = \text{Load matrix}\} \quad \text{Equation 82}$$

The solution to this system cannot be calculated, as applying a force to a fixed point will cause no displacement, as explained in figure 46. Where one element (that is element 1 in figure 45 a) occupies length of the sample (as this is a one-dimensional system), applying the boundary condition ( $u_1 = 0$ ) to this element prevents the force P from impacting elements 2, 3, and 4. The numerical matrix formulation depicts a simple one-dimensional analysis however this problem was performed as a two-dimensional system (or higher orders) in the current research, hence the elemental distribution would look more like that shown in figure 45 b. Hence the boundary condition ( $u_1 = 0$ ) was applied to the lower corners elements of the beam. This formulation of the system would allow the centre of the sample to deflect. This highlights the inaccuracy found in results, when using a coarse (fewer elements) mesh.

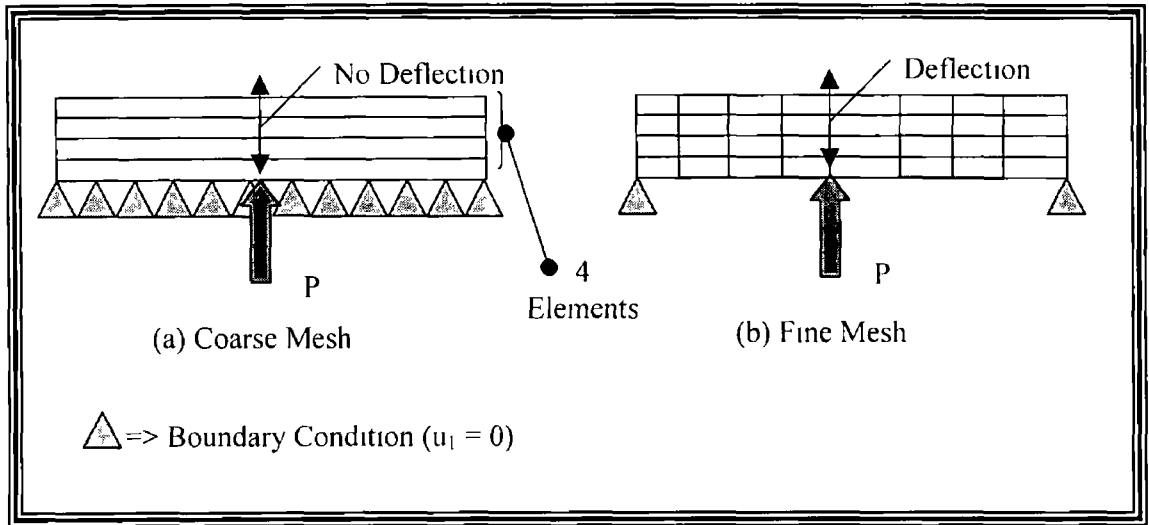


Figure 46, Applying boundary conditions to coarse and fine meshed problems

The residual stress determination was carried out as a two or in some cases a three dimensional system, however expressing the numerical formulation for a 2-D or 3-D system, would be too lengthy. Expressing the residual stress as an one-dimensional system provides sufficient information as to the mechanism of stress determination in deflected bimetallic beam. The analysis is based upon applying a load to one side of the system (at node 1), while fixing the opposite side of the system (at node 5), as shown in figure 47.

Using equation 81, adjusting its stiffness matrix to ensure that the equation in row 5 states

$$u_5 = 0 \quad \text{Equation 83}$$

Therefore the overall matrix for this system is expressed in equation 85

$$\begin{bmatrix} k_1 & -k_1 & 0 & 0 & 0 \\ -k_1 & k_1 + k_2 & -k_2 & 0 & 0 \\ 0 & -k_2 & k_2 + k_3 & -k_3 & 0 \\ 0 & 0 & -k_3 & k_3 + k_4 & -k_4 \\ 0 & 0 & 0 & 0 & 1 \end{bmatrix} \cdot \begin{Bmatrix} u_1 \\ u_2 \\ u_3 \\ u_4 \\ u_5 \end{Bmatrix} = \begin{Bmatrix} P \\ 0 \\ 0 \\ 0 \\ 0 \end{Bmatrix} \quad \text{Equation 84}$$

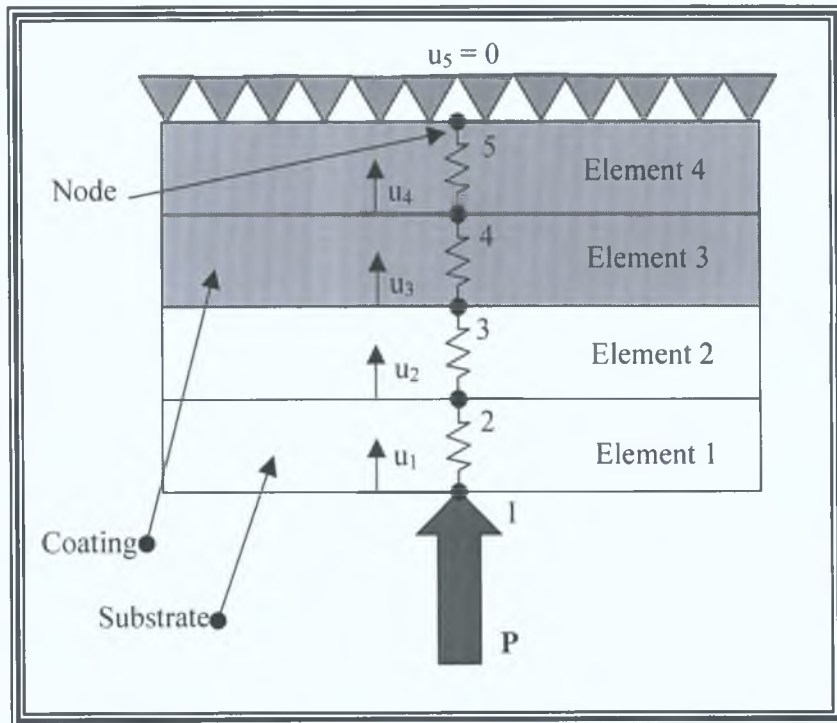


Figure 47, Schematic of the coated sample system used to demonstrate how the finite element technique arrives at a solution.

**Solution Phase**

*Solve a system of algebraic equations simultaneously.*

In order to obtain numerical values of the nodal displacements,  $E_s = 200 \times 10^3 \text{ N/mm}^2$  was used as the substrate stiffness [109] and  $E_c = 190 \times 10^3 \text{ N/mm}^2$  found in the current research, and the sample width  $W = 20\text{mm}$ , length  $L = 80\text{mm}$ , and a thickness of  $t_s =$

1 mm (substrate), and  $t_c = 1$  mm (coating), all values used in the experimental section of the research. The load applied will be assumed to be 5N.

The sample was discretized into four equal parts across its thickness, therefore the cross-sectional area of each element in the y-direction can be expressed as:

$$A(y) = W.L = (20)(80) = 1600\text{mm}^2 \quad \text{Equation 85}$$

as  $t_s = t_c = t = 1$  mm, therefore the length of each element, is as follows:

$$l = \frac{t}{2} = 0.5\text{mm} \quad \text{Equation 86}$$

The equivalent stiffness coefficient for each element is calculated from the following equations:

$$k_{eq} = \frac{A(y)E}{l} \quad \text{Equation 87}$$

$$k_1 = \frac{(1600)(200 \times 10^3)}{0.5} = 6.40 \times 10^8 \text{ N/mm} \quad \text{Equation 88}$$

$$k_2 = \frac{(1600)(200 \times 10^3)}{0.5} = 6.40 \times 10^8 \text{ N/mm} \quad \text{Equation 89}$$

$$k_3 = \frac{(1600)(190 \times 10^3)}{0.5} = 6.08 \times 10^8 \text{ N/mm} \quad \text{Equation 90}$$

$$k_4 = \frac{(1600)(190 \times 10^3)}{0.5} = 6.08 \times 10^8 \text{ N/mm} \quad \text{Equation 91}$$

Putting these into the global stiffness matrix given by equation 84, to get:

$$10^8 \cdot \begin{bmatrix} 6.4 & -6.4 & 0 & 0 & 0 \\ -6.4 & 12.8 & -6.4 & 0 & 0 \\ 0 & -6.4 & 12.48 & -6.08 & 0 \\ 0 & 0 & -6.08 & 12.16 & -6.08 \\ 0 & 0 & 0 & 0 & 1 \end{bmatrix} \cdot \begin{Bmatrix} u_1 \\ u_2 \\ u_3 \\ u_4 \\ u_5 \end{Bmatrix} = \begin{Bmatrix} 5 \\ 0 \\ 0 \\ 0 \\ 0 \end{Bmatrix} \quad \text{Equation 92}$$

The displacement solution to this matrix is:  $u_1 = 3.2 \times 10^{-8}$  mm,  $u_2 = 2.5 \times 10^{-8}$  mm,  $u_3 = 1.7 \times 10^{-8}$  mm,  $u_4 = 0.8 \times 10^{-8}$  mm, and  $u_5 = 0$  mm. The force of 5N caused the sample to deflect by varying displacements from node 1 (highest displacement at point of force) up to node 5 (no displacement). A contour line representation of this result is shown in figure 48.

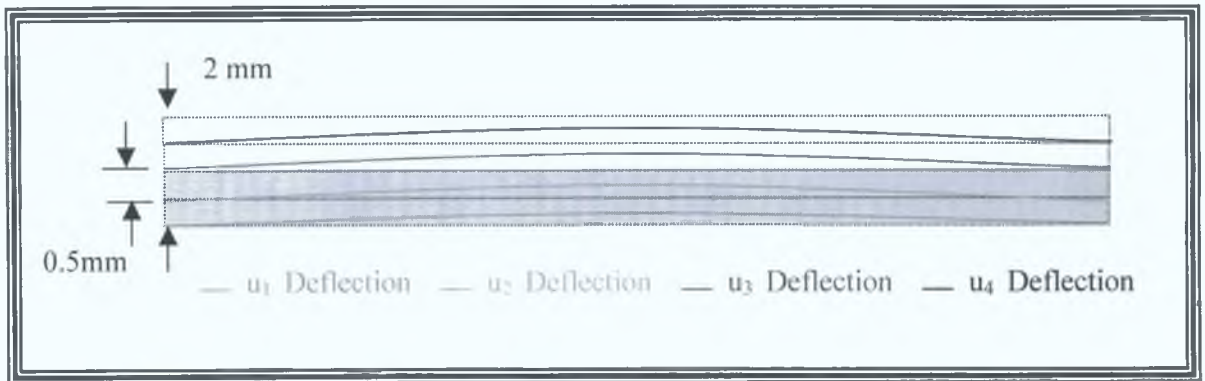


Figure 48, Schematic of the graphical contour lines showing the displacements of each node (solid lines) compared to pre-deformed shape (coloured lines).

Postprocessing Phase

*Obtain other Information.*

Additional information such as average normal stress in each element may be of concern. These values can be determined from the equation:

$$\sigma = \frac{f}{A_{avg}} = \frac{k_{eq}(u_{i+1} - u_i)}{A_{avg}} = \frac{A_{avg} E / l (u_{i+1} - u_i)}{A_{avg}} = E \left( \frac{u_{i+1} - u_i}{l} \right) \quad \text{Equation 93}$$

where  $\left(\frac{u_{i+1} - u_i}{l}\right) = \epsilon$ , the strain in each element. The average normal stress through each element is:

$$\sigma^{(1)} = E_s \left(\frac{u_2 - u_1}{l}\right) = (200 \times 10^3) \left(\frac{2.5 - 3.2}{0.5}\right) \times 10^{-8} = -280 \times 10^{-5} \text{ N/mm}^2$$

Equation 94

$$\sigma^{(2)} = E_s \left(\frac{u_3 - u_2}{l}\right) = (200 \times 10^3) \left(\frac{1.7 - 2.5}{0.5}\right) \times 10^{-8} = -320 \times 10^{-5} \text{ N/mm}^2$$

Equation 95

$$\sigma^{(3)} = E_c \left(\frac{u_4 - u_3}{l}\right) = (190 \times 10^3) \left(\frac{0.8 - 1.7}{0.5}\right) \times 10^{-8} = -342 \times 10^{-5} \text{ N/mm}^2$$

Equation 96

$$\sigma^{(4)} = E_c \left(\frac{u_5 - u_4}{l}\right) = (190 \times 10^3) \left(\frac{0 - 0.8}{0.5}\right) \times 10^{-8} = -304 \times 10^{-5} \text{ N/mm}^2$$

Equation 97

The compressive stress is experienced by both the substrate and the coating. The highest stress is found at the interface (bonding) point of the substrate and coating. The stress is highest here due to the mismatch in stiffness. In the ANSYS program these stresses would be represented by coloured contours, similar to that shown in figure 49.

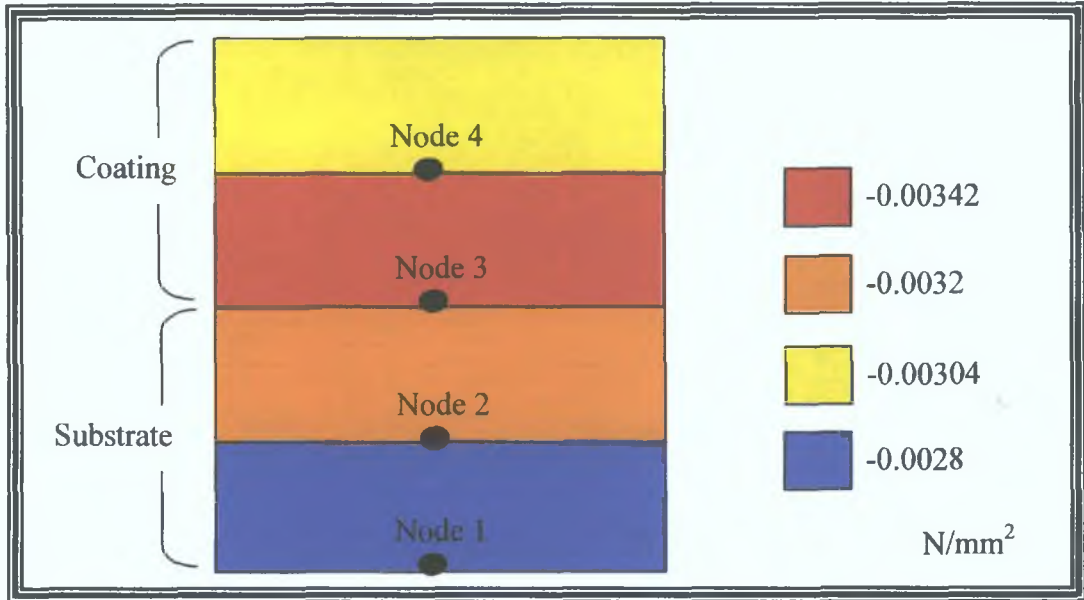


Figure 49, Schematic of the nodal stress contours based on the numerical formulation problem used in the present section.

The residual stress was simulation by applying a thermal load to the system (based on the suggestion from the ANSYS user manual [110]) and in parallel by creating a moment in the sample (applying a compressive force to the deposit while applying an equal tensile force to the substrate), as shown in figure 49. Each of these simulations should yield similar results to that found using Clyne’s Method and stress distributions through the sample thickness, as all three extend from ‘Beam Bending Theory’. The objective is to use the finite element analysis as a predictive method for determining residual stress in deposits.

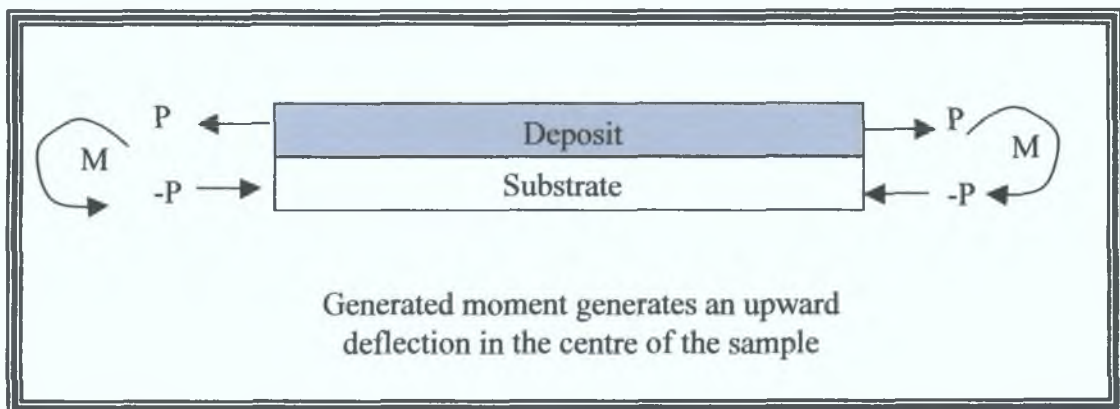


Figure 50, Generated moment finite element analysis system.

## 4.6 Verification of Results

In recent years, the use of finite element analysis as a design tool has grown rapidly. User friendly comprehensive packages such as ANSYS have become a common tool in engineering design [110]. Unfortunately, without proper training or a solid understanding of the underlying engineering principles on the part of the operator, the finite element procedures can create errors or incorrect results. Sources of errors include

*(a) Wrong input data such as physical properties and dimensions*

This mistake may be corrected by listing and verifying the physical properties and co-ordinates of nodes or keypoints before proceeding any further with the analysis. Units of the geometrical shape, properties and other influencing parameters must be consistent.

*(b) Selecting inappropriate types of elements*

It is important to fully grasp the limitations of a given type of element and understanding what element types belong to what system type, that is a two dimensional element would be used in a two dimensional system and so on.

*(c) Poor element shape and size after meshing*

Inappropriate element shape and size will influence the accuracy of the results. It is important to understand the difference between free meshing (using mixed-area element shapes) and mapped meshing (using all quadrilateral area elements or hexahedral volume elements) and the limitations associated with them.

*(d) Applying wrong boundary conditions and loads*

This step is usually the most difficult aspect of modelling [110]. It involves taking an actual system and estimating the loading and the appropriate boundary conditions for the finite element model.

Experimental testing (as carried out in this research) is the best way to check, verify and predict finite element results. Where finite element results are not verified by

experimental results (due to the expense and time consumption in producing experimental results), verification of finite element results may be found by other methods, such as comparing results to simply analytical solutions. Applying equilibrium conditions and energy balance to different parts of the model, to ensure that the physical laws are not violated is one method of verification. In static models, the sum of forces acting on a body must equal zero. In heat transfer systems under steady state conditions, the conservation of energies flowing in and out of nodes should be balanced.

## 4.7 CAPABILITIES AND ORGANISATION OF ANSYS

The basic steps involved in creating and analysing a model with ANSYS are described in this section. There are three processors used in ANSYS: (1) the *Preprocessor* (**PREP7**), (2) the *Processor* (**SOLUTION**), and (3) the general *Postprocessor* (**POST1**).

### 4.7.1 Creating A Model With ANSYS: Preprocessor

The preprocessor (**PREP7**) contains the commands needed to build a model, such as creating a model geometry and defining element types and element real constants and material properties, and defining meshing controls and to mesh the object created.

#### *Creating a Model Geometry*

There are two methods provided by ANSYS to construct a finite element model's geometry, direct or manual generation and the solid-modelling approach. Direct generation is a simple method where the user specifies the location of nodes and manually defines which nodes makes up an element. This approach is generally applied to simple systems that can be modelled with line elements, such as links or beams, similar to that shown in figure 51 (a). While in the solid-modelling approach, simple primitives (geometrical shapes such as rectangles, circles, polygons, blocks, cylinders, and spheres) are used to construct the model, as shown in figure 51 (b). Boolean operations (such as addition, subtraction, and intersection) are then used to combine the primitives.

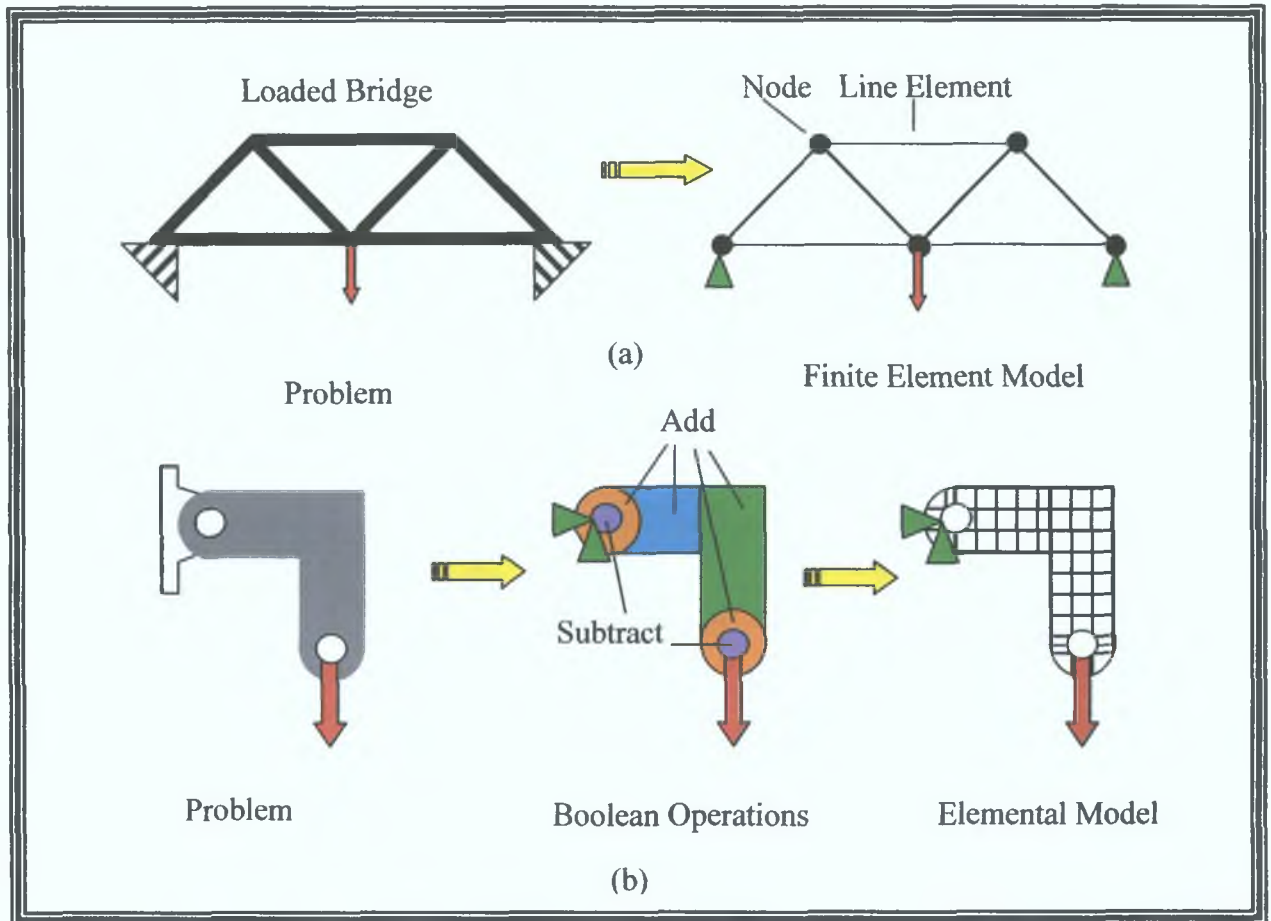


Figure 51, Finite element model generation, (a) direct generation, (b) solid modelling approach.

When creating primitives such as rectangles, the object is made up of entities including keypoints, lines, and areas or volumes. Keypoints define the vertices of an object, lines are used to represent the edges of the object, areas or volumes are used to represent either two or three-dimensional solid objects respectively, as shown in figure 52. These entities are automatically numbered by the ANSYS program, for data logging. In general volumes are bounded by areas, areas are bounded by lines, and lines are bounded by keypoints.

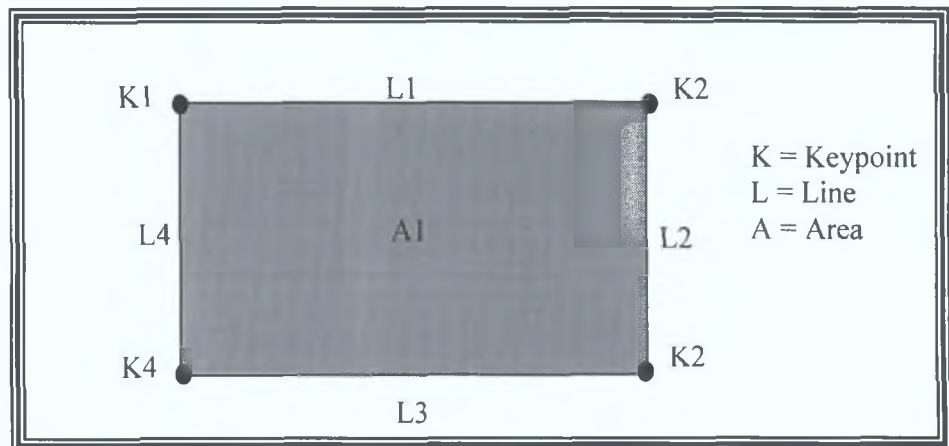


Figure 52, The relationship between keypoints, lines and areas.

### *Element Type Options*

ANSYS provides more than one hundred various element types, all of which may be used to analyse systems. Selecting the correct type of element type to use in a particular system, is crucial in deriving a 'true' solution. Elements may be of three types: one, two and three-dimensional elements.

The structural and heat transfer systems analysed earlier in the report, were both analysed using one-dimensional elements. The element is represented by a line bounded by two nodes, and acts in one direction. The line acts like a spring extending or compressing depending on the change of its state, as shown in figure 53.

Where an object reacts in two directions due to some external condition, two-dimensional elements are required to model the system. One-dimensional solutions are approximated by line segments, whereas the two-dimensional solutions are represented by plane segments. These two-dimensional plane functions may be in the form of rectangular elements (4 nodes), quadratic quadrilateral elements (8 nodes), triangular elements (3 nodes), or quadratic triangular elements (6 nodes), as shown in figure 54 [111].

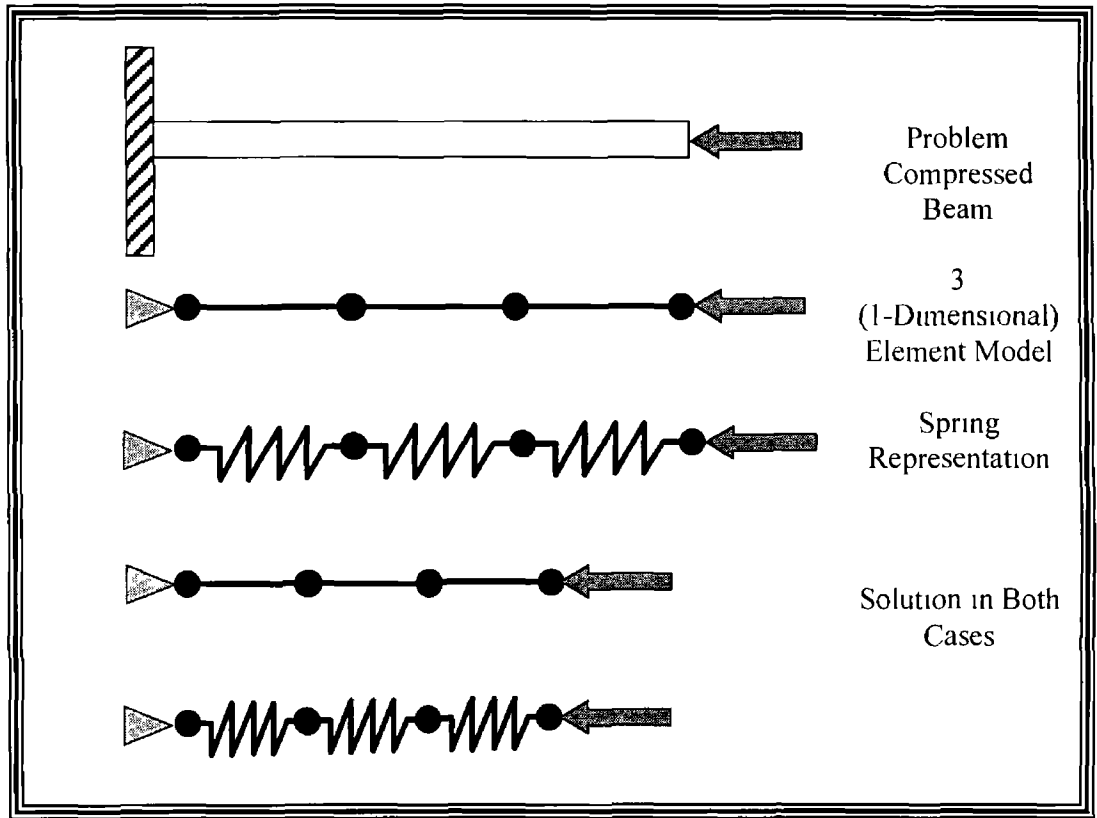


Figure 53, One-dimensional representation of a problem

An example of a thin plate with a perforated hole, held at the top left hand corner (boundary condition,  $\delta_{x&y}$ ) and subjected to an applied load  $P_{1&2}$ , is shown in figure 54. This depicts the four possible types of two-dimensional elements that may be found. Numerical equations apply in a similar way to two-dimensional elements as to one-dimensional elements, however in figure 54, nodal displacements are calculated in both x and y directions. A simple way to describe how an element behaves due to an external condition, is to imagine that each line that bounds a two dimensional element, reacts like springs, as shown in figure 55.

Just as a two-dimensional object reacts to external stimuli in two directions, a three-dimensional object will react in three directions. Examples of three-dimensional elements are brick elements (8 and 20 nodes) and tetrahedral (4 and 10 nodes) as shown in figure 56 [111].

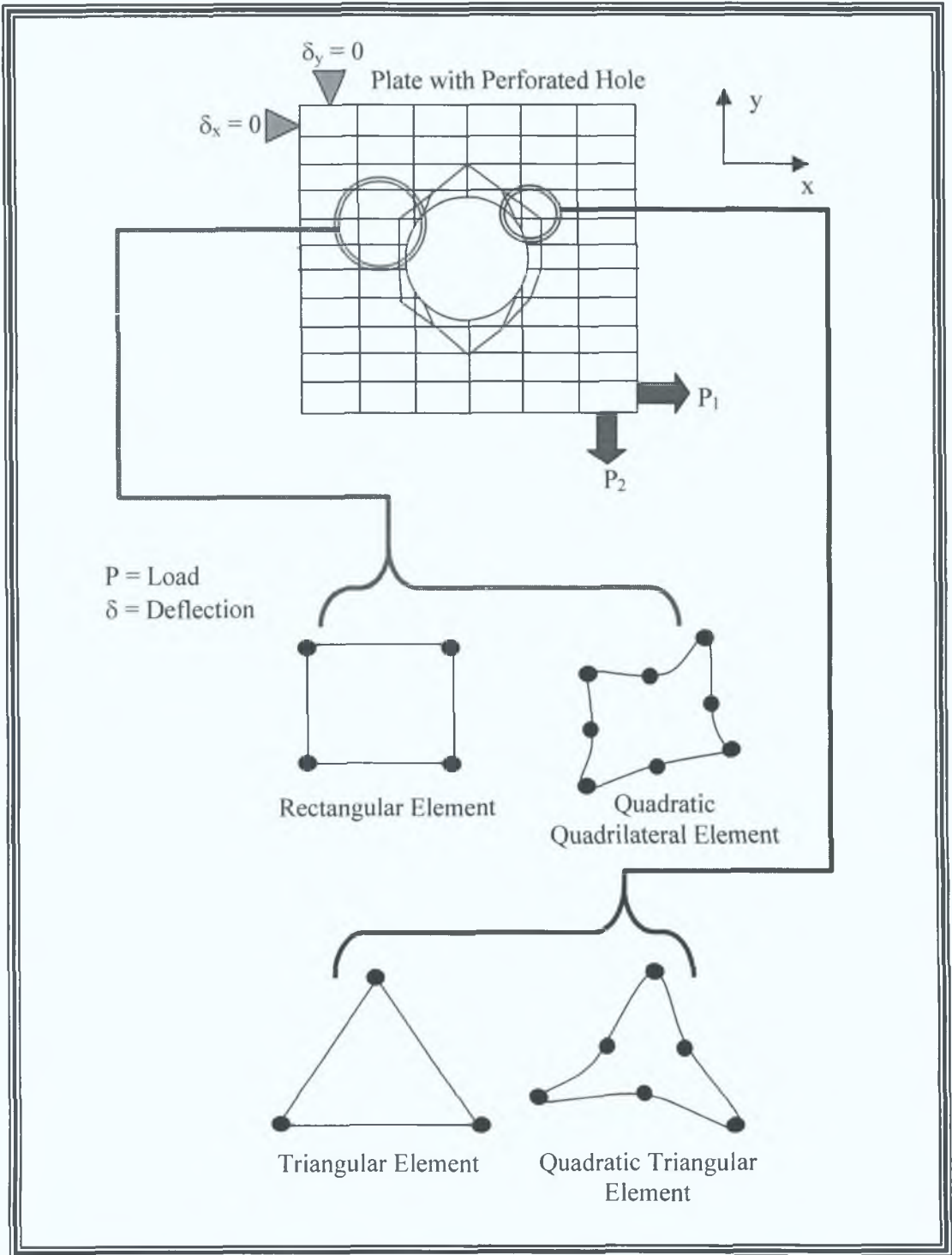


Figure 54, Various types of two-dimensional elements [111].

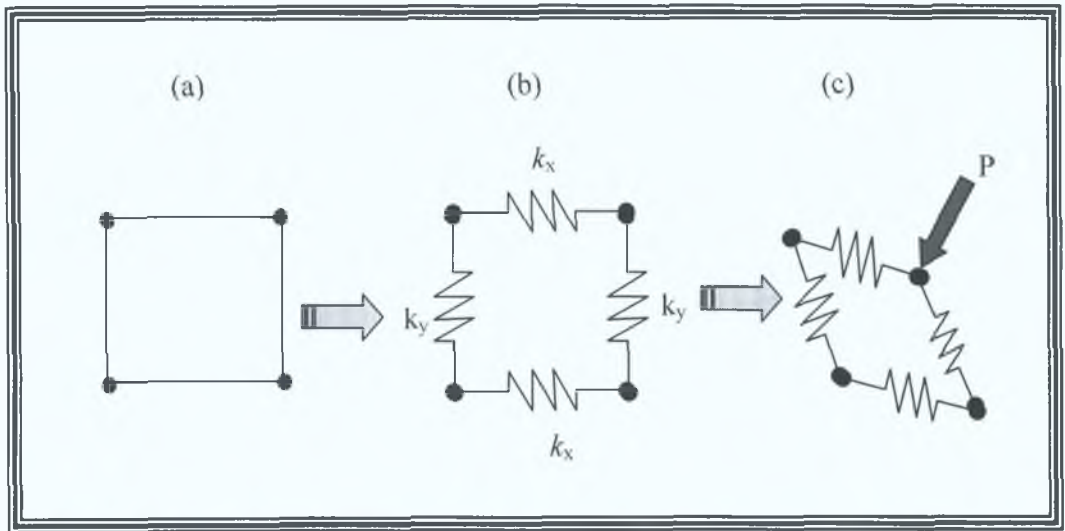


Figure 55, Simple representation of a two-dimensional element (a), as a series of springs (b) and subjected to a load (c).

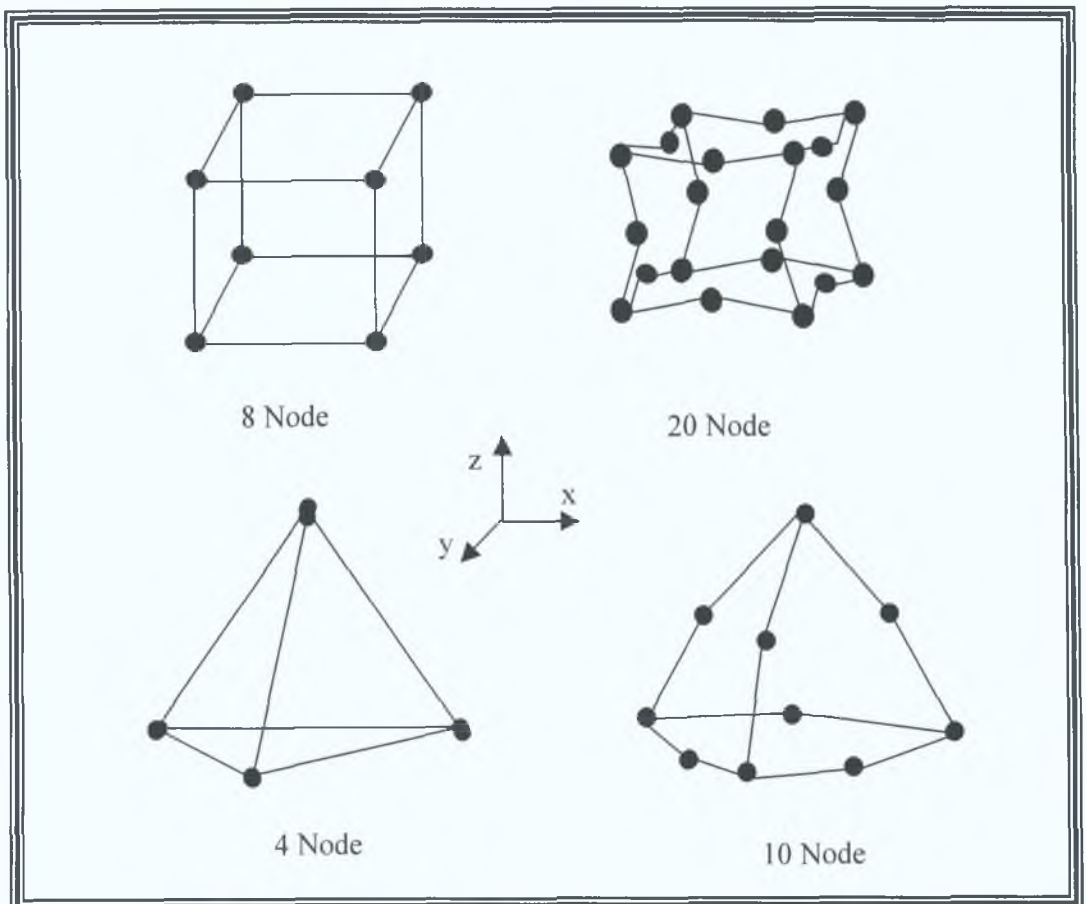


Figure 56, Schematic of various three-dimensional elements.

*ANSYS Element Types Used In Research*

As described, there are many element types to choose from, and the selection of the correct element for a specific system is important. The ANSYS user manual [110], lists the correct element types to use for specific systems, hence this is how the following element types were chosen. The detail of each element, is a synopsis of the detail given in the ANSYS manual [111].

Heat Transfer:

PLANE55 is a four-node quadrilateral element used in two-dimensional heat conduction systems. The element is defined by four nodes, with one degree of freedom at each node, temperature. Output data include nodal temperatures and elemental data, such as thermal gradient and thermal flux components.

PLANE77 is an eight-node quadrilateral element used in the modelling of two-dimensional heat conduction systems. It is basically a higher order version of the PLANE55 element. The element is capable of modelling systems with curved boundaries. At each node, the element has a single degree of freedom, temperature. Output data of this element type include nodal temperatures and elemental data, such as thermal gradient and thermal flux components.

SOLID70 is a three-dimensional brick element used to model conduction heat transfer systems. It has eight nodes having a single degree of freedom, temperature. Convection or heat fluxes are applied to the element's surface. In addition heat generation rates may be applied at the nodes. The element may be used to analyse steady-state or transient systems. The solution output consists of nodal temperatures and average face temperature, temperature-gradient components and the heat-flux components.

Residual Stress:

PLANE13 has a 2-D magnetic, thermal, electrical, piezoelectric, and structural field capability with limited coupling between the fields (thermal properties can be inputted into the system, while stresses may be outputted). PLANE13 is defined by four nodes with up to four degrees of freedom per node. The element has non-linear magnetic capability for modelling B-H curves or permanent magnet demagnetization curves. When used in a structural analysis PLANE13 has large deflection, large strain, and stress stiffening capabilities.

PLANE42 is a four-node quadrilateral element used in two-dimensional solid modelling systems. The element is defined by four nodes, with two degrees of freedom at each node, the translation in the x and y-directions. The element input data can include thickness if KEYOPTION 3 (plane stress with thickness input) is selected. Surface pressure loads may be applied to the element edges. Output data include nodal displacements and elemental data, such as directional stresses and principal stresses.

PLANE82 is an eight-node quadrilateral element used in two-dimensional solid modelling systems. It is a higher order version of the two-dimensional PLANE42 element. This element offers more accuracy when modelling systems with curved boundaries. At each node, there are two degree of freedom, the translation in the x and y-directions. Just like PLANE42, the element input data can include thickness if KEYOPTION 3 (plane stress with thickness input) is selected. Surface pressure loads may be applied to the element edges. Output data include nodal displacements and elemental data, such as directional stresses and principal stresses.

SOLID45 is an eight-node brick element used to model isotropic solid systems. Each node has three translational degrees of freedom in the nodal x, y and z-directions. Distributed surface loads may be applied to the element surfaces. This element is used to analyse large deflections, large strain, plasticity and creep systems. The output solution data consists of nodal displacements and elemental data, such as stresses in the x, y, and z directions, shear stresses and principal stresses.

SOLID186 is a higher order 3-D 20-node structural solid element with a block displacement behaviour (deforms in all three x, y and z-directions) and is well suited to modelling complex shapes (such as those produced by various CAD/CAM systems). The element has three degrees of freedom per node: translations in the nodal x, y, and z directions. The element supports plasticity, hyperelasticity, creep, stress stiffening, large deflection, and large strain capabilities

Finally, it may be worth noting that in general, better results and greater accuracy are achieved with higher order elements, however these elements require more computational time [111]. This time requirement is due to the numerical integration of more complex elemental matrices involved in the calculation of the solution.

#### *Element Real Constants*

Element real constants are quantities that are specific to a particular element. For example, a beam element requires a cross-sectional area, second moment of area and so on, therefore these real constants vary from one element type to another, furthermore not all elements require real constants. If the analyst has not used the real constant, an ANSYS warning prompts as to the missing information.

#### *Material Properties*

Physical properties of the model must be defined, before the solution can be calculated. For example, the modulus of elasticity, Poisson's ratio or the density of the material must be defined in solid structural systems, whereas in thermal systems, thermal conductivity, specific heat, or the density of the material must be defined.

#### *Define Meshing Controls*

The finite element model geometry is divided into nodes and elements, a process known as meshing. The ANSYS program automatically generates the nodes and specified elements, once the *element attributes* and *element size* have been specified:

- a) The *element attributes* include element type or types, real constants, and material properties.

- b) The *element size* controls the coarseness or fineness of the mesh. The larger the element size, the coarser the mesh, conversely the smaller the element size, the finer the mesh. If an element edge length of 10 units (unit will depend on the dimensional unit used to create the model, like millimetres) is specified, then the ANSYS program will generate a mesh of a series of elements with edge lengths no larger than 10 units. Another way to control the mesh size is by specifying the number of element divisions along a boundary line.

#### *Meshing the Model*

Once the meshing controls have been entered, meshing of the model may commence. Clicking on the 'Meshing' icon, meshing may be applied to areas or the entire volume. The meshing process can take some time, depending on the model complexity and the speed of the user's computer. During the meshing, ANSYS writes a *meshing status* to an output window.

There are two types of meshing options that can be used: free and mapped meshing. Free meshing uses either mixed area element shapes (triangular elements mixed with quadrilateral elements) or all triangular area elements. The mapped meshing options use all quadrilateral area elements and all hexahedral (brick) volume elements. Mapped area mesh requires the object to be analysed to have three or four sides, an equal number of elements on opposite sides of a four-sided object, and an even number of elements on all sides of a three-sided object. If an object is bound by more than four lines, the concatenate command is used to combine some of the area edge lines to form elements, to reduce the total number of lines.

#### 4.7.2 Solution

The solution processor (**SOLUTION**) has the commands that allow you to apply boundary conditions and loads. Once all of the boundary information is made available to the solution processor (**SOLUTION**), it solves for the nodal solutions.

### 4.7.3 General Postprocessor

The general postprocessor (**POST1**) contains the commands to read the results data from the results file, read element results data, plot results and list results of an analysis. There are other processors that perform additional tasks, such as the *Time-History Processor* (**POST26**), which contains the commands to review results over time in a transient analysis at a certain point in the model [112]. The *Design Optimisation Processor* (**OPT**) allows the user perform a design optimisation analysis.

## 4.8 ANSYS PROCEDURE

The procedure used in the current research, for both the heat transfer system and the residual stress determination is contained in Appendix 7. The procedure describes the following:

- Describing the system
- Building the geometry in the Preprocessor Phase
- Defining material properties
- Selecting the element type
- Generating the mesh
- Applying the boundary conditions in the Solution Phase
- Solving the system
- Obtaining the solution in the Postprocessor Phase
- Saving and exiting the ANSYS program

---

# RESULTS AND DISCUSSION

---

## 5.1 INTRODUCTION

The present study aims to establish the potential of producing tungsten carbide-cobalt free-standing components using the HVOF process. The report focuses on maximising the thickness of such components. However, residual stress limits the thickness achieved by causing adhesion loss between the deposit and its base material, interlaminar debonding, crack formation and buckling. In this chapter, the experimental results and discussions of the HVOF thermal spraying process are presented and analysed. The experimental results are grouped into five categories;

1. The optimisation of the process equipment and spraying parameters
  - Spraying Temperature
  - Spraying Distance
  - Powder feed rate
  - Post-heat Treatment
2. Residual stress analysis
  - Almen Test Method
  - Clyne's Method
  - XRD Diffraction
  - Hole Drilling Method
3. Investigate the mechanical properties of the WC-Co deposit
  - Young's Modulus
  - Hardness
  - Porosity
  - Phase Development

## 4. The fabrication of spray-formed engineering components

- Cylindrical components
- Tensile Components
- Forming complex components

## 5. Finite element analysis technique

- Heat Transfer
- Residual Stress Development

The study investigates the effect of various thermal spraying parameters on residual stress build up within the deposit material. Figure 57 describes the order of results presented in the report. Within these sections the experimental results are compared to finite element analysis simulated results.

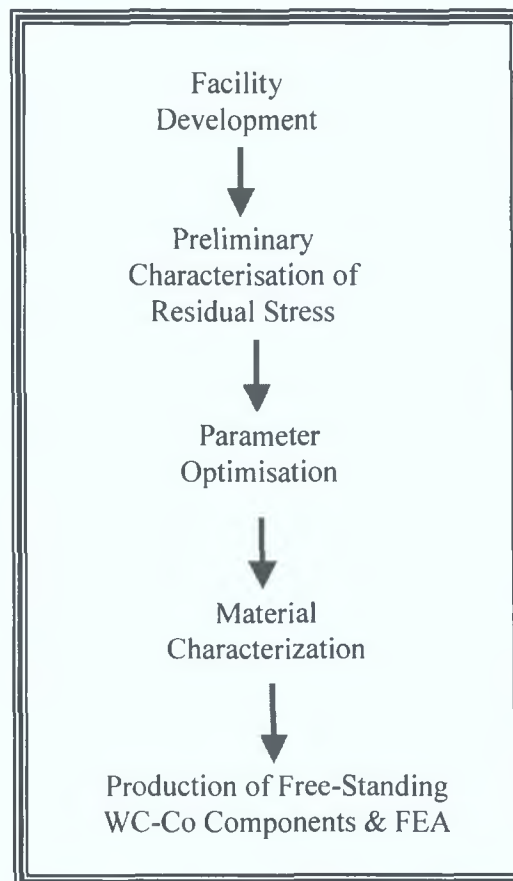


Figure 57, The order of the presented experimental results.

## 5.2 TEMPERATURE MEASUREMENT

Previous research in the Materials Processing Research Centre, has identified various temperatures (such as 200 [49] or 450 [61] for pre-spray and 475°C [30,113] for spraying temperature), as the recommended temperatures to be used during the thermal spraying of WC-Co. These temperatures were measured by optical pyrometer, however Helali [49] expressed low confidence in the accuracy of this device for flame-based temperatures. The objective of this phase of experimental work was to increase the accuracy of temperature measurement by using thermocouples.

### 5.2.1 Pyrometer Test

A experiment was carried out to determine the accuracy of the pyrometer by comparing its measured temperatures to that measured by thermocouples. Test 1 results were carried out with a distance of 35mm between the metallic pyrometer case and the block. The temperature measured by the pyrometer differ from the thermocouple readings by 20%. Tests 2 and 3, were carried out at distances of 150mm and 200mm, and showed a decrease of 2 and 2.5% respectively in this difference. In each of the tests, the relationship is linear (figure 58), with little or no scatter.

The accuracy of the pyrometer is expected to be of the order of 0.2% of the reading or 2°C whichever is smaller, and that of the thermocouples to be  $\pm 0.5^\circ\text{C}$ , hence their output would be expected to closely correlate. The large difference in readings seen here could arise in part from poor heat transfer from the solid to the thermocouple and inaccuracies from the pyrometer. In order to compare pyrometer readings with thermocouple measurements at a heat source, a correction factor is required as shown in equation 98. An implication of this is that temperatures recorded using the pyrometer by previous researchers in the Materials Processing Research Centre [30,49,61,113] can be corrected using the following:

$$T_{\text{actual}} \approx \frac{T_{\text{pyrometer}}}{1.2} \quad \text{Equation 98}$$

$T_{\text{actual}}$  = Actual temperature of heat source

$T_{\text{pyrometer}}$  = Temperature measured by pyrometer

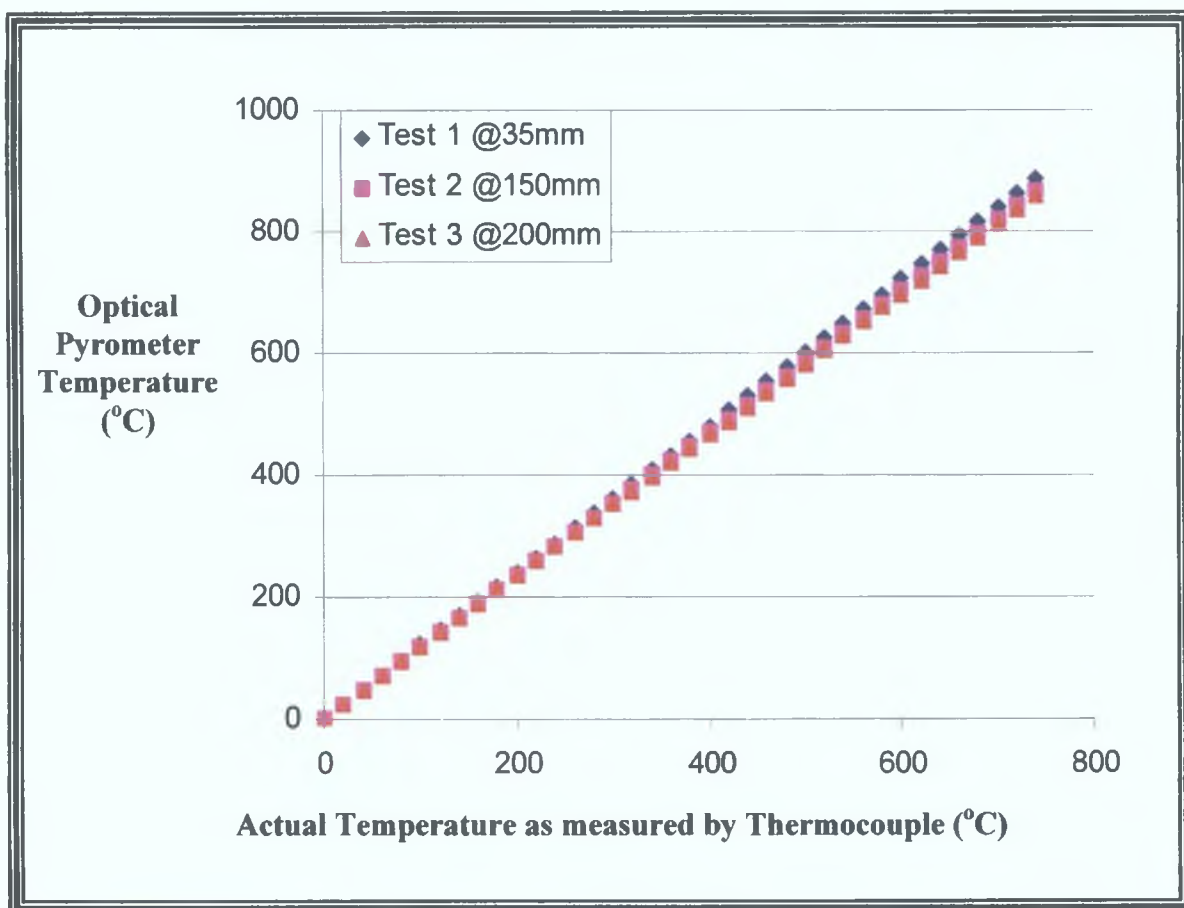


Figure 58, Graphical results of differing temperatures measured by optical pyrometry and using thermocouples.

Another test was carried out to examine the effect the Diamond Jet flame has on the pyrometer readings. The flame was focused onto a substrate, and both the pyrometer and thermocouples measured temperature readings during heating. The flame caused a deterioration in the stability of the pyrometer readings. For example when the

thermocouple recorded a temperature of around 650°C, the pyrometer output fluctuated in the range between 600 and 1200°C.

The explanation for this fluctuation is the fact that the pyrometer measures the intensity of radiation emitted by one or more spectral (wavelength or colour) bands. Whilst spraying, other emissions are also detected, namely the flame and the in-flight particles. Attempts were made to limit the focus spot of the pyrometer, but this proved unsuccessful. Results indicate that the pyrometer is not suitable for directly measuring temperatures during spraying. However it has been used, focused outside the periphery of the flame [114].

### 5.2.2 Calibration Of Remote Temperature Measurement Technique

The use of thermocouples as a method of temperature measurement in thermal spraying is constrained, as deposits coat the thermocouple and affect the measured readings, whereas the pyrometer had none of these disadvantages. To incorporate the use of thermocouples as a means of temperature measurement, a method was devised to estimate the spraying temperature, by knowing the temperature at the back of a substrate. The system was then simulated using the finite element technique.

#### (1) Experimental

The average temperature calibration results are illustrated in figure 59. The test was carried out three times and the scatter recorded was about 5 to 8°C. The relationship between front and back measurements is almost linear and it can be seen that the substrate on its own caused a reduction in temperature as measured from the back, whereas increasing the thickness of the WC-Co deposit has little effect on the temperature recorded from the back of the die (stainless steel substrate). For example if deposition commenced on the front side of the die, a temperature of 380°C recorded at the back of the die would indicate that the spraying temperature (at the front) is approximately 454.6°C. However if the aluminium releasing layer (75µm thick) together with several passes of WC-Co (a deposit thickness of 1mm) was deposited onto

the substrate, the temperature difference between the back and front change slightly more than that of the substrate on its own. A temperature now recorded of 380°C at the back of the substrate, would indicate that the spraying temperature had increased to approximately 483.8°C.

The stainless steel die thickness was 6mm compared to a maximum WC-Co deposit thickness of 2mm. The thermal conductivity for stainless steel is about 25 W(mK)<sup>-1</sup> [109], whereas the aluminium and WC-Co materials has a much higher values, 125 [109] and 90 W(mK)<sup>-1</sup> [33] respectively. The large difference in these properties, resulted in respective slopes when plotting the back temperature with respect to the front temperature.

The formula of each temperature gradient line is of the form:

$$T_{\text{front}} = m. T_{\text{back}} + CF \quad \text{Equation 99}$$

Where  $T_{\text{front}}$  and  $T_{\text{back}}$  are the front (unknown) and back temperatures (known) respectively and  $m$  is the slope of the graph and  $CF$  is the correction factor of results along the y-axis ( $T_{\text{front}}$  axis). An empirical formula was derived, knowing the slope of the substrates gradient line ( $m$ ), where the substrate thickness is negligible and the difference (correction factor) between this line and the other line gradients (includes increasing the substrate, aluminium releasing layer and WC-Co thicknesses). The formula exists where the thicknesses of each material is equal to 1mm. The aluminium foil has a low thickness (0.0075mm) compared to that of the other two materials, hence a multiplication factor (13.3) was required. The empirical formula found was as follows:

$$T_{\text{front}} = 1.02 T_{\text{back}} + 12 [ t_{\text{sub}} + 13.3 t_{\text{Al}} + t_{\text{WC-Co}} ] \quad \text{Equation 100}$$

Where  $t_{\text{WC-Co}}$  is the tungsten carbide-cobalt deposit thickness (mm),  $t_{\text{Al}}$  is the aluminium releasing layer thickness (mm) and  $t_{\text{sub}}$  is the stainless steel substrate thickness (mm). The formula was verified by substituting back temperatures into the formula, and

comparing the front temperature to that found experimentally. A maximum difference of  $\pm 4^{\circ}\text{C}$  was found between the experimental results and those found using the empirical formula. An example of where the empirical formula is in use is shown in figure 60. The front temperature is measured from this figure, for varying tungsten carbide-cobalt deposit thicknesses sprayed on a 0.075mm stainless steel substrate (without the releasing layer).

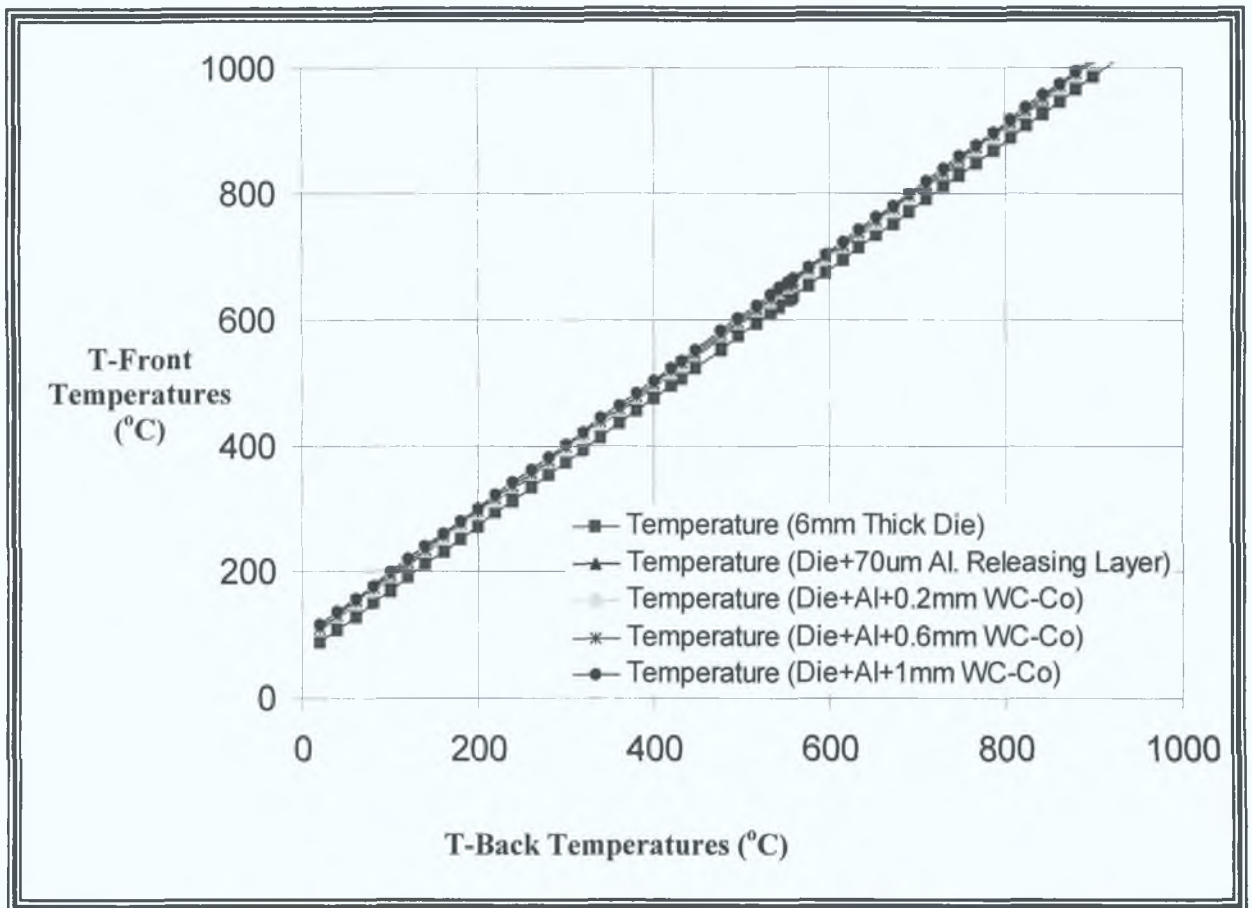


Figure 59, Temperature calibration graph for thermocouple measurement.

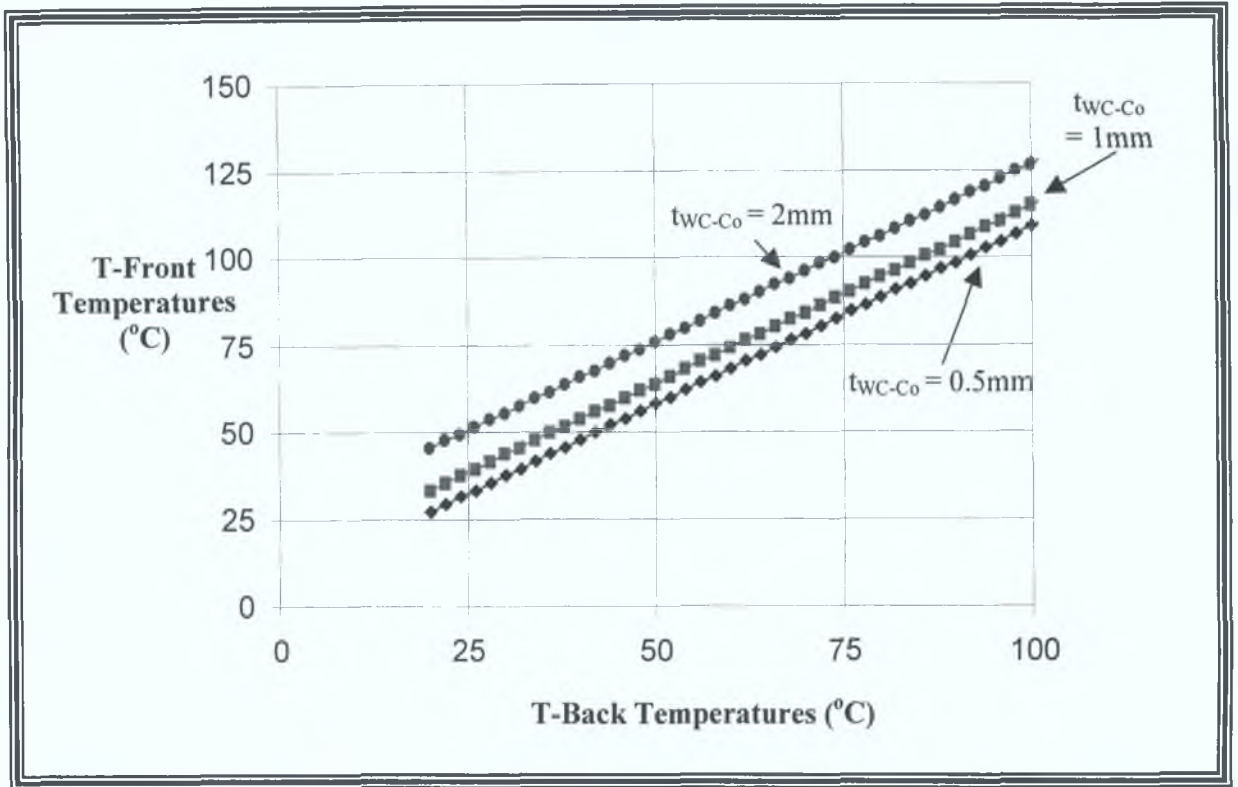


Figure 60, Use of the empirical formula to measure front temperature.

## (2) Finite Element Technique

The temperature distribution through the samples were simulated using the finite element technique. A finite element analysis of the temperature gradient starting from the flame (transferring heat onto the WC-Co surface) through to the releasing layer and finally the substrate, was carried out for various spraying temperatures. Figure 61, shows the mesh generated model used in the tests. Similar to that outlined in the heat transfer procedure, the flame temperature was applied to the nodes at the 'front' (WC-Co surface) of the sample, an air temperature was applied to the back area of the sample, and corresponding 'back' temperatures results (back of substrate) were recorded.

Various flame temperatures were applied from 0 to 950°C, while finite element coating thicknesses from 0.2mm up to 1mm were compared to their associated experimental results. The finite element 'front' and 'back' temperatures for both the experimental and finite element analysis results, are presented in figure 62. In general the deposition is carried out at a flame temperatures of around 500°C, hence figure 62 (b) focuses on this temperature range, showing the experimental and finite element flame temperatures between 400 and 600°C and the corresponding 'back' (or measured) temperatures respectively. Figure 62 (b), clearly shows the differences in results, the finite element results predicting measurements approximately 18% above that of the experimental values (for the same front temperature), in each of the results presented. For a measured back temperature of 410°C, the experimental front temperature for a 1mm deposit was measured as 502.2°C, this corresponds to a front temperature of 520.7°C found using the finite element technique for the same deposit. Figure 63 shows an example of the temperature gradient found in the finite element analysis at a flame temperature of 500°C for a 0.2mm deposit on a 6mm substrate.

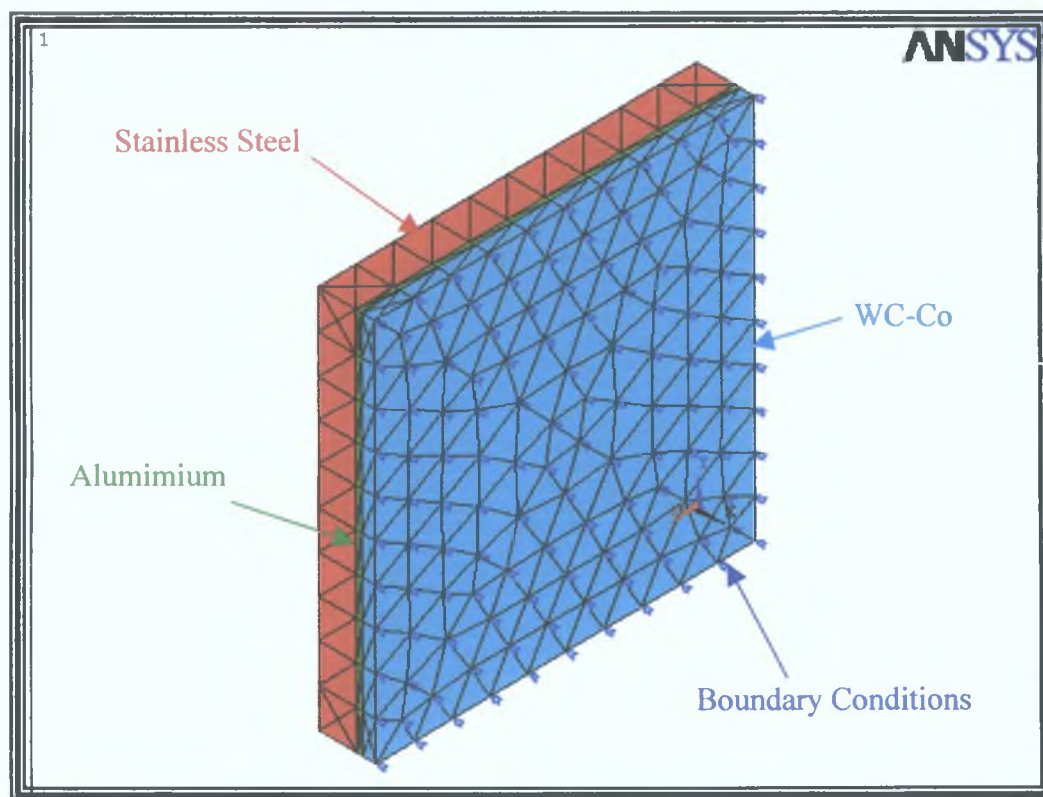


Figure 61, Mesh generated model used for the heat transfer problem.

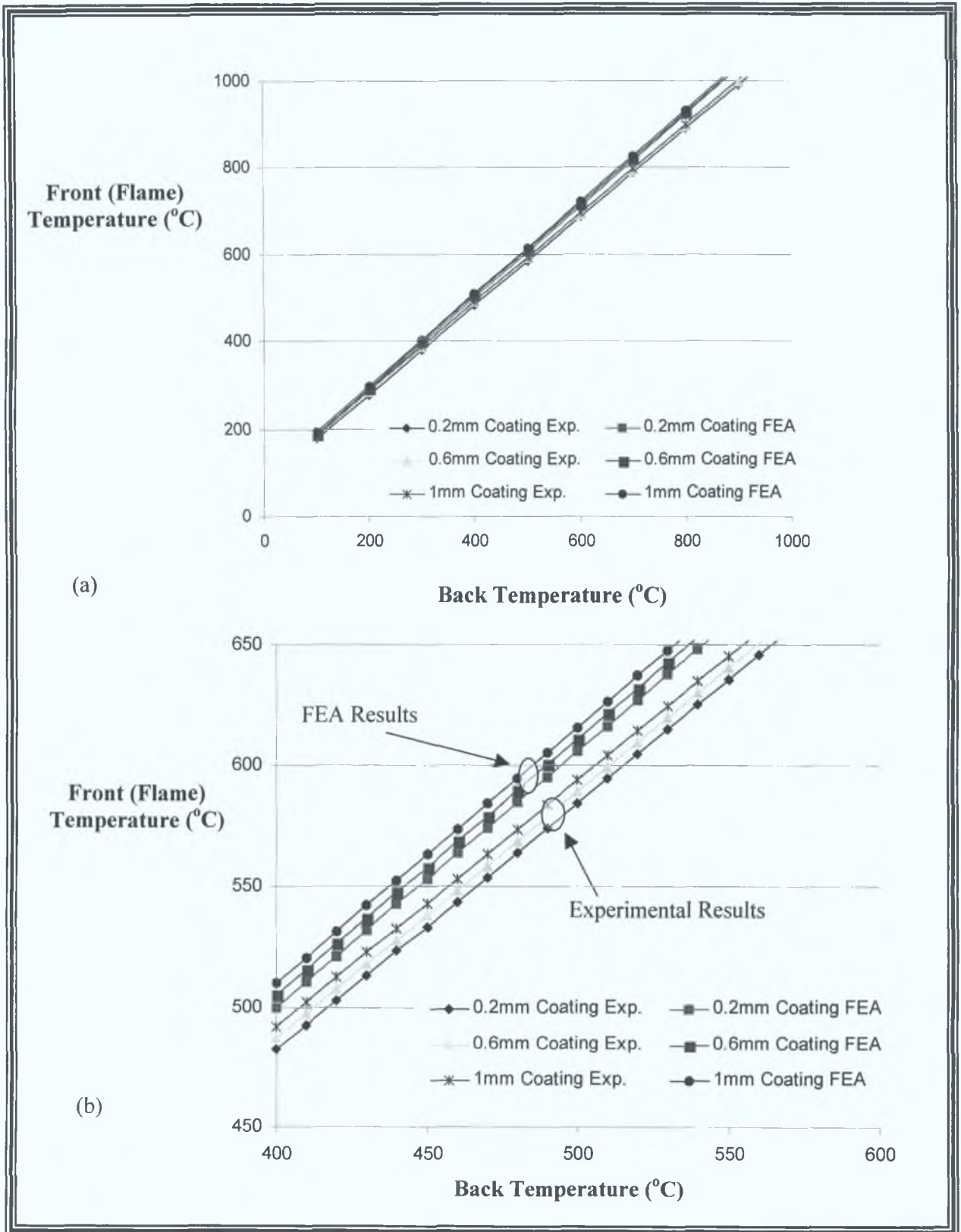


Figure 62, Comparison of finite element and experimental temperature gradient results, from the front (flame temperature) of the sample, through to the back (measured temperature) of the sample.

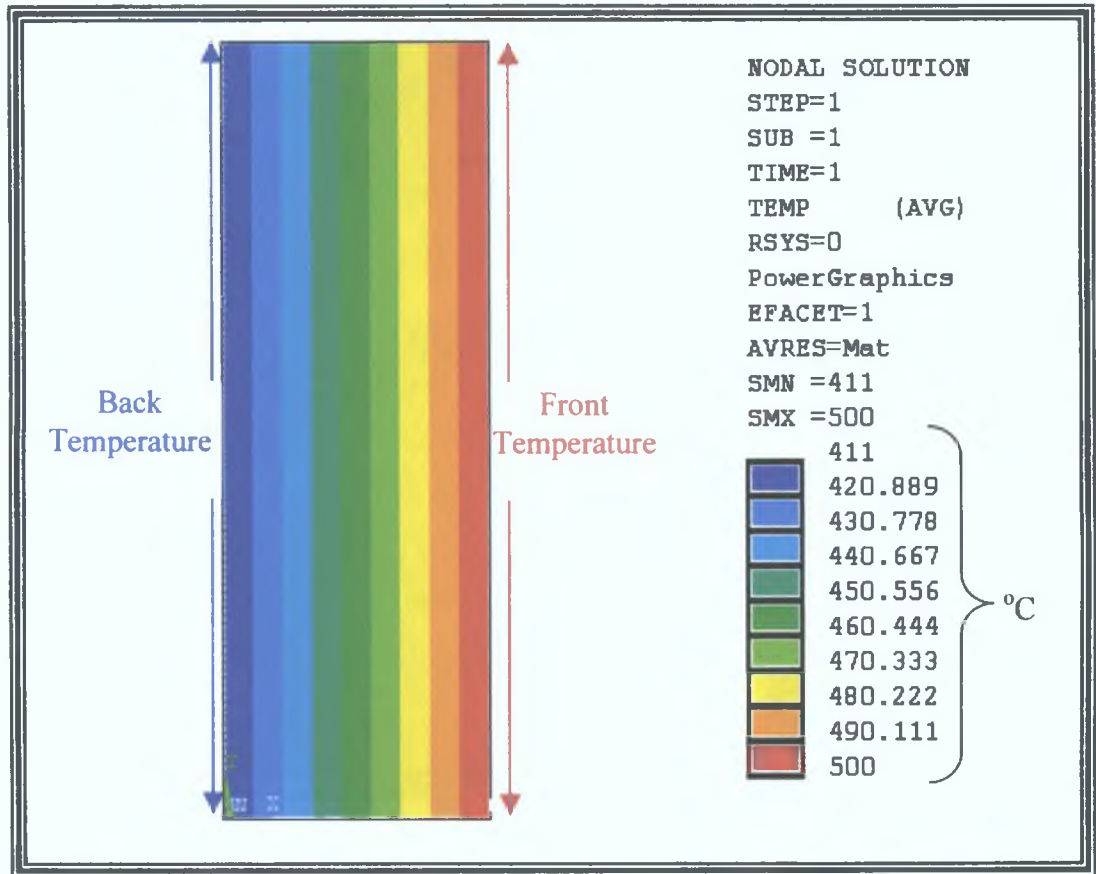


Figure 63, Finite element heat transfer result at a flame temperature of 500°C.

The difference between the finite element and experimental results is due to numerous factors. The finite element model was analysed as a two-dimensional problem, hence thermal losses (convective heat loss) through the sides of the samples were ignored. Radiation effects were ignored, which would account for thermal cooling in the system. The material properties used to analyse the problem arise from a literature search, and errors in these property values would either decrease or increase the difference between the finite element and experimental results. Use of thermocouples attached to the front and back of a sample may not give exact surface temperatures, therefore errors in the experimental results may have been encountered.

In summary, an empirical relationship between the deposition temperature and that measured remotely at the back of the substrate / die, has been established. An finite

element model of heat transfer in this simple system has shown reasonably close correlation with empirical data, thus validating its application where deposition is carried out using forced cooling.

### 5.2.3 Effect Of Spraying Distance And Cooling On Temperature

Figure 64 illustrates the spraying temperature for deposition carried out at various distances with, and without carbon dioxide cooling. The temperature readings were derived from measurements taken on the back surface of the die, by conversion using the calibration curve in figure 59. The results reveal a dramatic difference between normal and forced cooling. For instance at a spraying distance of 125mm, spray temperatures with and without cooling were found to be approximately 656 and 912°C respectively (a reduction of 28%). At longer spray distances, lower spray temperatures were found, however the proportional effect of the forced cooling increased (as high as 50%). Six temperature measurements (three for without forced cooling and three with) were recorded at 10mm intervals. The results were not linear. A second order polynomial curve was fit to the data using the root mean square method, for both the without and with forced cooling. There was little scatter in results ( $\pm 8^\circ\text{C}$ ).

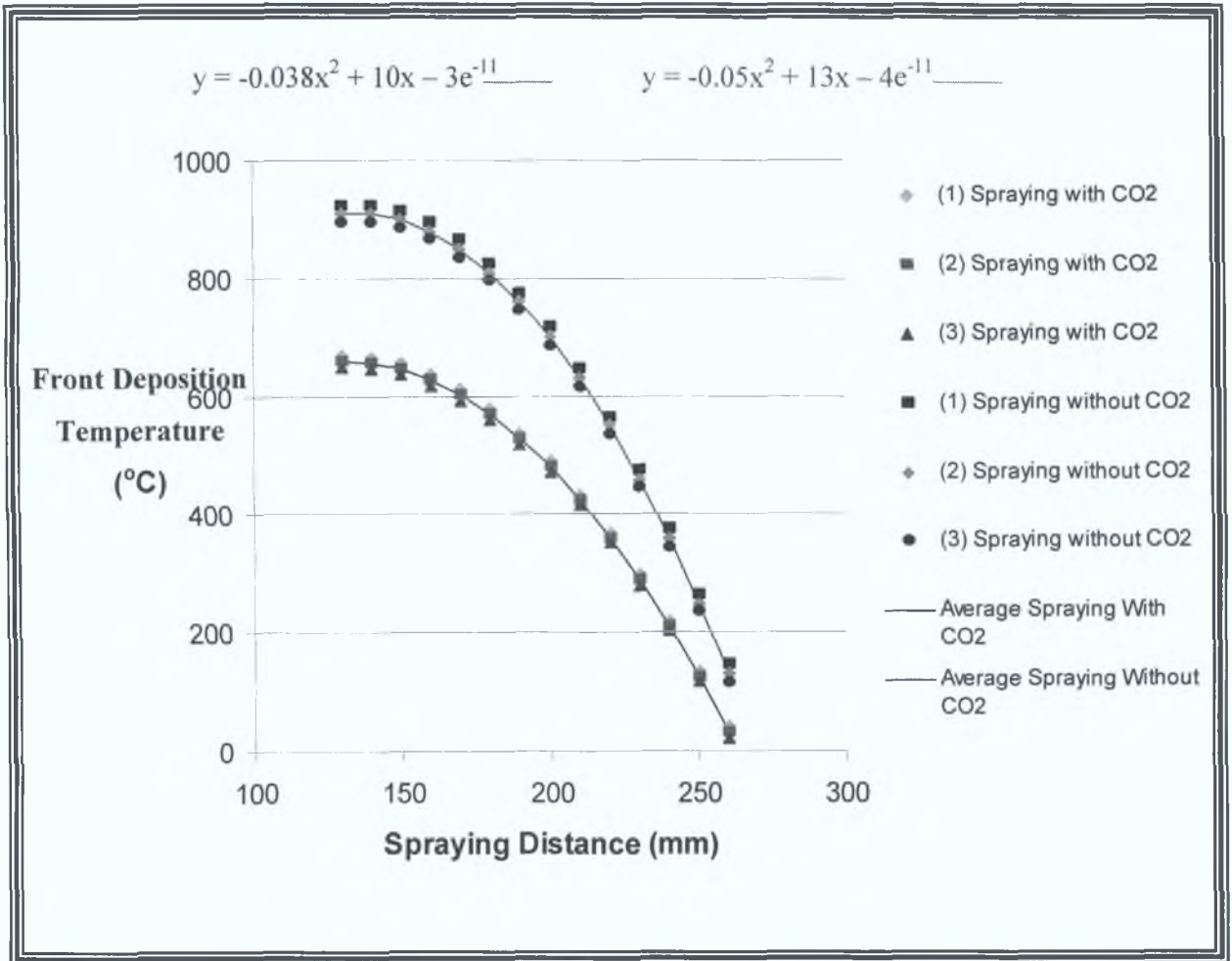


Figure 64, Spraying temperature at various distances with/without cooling.

Figure 65 shows a two dimensional finite element analysis of the flame temperature (centre) surrounded by the CO<sub>2</sub> cooling jet, and their effect on the WC-Co sample. The temperature decreases as one moves out from the centre point of the rectangular block towards its edge. Figure 66 shows the variation of front (flame temperatures between 400 and 600°C and shrouded by a cooling temperature of -80°C in figure 66 (b)) and back temperatures for both the experimental and finite element analysis results, for coating thicknesses from 0.2 to 1mm. Again a differences was observed between the linear finite element results and the experimental values, where the back FEA

temperature was found to be between 1.04 to 1.08 times the back experimental temperature, at the same front temperature. For a front temperature of 500°C, the experimental back temperature for a 2mm deposit was measured as 378°C, this corresponds to a back temperature of 395°C found using the finite element technique for the same deposit. The reasons for the difference are similar to those stated in the previous section, convective heat transfer was only analysed in two directions, radiation effects were ignored and material properties may not be correct.

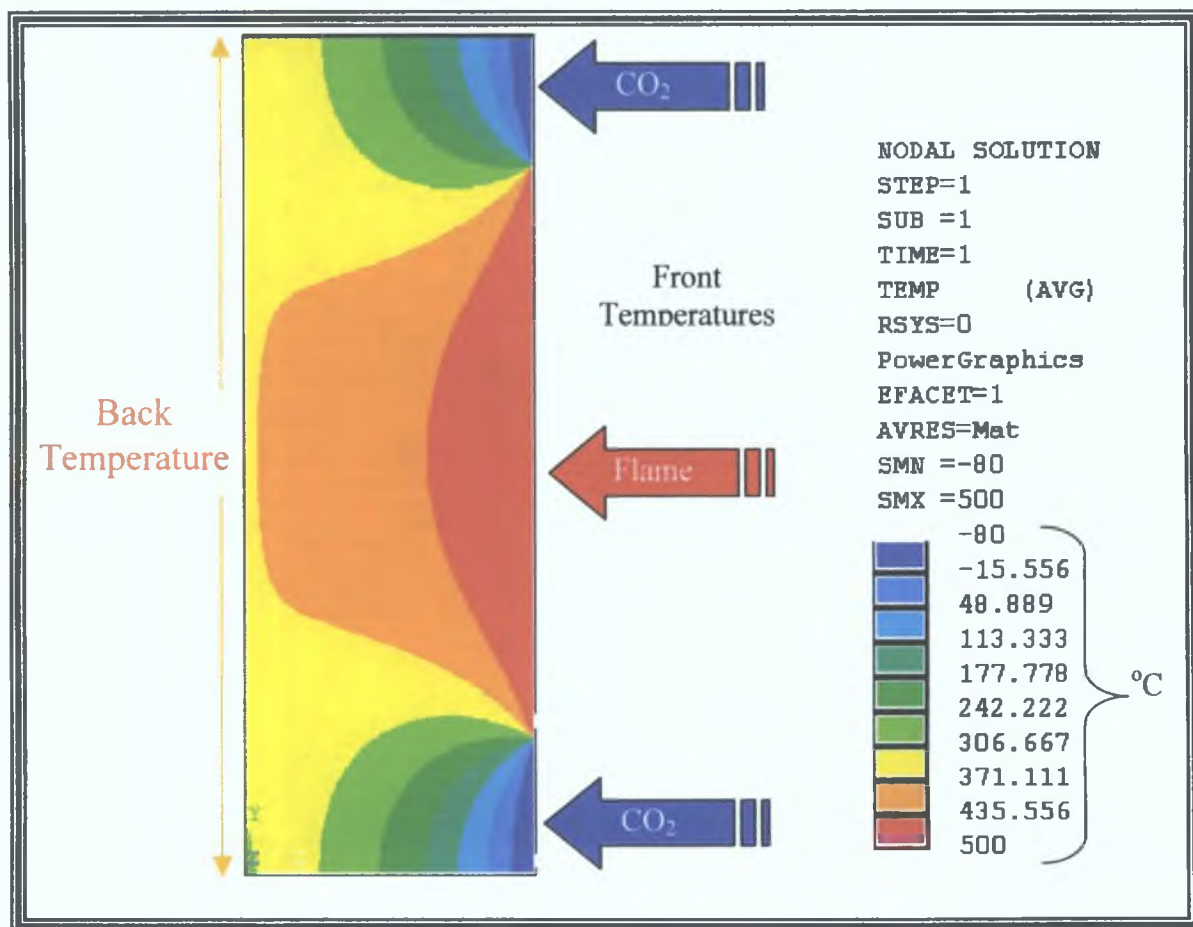


Figure 65, Finite element analysis of the temperature gradient found through a sample when CO<sub>2</sub> cooling is involved.

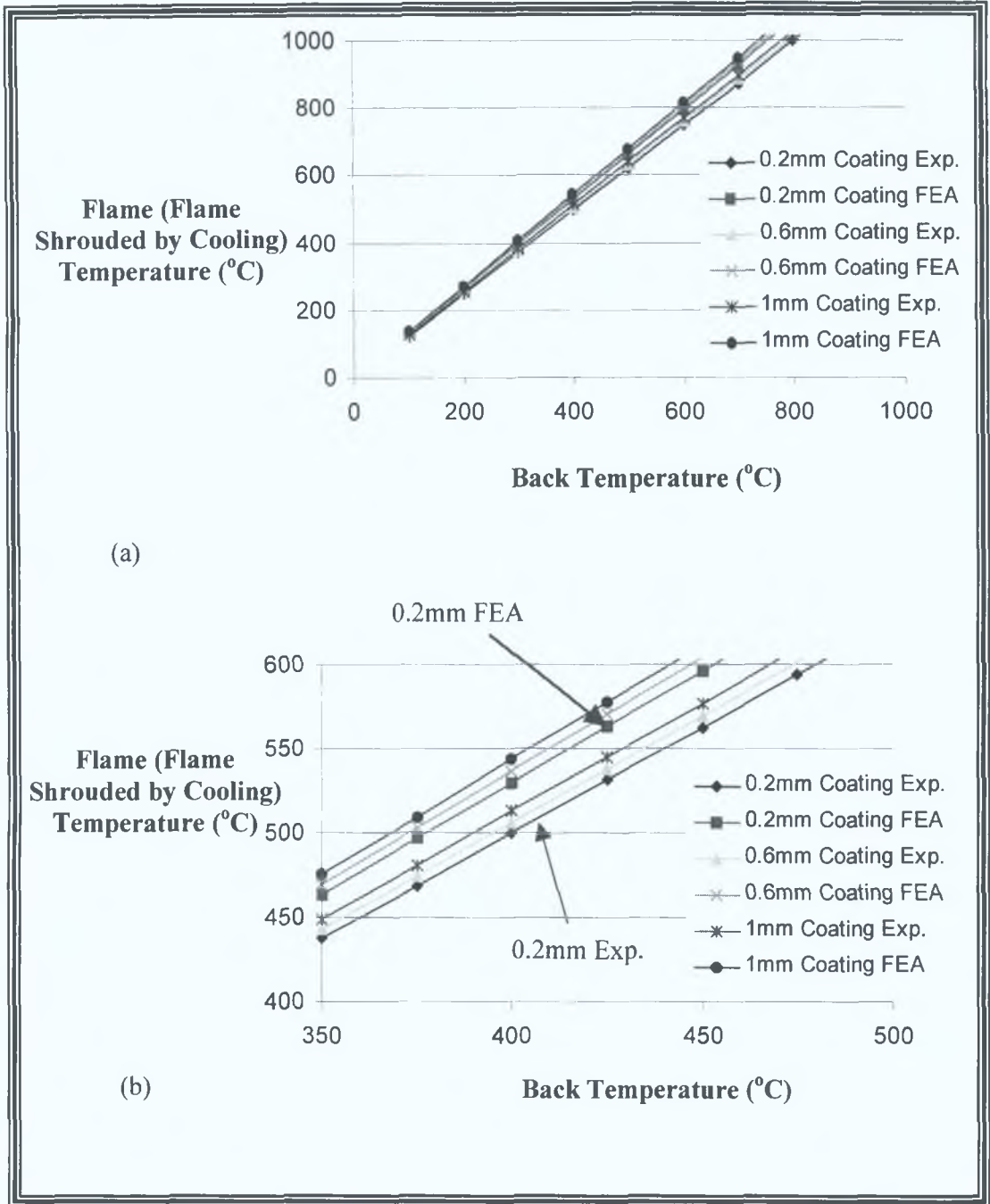


Figure 66, Graphical representation of the front (flame surrounded by cooling) temperature versus the back temperature.

In the previous tests, substrate thicknesses were kept constant at 6mm, figure 67 shows the finite element front (flame shrouded by cooling) temperature plotted against its corresponding back temperature, for various substrate thicknesses. The coating thickness remained constant at a value of 0.2mm. For lower substrate thicknesses, the experimental temperature at the front was found to be approximately 1.046 (4.6% in figure 67) greater than the back temperature, compare to the finite element result which was found to be approximately 10% higher. The finite element results were approximate 5% higher than the experimental results measured in the research. For a back temperature of 500°C on a 1mm thick substrate, the experimental front temperature was measured as 524°C, this corresponds to a front temperature of 552°C found using the finite element technique for the same deposit. The errors described earlier were assumed to contribute to this difference.

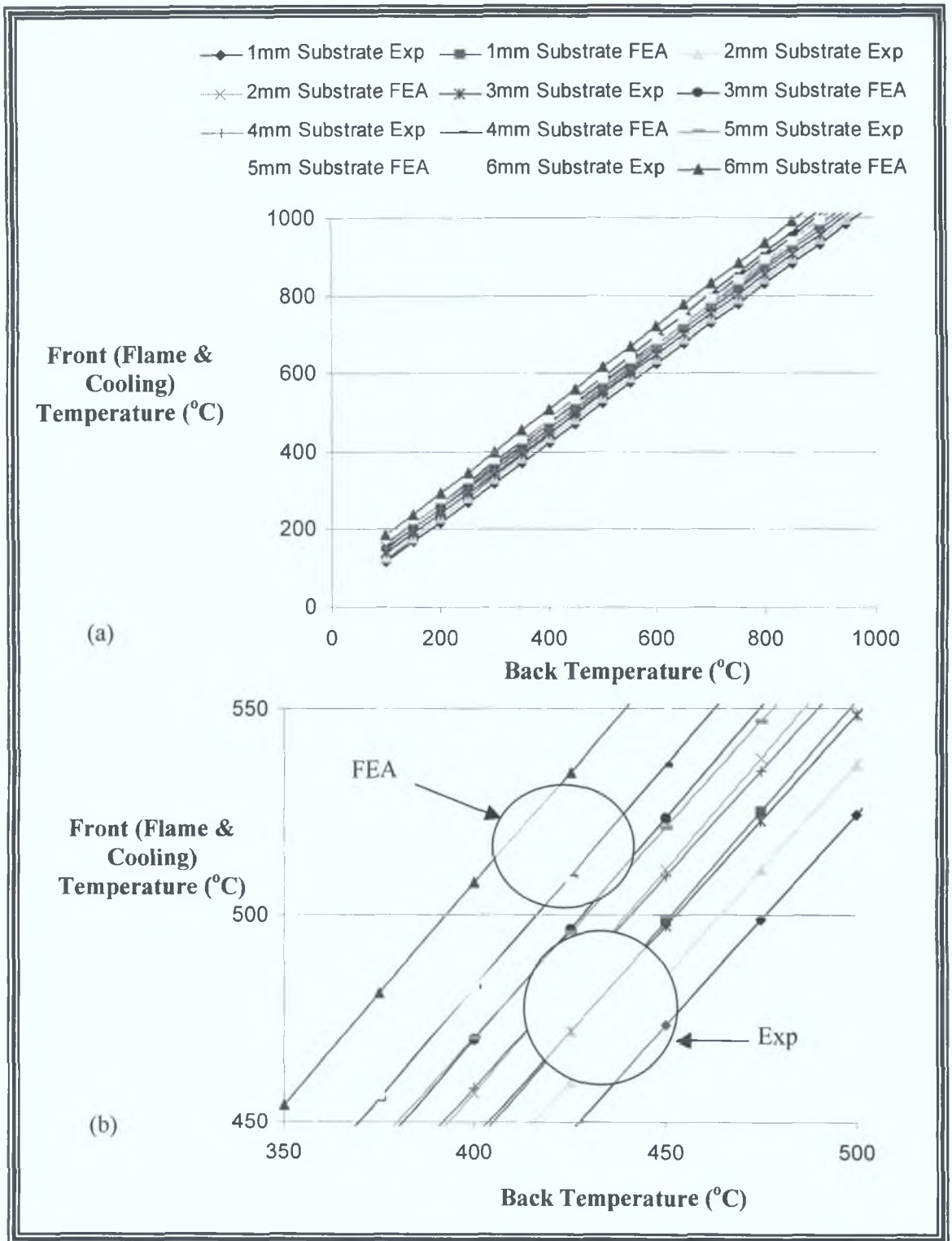


Figure 67, Graphical representation of the finite element analysis front (flame shrouded by cooling) temperature plotted against the back temperature for various substrate thicknesses.

### 5.3 THE AUTOMATION OF THE PROCESS EQUIPMENT

This section details the benefits found by introducing a linear traverse unit and a third-axis directional unit into the process. Each unit was optimised in terms of traverse speed and height variation per pass.

#### 5.3.1 Linear Traverse Unit

In this test, the objective was to achieve repeatable and controlled results, by using the linear traverse unit. However, in order to achieve such results, a traverse speed for deposition was required.

The forcer element of the linear traverse unit, is capable of output traverse speeds of up to 100 inches per second ( $2540\text{mms}^{-1}$ ), using the V100 command. However depending on the application, limitations to this speed exist [115]. The mass applied to the forcer has a dramatic effect on the traverse speed. The forcer in the current studied is loaded by several components. The average mass for each component is as follows:

Gun Mount = 0.5kg

Diamond Jet HVOF gun = 2.27kg

Carbon Dioxide consoles and nozzles = 0.2kg

The total mass applied to the forcer is approximately 3 kilograms. Preliminary speed tests demonstrated that the effect of this mass is to reduce the traverse speed command range from V0 to V100, down to a range of V0 to V15 inches per second (figure 68). The extra weight applied to the forcer reduced the actual traverse speed from that indicated in the control program by an unknown amount. Therefore a test was set up to measure the actual traverse speed of the forcer (including DJ gun, mount and CO<sub>2</sub> cooling accessories), when various commands were entered (figure 68). The maximum resulting traverse speed (after varying the acceleration and air pressure between the forcer and platen) for the V10 command was found to be  $200\text{mms}^{-1}$  or 7.9 inches per

second. Therefore effect of loading the forcer, reduced the traverse speed by 21% (from 254 to 200 $\text{mms}^{-1}$ ).

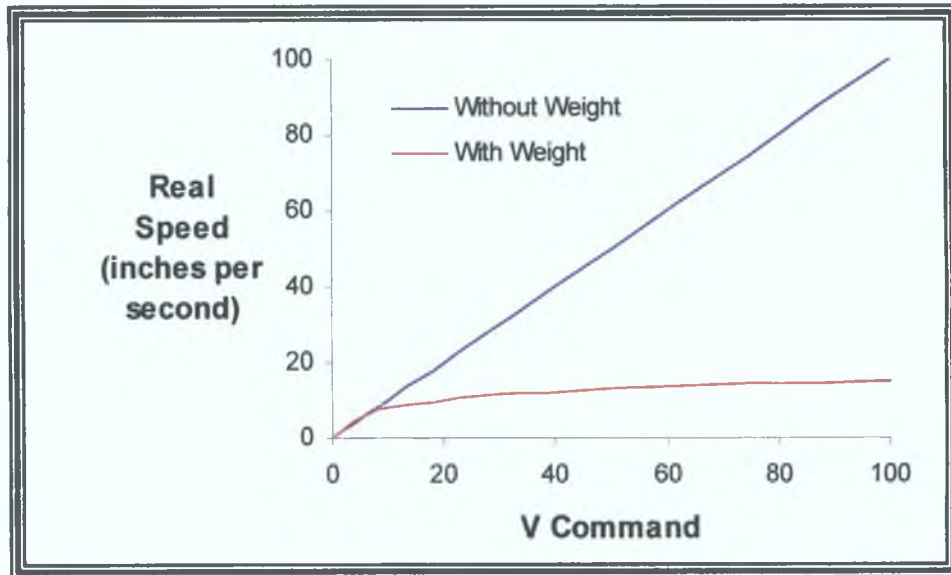


Figure 68, Calibration of the traverse unit.

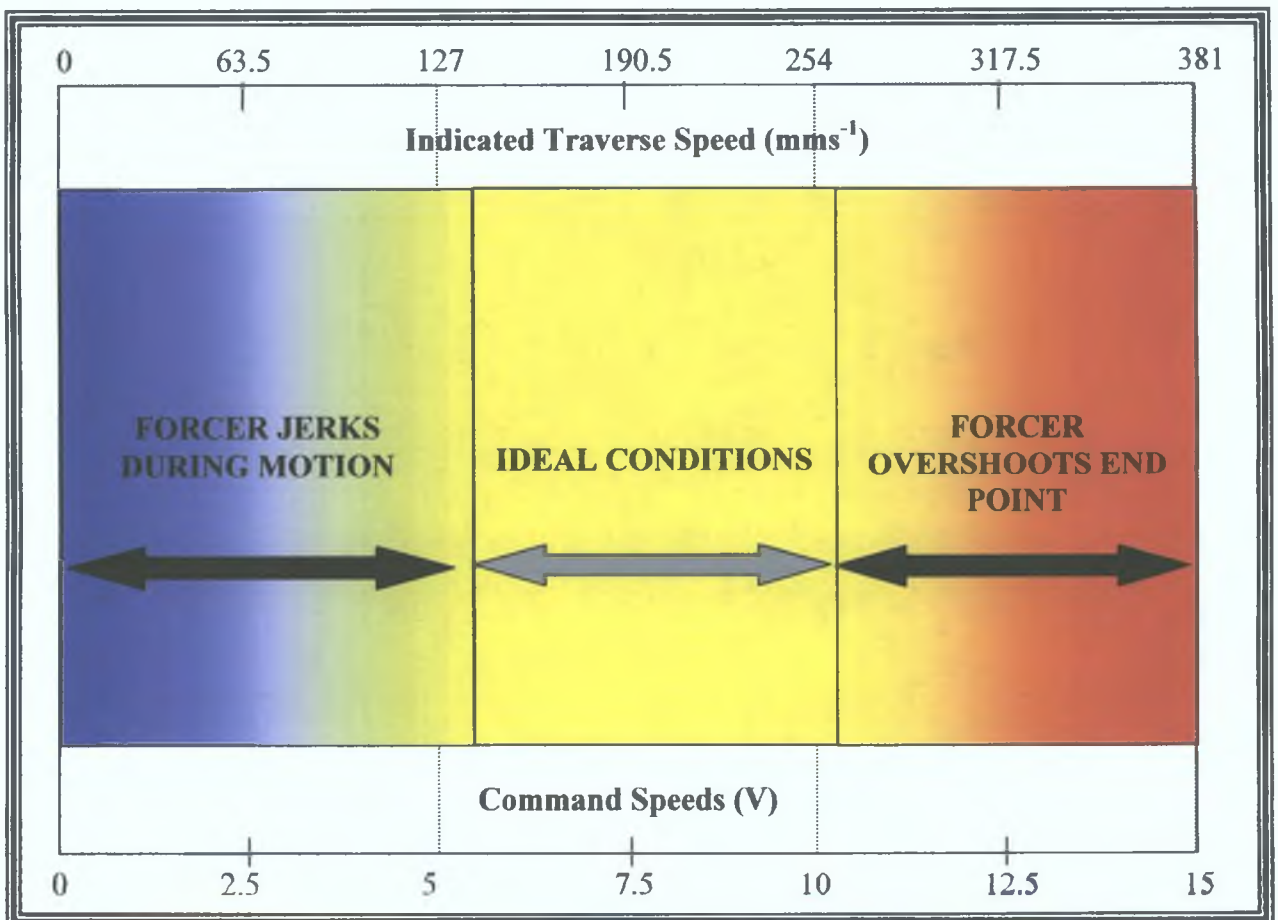


Figure 69, Effect of traverse speed on the motion of the forcer.

However other limitations occurred within this range, as shown in figure 69. Low speeds such as 0 to 6 inches per second (0 to  $152.4\text{mms}^{-1}$ ), cause the forcer to jerk through each incremental step during its motion, but the jerking diminishes with increased traverse speed. Traverse speeds of 6 through to 10 inches per second ( $152.4$  through to  $254\text{mms}^{-1}$  respectively), result in a uniform smooth motion of the forcer. Speeds greater than 10 inches per second ( $254\text{mms}^{-1}$ ), produce unsatisfactory results, by overshooting the forcer beyond its expected end point, because of the high momentum of the system.

The V10 command yielding an actual speed of  $200\text{mms}^{-1}$  was selected from the range available, as this allowed the lowest thickness (measured using the microscopic method) to be produced per pass, measured as approximately  $30\mu\text{m}$  and according to Irons [59], lower pass thicknesses result in lower residual stress build up in the deposit. A low acceleration was used (range of 0g to 0.5g, 0 to  $4.9\text{ms}^{-2}$  respectively), as higher accelerations caused the forcer to overshoot in a manner similar to that found when using high traverse speeds.

### 5.3.2 Third-Axis Directional Unit

Using the traverse speed found in the last section, the DJ gun was placed at a distance of 200mm and the powder feed rate was set at  $38\text{gmin}^{-1}$  based on the data in table 5, spraying was carried out using the third-axis unit. Ten passes were made between increments (distance the substrate move up or downwards). Ten passes were used to produce a significant gaussian profile (name given to the hump shape of thermal spray deposits). The increments analysed were 0, 1, 2.5, 5, 7.5 and 10mm.

The first test was carried out at 0mm increment and the surface profile measured microscopically is shown in figure 70. The surface profile was modelled as a Gaussian distribution (commonly used in statistical analysis), which peaked in the centre of the deposit at a height of  $295\mu\text{m}$  and the spread of the deposit was approximately 12mm. The next test was carried out using an increment of 10mm (ten passes at 0mm and ten

passes at 10mm shifted up from the 0mm point). The result as shown in figure 71 (a), was a combination of two gaussian profiles (both peaking at  $305\mu\text{m}$ ) with a dip in the centre of the deposit of approximately  $150\mu\text{m}$  (measured from the maximum height of the deposit down to central minimum height). The dip in the centre was quite unfavourable as increasing the numbers of passes per increment would produce a rough surface. The increment distance was reduced to 7.5mm to reduce this 'dipping' effect. Figure 71 (b) shows the profile measured. Two peaks were produced at a maximum height of  $315\mu\text{m}$  and the dip was reduced to  $95\mu\text{m}$ , however the overlap zone was insufficient to prevent the 'dipping' effect. The addition of two gaussian shaped profiles shows mathematically and graphically that the increment should be approximately half the spread of the shape. The next increment distance used was 5mm. Figure 72 shows the profile measured. The peak produced had a flat section with a maximum height of  $350\mu\text{m}$  and ranging over a width of 4mm. The 'dipping' effect was negligible, therefore this was an acceptable increment distance.

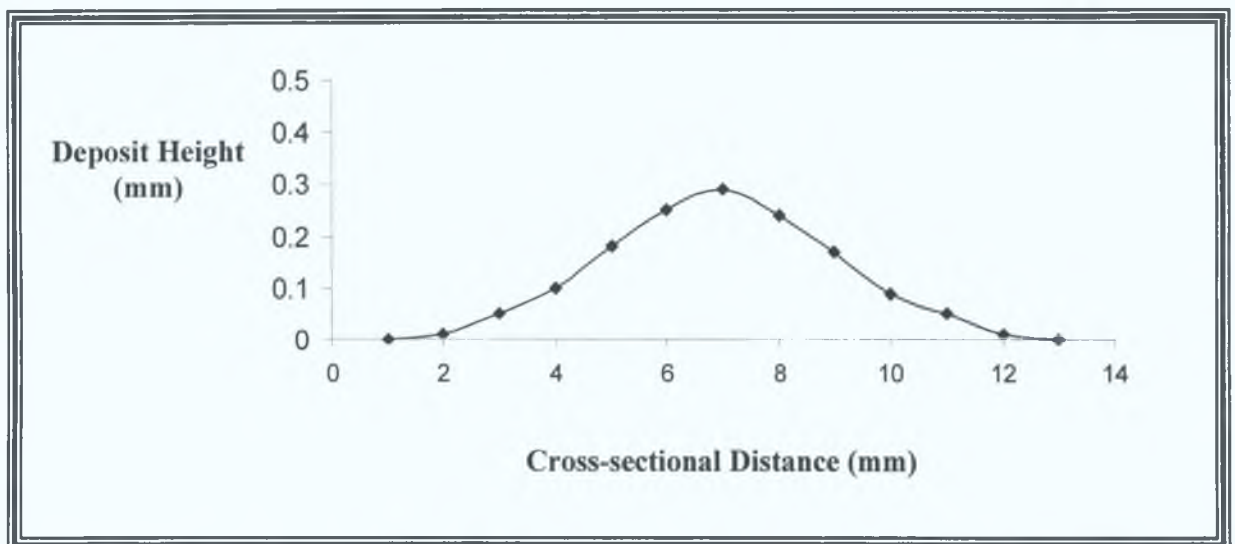


Figure 70, Deposit with ten passes and 0mm vertical increment.

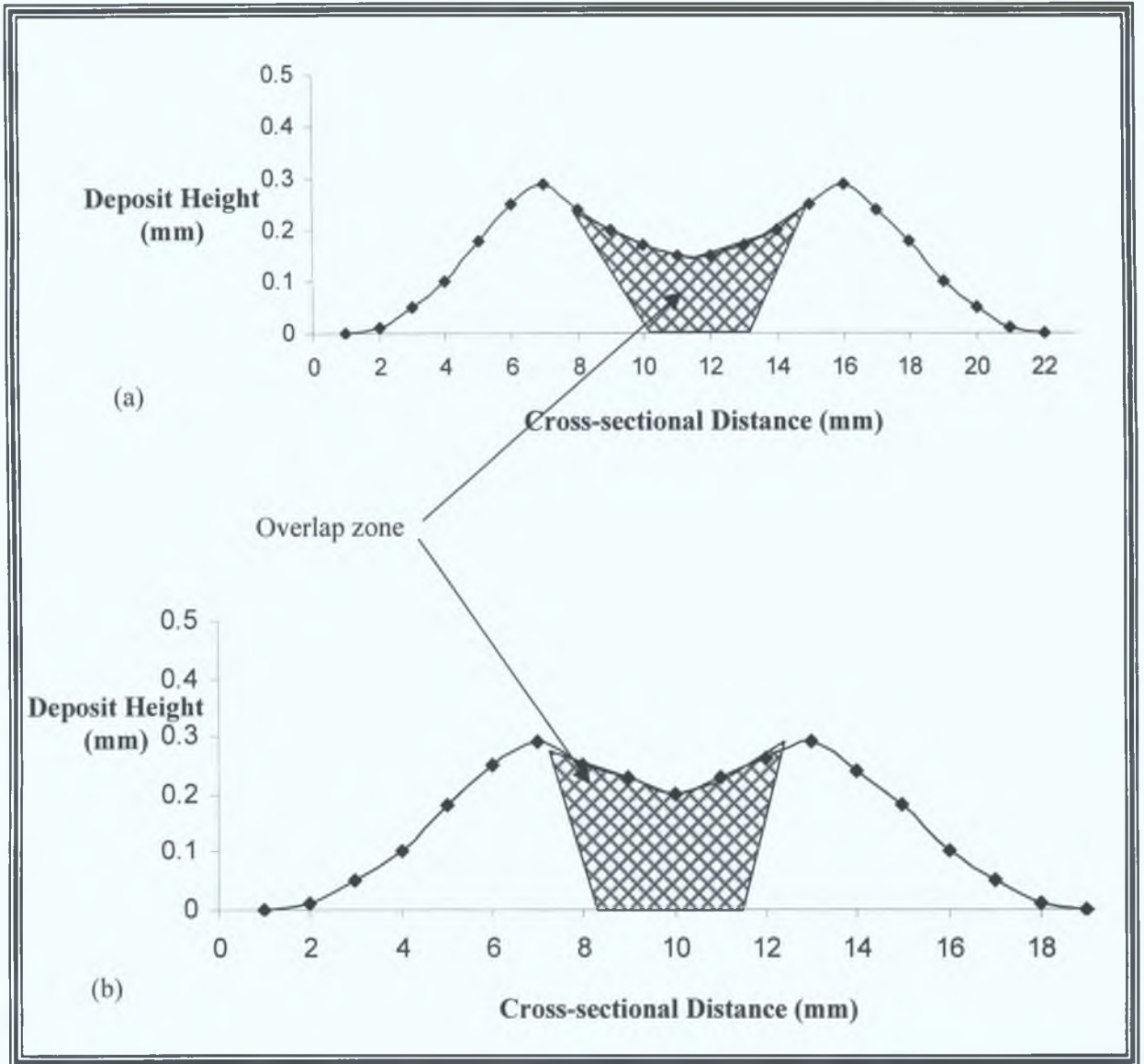


Figure 71, Deposit with twenty passes set at a 10mm (a) and 7.5mm (b) vertical increment.

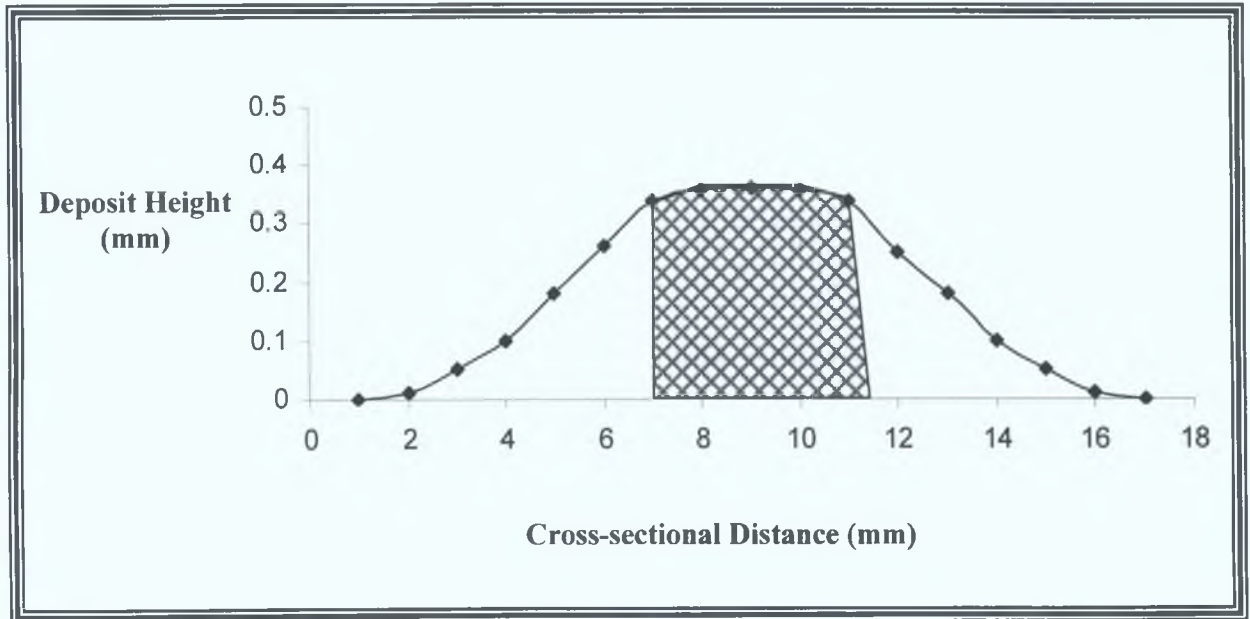


Figure 72, Deposit with twenty passes and 5mm vertical increment.

Lower increment distances of 2.5 and 1mm were examined. Figures 73 (a) and (b) show that such increment distances produce single peaks similar to that found at a 0mm increment, however the peak heights are excessively high (460 and 520 $\mu$ m respectively). These heights would have a major influence on residual stress build up, compared to lower deposits of 350 $\mu$ m.

The incremental distance used in the rest of the report was 5mm and this supports findings found by Irons [59], where he states 'The offset distance between each spray stroke should be less than half the width of the spray pattern'. The width of the HVOF spray deposit is approximately 12mm (figure 70), therefore a 5mm increment supports that statement. Figure 74 shows a photo of three of these samples (0, 5 and 10mm increments), the 5mm increment sample macroscopically looks flat, while some adhesion loss was found when using the 10mm increment, possible due to the fact that a portion of the substrate/previously deposited material cooled down while a series of

passes was carried out on a separate section of the sample. The microscopic micrographs of these three samples are shown in figure 75.

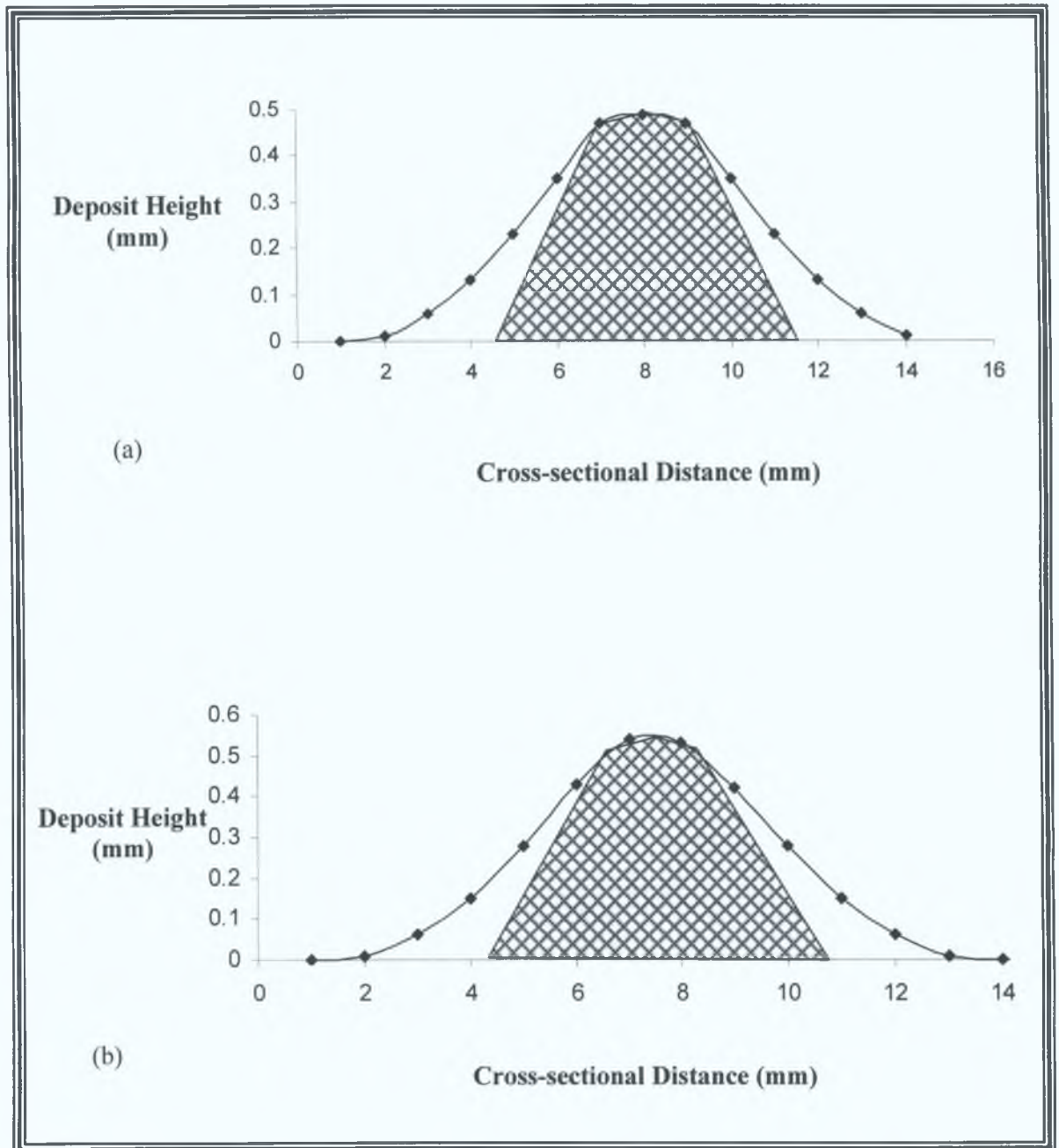


Figure 73, Deposit with twenty passes set at a 2.5mm and 1mm vertical increment.

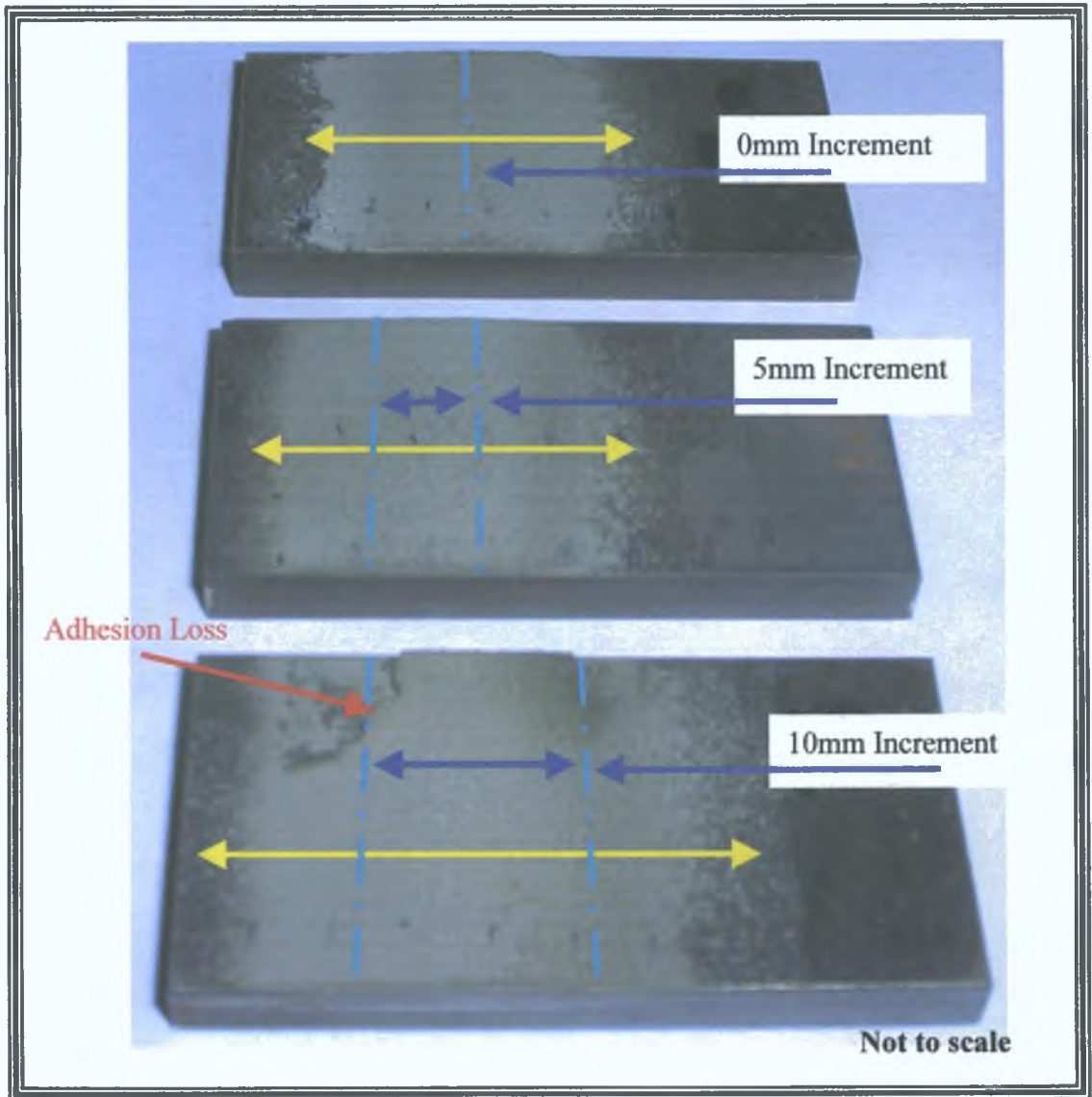


Figure 74, Three samples showing the difference between spray deposits produced using the third-axis traverse unit at various height increments.

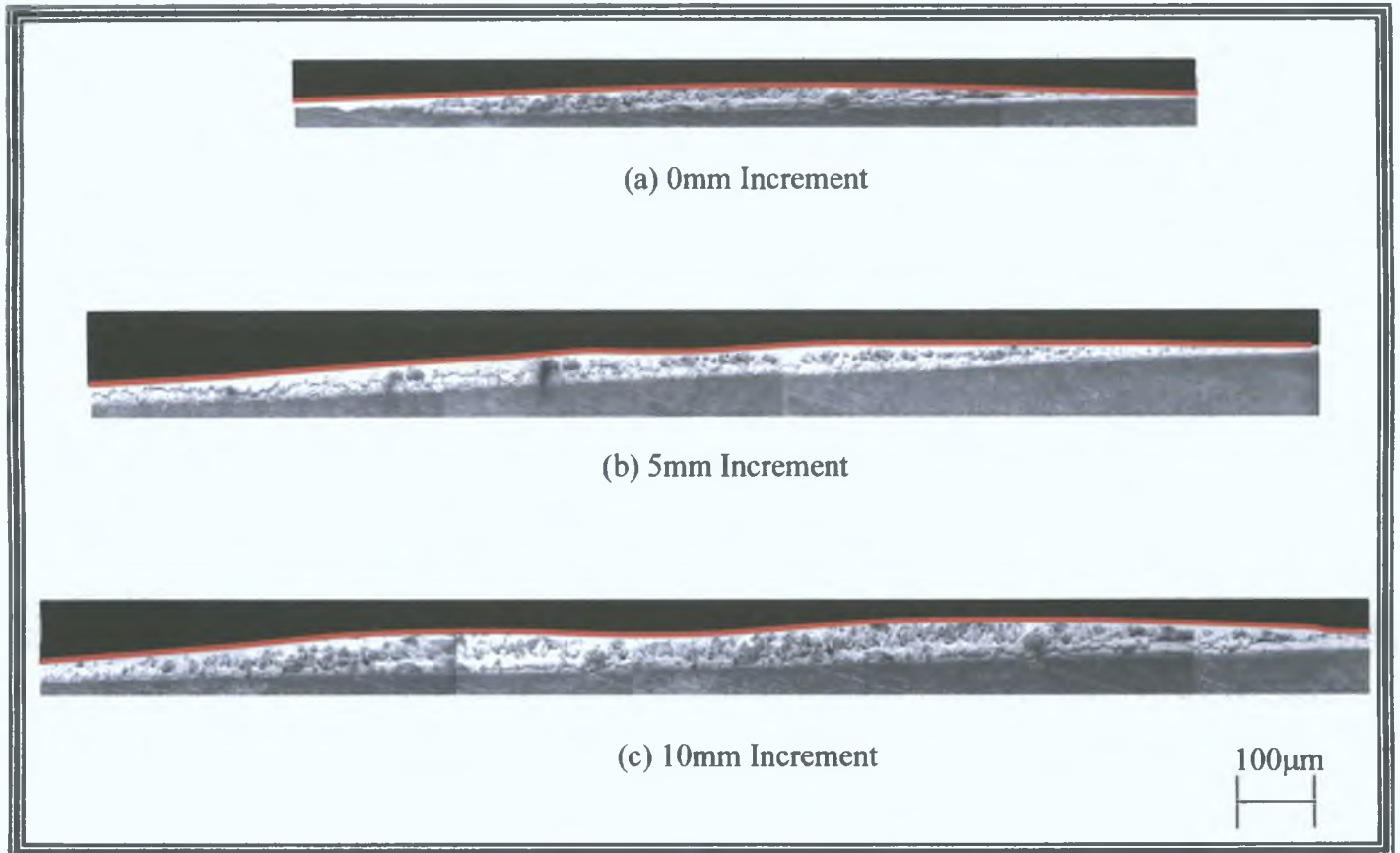


Figure 75, Scanning electron microscope micrographs of the end view of samples produced using the third-axis traverse unit, (a) 0mm increment, (b) 5mm increment and (c) 10mm increment.

#### 5.4 ELASTIC PROPERTIES OF SPRAYED WC-Co

Residual stress results are presented in subsequent sections, therefore it was necessary for the Young's modulus and Poisson's ratio for the WC-Co deposit to be measured. This was done using the cantilever test described earlier at two load levels (2 and 10N). The method is based on a least squares fit of the equilibrium equations utilising the strain gauge data (figure 76). The function described in equation 14 was analysed using Microsoft Excel to evaluate a Young's modulus and Poisson's ratio for the WC-Co deposit which minimised the stress difference in the equation. Minimising the function yielded a Young's modulus of 184.9 GPa and Poisson's ratio of 0.278 for the tungsten carbide-cobalt material, with a error of 0.5 GPa and 0.005 respectively. In a survey produced by Bhushan et al. [33], the stiffness for a thermally sprayed WC-Co range from 150 to 210MPa, where higher stiffness results were found using HVOF systems. Similarly the Poisson's ratio for the material is around 0.26 [33], hence supports the results found in the present study.

Microsoft Excel Young's Modulus Cantilever Test

File Edit View Insert Format Tools Data Window Help

Ariel 12 B I U

P31

1  
2  
3  
4  
5  
6  
7  
8  
9  
10  
11  
12  
13  
14  
15  
16  
17  
18  
19  
20  
21  
22  
23  
24  
25  
26  
27  
28  
29  
30  
31  
32  
33  
34  
35  
36

**YOUNGS MODULUS VIA CANTILEVER BEAM TEST**

RESULTS	F	l (sub 1)	l (coat)	l (sub 2)	l (coat)	microstrain
	0	-693	105	-623	2558	
	1	-733	283	-688	2638	
	2	-778	414	-992	2709	
	4	-875	527	-1155	2869	
	6	-980	628	-1306	3048	
	8	-1100	672	-1385	3231	
	10	-1260	714	-1486	3470	

F	Es	Vs	Ee	Ve	w	Sub thk	Coat thk	eYCG	eYSG	eXCG	eXSG	eXCI	eXSI	eYCI	eYSI
0	6.90E+10	0.33	1.80E+11	0.278	0.02	0.002	0.0002	0.0E+00	0.0E+00	0.0E+00	0.0E+00	0.0E+00	0.0E+00	0.0E+00	0.0E+00
1	6.90E+10	0.33	1.80E+11	0.278	0.02	0.002	0.0002	4.0E-05	-1.8E-04	1.9E-04	-7.8E-05	-1.6E-04	-1.6E-04	2.0E-05	2.0E-05
2	6.90E+10	0.33	1.80E+11	0.278	0.02	0.002	0.0002	8.3E-05	-3.1E-04	3.7E-04	-1.5E-04	-3.2E-04	-3.2E-04	4.7E-05	4.7E-05
4	6.90E+10	0.33	1.80E+11	0.278	0.02	0.002	0.0002	1.8E-04	-4.2E-04	5.3E-04	-3.1E-04	-4.6E-04	-4.6E-04	1.3E-04	1.3E-04
6	6.90E+10	0.33	1.80E+11	0.278	0.02	0.002	0.0002	2.3E-04	-5.2E-04	6.8E-04	-4.9E-04	-5.8E-04	-5.8E-04	2.1E-04	2.1E-04
8	6.90E+10	0.33	1.80E+11	0.278	0.02	0.002	0.0002	4.1E-04	-5.7E-04	7.6E-04	-6.7E-04	-6.3E-04	-6.3E-04	3.2E-04	3.2E-04
10	6.90E+10	0.33	1.80E+11	0.278	0.02	0.002	0.0002	5.6E-04	-6.1E-04	8.6E-04	-9.1E-04	-7.0E-04	-7.0E-04	4.5E-04	4.5E-04

F	Sxsg	Sxsl	Sxsg	Sxsl	Sysg	Sysl	Sygg	Sysl	Fx	Mx	Fy	My	Phi
0	0.0E+00	0.0E+00	0.0E+00	0.0E+00	0.0E+00	0.0E+00	0.0E+00	0.0E+00	0.0E+00	0.0E+00	0.0E+00	0.0E+00	0.000
1	-1.1E+07	-1.2E+07	3.8E+07	-3.0E+07	-1.6E+07	-2.6E+06	1.8E+07	-4.8E+06	-4.4E+02	-2.8E+01	-3.7E+02	-2.2E+01	0.204
2	-2.0E+07	-2.4E+07	7.6E+07	-6.0E+07	-2.8E+07	-4.6E+06	3.6E+07	-8.2E+06	-8.3E+02	-6.0E+01	-6.5E+02	-3.7E+01	0.331
4	-3.5E+07	-3.2E+07	1.1E+08	-8.2E+07	-4.1E+07	-1.8E+06	6.4E+07	-9.8E+04	-1.3E+03	-1.0E+00	-8.5E+02	-3.1E+01	0.451
6	-5.1E+07	-3.9E+07	1.8E+08	-1.0E+08	-5.3E+07	1.8E+06	9.3E+07	1.0E+07	-1.7E+03	-1.5E+00	-1.0E+03	-2.2E+01	0.488
8	-6.7E+07	-4.1E+07	1.7E+08	-1.1E+08	-6.1E+07	8.5E+06	1.2E+08	2.8E+07	-2.0E+03	-1.8E+00	-1.0E+03	4.3E+02	0.523
10	-9.6E+07	-4.3E+07	2.0E+08	-1.1E+08	-7.0E+07	1.7E+07	1.6E+08	5.0E+07	-2.4E+03	-2.3E+00	-1.1E+03	3.8E+01	0.560

Using Minimum Function in Excel

	Es	Vs	Ee	Ve	w	Sub thk	Coat thk	Phi
USE	184.9	0.278	8.560	184.9	0.278	0.331		

Figure 76, The cantilever test results presented in an excel sheet.

## 5.5 STRESS DISTRIBUTION THROUGH A DEPOSIT

The Young's modulus values used in the residual stress equations, for the coating and the substrate were 184.9GPa (found in the cantilever test) and 200GPa [86] respectively. Tests were carried out on three samples according on the data shown in table 5. A photo of the sample is shown in figure 77. Figure 78 shows the residual stress distribution through a 0.6mm thick WC-Co deposit found using the Modified Almen Test Method. The figure shows the relationship between the average coating stress (ranging from 6.38 to 8.23MPa) and the stress distribution through the sample. The deposit has a tensile stress (ranging from 91 to 107MPa) on its top surface and the residual stress at the coating – substrate interface (coatings side) is between –70 and –82MPa. Therefore, the coating experiences a stress change through the coating ranging between 161 and 189MPa.

Figure 79 shows the residual stress distribution using Clyne's Analytical Method accounting for misfit strain, through a 0.6mm thick WC-Co deposit. The figure shows the four calculated points (equations 17 to 21), and these have been connected by straight lines, indicative of the stress distribution through the sample. The deposit has a tensile stress ranging from 13 to 16MPa on its top surface and –72MPa at the coating – substrate interface. Here it changes to a substrate stress of approximately +40MPa. Hence the interface has a stress increase of approximately 222MPa, whereas the coating experiences a stress change through the coating ranging between 85 and 88MPa.

The reason for the difference between the results observed using the Modified Almen Test Method (MAM) and Clyne's Analytical Method, is that the interfacial strain effect (misfit strain) is ignored in the MAM test. The MAM test shows a slight change in stress (12MPa) at the interface, which can be contributed to the difference in stiffnesses and thermal expansion between the deposit and the adjoining substrate. Clyne's Method however also accounts for misfit strain at the interface. For the remainder of the report, Clyne's Analytical Method is used to identify the stress distribution through

various samples. Experimentally measured deflections and material properties were placed into the analytical equations (equations 17 to 20), to establish the distribution.

While obviously the maximum deposit stress is important, the current research also focuses on stress change across the deposit, and the stress change at the interface, as these more completely reflect the stress situation in the deposit. The change from tensile (at the top of the deposit) to compressive stress (deposit / substrate interface) can cause the deposit to fail at high stress levels. The stress change at the deposit / substrate interface can cause cohesion loss. Reduction of these quantities (stress change through the deposit and across the interface) will increase the life of the deposit.

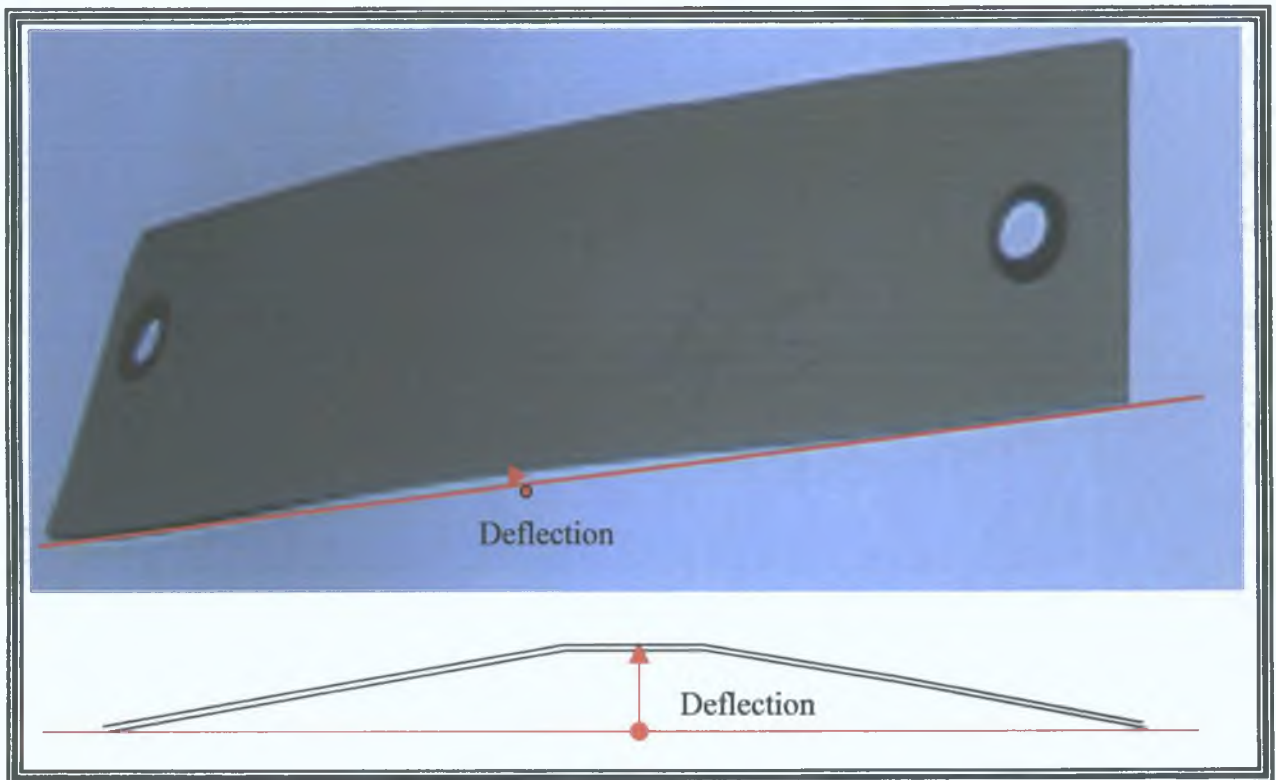


Figure 77, An example of a deflected sample.

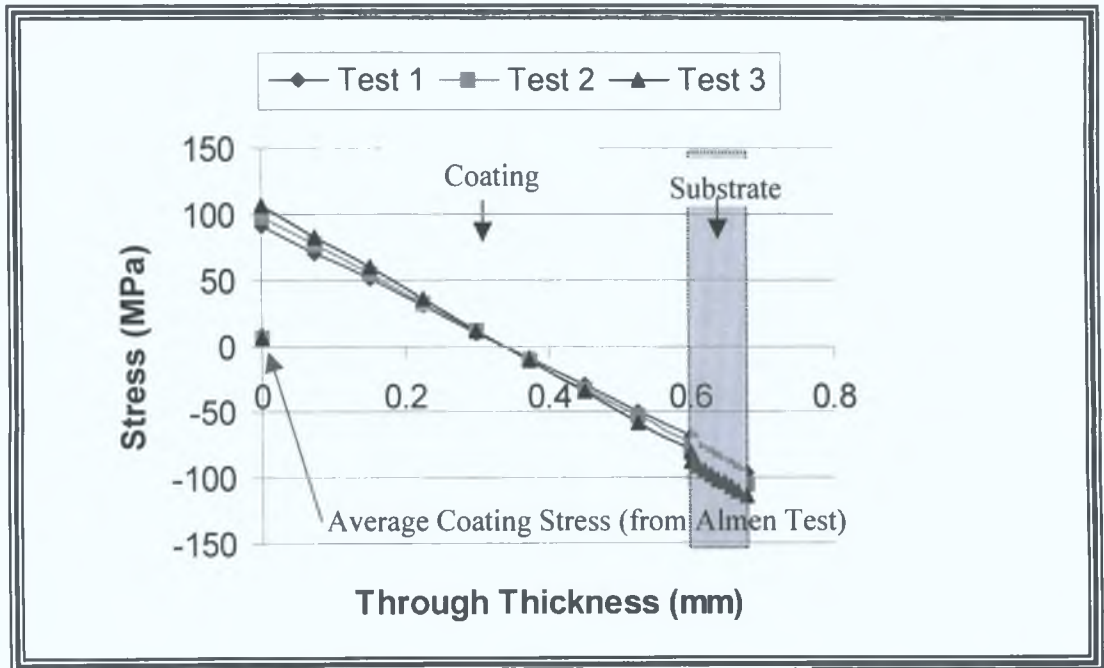


Figure 78, Average and distributed residual stress through a 0.6mm WC-Co deposit found using the MAM test.

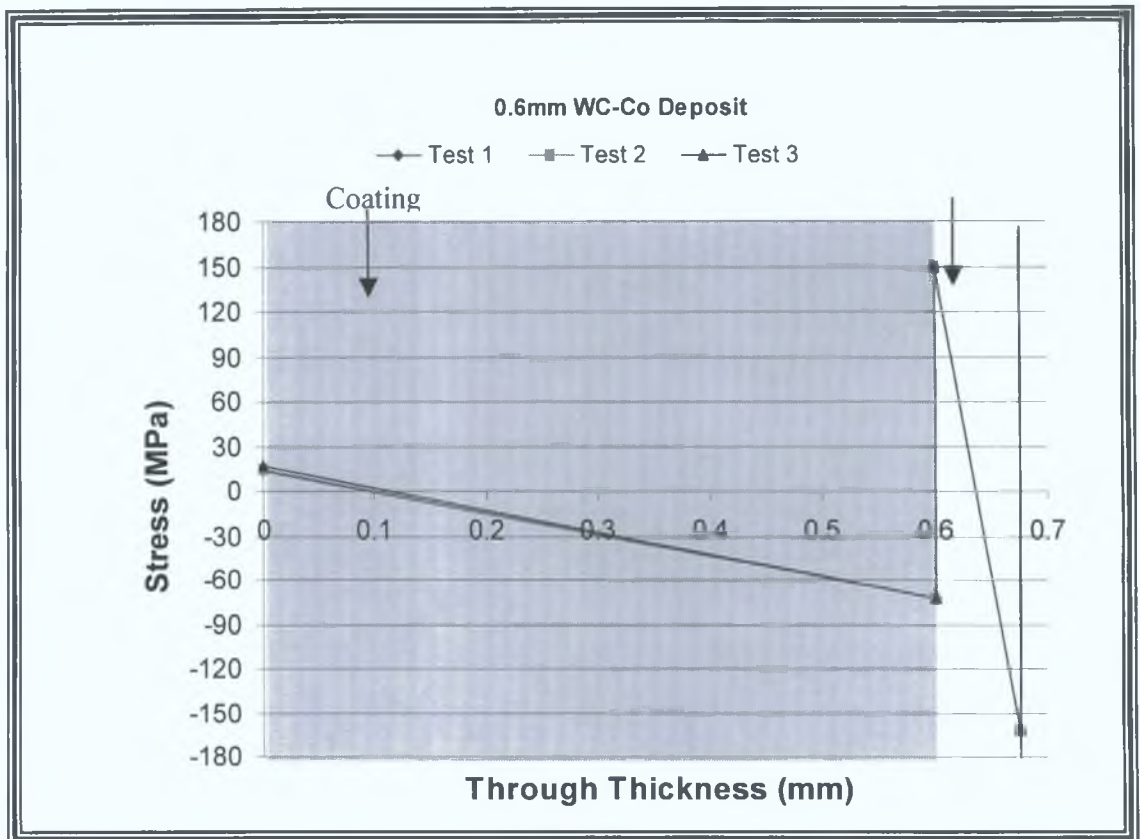


Figure 79, Distributed residual stress through a 0.6mm WC-Co deposit calculated using Clyne's Analytical Method.

## 5.6 OPTIMISATION OF THE SPRAYING TECHNIQUE AND SPRAYING PARAMETERS

This section demonstrates the benefits found by introducing the facilities of linear and third-axis traverse units and a carbon dioxide cooling system (forced cooling) into the spray process. The process was optimised to reduce the build up of residual stress within the deposit and later this reduction in residual stress proved essential in the production of thick spray-formed components.

The spraying parameters, spraying distance and powder feed rate for Diamalloy 2003 WC-Co were varied with the utilisation of the two traverse units (linear and third axis) and the carbon dioxide cooling system. The process was optimised to reduce the build up of residual stress within the deposit.

### 5.6.1 Manual Spraying

Five stainless steel strips (80 x 20 x 0.075 mm<sup>3</sup>) were pre-heated to 450°C, then deposited with WC-Co (thickness of 300µm). The residual stress results are presented in figure 80. Manual spraying yielded high and scattered stress change results, ranging from 176 to 241MPa. In any manufacturing process, repeatability and control of results is essential to the production of engineering components, therefore these manually sprayed results are unsatisfactory. The variation of the results may be due to the inconsistency of spraying distance over the duration of each spray, which is a common problem whilst spraying manually. For coating quality to be achieved, tolerances have to be observed. Errors of ± 30mm are estimated to occur when manually spraying at a distance of 200mm from the substrate, hence yielding such a large stress range. Fatigue of the manual operator over long periods, would lead to even wider tolerances.

### 5.6.2 Linear Traverse Unit

Similarly, five stainless steel test strips were deposited with WC-Co with the use of the traverse unit. The introduction of the linear traverse unit decreased both the deposit stress change values, and the scatter of results quite significantly. Values ranging from 160 to 179MPa are illustrated in figure 80. The traverse linear unit has a dramatic effect on the repeatability and control of results. Uniformity of the coating was constant (samples were viewed by the scanning electron microscope) and the gun was maintained perpendicular to the substrate throughout deposition, with the use of this unit. However, the residual stress values found were for coating thicknesses of 300 $\mu$ m. In order to achieve higher thicknesses, the change in stress must be further reduced; hence a cooling system was implemented.

### 5.6.3 Forced Cooling

300 $\mu$ m of WC-Co was deposited onto five steel strips, with the use of the traverse unit and the carbon dioxide cooling system. Figure 80 illustrates the compressive stress change results found. The carbon dioxide cooling not only reduced the scatter in stress change in the deposit values to a narrow range (16MPa), it also reduced the extent of change across each coating. The results using forced cooling are between 49.4 to 53.0% of those found without forced cooling. Hence the combination of a traverse unit and forced CO<sub>2</sub> cooling, provide controllable and repeatable results, reducing the stresses within the deposit as much as approximately 58%.

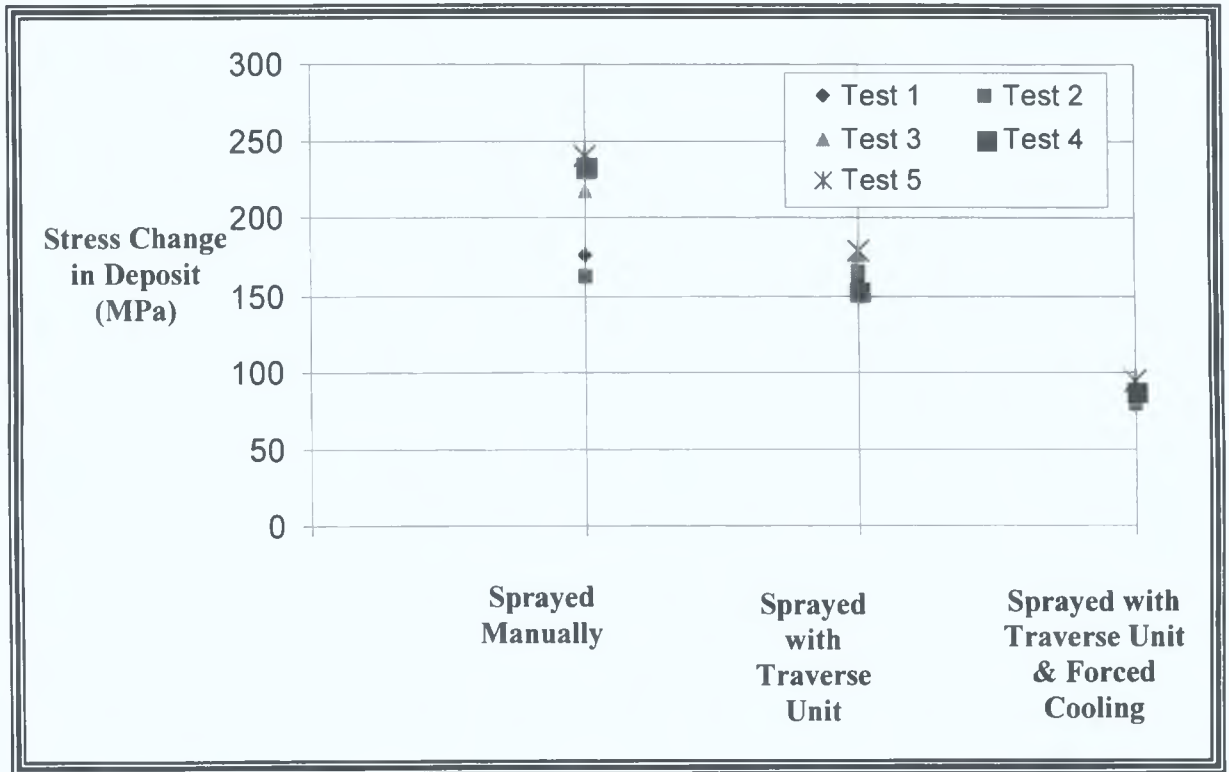


Figure 80, Differences in stress ranges as a function of spraying techniques.

#### 5.6.4 Variation Of Residual Stress With Spraying Distance

The objective of this section was to establish if residual stress changed with increased spraying distance, and to identify optimum conditions. Figure 81 illustrates the effect of spraying distance on maximum residual stress change (measured using the Clyne's Analytical Method) within the deposit, at various powder feed rates. At each spraying distance (150, 180, 200 and 250mm), three tests were carried out for each of the four powder feed rates (25, 38, 45 and 55gmin<sup>-1</sup>). The scatter of the residual stress results in the deposit was between  $\pm 5.1$ MPa for lower stress values, and up to  $\pm 51$ MPa for higher stress results.

Coatings deposited under each spraying condition were examined using optical and scanning electron microscopes. The results may be considered as falling into three zones;

Zone 1: High residual stress values at spraying distances of between 150 to 180mm were a result of extremely high deposition temperatures (samples had burn discolorations as shown in figure 82), which in turn give rise to high cooling stresses. Effective reduction of such high temperatures proved impossible, even with the use of the CO<sub>2</sub> cooling system. Residual stress ranges reduced (non-linearly) from an average of 865MPa to 272MPa over this 30mm change in spray distance, a reduction of approximately 69% (scatter was high). The stress change at the interface from the deposit to the substrate reduced by approximately 14MPa (from 262 to 248MPa), which would be attributed to higher temperatures during spraying at lower spraying distances.

Zone 2: Stress values were significantly lower at 200mm spraying distance. The deposition temperature was found to remain constant at 500°C at this spraying distance. Post deposition the samples had no heat marks, just a grey matt colour finish discoloration (a sample produced at 180mm is compared to one at 200mm in figure 83). Residual stress ranges reduced from an average of 272 to 143MPa over the 20mm distance (180 to 200mm), a reduction of approximately 47%. The percentage reduction in stress at 200mm compared to tests carried out at 150mm was calculated at 84%. The stress at the interface changed reduced by approximately 11MPa (from 248 to 237MPa) from the deposit to the substrate in this zone.

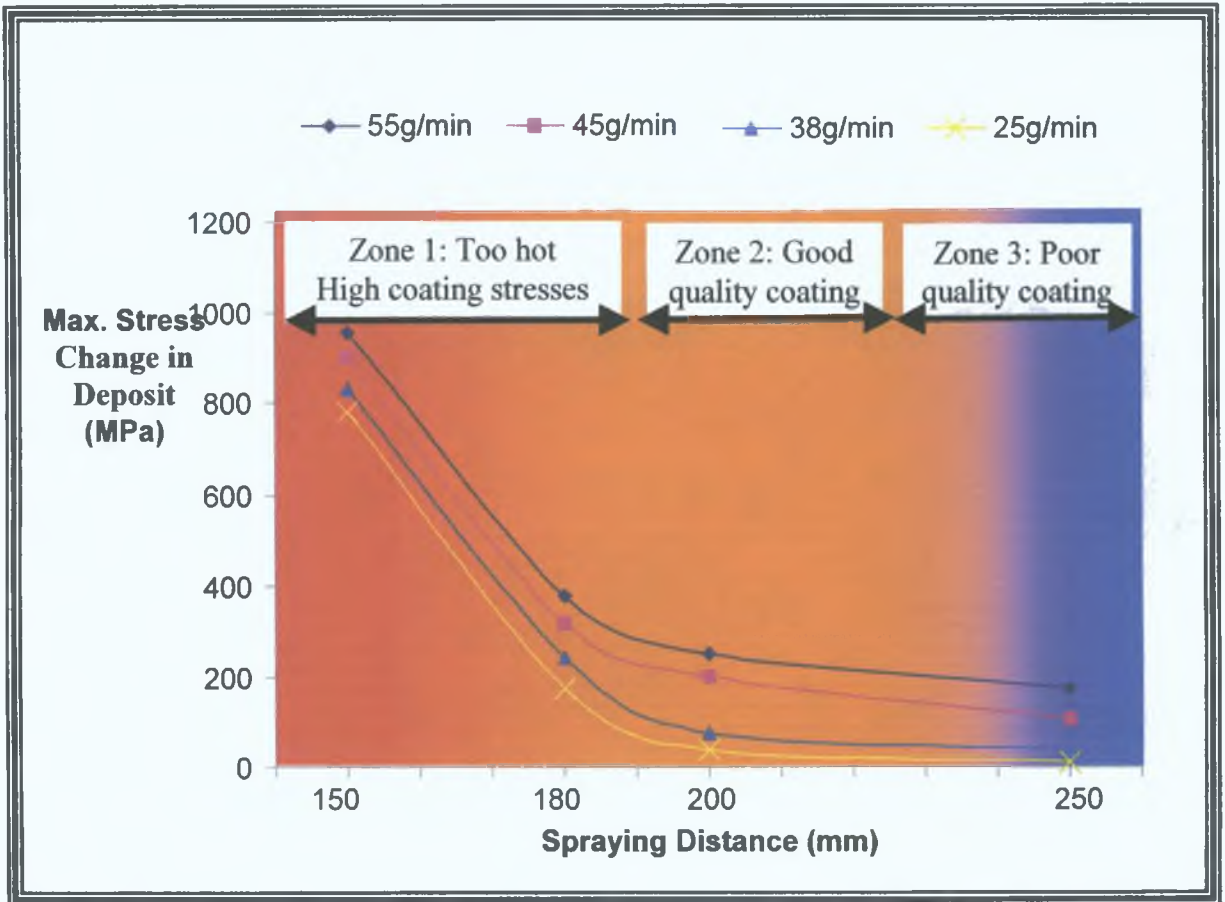


Figure 81, Maximum stress change as a function of spraying distance carried out at various powder feed rates.

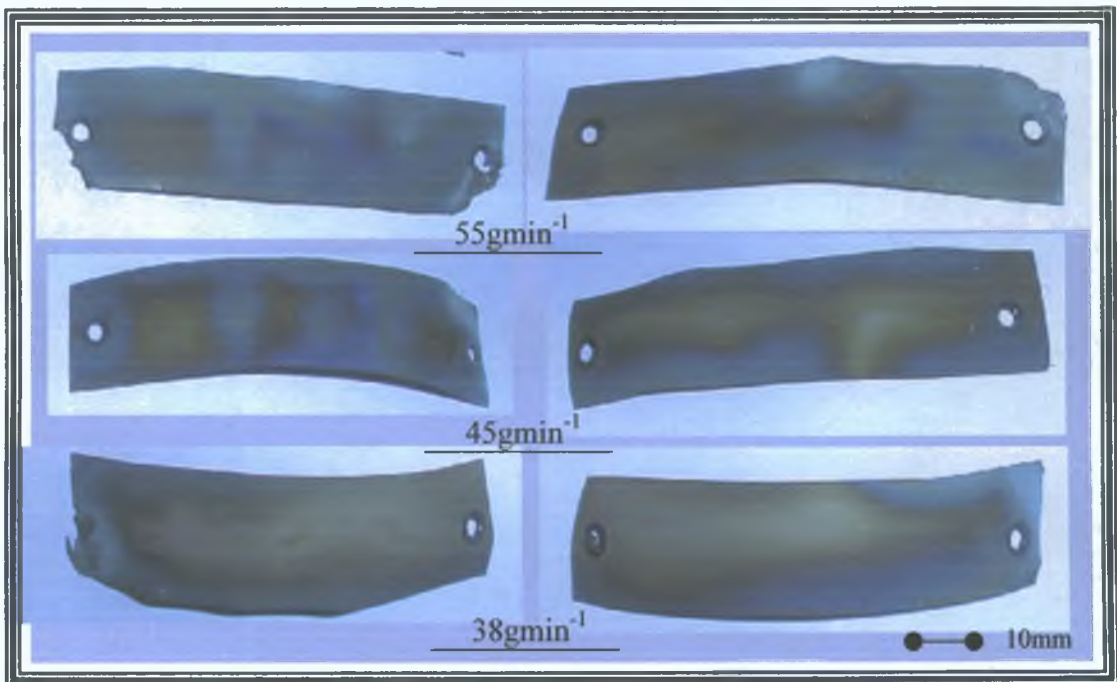


Figure 82, Deformed residual stress samples deposited at a spraying distance of 150mm at various powder feed rates.

Zone 3: Stress values were further reduced at higher spray distances (>200mm). However, the quality of these coatings was poor (figure 84). Under the microscope it was observed that individual particles were only loosely bound to the substrate or the previously deposited material, and a high percentage of solid particles existed in the coating. The reason for the poor adhesion of the individual particles is that the increased flight time at these spraying distances produces low velocities and impact temperature of the particles. The effect causes some particles to solidify before impact. The spray deposit thickness reduced from 0.5 to 0.3mm when the gun was moved from 200 to 250mm respectively, as a high majority of the particles rebound off the surface due to the solidification. Residual stress ranges across deposits reduced (non-linearly) from an average of 143 to 82MPa over the 50mm distance (200 to 250mm), and the percentage reduction in stress at 250mm compared to tests carried out at 150mm was calculated at 90.5%. The stress at the interface changed by approximately 2MPa (from 237 to 235MPa) from the deposit to the substrate, which would be attributed to the controlled temperature during spraying.

In summary a spraying distance of 200mm, yielded good quality deposits for the tungsten carbide-cobalt material, with an adequate pass thickness (30 $\mu$ m which supports findings found by Irons [59]), and a low stress gradient. The METCO application data [31] states that the most efficient WC-Co deposit is achieved at a spray distance of 200mm.

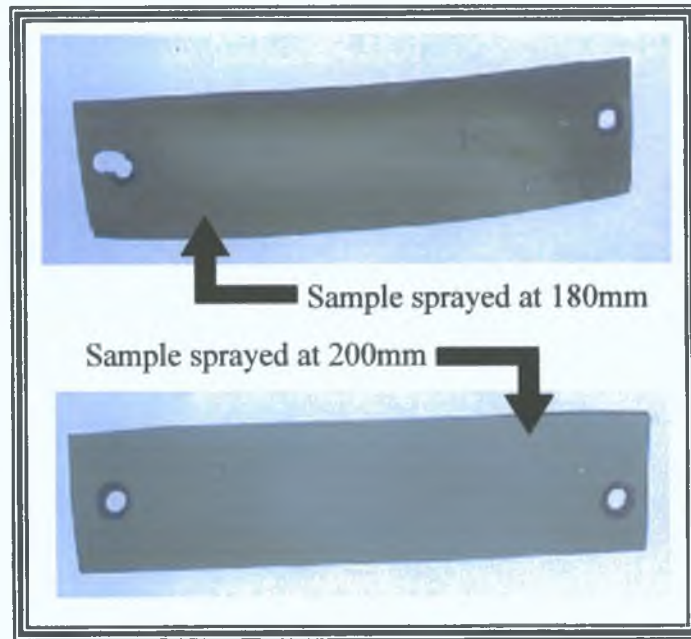


Figure 83, Residual stress samples sprayed at 180 and 200mm.

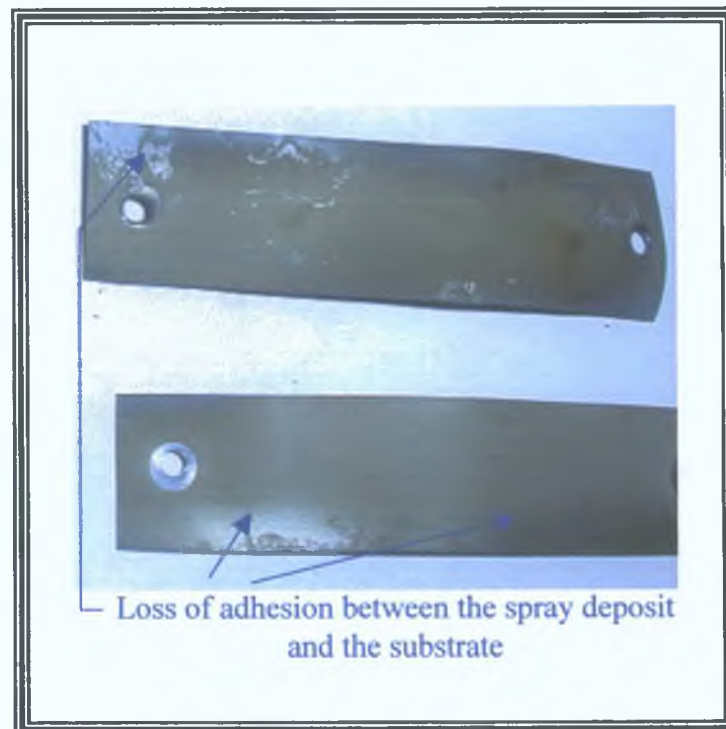


Figure 84, Residual stress samples sprayed at 250mm.

### 5.6.5 Variation Of Residual Stress With Powder Feed Rate

Powder feed rate is another parameter which has an effect on residual stress. Feed rates of 25, 38, 45 and 55gmin<sup>-1</sup> were investigated with varying spraying distance (figure 81). The powder feed rates were pick based on the sensitivity of the powder feed unit (the control of the feed rate made it difficult to attain specific values). The stress change in the deposit sprayed at a distance of 200mm, was on average 252MPa when a feed rate of 55gmin<sup>-1</sup> was use. The stress reduced (at the same distance) to 203MPa when a feed rate of 45gmin<sup>-1</sup> was used. Similarly, the stress reduced to 73 and 36MPa for feed rates of 38 and 25gmin<sup>-1</sup> respectively. A micrograph of the top of sprayed surfaces, formed using the various powder feed rates, is shown in figure 85. Lowest stress change results were observed at feed rates of 25gmin<sup>-1</sup>, however the coating was of such poor quality, that the stress is not relevant. This is because the small amount of material deposited on each pass of the HVOF gun, results in a sparse distribution of particles. At this rate, inter-particulate bonding was impossible until several passes were made and this yielded poor bond strength between the substrate and the deposit, and increased porosity (shown as points A in figure 85).

Residual stress values increase with increasing powder feed rate, at each spray distance (figure 81). At feed rates of 38gmin<sup>-1</sup> and greater, inter-particulate bonding was observed on the first pass. However at feed rates of 45gmin<sup>-1</sup> and higher, the number of voids decreased, but the quantity of unmelted particles increased. These are indicated by symbol B in figure 85. The higher feed rates of particles during deposition could 'shot-peen' the substrate / previously deposited material [116], generating high compressive residual stress within the deposit, however this would account for a relatively small amount of stress. The effect of increasing the powder feed rate increases the pass thickness, thus causing some high tensile stresses between each pass and the previously deposited material, due to the free-edge debonding effect [51,52]. Minimisation of residual stress within a deposit is only achieved by reducing each pass thickness [59].

In summary a powder feed rate of  $38 \text{ gmin}^{-1}$ , yielded good quality deposits for the tungsten carbide-cobalt material, with a minimum pass thickness together with low residual stress. This is in agreement with the METCO application data [31] which states that the most efficient WC-Co deposit is achieved using a feed rate of  $38 \text{ gmin}^{-1}$ .

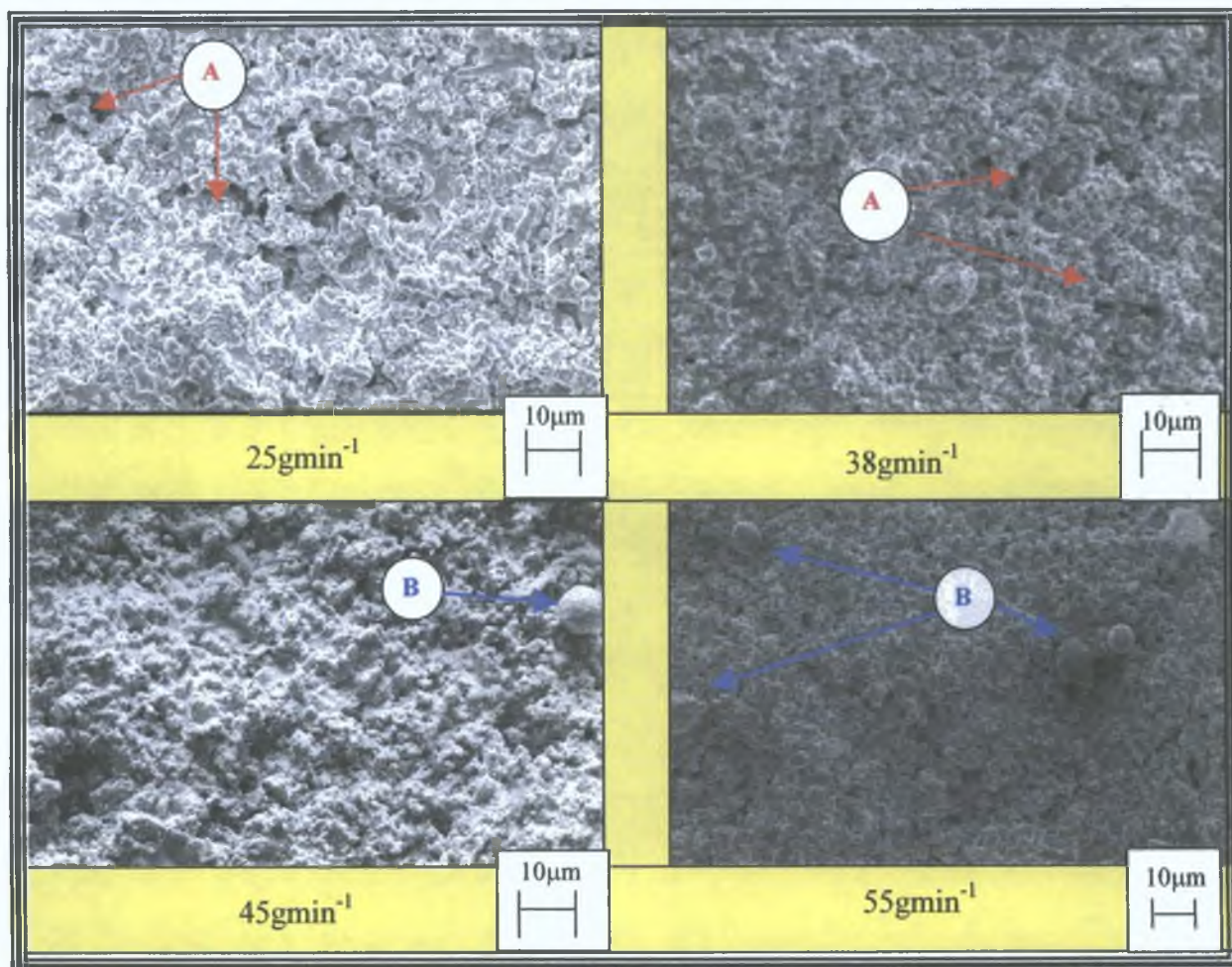


Figure 85, Scanning electron microscope surface images of WC-Co formed at various powder feed rates, showing the presence of unmelted particles and voids. A = Voids, B = Solid particles.

## 5.7 MAXIMIZING THICKNESS OF THE DEPOSIT

In order to fabricate free-standing engineering components using the HVOF process, it is essential that a maximum thickness of deposit is achieved. This section presents results of an investigation into the effect of geometrical shape (thickness, length and width) on the residual stress in the deposit, while using a spraying distance of 200mm and a powder feed rate of  $38\text{gmin}^{-1}$ . The tests were carried out using the automated traverse unit together with the carbon dioxide cooling. The residual stress was simulated using the finite element technique to compare this analysis to the experimental results measured.

### 5.7.1 Effect Of Deposit Thickness On Residual Stress

#### (1) Analytical Results

The stainless steel substrates (80mm long, 20mm wide, and 0.075mm thick) were used together with Clyne's Method to measure residual stress for various thicknesses of WC-Co deposit. The individual steel strips were pre-heated to  $450^{\circ}\text{C}$ , then deposited with WC-Co. Three tests were carried out for each thickness of the WC-Co deposit (0.2, 0.6, 1, 2, 2.5 and 3mm). Figures 86, 87 and 88 show the relationship found between residual stress and each of the thicknesses sprayed.

In figure 86 (a), the residual stress distribution through a 0.2mm deposit on a 0.075mm substrate shows the top surface of the deposit to be in tension. Test results average in the range of the ultimate tensile strength of the WC-Co material. However surface cracking was not evident, indicating either some over estimation of actual stresses in the deposit or the effects of constraints. There is a negative stress change of approximately 115MPa ( $\pm 21\text{MPa}$  difference between tests) from top of the deposit to the deposit / substrate interface. The stress at the interface ranges from  $-32\text{MPa}$  on the deposit interface side to  $40\text{MPa}$  at the substrate side. The distribution through the complete sample is not smooth, which is a result of using equations 17 through to 20.

The residual stress distribution through a 0.6mm deposit, shown in figure 86 (b), includes a stress change of approximately 87MPa ( $\pm 2$ MPa difference between tests), from a top surface tensile value of 14.5MPa to an interface compressive value of 72MPa. The stress change in the deposit has reduced by 24.3% compared to that found for the 0.2mm thick deposit. The stress at the interface varied from the deposit interface side to the substrate side by 222MPa. The results show that the deposit is tending towards a stress free state as the deposit thickness increases.

In figure 87 (a), the residual stress distribution through a 1mm deposit shows a stress change across the deposit of approximately 84MPa ( $\pm 1$ MPa difference between tests), from a top surface tensile value of 7MPa to an interface compressive value of 77MPa. The tensile stress at the deposit top surface has reduced by 91.6% compared to that found for the 0.2mm thick deposit. The stress at the interface ranges from  $-77$ MPa on the deposit interface side to 128MPa at the substrate side. The results show that the deposit surface is close to a stress free state.

The residual stress distribution through a 2mm deposit shown in figure 87 (b), illustrates a stress increase of approximately 104MPa ( $\pm 1$ MPa difference between tests), from a top surface compressive value of 26MPa to an interface tensile value of 79MPa. The samples curved inwards. The stress at the interface varied from the deposit interface side to the substrate side by -148MPa. The results show that the deposit has passed the stress free state.

In figure 88 the residual stress distribution through a 2.5mm and a 3mm deposit is shown. A positive stress change of approximately 153MPa and 200MPa respectively is seen. The 2.5mm deposit had a top surface compressive value of approximately 74MPa to an interface tensile value of 79MPa, whereas the 3mm deposit had a top surface compressive value of 120MPa to an interface tensile value of 80MPa. The stress at the interface varied from the deposit interface side to the substrate side by -152 and -155MPa respectively. The residual stress was so high that the samples deformed both longitudinally and across the samples width. The generation of residual stress due to

increasing deposit thickness reduces the bond strength of the material, hence failure of the deposit occurs due to a peel back mechanism [51,52]. In the case of the 3mm thick deposit, two tests failed by cracking (figure 89), hence only one result was achieved. The failure was expected as Helali [110] found that the ultimate tensile strength of the WC-Co deposit to be approximately 70MPa. Inaccuracies were inevitable when measuring the deflection of these samples due to the buckling of the samples.

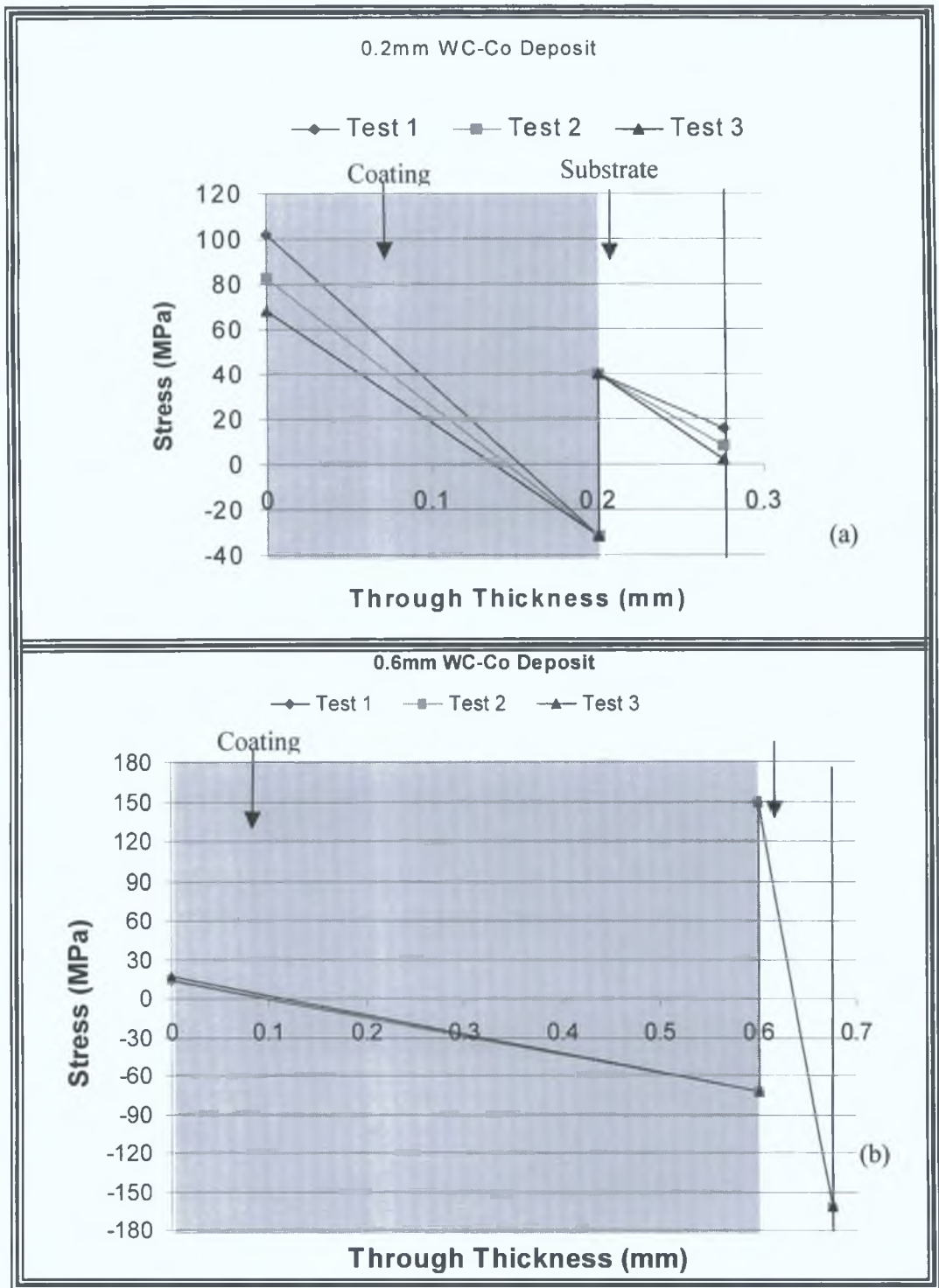


Figure 86, Residual stress in a 0.2 and 0.6mm thick deposit of WC-Co plus substrate.

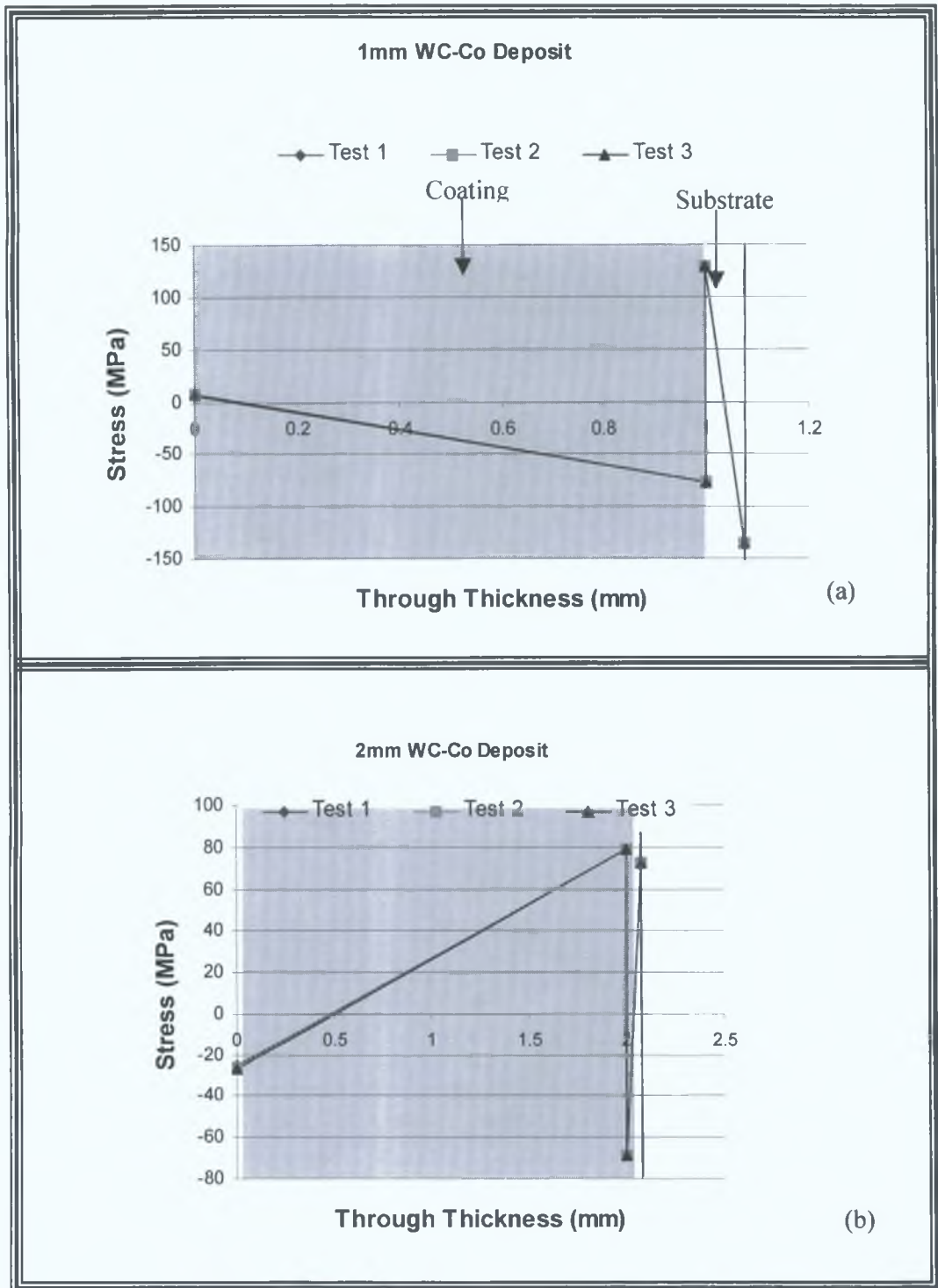


Figure 87, Residual stress in a 1 and 2mm thick deposit of WC-Co plus substrate.

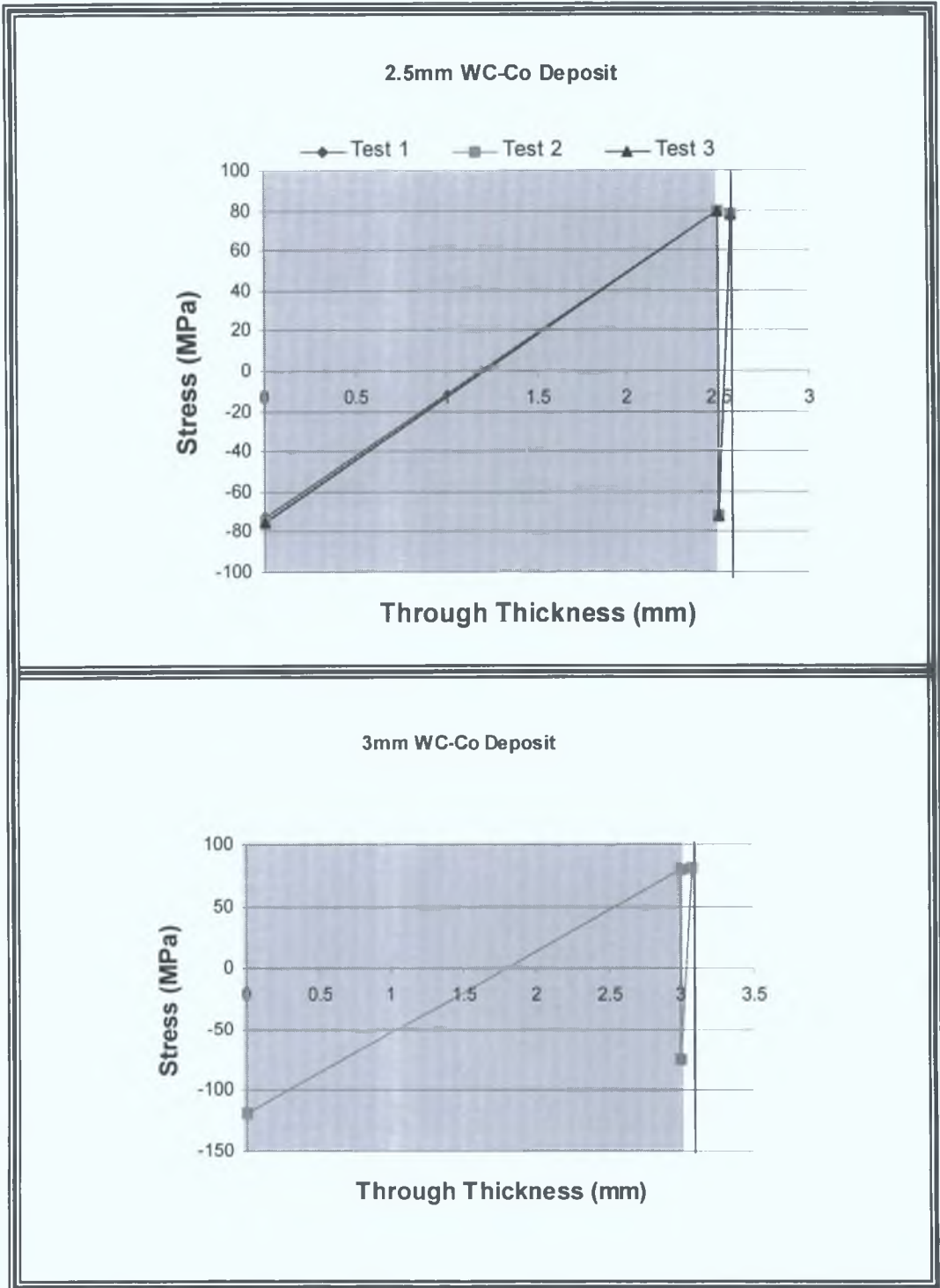


Figure 88, Residual stress in a 2.5 and 3mm thick deposit of WC-Co plus substrate.

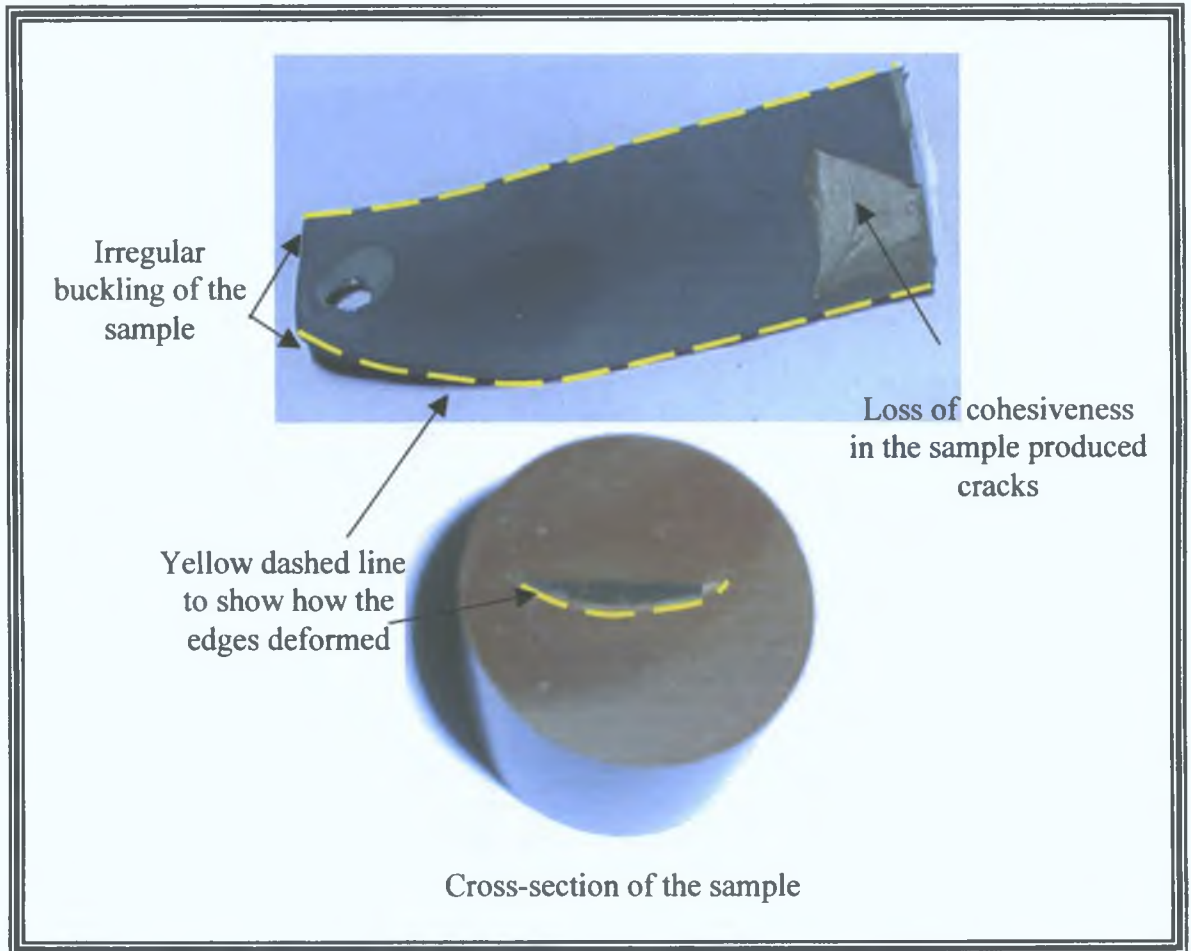


Figure 89, Deformed and cracked sample due to excessive residual stress.

Figure 90 shows how the shape of the deposit changed between 1 and 2mm. An effect of thickness on residual stress was observed, where an increase in coating thickness decreased the residual stress. This finding was also observed by McGrann et al. [117] as the effect which occurred in a plasma sprayed nickel deposit and a HVOF sprayed Inco718 material where coating thickness increases. Unfortunately, no process based explanation was given as to this stress change.

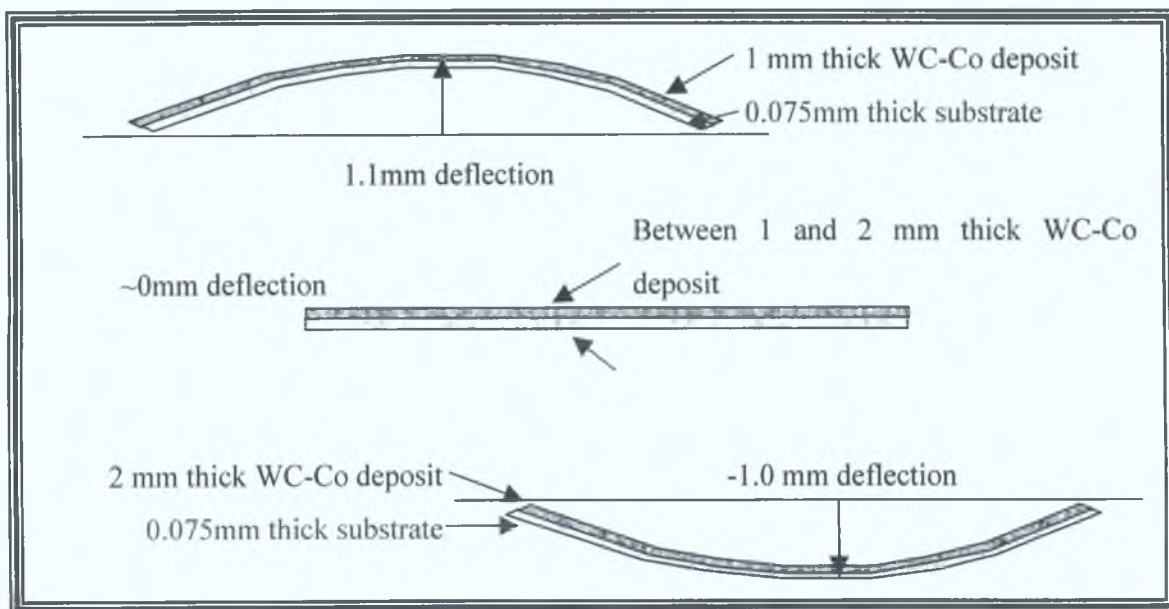


Figure 90, Change in the shape of the deposit as the deposit thickness increased from 1mm to 2mm.

Plotting the stress values found at the top of the deposit (for each deposit thickness: 0.2, 0.6, 1, 2, 2.5 and 3mm) as a function of deposit thickness, reveals the thickness where the deposit would be stress free. The results are not linear. Three zones can be noted; zone A where the deposit top surface stress decreases dramatically (by approximately 95MPa per mm thickness), with the deposit thickness up to 1mm. The stress decreases at a lower rate (by approximately 33MPa per mm thickness) from 1mm thickness increased to 2mm thick (zone B). In zone B the stress on the deposit surface changes from a compressive to a tensile stress. Greater than 2mm thick (zone C), the stress at the deposit top surface decreases at a high rate again (by approximately 94MPa per mm thickness). According to a curve in figure 91, a deposit thickness of around 1.2mm produces a stress free deposit.

WC-Co was therefore sprayed to a thickness of 1.2mm and the results (figure 92) showed that the deposit was relatively stress free (approximately -2MPa). The tensile

stress change was measured as approximately 80MPa ( $\pm 1.5$ MPa difference in results) and the interface stress change by  $-134$ MPa, which was the lowest interface stress found for all deposit thicknesses tested. The stress change both through the deposit and at the interface did not produce a deformed specimen, rather a flat specimen. Therefore, spraying WC-Co at a spraying distance of 200mm and a powder feed rate of  $38\text{gmin}^{-1}$ , using the traverse unit (at a speed of  $200\text{mms}^{-1}$  and an acceleration of  $4.9\text{ms}^{-2}$ ) and forced cooling (controlling the deposition temperature at  $500^\circ\text{C}$ ), produced a relatively stress free deposit of thickness 1.2mm (80mm long by 20mm wide).

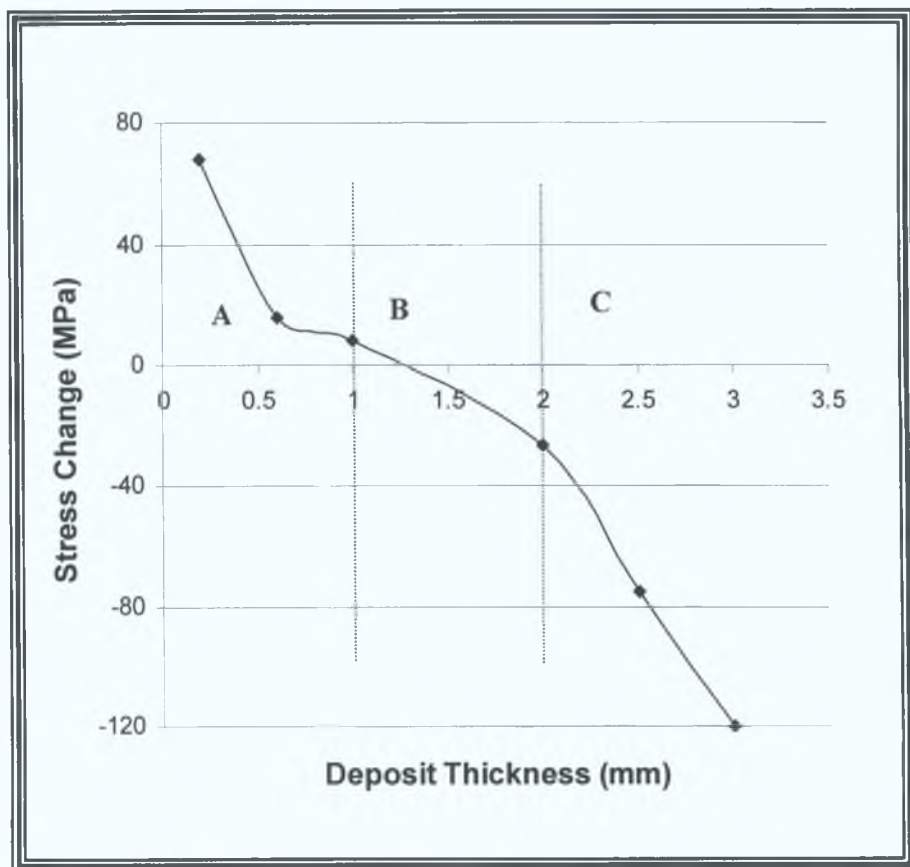


Figure 91, Maximum stress change as a function of deposit thickness.

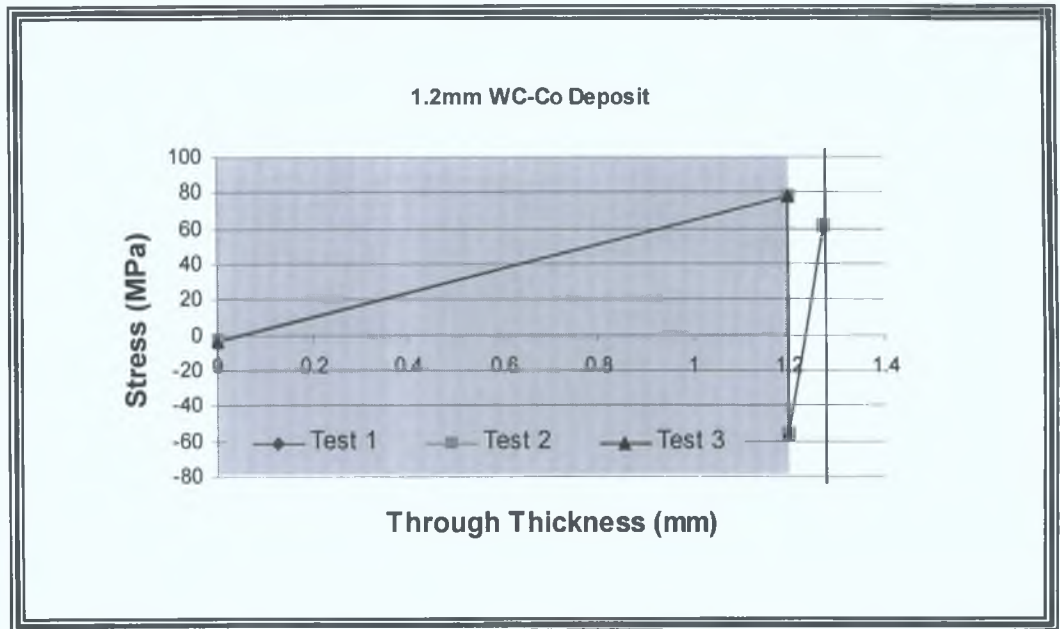


Figure 92, Stress distribution for a 1.2mm thick WC-Co deposit.

Figure 92 showed that a relatively stress free deposit existed for a deposit thickness of 1.2mm, where the length and width of the substrate were 80 and 20mm respectively. A component 50mm long and 26mm wide with a thickness of 1.2mm was fabricated by depositing the WC-Co material onto a stainless steel base (previously coated with an aluminium releasing layer). The flat component is shown in figure 93 (a). The same width and length was used in the fabrication of a 1.5mm thick component. This increase of 25% in thickness produced a deformed component, bent due to residual stress, as shown in figure 93 (b). Similarly other components (with lengths of 120mm and widths of 50mm) were fabricated at a thickness of 1.2mm and again at a higher thickness (figure 93 (c)). The results showed that components sprayed at 1.2mm remained flat for various geometrical sizes, however thicknesses above 1.2mm either deformed or failed due to cracking. The conclusion is that the maximum deposition thickness (0.6mm [31]) generally achieved by the HVOF for the tungsten carbide-cobalt material was increased with the introduction of the CO<sub>2</sub> cooling to a maximum thickness of 1.2mm.

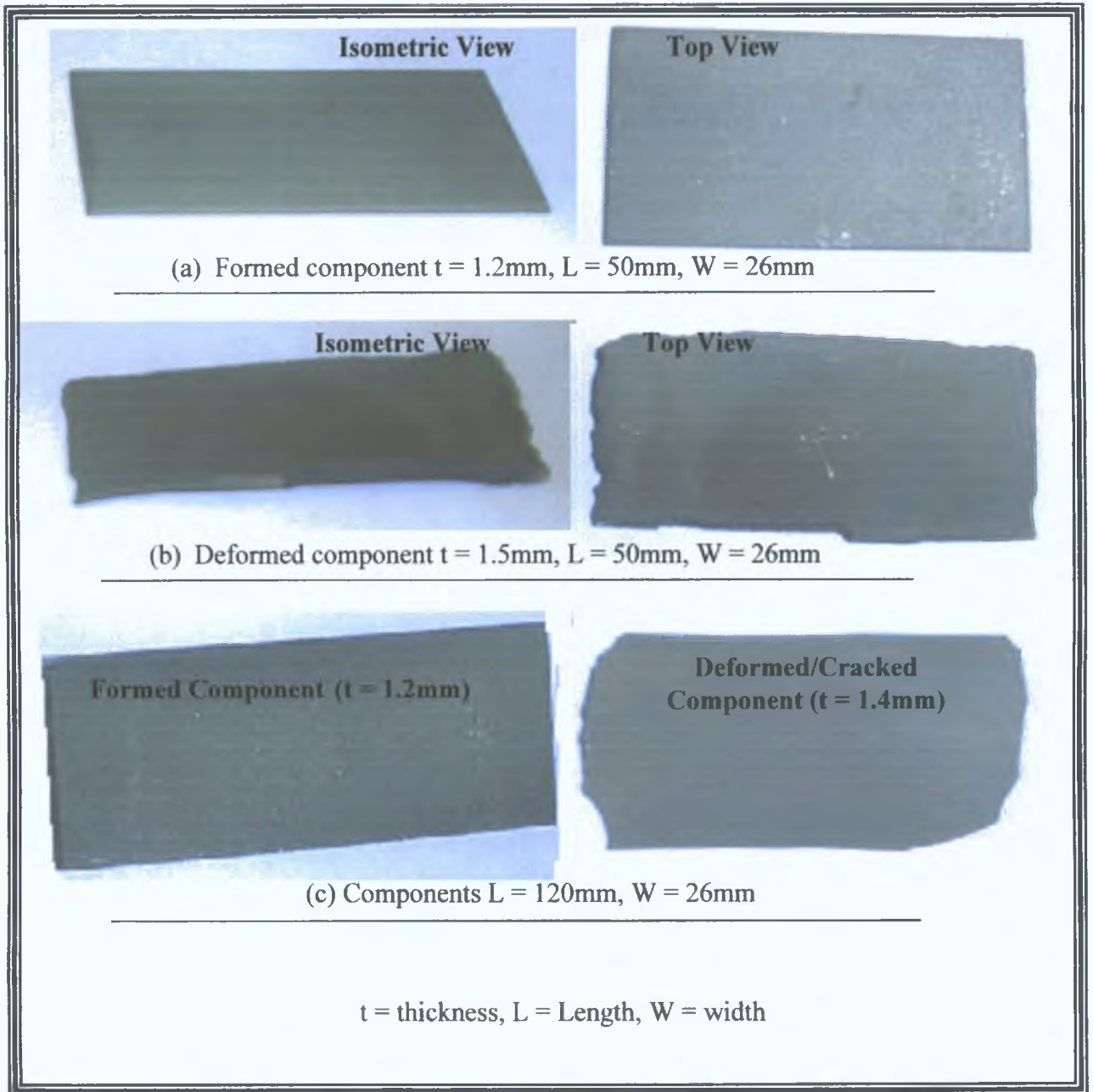


Figure 93, Various sized spray-formed components.

The quenching stress has already been shown to be [43, 118]:

$$\text{Quenching Stress} = \sigma_q \approx \alpha_c (T_m - T_s) E_c \quad \text{Equation 3}$$

Where  $\alpha_c$ ,  $T_c$ ,  $T_s$ , and  $E_c$ , are the respective deposit coefficient of thermal expansion, lamella temperature, substrate temperature and deposit stiffness (184.5GPa). Equation 101 estimates the stress generated in the coating due to the thermal expansion mismatch between coating and the substrate [119-121].

$$\sigma_{\text{cooling}} = \frac{[E_c \Delta T (\alpha_c - \alpha_s)]}{\left[1 + 2 \left( \frac{E_c t_c}{E_s t_s} \right)\right]} \quad \text{Equation 101}$$

Where  $\Delta T$  is the difference in temperature between the coating and the substrate, and  $\alpha_c$  and  $\alpha_s$  are the thermal expansion coefficients for the deposit ( $8.1 \times 10^{-6} \text{ }^\circ\text{C}^{-1}$ ) and substrate ( $16 \times 10^{-6} \text{ }^\circ\text{C}^{-1}$ ). The final stress at the coating surface is obtained by adding the quenching stress result to the cooling stress result [118].

Figure 94 (a) shows the substrate expands during the pre-heat treatment cycle, while subjected to a pre-heat temperature of  $450^\circ\text{C}$ . As the change over from pre-heating to spraying occurs, the substrate temperature drops by  $30^\circ\text{C}$  (figure 94). During spraying the deposition temperature increases up to  $500^\circ\text{C}$ , therefore the substrate expands further. When the individual particles strike the substrate surface, they try to contract (quench), however the substrate resists this contraction, generating a tensile stress in the lamella (figure 94 (b)). For a thin deposit (0.2mm thick), the quenching stresses would equal to approximately 120MPa using equation 3. The assumption here is that the lamella temperature is the same as that of the flame.

Once deposition ceases, cooling stresses generate (figure 94 (c)). The substrate contracts to a greater extent than that of the deposit, producing a compressive stress during cooling. The cooling stresses using equation 101 can be calculated for a 0.2mm thick deposit as  $-105.9\text{MPa}$ . The sum of these results yields a tensile residual stress of  $13.98\text{MPa}$  (at the top surface of the deposit), which demonstrates that the deposit is tensile for thin deposits (0.2mm). The tensile stress is a result of the difference between the pre-heat temperature together with the loss of temperature during change over (that

is substrate temperature during deposition, say approximately  $420^{\circ}\text{C}$ ), compared to the lamella temperature, resulting in a large thermal difference in equation 3.

In thicker deposits, this difference between the substrate and lamella decreases, as the substrate increases in temperature during the longer spray period (due to heating of the flame), as illustrated in figure 95. For a 2mm thick deposit, using the empirical formula derived earlier (equation 100), the substrate would be at an approximate temperature of  $467^{\circ}\text{C}$ , however this temperature increases up to the deposition temperature. The quenching stress reduces to  $+7.49\text{MPa}$  for the 2mm thick deposit. The cooling stress decreases (as the result is inversely proportional to the deposit thickness) to  $-14.5\text{MPa}$ . Hence the deposit has a resultant surface compressive residual stress of  $-7.01\text{MPa}$ .

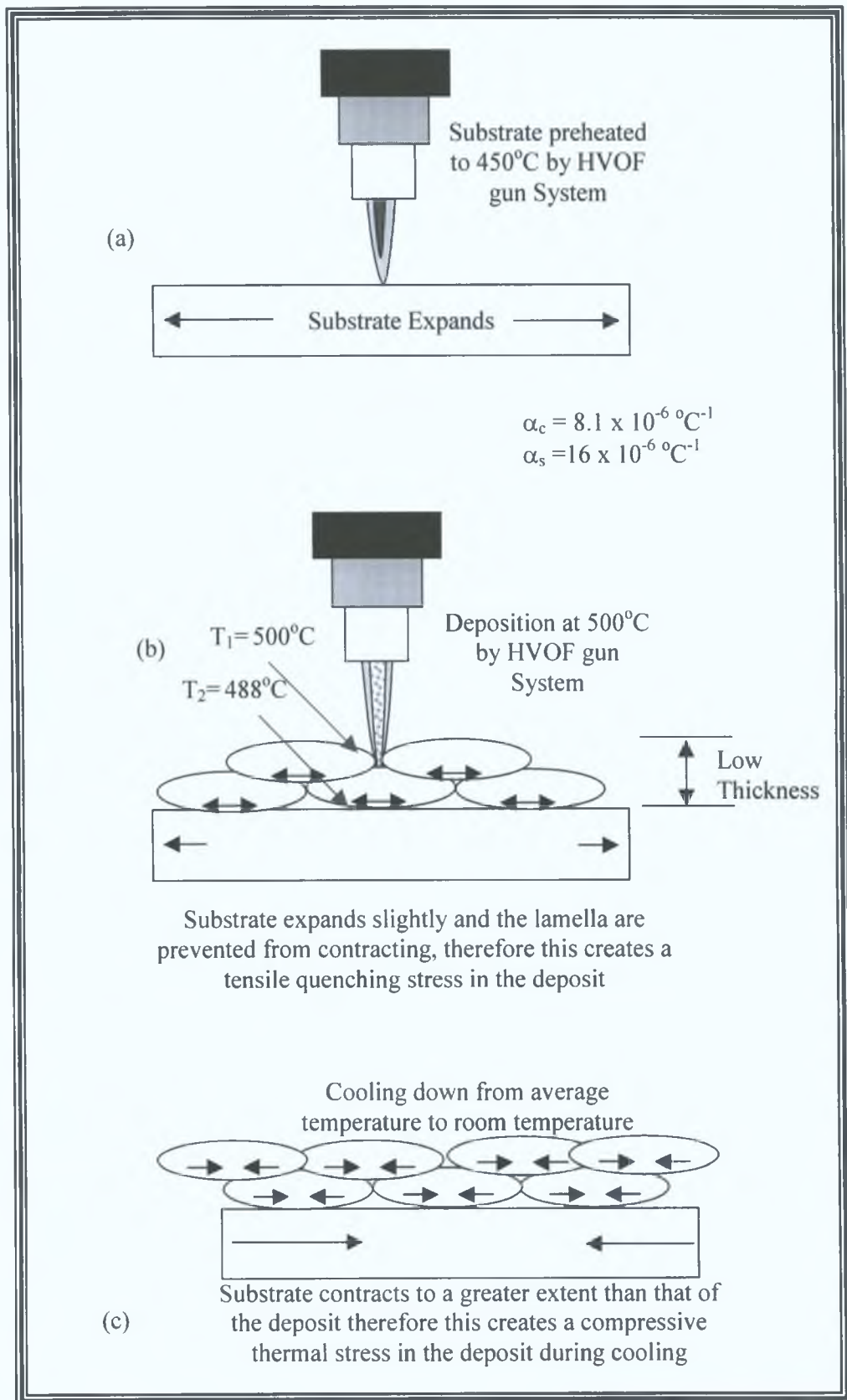


Figure 94, Residual stress development in thinner deposits.

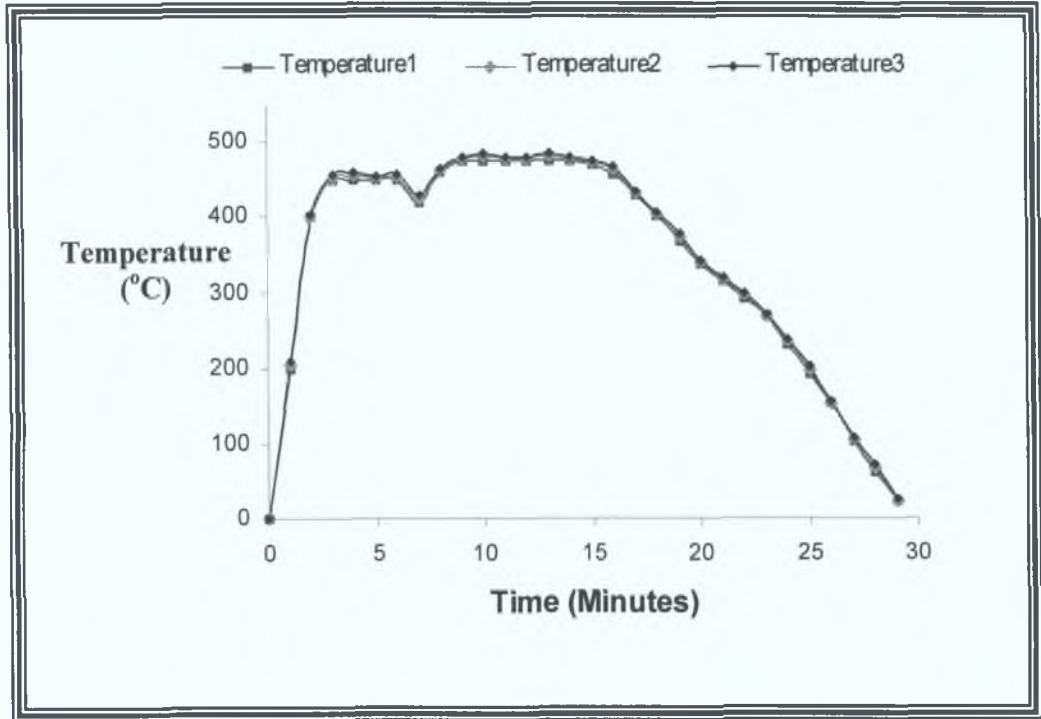


Figure 95, Pre-heating and spraying temperature.

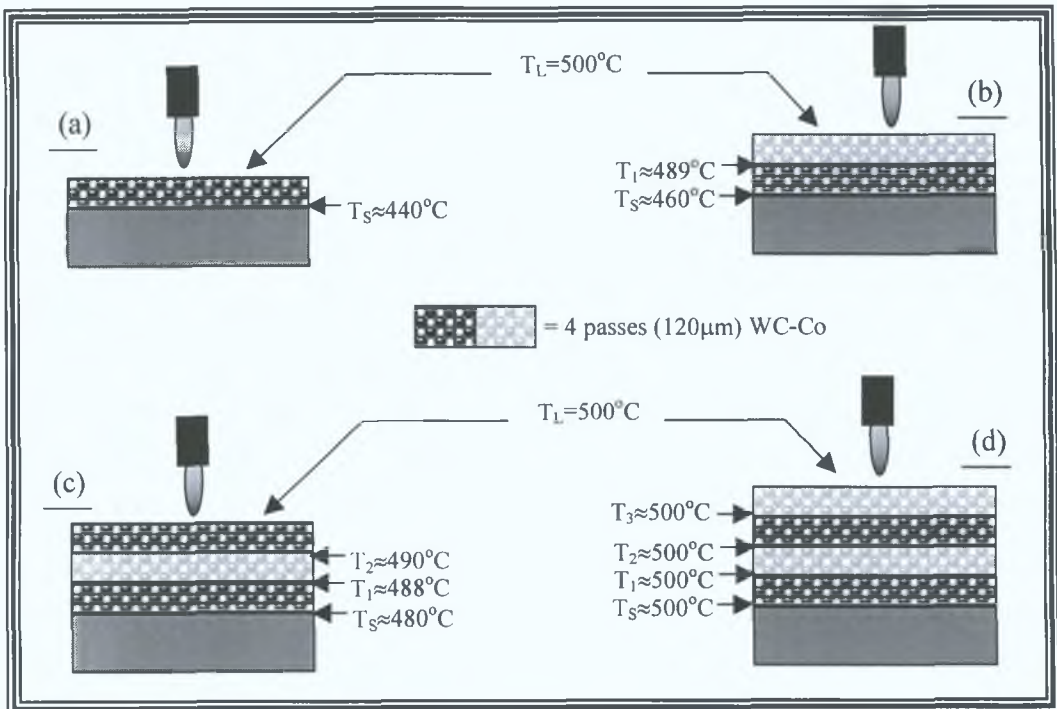


Figure 96, Temperature development in thick deposits.

## (2) Finite Element Analysis

The following results have been calculated using the procedures shown in Appendix 7. Modelling of the residual stress was carried out in two ways; one by subjecting the sample to a various temperatures until the resulting deflection equalled that found in the experimental results (figure 97), labelled as the thermal load system; the second by applying various loads horizontally to the deposit in a tensile manner and similar loads to the substrate in a compressive manner, to generate a moment. The choice of tensile or compressive applied to either the deposit / substrate depends on the stress that exists in the experimental sample. The results for the latter is shown as the generated moment system. For both systems the stress distribution was compared to that found from the experimental data.

The first test was carried out for a 0.2mm WC-Co deposit on a 0.075mm stainless substrate. Various temperatures were applied to the system to yield a deflection of 1.8mm (resulting deflection found in the experimental data). The stress distribution (at the maximum deflection point) for this sample is shown in figure 98 (a). Similarly, various loads were applied to the system to yield a deflection of 1.8mm in the generated moment system and its resulting stress distribution (at the maximum deflection point) is shown in figure 98 (b).

The finite element analysis results were compared graphically in figure 99, to the experimental results. The stress at the top of the deposit in the thermal load system is approximately 60% of that found at the same point in the experimental results. The stress at the top of the deposit in the generated moment system is approximately 80% of that found at the same point in the experimental results. Hence the generated moment finite element result shows the closest result to that found using Clyne's Method. The stress change at the interface for the thermal and generated moment systems were  $-98\text{MPa}$  and  $-177\text{MPa}$  respectively compared to  $-72\text{MPa}$  found in the experimental data. The thermal system interface stress change is approximately 74% of that found for the

same region in the experimental results. Hence the thermal finite element result shows the closest correlation with that found using Clyne's Method. The stress at the bottom of the substrate in the generated moment system is approximately 98% of that found at the same point in the experimental results, compared to 25% for the thermal system. Hence in this aspect the generated moment finite element result shows the closest correlation with that found using Clyne's Method for this point.

These results suggest that the generated moment finite element results are closest to the experimental results for the top and bottom of the sample, whereas the thermal load finite element results are closest to the experimental results for the interface region of the sample. This is illustrated in figure 99. In order to verify if this relationship between experimental data and the two finite element techniques is repeatable, model results was compared to experimental results at higher thicknesses.

The thermal load and generated moment finite element analysis was compared to the experimental data for deposit thicknesses of 1 and 2mm in figure 100. The stress at the top of the 1 and 2mm deposits in the thermal load system is approximately 62% of that found at the same point in the experimental results. The generated moment system is approximately 82% of that found at the same point in the experimental results. The thermal finite element result shows the closest result for stress change (approximately 75%) to that found using Clyne's Method at the interface. The generated moment finite element result shows the closest result (approximately 90%) to that found using Clyne's Method for bottom of the sample.

Hence the generated moment finite element results are close to the experimental results for the top and bottom of the sample, whereas the thermal load finite element results are close to the experimental results for the interface region of the sample. The explanation for this is that the generated moment is based on bending theory, hence the deflection of the beam estimates accurately the tensile and compressive stresses at the top and bottom of the sample. This method however does not account for thermal effects and overestimate the stress jump at the interface. The thermal load system accounts for thermal expansion / contraction (misfit strain), hence this model is more successful in

predicting the effect this has at the interface. However the use of the two models would predict quite closely the results found using Clyne's Method.

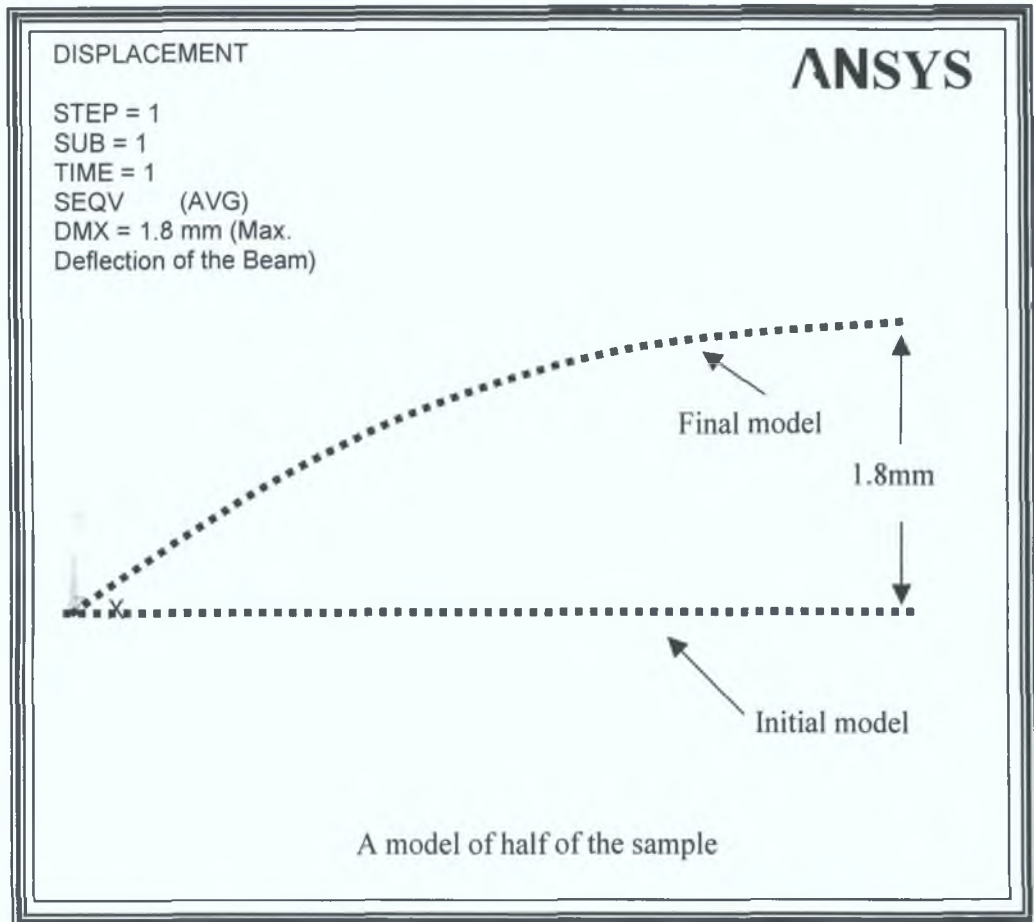


Figure 97, Resultant deflection for a 0.2mm deposit on a 0.075mm substrate.

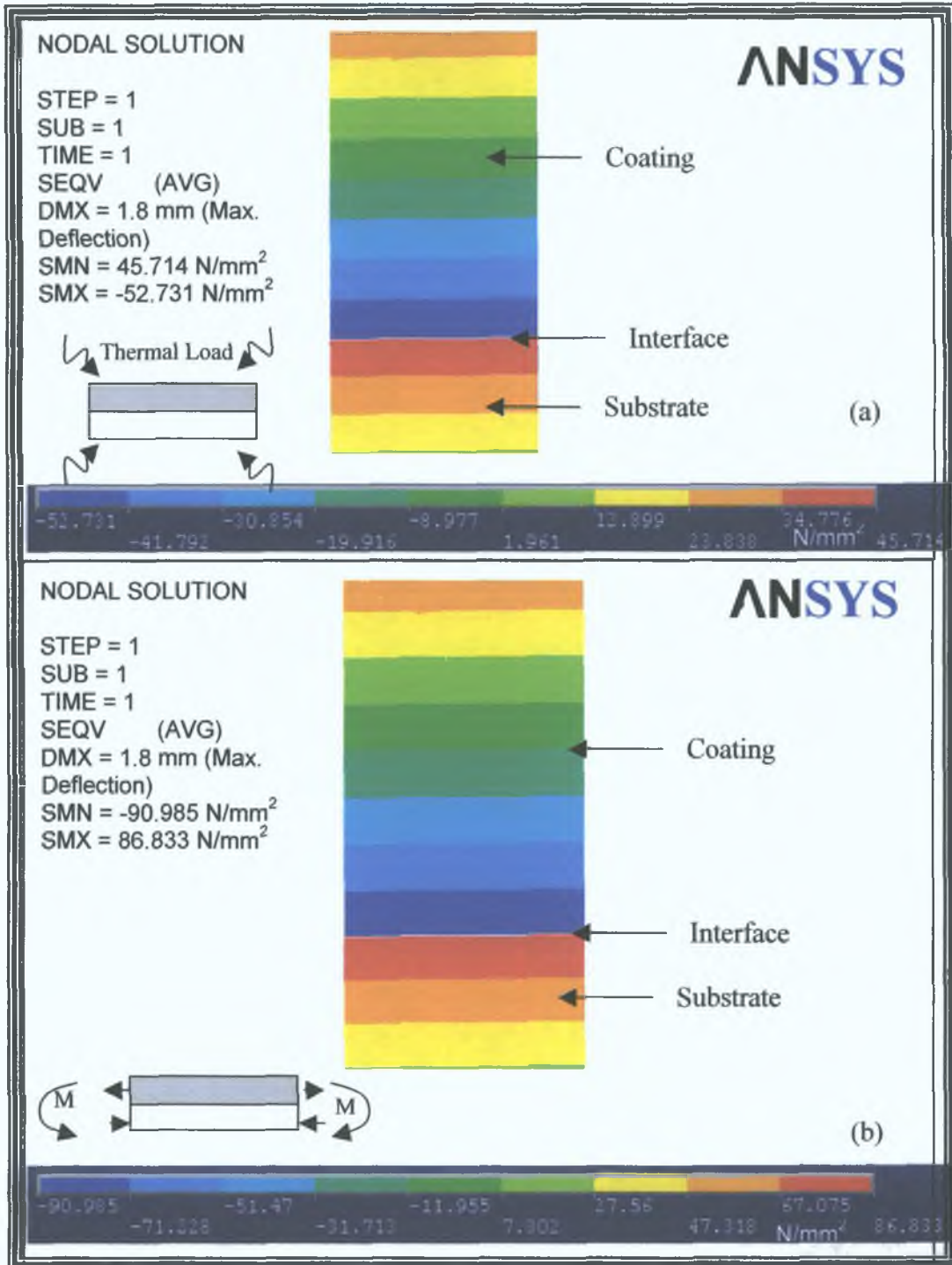


Figure 98, The finite element distribution through a 0.2mm deposit on a 0.075mm substrate.

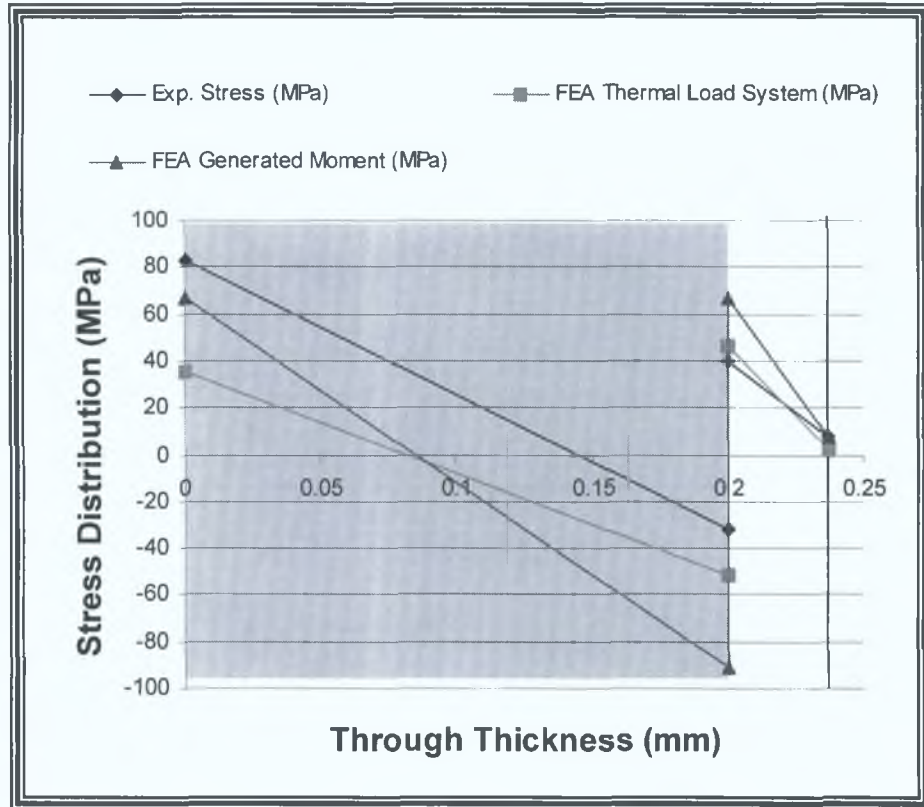


Figure 99, Finite element and experimental stress analysis of a 0.2mm thick deposit.

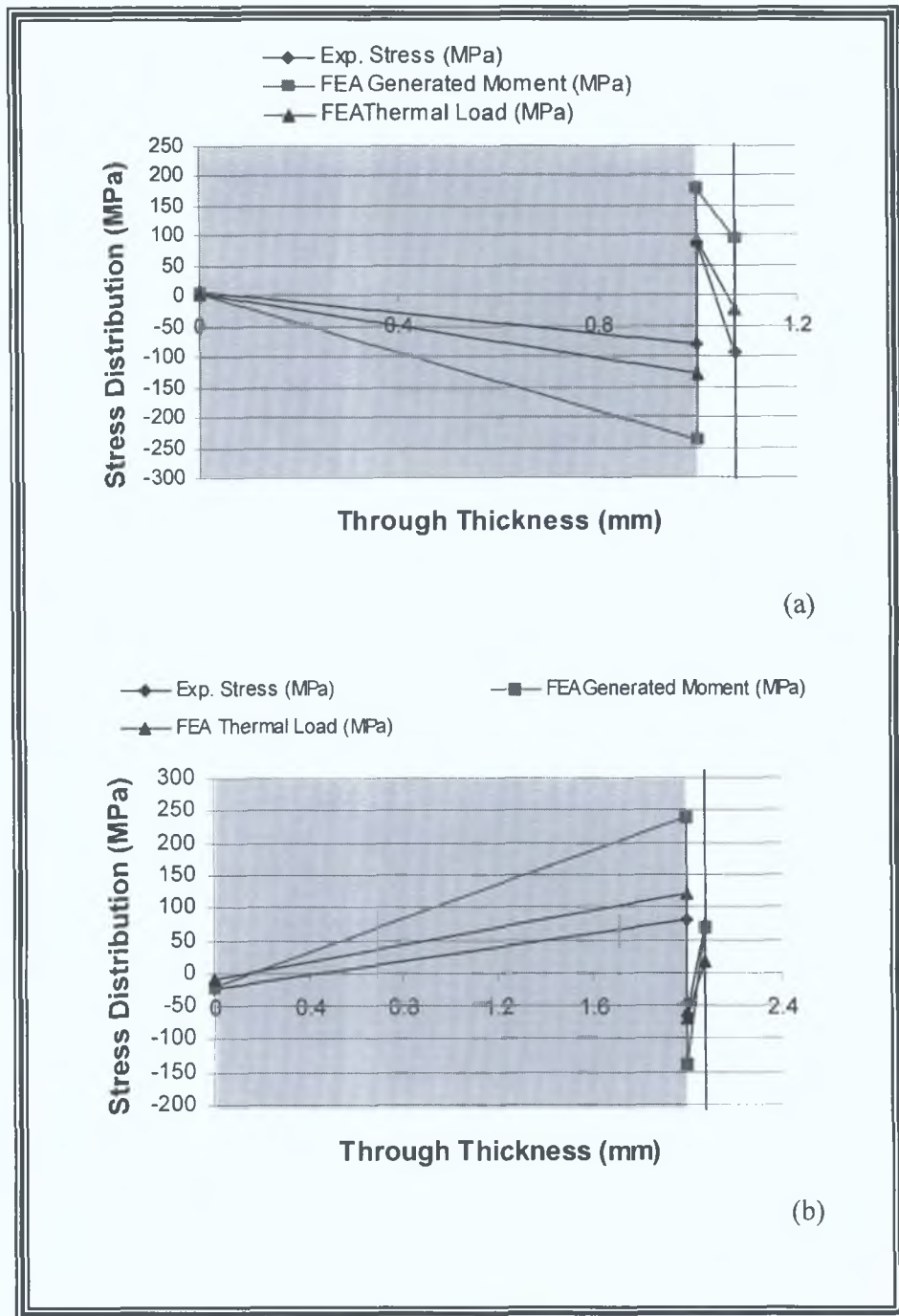


Figure 100, Finite element and experimental stress analysis of a 1mm (a) and 2mm (b) thick deposit.

## 5.7.2 Effect Of Substrate Thickness On Residual Stress

### (1) Analytical Results

In the previous section the substrate thickness remained constant (0.075mm), therefore this section investigated whether increasing the thickness of the substrate increased or reduced residual stress. Three tests were carried out for a substrate thickness of 1mm and the results were compared to the results found using a 0.075mm thick substrate. Two deposit thicknesses were analysed, 0.2 and 1mm. The results are presented in table 9.

For lower deposit thicknesses (0.2mm thick), the increase in substrate thickness resulted in a reduction in change in stress from top of the deposit to the deposit / substrate interface (from -114 to +100MPa), changing from compressive to tensile stress. Similarly the tensile stress at the top of the deposit for a low substrate thickness changed from a tensile stress of 82MPa to a compressive stress of 64MPa for the 1mm thick substrate.

At higher deposit thicknesses (1mm thick), the increase in substrate thickness resulted in the stress change from the top of the coating to its interface, from -84 to -65MPa respectively. The stress at the top of the deposit changed from a tensile stress of 4MPa to a compressive stress of 1MPa.

The effect of increasing the substrate thickness has on the residual stress in the deposit, is to almost 'invert' the stress distribution, demonstrated in figure 101. This can be explained using quenching and cooling stresses. The quenching stress for the deposit should be the same for both substrates (0.075mm and 1mm), as the the deposit thickness remains constant. By equation 102, it can be deduced that:

$$\sigma_{\text{cooling}} \propto t_s \quad \text{Equation 102}$$

Therefore increasing the substrate thickness has the effect of increasing the cooling stress. In this test the substrate thickness is increased by a factor of 13.33, therefore the cooling stress would increase by the same factor. When the quenching and cooling stresses are then combined together (for a substrate thickness of 1mm), they result in an overall compressive stress at the deposit surface, as opposed to the tensile stress found at this point for a substrate thickness of 0.075mm. Clyne (2002) [83], states that the analytical curvature of a thermally sprayed sample is related by the following equation:

$$\kappa = \frac{6E_c E_s (h_c + h_s) h_c h_s \Delta \varepsilon}{E_c^2 h_c^4 + 4E_c E_s h_c^3 h_s + 6E_c E_s h_c^2 h_s^2 + 4E_c E_s h_c h_s^3 + E_s^2 h_s^4} \quad \text{Equation 103}$$

It may be noted that, for a given deposit/substrate thickness ratio ( $h_c/h_s$ ), the curvature is inversely proportional to the substrate thickness,  $h_s$  (equation 103). Clyne (2002) [83] states that this scale effect is very important in practical terms, since relatively thin substrates are essential if curvatures sufficiently large for accurate measurement are to be generated. Therefore increasing the substrate thickness may reduce the accuracy of the results, but it also has an inverse effect ( $\kappa \propto \frac{1}{h_s^3}$ ) on the curvature of the sample, turning the sample surface stress from tensile to compressive.

Table 9, The effect of substrate thickness on stress.

Stress (MPa)	Deposit Thickness 0.2mm		Deposit Thickness 1mm	
	Substrate Thickness 0.075mm	Substrate Thickness 1mm	Substrate Thickness 0.075mm	Substrate Thickness 1mm
Top of Deposit	+82MPa	-64MPa	+4MPa	-1MPa
Deposit Interface	-32MPa	+36MPa	-80MPa	+64MPa
Substrate Interface	+40MPa	-35MPa	+87MPa	-78MPa
Bottom of Substrate	+8MPa	+27MPa	-94MPa	-55MPa
Change Across Deposit	-114MPa	+100MPa	-84MPa	+65MPa
Positive (+) = Tensile Stress Negative (-) = Compressive Stress				

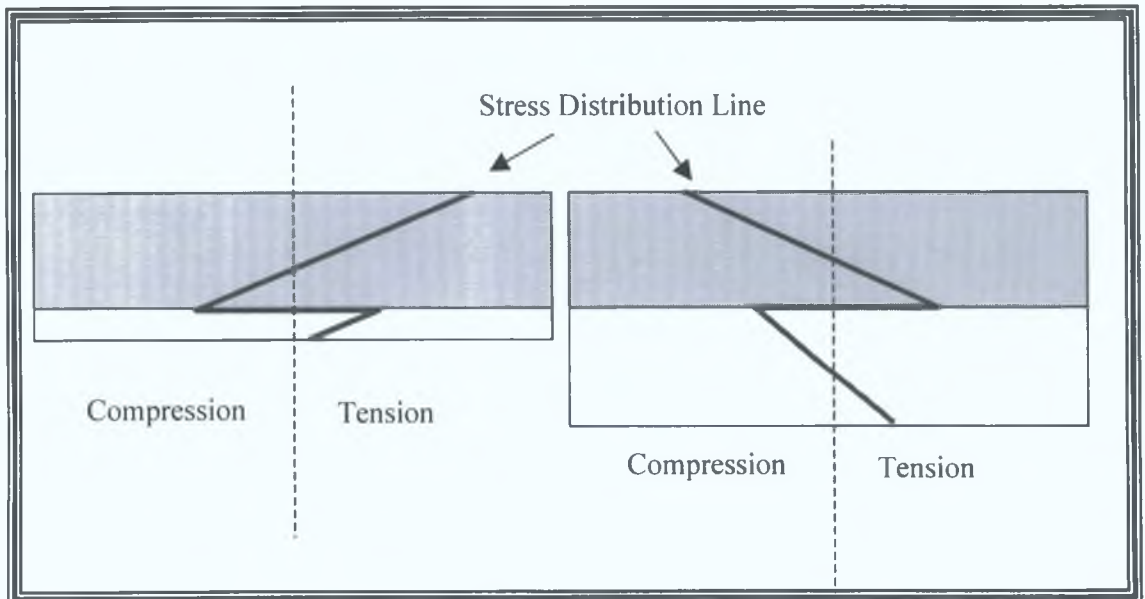


Figure 101, The effect of substrate thickness on stress.

## (2) Finite Element Analysis

The experimental results were simulated using the two finite element models. Table 10 lists the stresses found at the top of the deposit, both experimentally and numerically (thermal load and structural system). Due to the inaccuracies in the finite element technique, described in the previous section, a difference was observed between the stresses at the top of the deposit. However both models replicate the effect of increasing the substrate thickness causing the sample to go from tensile to compressive at the top of the deposit. However the thermal load system does yielded a stress value 58.5% below that of the experimental value. This compares to a stress 18.3% below found using the generated moment system, thus verifying that the latter yields closer values to the experimental results found.

Table 10, The effect of stress on substrate thickness experimentally and using the finite element technique.

Stress (MPa)	Deposit Thickness 0.2mm					
	Experimentally		Finite Element Analysis			
			Thermal Load		Generated Moment	
	Substrate Thickness 0.075mm	Substrate Thickness 1mm	Substrate Thickness 0.075mm	Substrate Thickness 1mm	Substrate Thickness 0.075mm	Substrate Thickness 1mm
Top of Deposit	+82MPa	-64MPa	+38MPa	-26MPa	+80MPa	-51MPa
Deposit Interface	-32MPa	+36MPa	-50MPa	+40MPa	-30MPa	+36MPa
Substrate Interface	+40MPa	-35MPa	+50MPa	-40MPa	+30MPa	-36MPa
Bottom of Substrate	+8MPa	+27MPa	+5MPa	-7MPa	+5MPa	-6MPa
Change Across Deposit	-114MPa	+100MPa	-88MPa	+66MPa	-110MPa	-87MPa
Positive (+) = Tensile Stress Negative (-) = Compressive Stress						

### 5.7.3 Effect Of Sample Length And Width On Residual Stress

#### (1) Analytical Results

This section investigates whether the size of a thermally sprayed component effected residual stress. While it is obvious that similar deposits would result in greater amounts of curvature when sprayed onto longer samples, it is not clear what the effect is of substrate geometry on stress. Tests were carried out for various lengths and widths of sample while keeping the thickness of the deposit (0.2mm) and the substrate (0.075mm) constant. The length of the sample was varied from 80mm (used in the last section) to 100mm and 40mm, keeping the width of the sample (20mm) constant. Three tests were carried out for each sample length. The average results are presented in table 11. The scatter was  $\pm 2$ MPa. Increasing the length to 100mm caused an increase in stress across the sample of approximately 18%, compared to the 80mm long sample. Decreasing the length to 40mm caused a decrease in stress across the sample of approximately 35%, compared to the 80mm long sample. The width of the sample was varied from 20mm (used in the last section) to 10mm, keeping the length of the sample (80mm) constant. The average results are presented in table 12 (the scatter was  $\pm 1$ MPa). Decreasing the width to 10mm caused little change in stress across the sample (approximately 2.5%), compared to the 20mm wide sample.

Within the size range tested the effect of decreasing the width of the sample is minimal. Reducing length however does have some impact on stress to decrease the stress quantities described in both tables 11 and 12, whether the stresses were tensile or compressive. Where multi-directional curvatures leading to mechanical instability occurs then this results in bifurcation. Under an equal biaxial stress state, an initially plane surface will tend to become convex or concave, with a curvature which should be equal in all directions (that is a spherical surface). However, high curvatures cannot be simultaneously accommodated in all in-plane directions. On increasing the curvature sufficiently, a bifurcation point will be reached, at which the curvature increases sharply in one plane and decreases sharply in the plane normal to this (that is the shape becomes

ellipsoidal). This should be avoided, since it is difficult to relate a measured curvature to an internal stress distribution once a specimen has bifurcated. According to Clyne (2000) [83], the critical curvature (point where bifurcation occurs) of the sample depends on the elastic constants, deposit / substrate thickness ratio ( $h_c/h_s$ ), substrate thickness/length ratio ( $h_s/L$ ), substrate width/length ratio ( $b/L$ ) and substrate length ( $L$ ). The predicted behaviour is shown in figure 102. The critical curvature reduces as the width/length ratio goes up. It is relatively insensitive to the elastic properties and to the deposit/substrate thickness ratio. It can be seen from the plot that there will be little or no danger of bifurcation instability (that is  $\kappa_b > \sim 10 \text{ m}^{-1}$ ) if a long ( $L \sim 100 \text{ mm}$ ), fairly narrow ( $b/L < \sim 0.2$ ) strip specimen is used. This is convenient, since such specimens are well suited to accurate measurement of curvature along the length of the strip (equation 103). The variation of length and width should not result in a variation in stress, however by the relationship shown in figure 102, if the substrate width/length ratio is greater than 0.2 then bifurcation may occur, resulting in a change in stress in the deposit.

Table 11, The effect of sample length on stress.

Stress (MPa)	Deposit Thickness 0.2mm Substrate Thickness 0.075mm Width = 20mm		
	Sample Length	Sample Length	Sample Length
	100mm	80mm	40mm
<b>Top of Deposit</b>	+96MPa	+82MPa	+53MPa
<b>Deposit Interface</b>	-38MPa	-32MPa	-21MPa
<b>Substrate Interface</b>	+47MPa	+40MPa	+25MPa
<b>Bottom of Substrate</b>	+10MPa	+8MPa	+5MPa
<b>Change Across Deposit</b>	-134MPa	-114MPa	-74MPa
Positive (+) = Tensile Stress : Negative (-) = Compressive Stress			

Table 12, The effect of sample width on stress.

Stress (MPa)	Deposit Thickness 0.2mm Substrate Thickness 0.075mm Length = 80mm	
	Sample Width 20mm	Sample Width 10mm
Top of Deposit	+82MPa	+80MPa
Deposit Interface	-32MPa	-31MPa
Substrate Interface	+40MPa	+39MPa
Bottom of Substrate	+8MPa	+7MPa
Change Across Deposit	-114MPa	-111MPa
Positive (+) = Tensile Stress : Negative (-) = Compressive Stress		

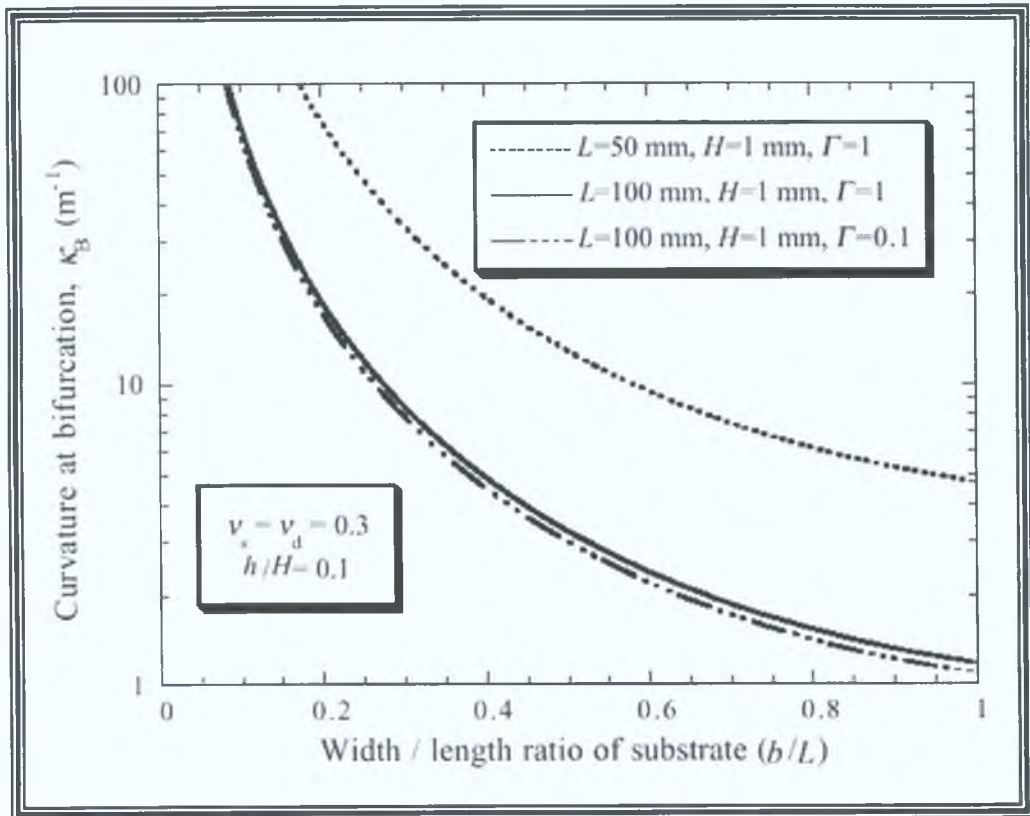


Figure 102, Predicted dependence on specimen width/length ratio of the critical curvature at a bifurcation instability [83].

## (2) Finite Element Analysis

The finite element analysis technique was used to determine whether the size of a thermally sprayed component affected residual stress calculated numerically in the same way as that found experimentally. The analysis was carried out for various lengths and widths of sample while keeping the thickness of the deposit (0.2mm) and the substrate (0.075mm) constant. The reduction in sample length from 80 to 40mm, caused the experimental stress change across the deposit (figure 103) to lessen by approximately 35%, this is in contrast to a reduction of 43% and 33% using the respective thermal load and generated moment finite element techniques. Clyne (2002) [83] states that longer samples produce sufficiently large curvatures, therefore produce accurate measurement of the samples deflection. Hence the accuracy of the FEA results do depend on the experimental deflections measured. The generated moment finite element technique proves to be the closest to the experimental results for the stress at the top of the deposit.

The width of the sample was also analysed, however as the thermal load was applied uniformly across the sample's width, the results did not vary by increasing the width of the sample.

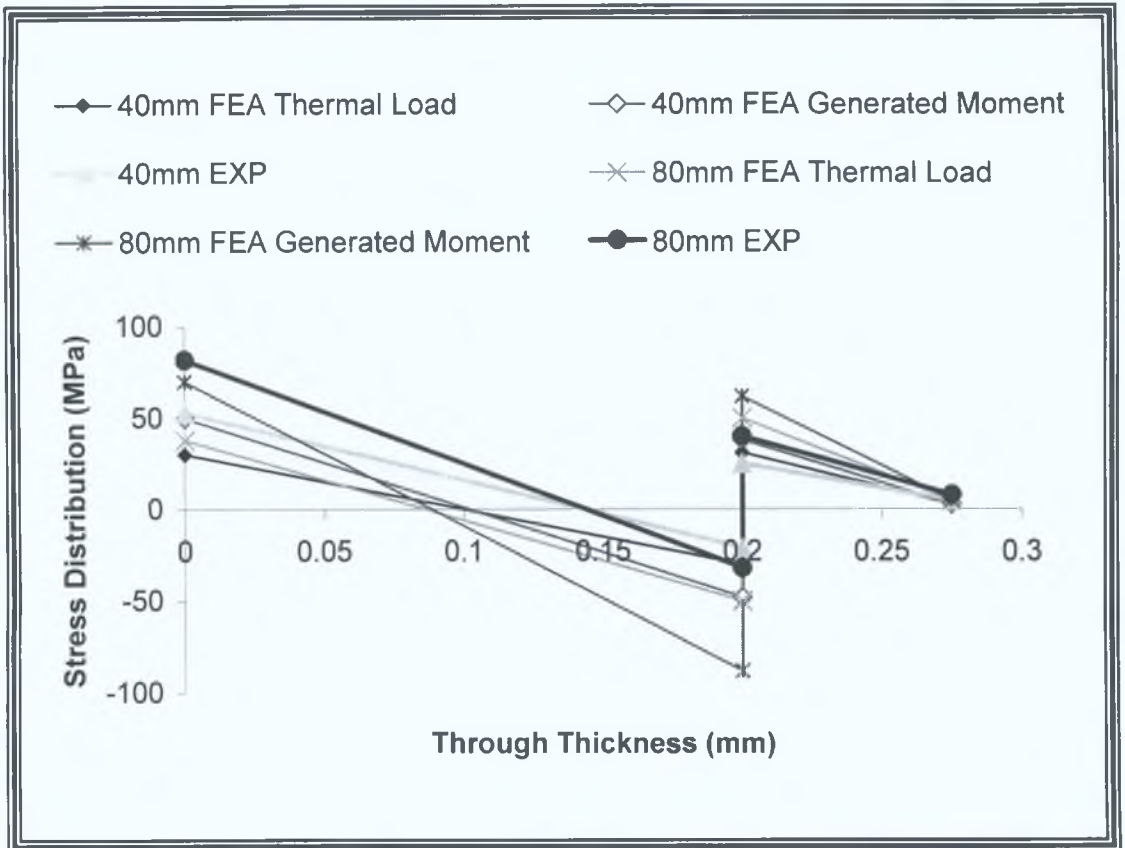


Figure 103, Effect of increasing the substrate length on residual stress calculated using the finite element technique.

#### 5.7.4 Effect Of Sample Size On Deposit Thickness

This section investigates whether reducing the size of sample (thus reducing residual stress in the deposit) would increase the maximum thickness of deposit achievable. The length and width of the stainless steel strips were reduced while keeping the substrate thickness at 0.075mm. Individual strips were deposited with WC-Co to thicknesses from 0.2 up to 8mm. Square samples were used for each test, with side length being reduced for thicker deposits. The maximum thickness for each square resulted in deflections which were converted into stress change values (residual stress) and the result is shown in figure 104. At higher thicknesses, high heat generation was experienced, especially as the length and width of the sample reduced to 12mm each (deposit thickness of 8mm), hence the stress change increased to 80MPa. Inaccuracies may have been encountered as reducing in length, reduced the deflection of the sample.

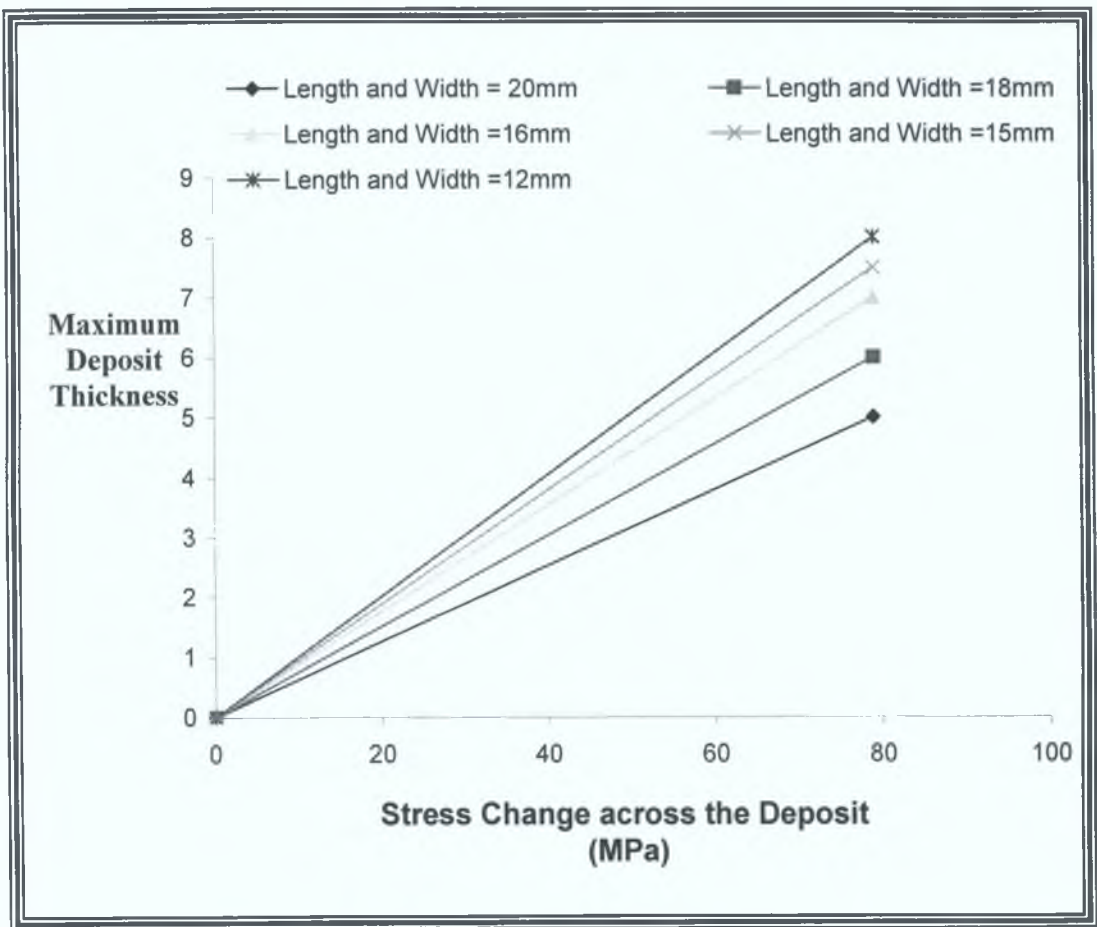


Figure 104, Higher deposit thickness as a function of residual stress.

### 5.7.5 Comparison Of Residual Stress Techniques

Samples used in Clyne's Analytical Method were used to measure residual stress using two other techniques; XRD diffraction and the Hole Drilling method.

For the XRD determination method (using  $\text{CrK}\alpha$  radiation), readings were taken from the top face of the samples. The author did not carry out the XRD tests as an XRD facility was not available in DCU, and the measurement was out sourced. Interpretation of results is presented in this context. A WC X-ray diffraction peak was identified (at approximately  $2\theta = 48.5$ ) at the surface of the specimen. This phase was chosen to measure the residual stress, as it was the broadest peak available within the  $2\theta$  scanning range. Figure 105 shows a slow scan of peak from 46 degrees to 51 degrees with  $\psi = 0$  and  $\psi = 45$  degrees. Using Bragg's law the values of  $2\theta$  were taken to calculate three values of planar spacing  $d_0$ ,  $d_{15}$  and  $d_{45}$  respectively. The changes between the spacings from  $\psi = 0$  to 45 degrees was plotted against  $\sin^2\psi$ . The results were fitted with a straight line using a least square regression technique. A WC stiffness value of 690GPa [33] was used for calculation. Deviation of the measured points from the fitted line was at maximum 4%. The stress was calculated using equation 25.

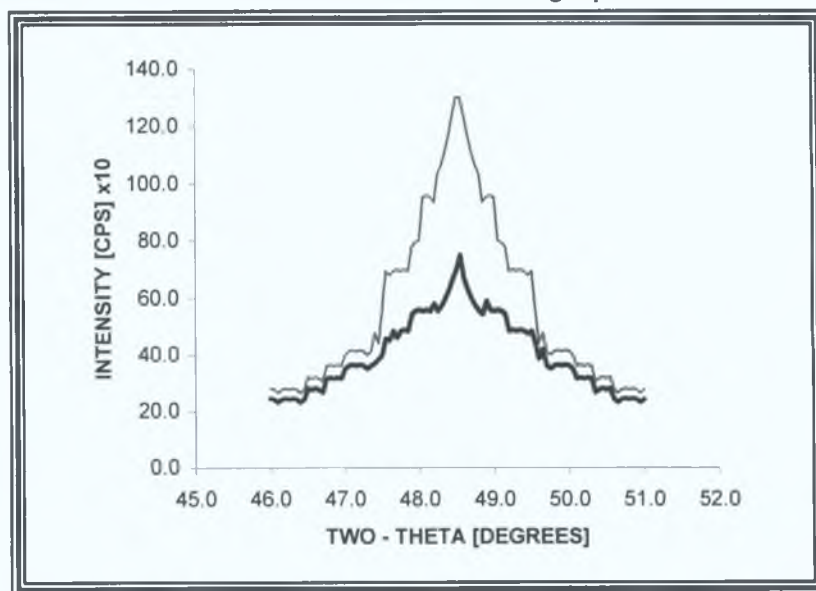


Figure 105, A typical X-ray diffraction measurement profile.

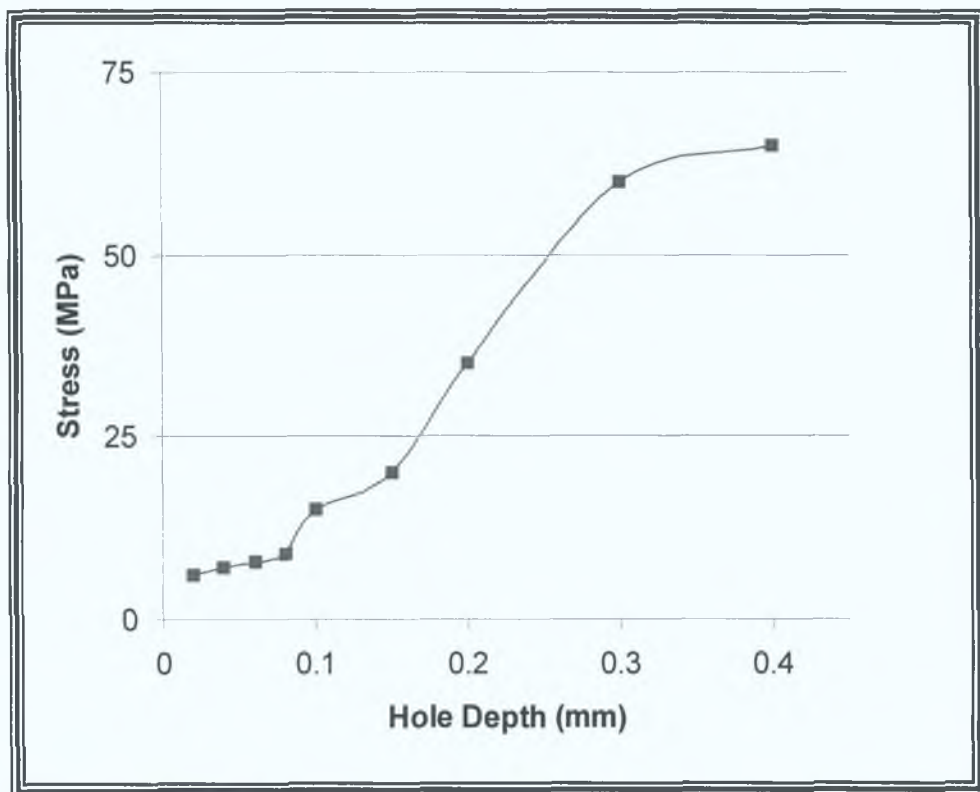


Figure 106, Stresses relieved with the hole drilling method.

In the hole drilling method, the samples are relieved using a semi-destructive method, where a hole is milled through the sample. Figure 106 shows the average stress measured as the carbide cutter mills through a 0.4mm thick sample. Within the close vicinity of the hole, the relief is nearly complete when the depth of the drilled hole approaches 0.4D (the mean diameter of the strain gage circle) or in the case of a material whose total thickness is less than 1.2D, a hole passing through the entire thickness. The relief stress (the residual stress in deposit) in figure 106 is taken to be 60.2MPa for example.

Table 13 shows the relationship between the residual stress measured using the Clyne's method and the results found using the XRD and hole drilling method.

Table 13, Comparison of residual stress measurement techniques.

<b>Sample Type</b>	<b>Clyne's Method Surface Stress (MPa)</b>	<b>XRD Method Surface Stress (MPa)</b>	<b>Hole Drilling Method Surface Stress (MPa)</b>
0.2mm thick deposit	+82	+63	+60
0.6mm thick deposit	+14	+31	+30
1mm thick deposit	+7	+10	+8
1.2 mm thick deposit	-1	+3	+3
2mm thick deposit	-26	-21	-23

While there are differences in the three measurement methods, correlation between the methods is reasonable, particularly for higher thicknesses. The XRD method indicates in most cases marginally higher stress results than the hole drilling method (this finding supports results observed by Tan [61]). In the case of deposits 1mm or greater the XRD results also correlate well with those found using Clyne's method. Divergence is seen for thinner deposits however. Samples used for the XRD method were sectioned to accommodate the XRD equipment, therefore scatter in results is expected.

## 5.8 POST TREATMENT

### 5.8.1 Post-Heat Treatment

Samples were stress relieved by post-heat treating them in a furnace. Figure 107, describes the post-heat thermal cycle carried out where the WC-Co samples were allowed to cool after deposition. Figure 108, describes the full thermal cycle (pre-heating at 450°C for 3 minutes, spraying at 500°C for 5 minutes and post-heating) of the deposit, where the sample was transferred from its spraying position to the furnace. In both cases, the sample was post-heated to a temperature of 650°C, then soaked at that temperature for various times, such as 80minutes, as recommended by Helali [49] with the aim of producing a stress free component. Following the soaking cycle, the samples were allowed to cool, either by fast or slow cooling. Fast cooling was achieved by removing the samples from the furnace to allow them to cool in air. Keeping the samples inside the closed furnace reduce the cooling rate than the sample thus slow cooling was achieved.

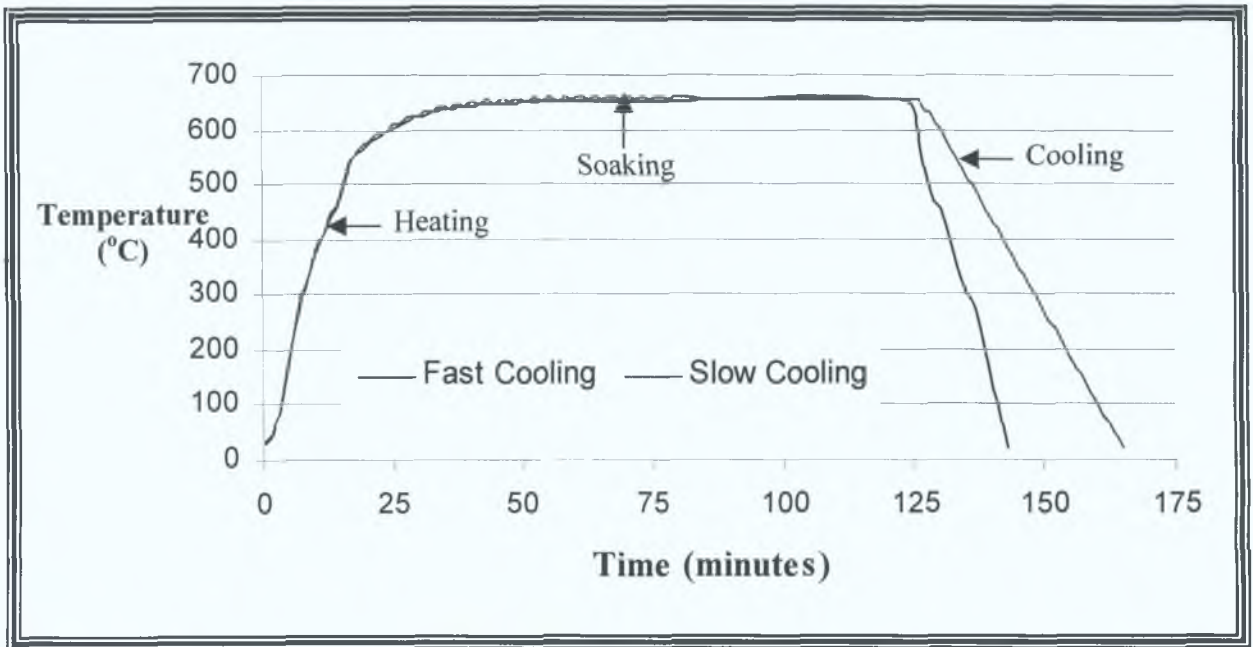


Figure 107, Time-temperature curve showing the post-heat treatment used on the WC-Co samples.

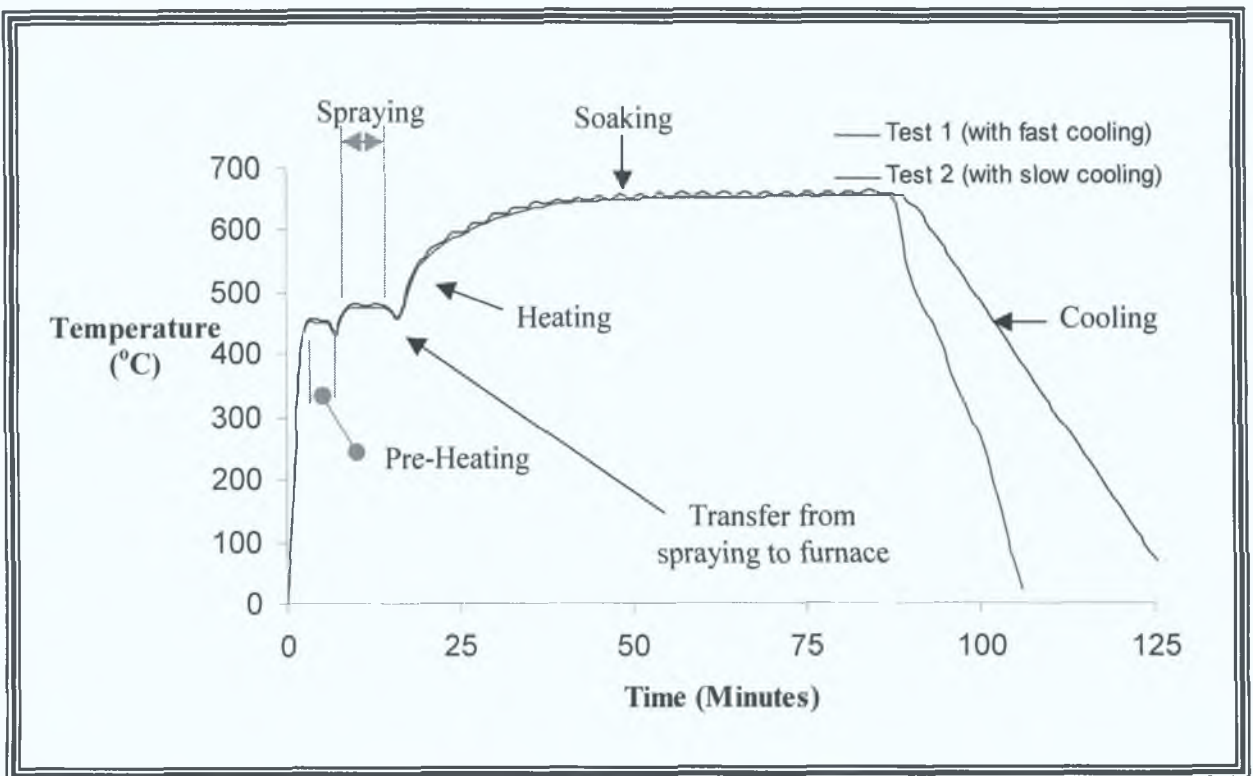


Figure 108, Time-temperature curve showing all three cycles, pre-heat, spraying and post-heat treatment used on the WC-Co samples.

Figure 109 shows the effect of post-heating temperature and soaking time on residual stress respectively. Tests labelled as sample 1 to 5 were carried out in the present research. Tests labelled as Helali and Tan were carried out in their respective research [49,61].

A thermocouple was placed into the furnace, however it was found that when the furnace was set to a temperature of 650°C, the actual temperature of the furnace was measured at 675°C. Therefore, the temperatures used by both Helali [49] and Tan [61] had to be verified.

Samples 1 to 4 were post-heat treated using the time-temperature dependence shown in figure 107. Sample 1 and 2 were post-heat treated at 650°C for 80 and 120mins respectively. The results showed that the sample did not reach a stress free state (residual stress equal to 0MPa) after a time of 80 minutes. The temperature was increased up to 675°C, and two linear results (samples 3 and 4) were measured. The trend in these two results showed that the rate of change in stress had increased. Sample 5 was transferred from its spraying position to the furnace (thermal cycle as shown in figure 108), raised to 675°C for 80 minutes and then allowed to cool slowly in the furnace. The linear result shows that the deposit relaxed and remained in a stress free state without becoming tensile.

Therefore a post-heat temperature of 675°C produced a stress free deposit, however this depended on transferring the sample to the furnace once deposition ceases and allowing for slow cooling rates following post-heat treatment. The cooling stress, which is normally generated when deposition ceases, was eliminated by transferring the deposit to the furnace. In the furnace, the deposit undergoes a tensile stress as the substrate extends. The deposit then relaxes and recovers through the rearrangement of the dislocations in the deposit. The slow cooling rate minimises the any stress generated through the cooling cycle.

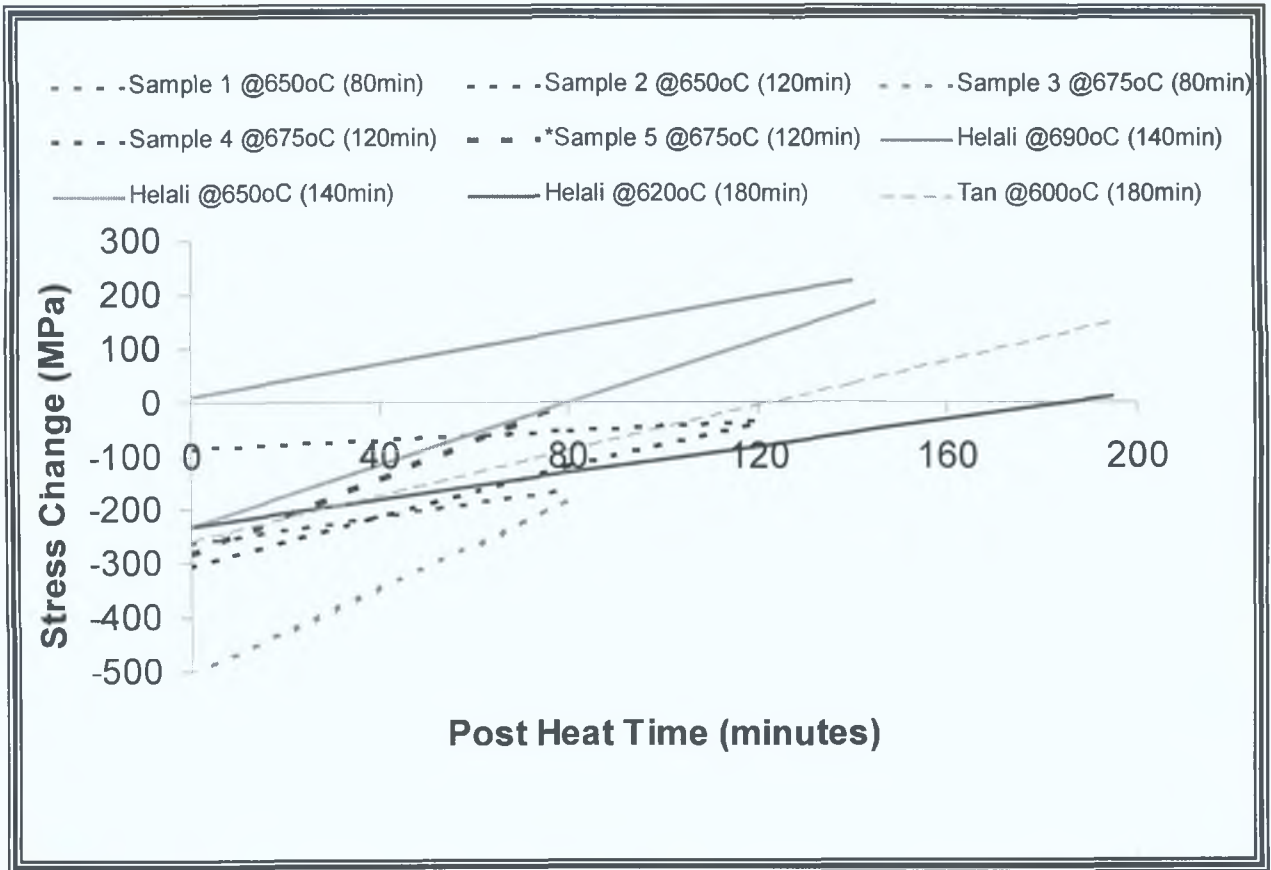


Figure 109, Graph showing the relationship between residual stress and post-heat treatment.

### 5.8.2 Shot Peening Method

Shot peening is intended to induce surface compressive stresses in metal parts [122], to improve the materials resistance to fatigue and stress corrosion cracking [77]. This method was used to reduce the tensile stress at the surface of the WC-Co deposit. Silicon carbide shots impacted the back (substrate) of a 0.2mm thick deposit at 90° at a force of approximately 690N for two minutes. Figure 110 shows that shot peening, reduced the deposit surface stress from 82MPa to 10MPa. Hence a compressive stress of approximately 72MPa was induce onto the deposit surface, as a result of shot peening the back of the sample. The overall stress in the sample was reduced using this technique and the final sample was relatively flat. Extensive research was not carried out in the present investigation, however this area will be recommended as a future study, as this method has been shown to be effective process of reducing residual stress in thermally sprayed components [123,124].

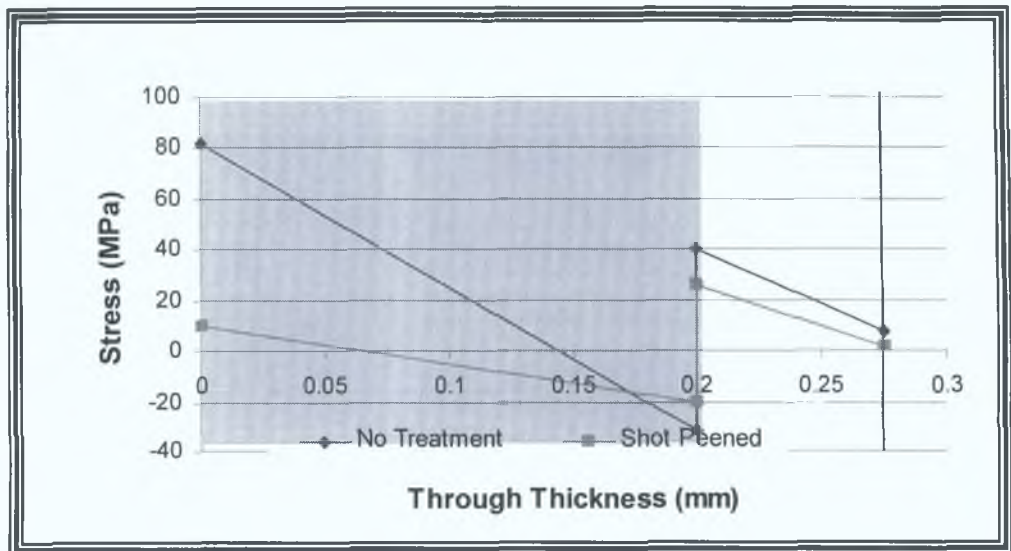


Figure 110, Through thickness residual stress distribution for non-treated and a shot peened sample.

## 5.9 PHASE CHARACTERIZATION

Observing a specimen visually is one of the simplest way of controlling the production quality of thermally sprayed deposits, however the quality of the micrographs is of great importance. The grinding and polishing techniques describe earlier in the study, was used for the WC-Co materials, however often these procedures may vary to achieve a clear image. Examples could be carrying out a fine grinding procedure for a longer duration, or if another material was under investigation, then different abrasives would be used. Figure 111 shows the quality of the micrographs found during the fine grinding techniques. The quality improved slightly when the abrasives P240 to P1200 were used, however the introduction of the polycrystalline diamond abrasives (6, 3 and 1 $\mu$ m) and the acidic colloidal alumina abrasive (0.02 $\mu$ m), accelerated the clarity of the image (further information on these abrasives may be found in my additional report [34]). Microstructural observation of the tungsten carbide-cobalt samples, was enhanced through careful preparation of the material surface.

The XRD analysis was again not carried out in-house, due to the lack of a XRD facility in the university. X-ray diffraction analysis was carried out the tungsten carbide-12wt%cobalt powder material (Diamalloy 2003). The powder was composed of WC, W<sub>2</sub>C with lesser amounts of Co<sub>3</sub>W<sub>3</sub>C phases and elemental W, as shown in figure 112. After spraying the coating contained a high concentration of WC crystals (shown in figure 113 as a dark grey phase under a microscope [125]). Figure 114 (a) and (b) shows the HVOF sprayed WC-Co X-ray diffraction analysis results, where (a) is a sample sprayed with pre-heating the substrate and (b) is a sample sprayed without pre-heat treatment. The results show that pre-heat treatment has no effect on phase formation during spraying. The X-ray analysis shows substantial amounts of WC, W<sub>2</sub>C phase and amounts of subcarbide phases such as Co<sub>3</sub>W<sub>3</sub>C.

After deposition the cobalt exists in an amorphous state according to Nerz, et al. [125], therefore it should recrystallize into various cobalt containing phases, if heated to the right temperature in an argon atmosphere. Figures 115 show the X-ray analysis found

after post-heating the coatings to 690°C and 890°C respectively. The analysis depict the presence of  $\text{Co}_6\text{W}_6\text{C}$  phase in the 650°C post-heated sample (figure 196 (a)), however as post-heat temperature is increased (sample at 890°C), there was an increase in this phase as shown in figure 115 (b). Further recrystallization of cobalt containing phases  $\text{Co}_6\text{W}_6\text{C}$  have been shown to develop with increased post-heat treatment temperatures [125]. According to Stewart, et al. [126], heat treatment of a WC-17%Co deposit in an inert atmosphere above 600°C promoted the formation of the  $\text{Co}_6\text{W}_6\text{C}$  phase from the amorphous phase. Similarly, HVOF sprayed WC-Co has reasonable agreement with deposits produced by powders with higher cobalt levels (such as WC-17%Co) [127]. Increasing post-heat treatment time above the recrystallization temperature increases the wear performance of the material, due to the formation of carbide phases within the deposit [128]. Tungsten monocarbide (WC) and the  $\text{W}_2\text{C}$  phase appears to decrease with increased post-heat temperature. Figure 116 shows the X-ray analysis for a sample post-heat treated at 1350°C. The analysis depict the presence of  $\text{Co}_6\text{W}_6\text{C}$  and lower amounts of WC and  $\text{W}_2\text{C}$  phases. At this temperature the cobalt (binder) is close to its melting temperature, hence the material started to break down and a high amount of oxidation was found at a post heat treatment of 1350°C.

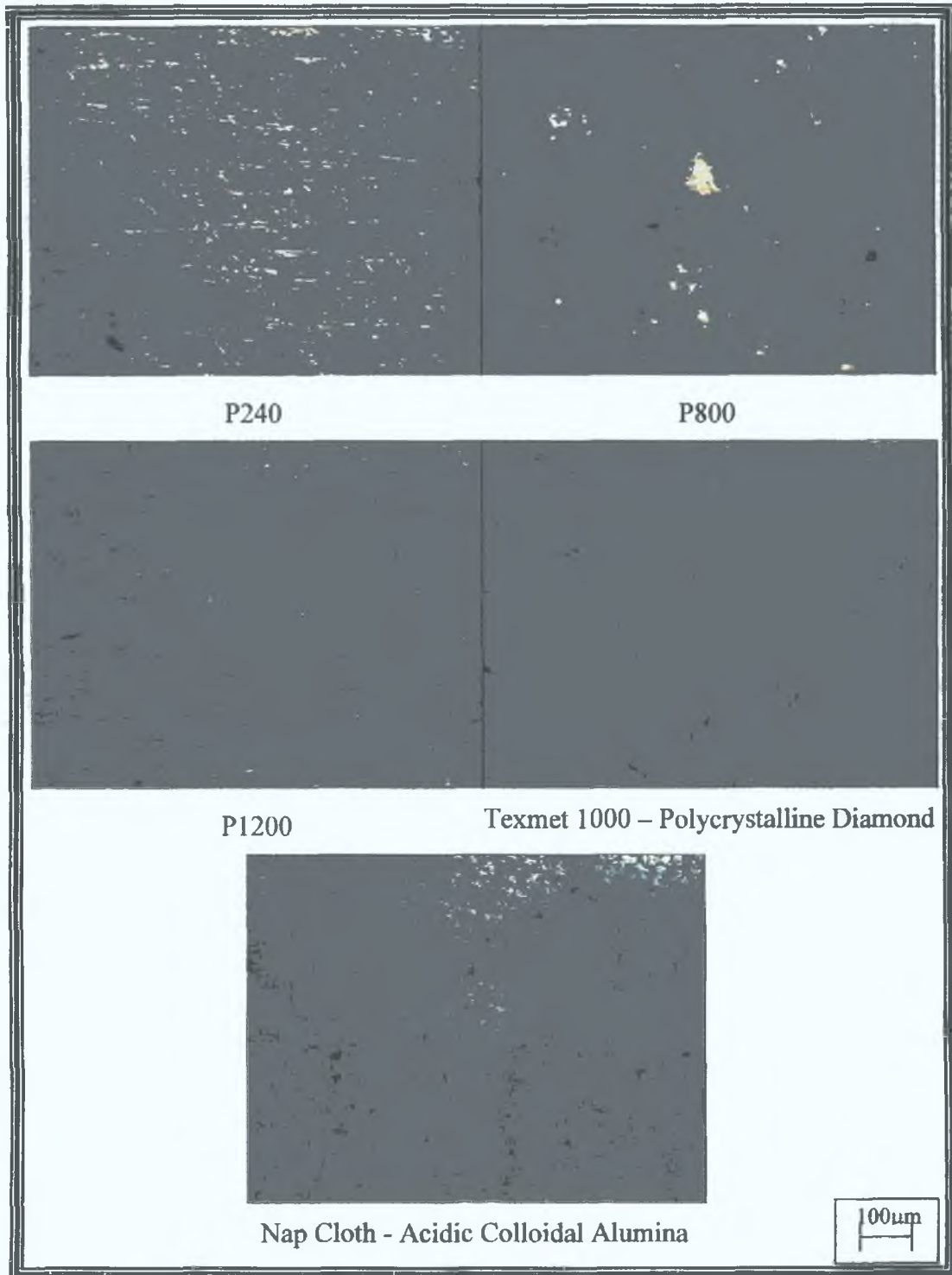


Figure 111, Images of the resulting microstructures after various polishing techniques.

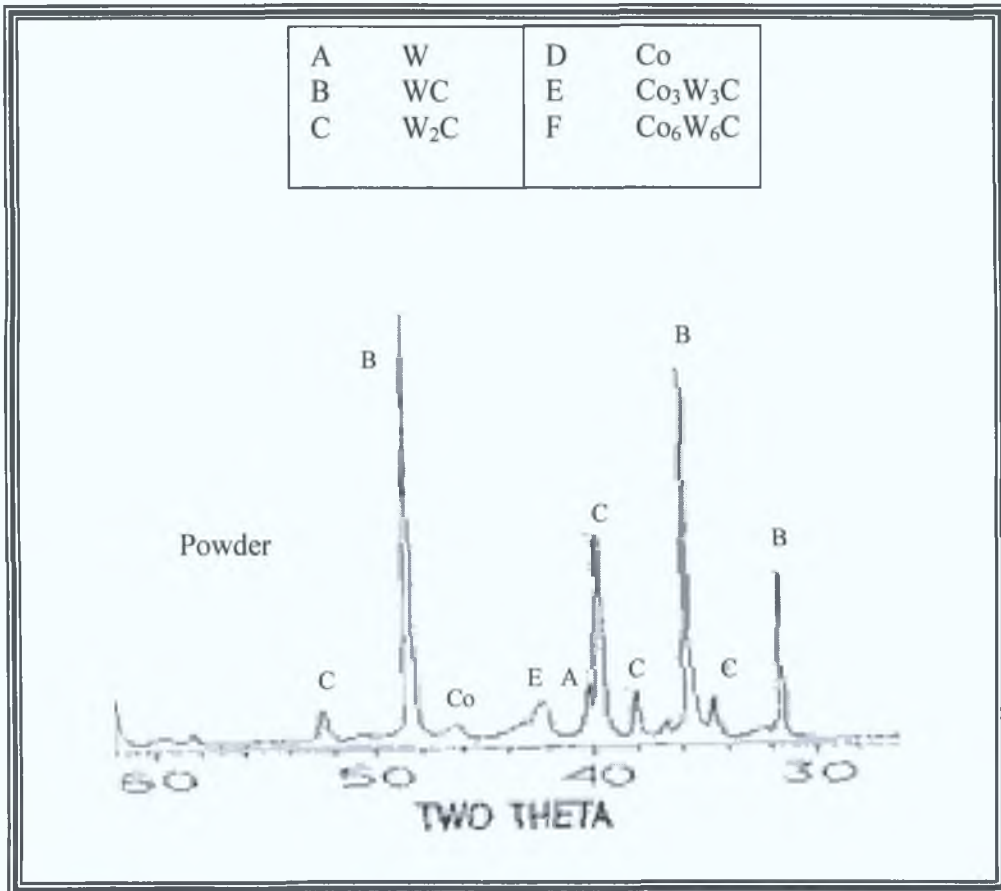


Figure 112, X-ray diffraction pattern for the starting powder Diamalloy 2003 WC-12%Co [125].

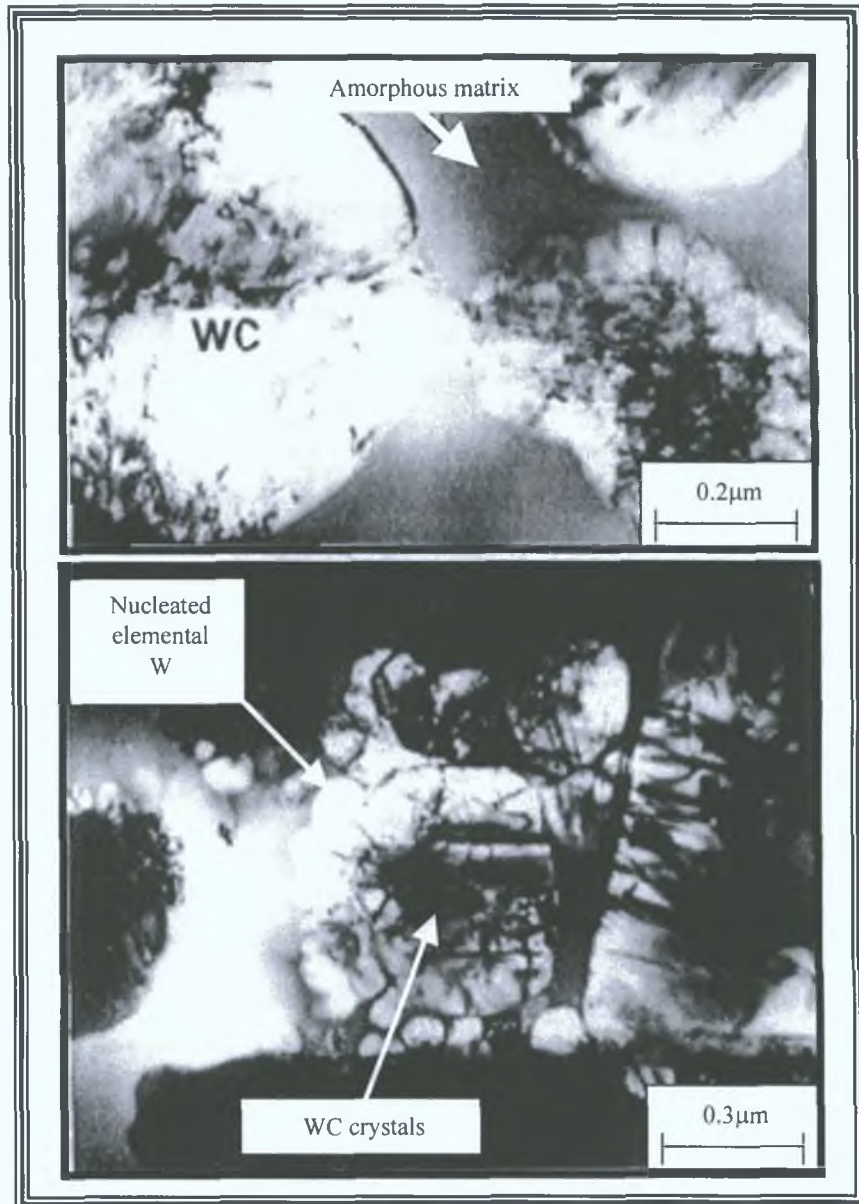


Figure 113, Top image shows crystalline WC particles embedded in an amorphous matrix. Bottom images shows the nucleation of elemental tungsten due to the oxidation during spraying and post-heat treatment, adapted from Nerz et al. [125]

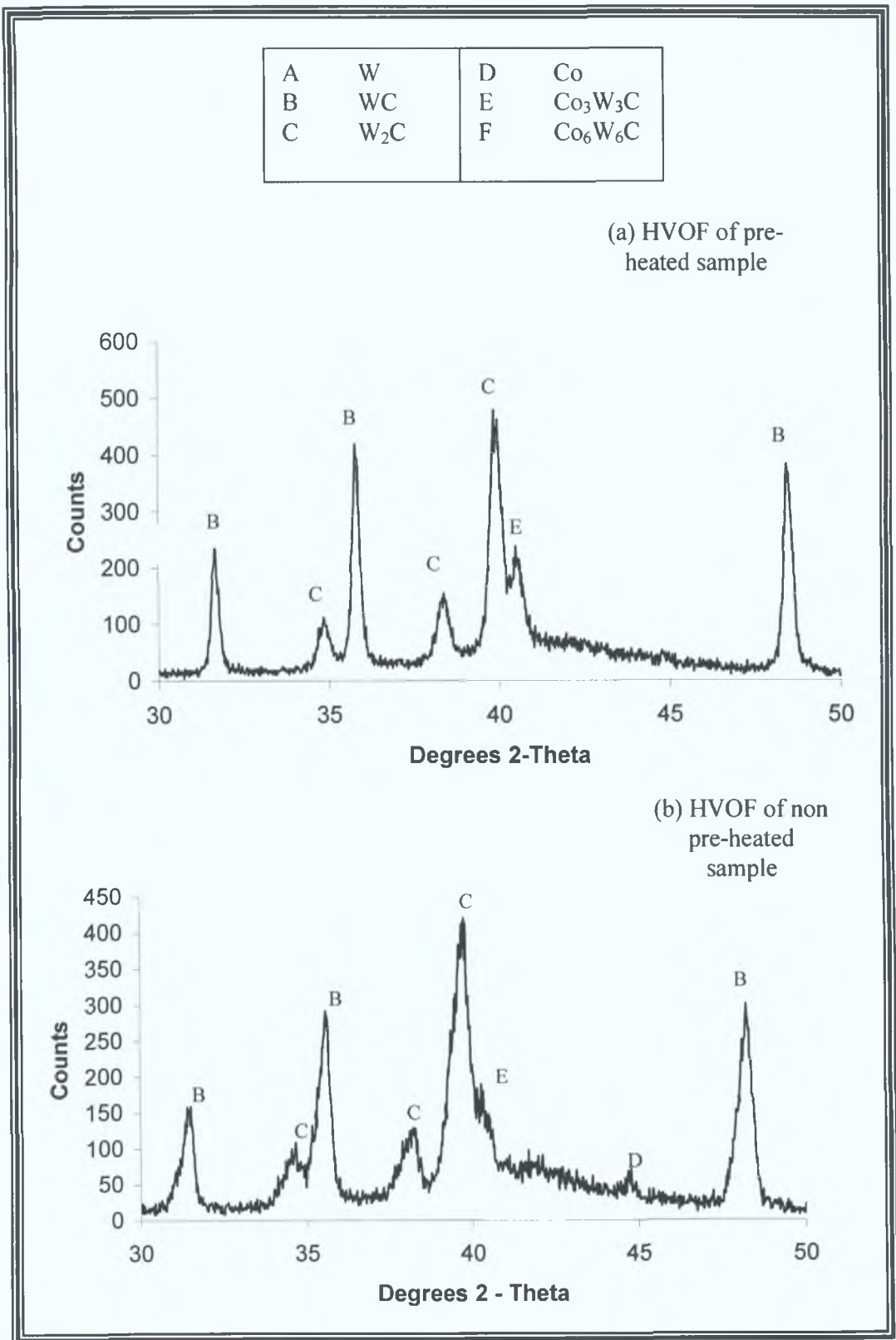


Figure 114, X-ray diffraction patterns for HVOF sprayed WC-12%Co.

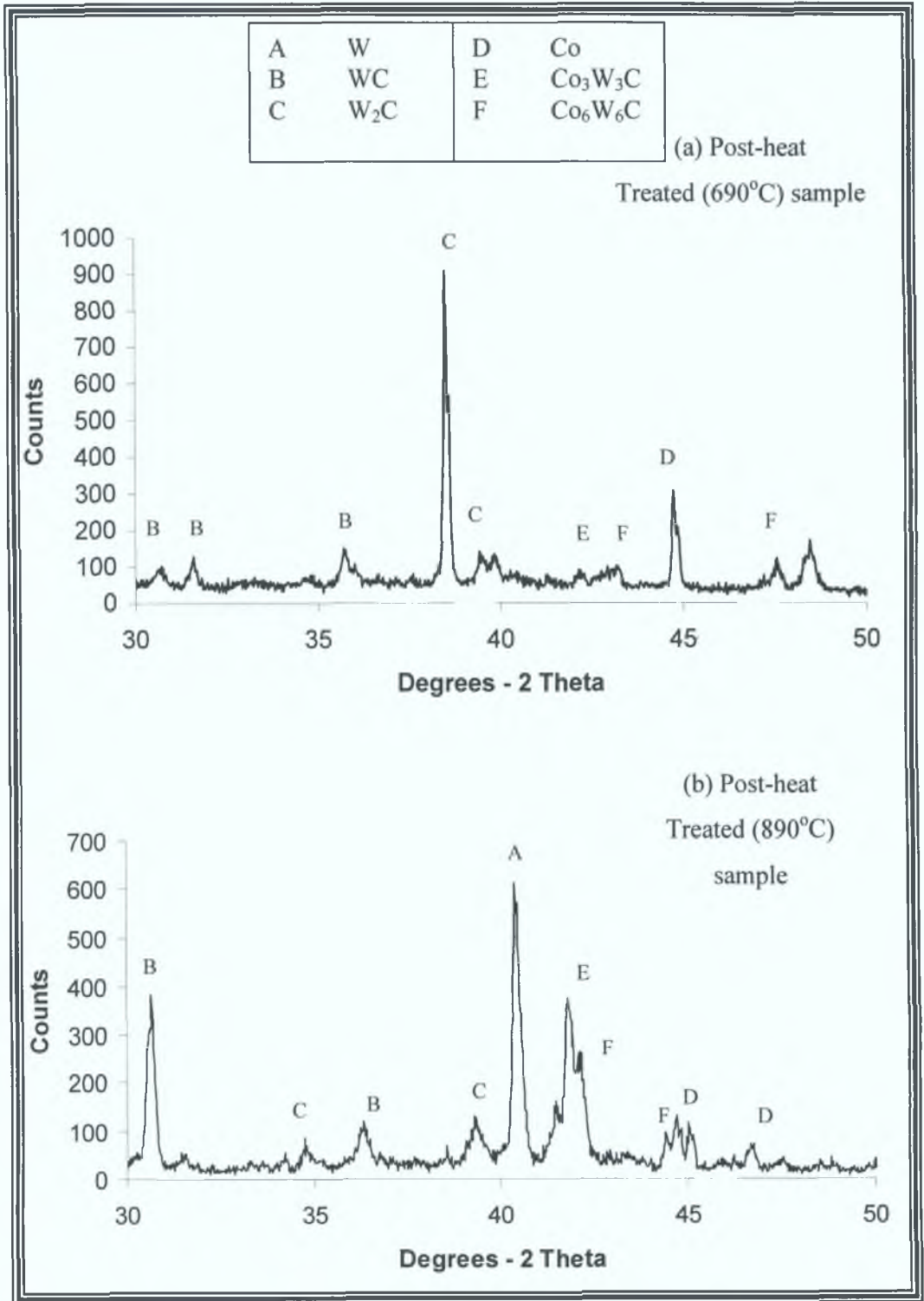


Figure 115, X-ray diffraction patterns for HVOF sprayed Diamalloy 2003 WC-12%Co, post-heated at 690°C and 890°C.

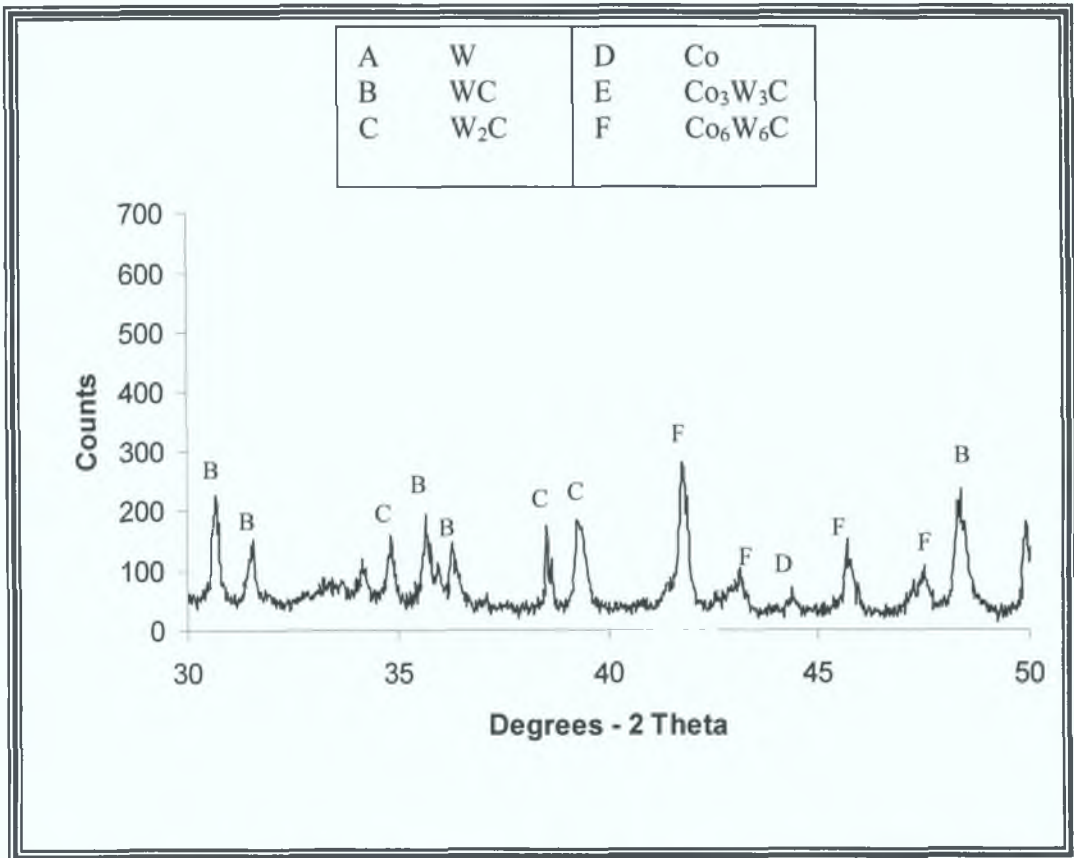


Figure 116, X-ray diffraction patterns for WC-Co coating heat-treated at 1350°C.

## 5.10 HARDNESS MEASUREMENT

The hardness of the WC-Co deposit was measured by the Vickers test method using the Leitz Miniload hardness tester. The load applied was 300 grammes and the indentation was observed using a microscope at a magnitude of 50X. The indentation width was measured and from this the hardness values were determined using equation 31. Various samples were tested for hardness, to measure the effect of WC-Co deposit thickness and post-treatment, on hardness.

Three samples were used to determine the relationship between thickness and hardness. The samples were section and prepared before measurement. Hardness results were measured from a thickness of 1 up to 8mm. Figure 117 shows the individual sample and average hardness relationship with respect to deposit thickness. The maximum and minimum Vickers hardness values found were 1210 and 1148 Hv,0.3 respectively. An average fit line shows that there was little difference between the maximum (1200 Hv,0.3) and the minimum (1157 Hv,0.3) average hardness. The line shows a slight increase in hardness with increased thickness, possibly due to the spraying distance decreasing, hence the particles are impact at higher velocities as the thickness increases, increasing the hardness [129]. However, the difference in results was considered slight (on average  $\pm 10\text{Hv}$ ), when considering the difference in diagonal distances and often inaccuracies associated with hardness tests are contributed to the number of tests carried out [130,131].

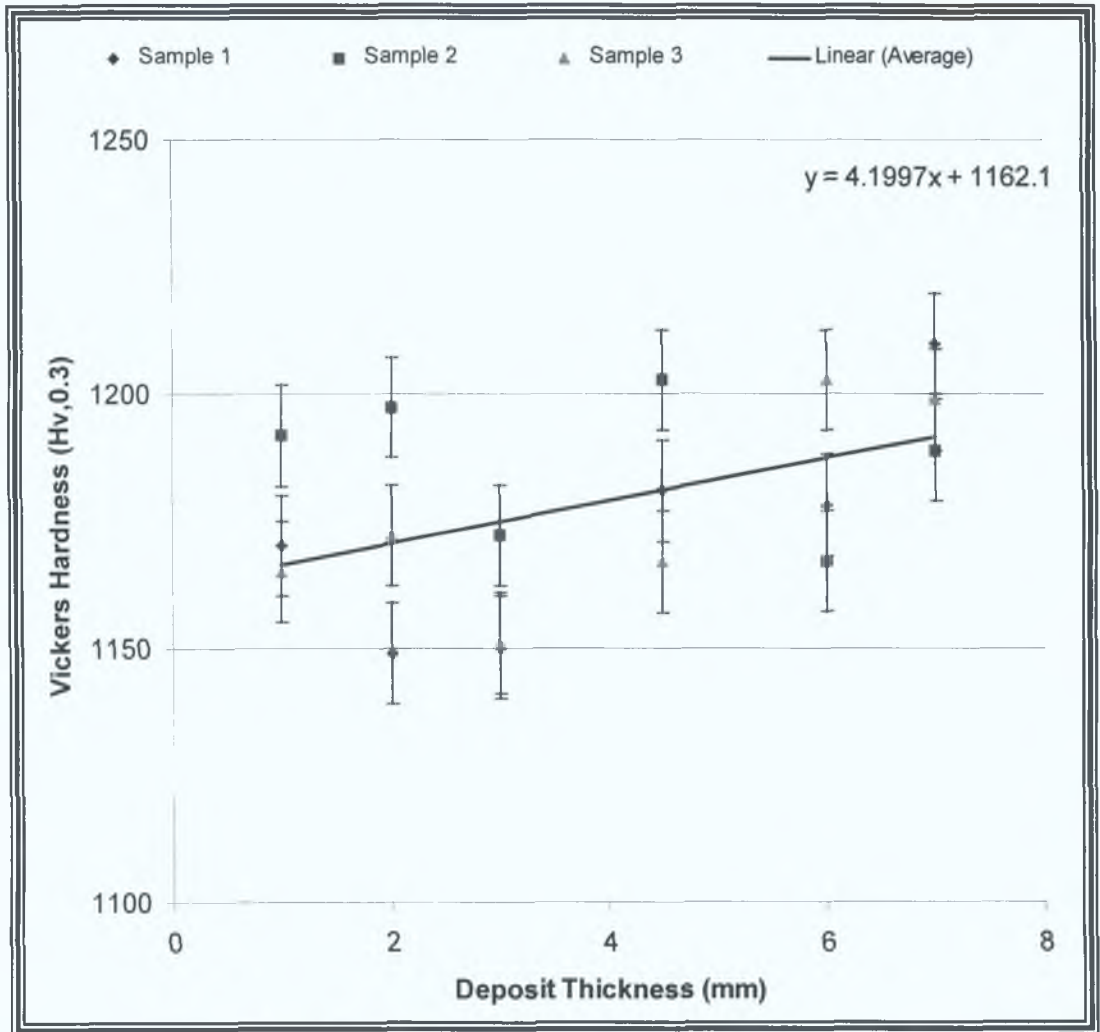


Figure 117, The variation hardness with deposit thickness.

The samples post-heat treated at 690, 890 and 1320°C using the Lenton Eurotherm Controller 902P were tested for hardness. The results are presented in figure 118. The hardness increased from a non-treated value of 1167 to 1215 Hv,0.3, when the sample was subjected to 690°C. According to [132,133], increasing post-heat treatment time above the recrystallization temperature increases the wear performance and increases hardness, due to the formation of the new carbide phases. Similarly, an increase was observed for the 890 (1230 Hv,0.3) and 1320°C (1245 Hv,0.3) post heat treatments, however the rate of increase was not as high as that found for the 690°C post-heat

treatment. This change in increased hardness was associated to the type of carbide phases formed during each of these treatments [125].

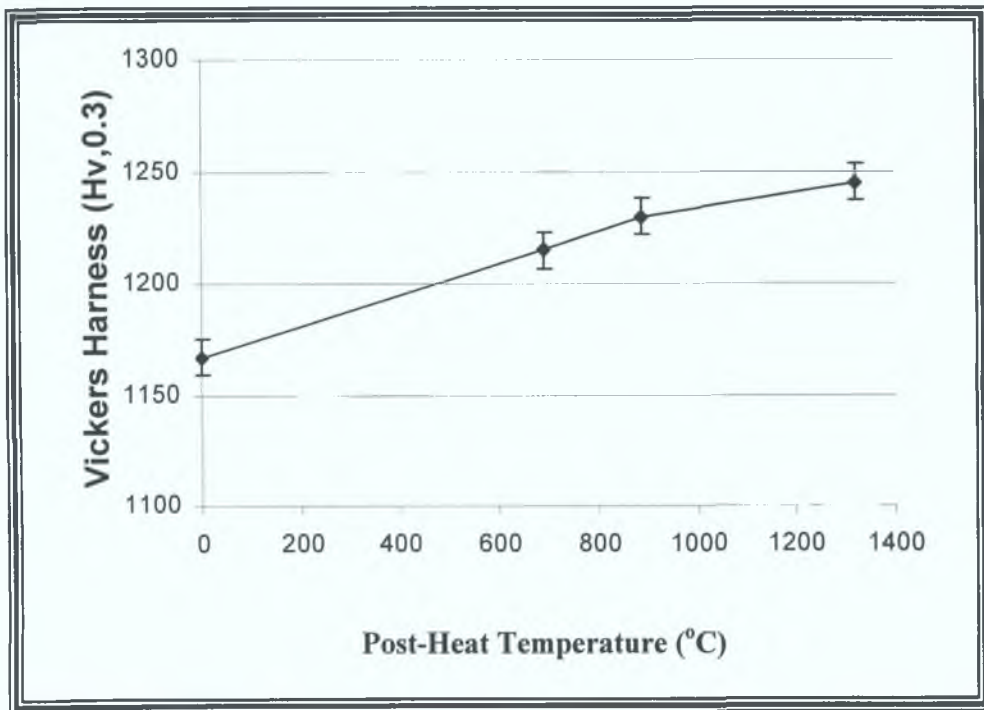


Figure 118, Relationship of hardness on post heat temperature.

### 5.11 POROSITY MEASUREMENT

The 'Reichert MEF2 Optical Microscope' and the Buehler Omnimet image analysis system, was used to determine porosity values in the Materials Processing Research Centre. Various coated samples were sectioned, ground and polished to reveal the coating microstructure. Three samples were used to determine the relationship between deposit thickness and porosity as shown in figure 119. An average fit line was applied to the results, which showed that the porosity decreased with increased deposit thickness from 0.83 to 0.3%. This decrease was associated to the change in spraying distance while deposition took place, that is as the thickness increased the distance between the DJ gun's outlet and the deposit surface decreased. Decreasing the spraying distance increases particle speeds on impact and deposition temperature, therefore closing more voids in the microstructure.

The preparation of the samples used for porosity testing often smear debris material into the voids (usually associated to softer materials, generally not a concern for WC-Co materials). All of the samples used in the test shown in figure 119, were prepared together, so as similar amount of errors would be compared. Results varied as little as  $\pm 0.09\%$ .

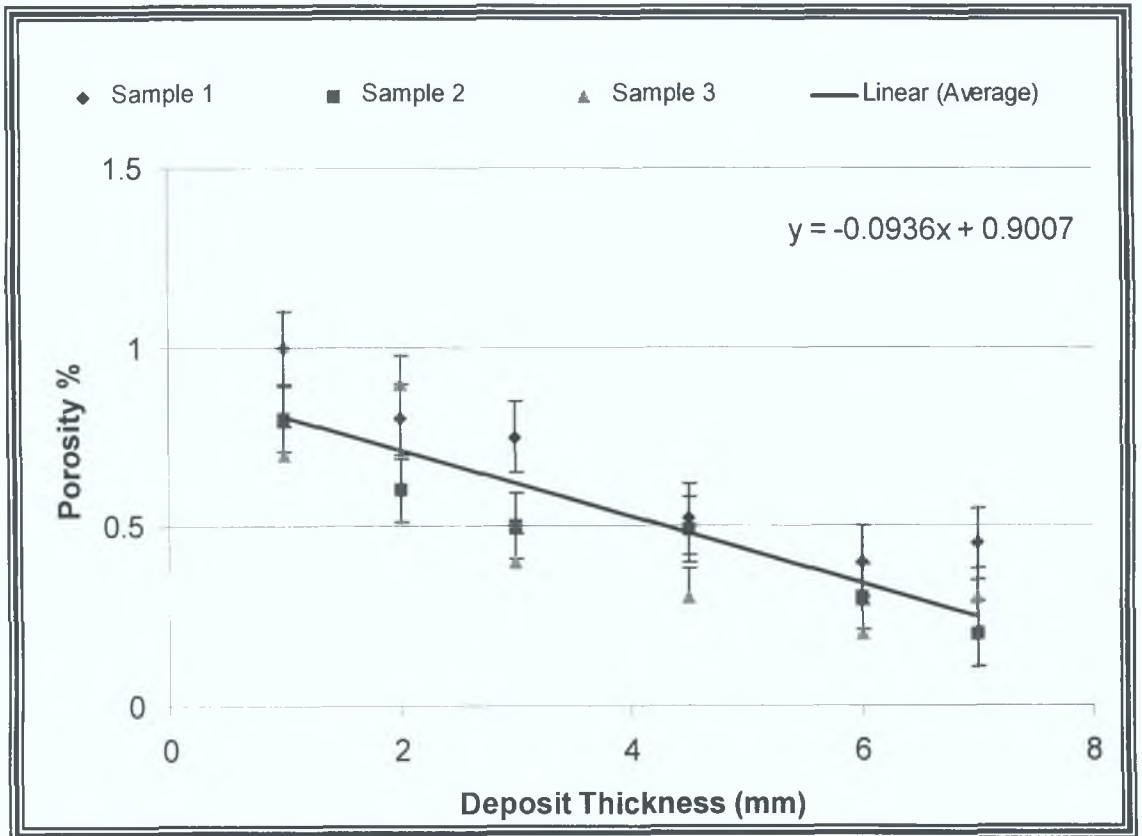


Figure 119, Relationship of porosity on deposit thickness.

## 5.12 THE FABRICATION OF SPRAY-FORMED ENGINEERING COMPONENTS

The following section describes the spray-forming of various tungsten carbide-cobalt engineering components (cylindrical components and tensile specimens) using the HVOF process.

### 5.12.1 Forming Die Design

The measures taken to reduce residual stress and therefore optimise component thickness were successful. The use of CO<sub>2</sub> cooling has reduced residual stress within the deposit. Aluminium was introduced as a releasing layer, positioned between the tungsten carbide-cobalt deposit and the stainless steel forming die. Initially a residual stress test was carried out to investigate how the aluminium material would perform as a substrate / supporting material. Table 14 shows the results found where a 0.075mm thick aluminium substrate was coated with WC-Co and its stress compared to that of a similar sized coated stainless steel. The observation was that the aluminium substrate generated higher residual stresses in the deposit. The increase is on average 10% and is based on the material properties of the aluminium material. The thermal expansion coefficient of the aluminium material (23.6 °C<sup>-1</sup>[109]) is higher than that of the stainless steel, hence the quenching stresses increase to a higher extent than those of the cooling stresses, resulting in a higher tensile residual stress in the deposit.

Table 14, The effect of changing the substrate material on stress.

Stress (MPa)	Deposit Thickness 0.2mm Substrate Thickness 0.075mm	
	Stainless Steel Substrate	Aluminium Substrate
Top of Deposit	+82MPa	+90MPa
Deposit Interface	-32MPa	-42MPa
Substrate Interface	+40MPa	50MPa
Bottom of Substrate	+8MPa	25MPa
Change Across Deposit from the top to the interface	-114MPa	-132MPa
Positive (+) = Tensile Stress Negative (-) = Compressive Stress		

The objective was to produce free-standing spray-formed cylindrical components. The dimensions of the cylindrical component (12mm diameter with varying thickness) was decided on due to the results found in figure 103, where minimising the width and length of a coated sample produced lower residual stress.

The forming die made of three plates (with two 12mm diameter holes in two of the plates as previously described) was pre-heated to 475°C. After pre-heating, spraying of the components was carried out at 500°C with forced cooling. Release of the spray-formed components became more difficult as the forming thickness increased. Table 15, describes the effects of using this forming procedure, in the production of engineering components. Aluminium sprayed onto cylindrical forming cores enabled the release of WC-Co cylindrical thin-shelled components [49]. However, this method of applying the layer into a forming die proved difficult, as the spray area was small and the aluminium deposit heaped at the corner edges of the forming die and only small amounts of aluminium adhered to the horizontal internal sides of the die. A schematic

diagram of this is shown in figure 120. The resulting components had curved corners and proved impossible to release from the die due to the adhesion of the WC-Co deposit to the internal sides of the die.

Table 15, Effect of different releasing layer techniques on the formation of thick components.

Releasing Layer Type	Comment
Aluminium deposited by HVOF system	<ul style="list-style-type: none"> <li>▪ Found uneven deposition within the forming die</li> <li>▪ Difficulty in removing WC-Co deposit</li> </ul>
Aluminium foil	<ul style="list-style-type: none"> <li>▪ Foils of 75<math>\mu</math>m and less, caused the foil to peel away during deposition</li> <li>▪ Foils of 125<math>\mu</math>m and greater posed problems during releasing</li> <li>▪ Foil of 100<math>\mu</math>m proved the best releasing layer thickness needed to fabricated components</li> </ul>
Other Comments	<ul style="list-style-type: none"> <li>▪ Forming die posed releasing problems at higher thicknesses</li> </ul>
Pre-heat treatment carried out at 450°C Spraying carried out at 200mm and a powder feed rate of 38g/min, with forced cooling Spraying temperature 500°C Post-heat treatment at 675°C for 80 minutes	

Another method of releasing the components was introduced, using aluminium foil. Aluminium foils provided a more effective method to aid the release of deposited components. However, the foil had to be applied carefully inside the internal walls of the die. Initially foils of 75 $\mu$ m were used, however the gun's flame peeled the foil away during pre-heat treatment. Foils of thicknesses 125 $\mu$ m and greater were used, however it proved difficult to remove the layer after post-heat treatment. Foil thicknesses of 100 $\mu$ m proved the most successful. Figure 121 shows examples of a 2.5 and a 5mm thick-formed component. One problem encountered was the 'humped' profile, which is

characteristic of thermal sprayed coatings. Difficulties were experienced in removing the components from the forming die, successfully removed components were damaged (scored) down along their sides (difficult to separate from the side walls of the die). The forming plate was split across its face to aid the release of thick WC-Co components and proved successful.

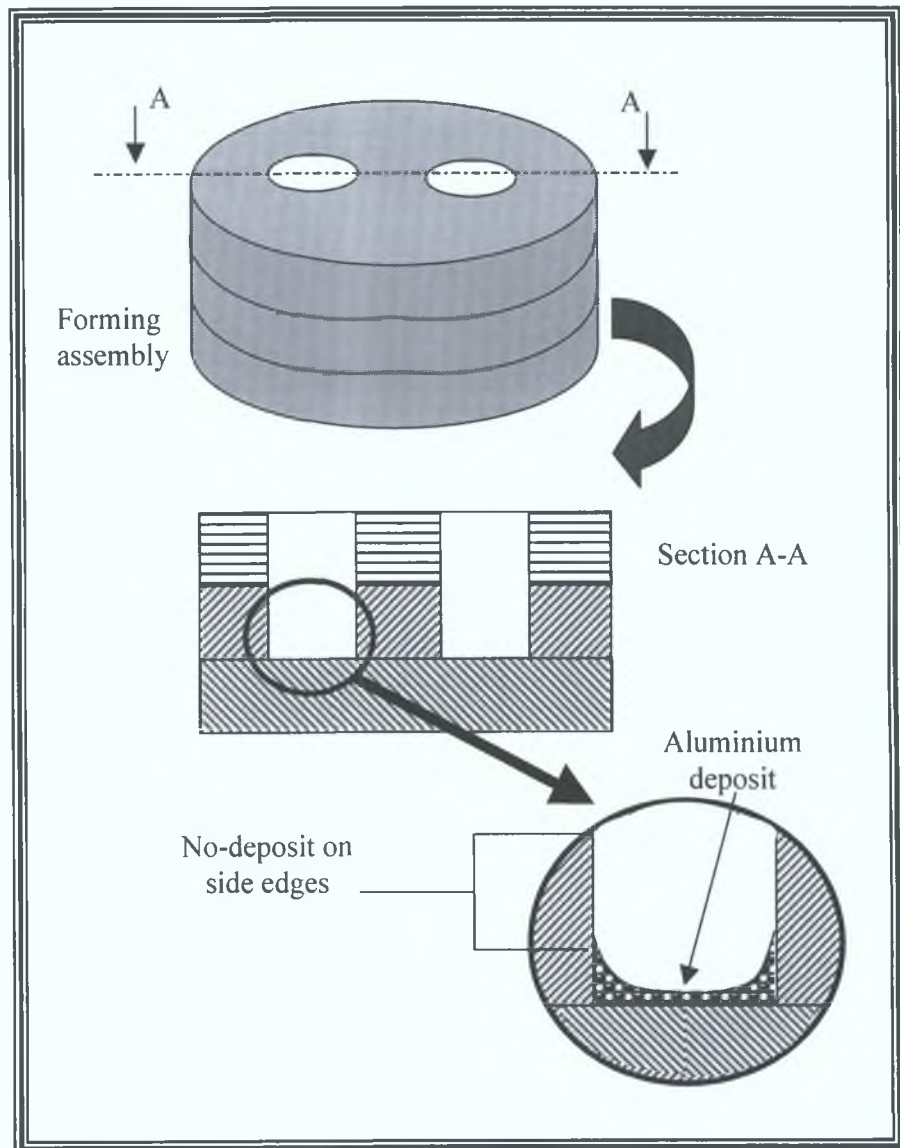


Figure 120, Schematic of uneven distribution of the as-sprayed aluminium releasing layer.

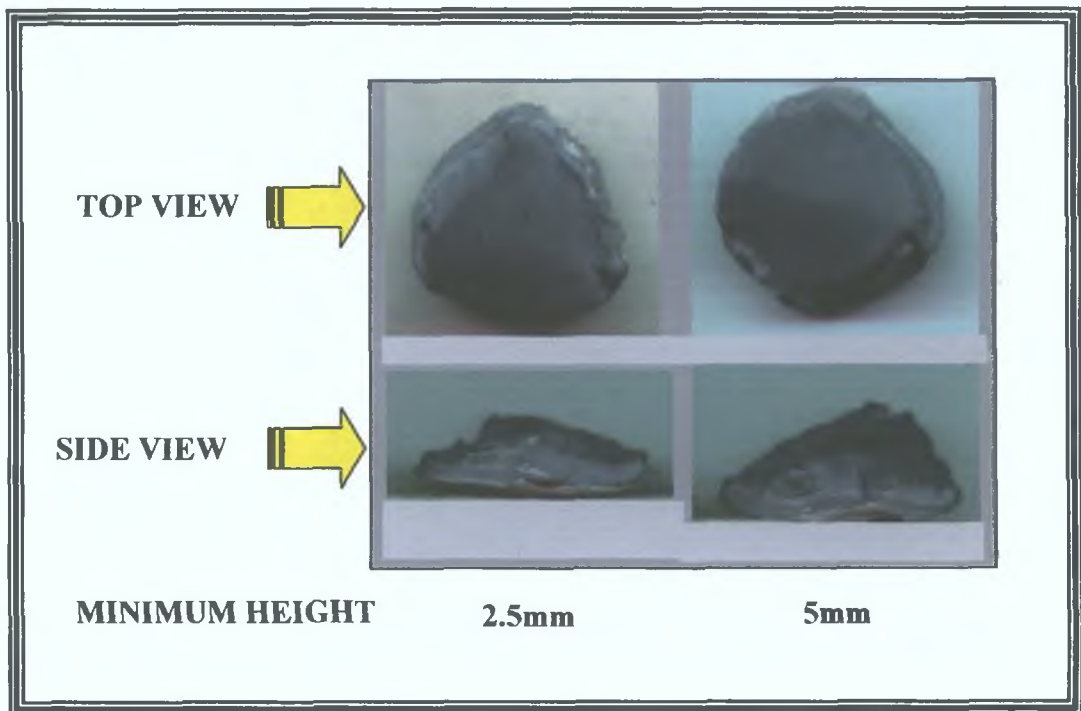


Figure 121, Thick WC-Co spray formed components, deposited before the split die technique was used.

### 5.12.2 Production Of Thick-Formed Components

The formation of thicker free-standing cylindrical components was made possible with the use of the carbon dioxide cooling system and the linear traverse unit. WC-Co cylindrical components of 12mm diameter were spray-formed, at various thicknesses (1, 2.5, 5, 8 and 9mm). In each case four samples were produced at each thickness. In figure 122, a 9mm thick WC-Co component was spray-formed to a higher thickness (approximately 12.2mm), thereafter grinding and polishing reduced the hump effect, leaving the component shown. The split die caused relatively no scoring to the sides of the component. Higher forming thicknesses (>12.2mm) were deposited, however overheating caused to components to crack and fail.

The measured flame temperature rise whilst forming was minimal, (maximum increase of 30°C for the 9mm thick component). This is seen to be particularly stable when the duration of spraying is taken into consideration (the 9mm component was sprayed over a period of 15 minutes). It is obvious that crack formation within the formed components, which is a result of residual stress build up whilst spraying, was prevented with the use of the carbon dioxide cooling system. Once the desired coating thickness was achieved, the components were post-heat treated.



Figure 122, Free-standing WC-Co spray-formed components.

### 5.12.3 Tensile Specimen

The tensile specimen was fabricated using a similar method to that used to fabricate the cylindrical components. The residual stress within the specimen was predicted using the finite element technique and finally using the specimens the stiffness of the tungsten carbide-cobalt material was determined.

#### (1) Fabrication

The spray-forming method was used, to attempt to produce a free-standing tensile specimen, with the aim of determining a Young's modulus value for thermally sprayed tungsten carbide-12%cobalt, without the influence of an attached substrate.

Deposition of the tensile specimen was unsuccessful in most cases, as the length of the specimen was subjected to a high amount of bending during deposition. Removal of the specimens proved troublesome, even when a split die was used (figure 123), due to the complex shape of the die. Similarly the shape created difficulty during the masking of the internal sides of the die with the aluminium foil. Figure 124 shows various unsuccessful tensile components produced to various forming thicknesses. Specimen thicknesses of 1mm and lower fractured during separation, whereas thicknesses greater than 1.3mm fractured during deposition. Two specimens were produced at a thickness of 1.2mm, however the thickness required by the standards ASTM E8M-96 [74], ASTM B823-93 [99] and MPIF [100], is given as between 3.56 and 6.35mm. The two specimens showed little bending, with a deflection of approximately 3mm in its centre.

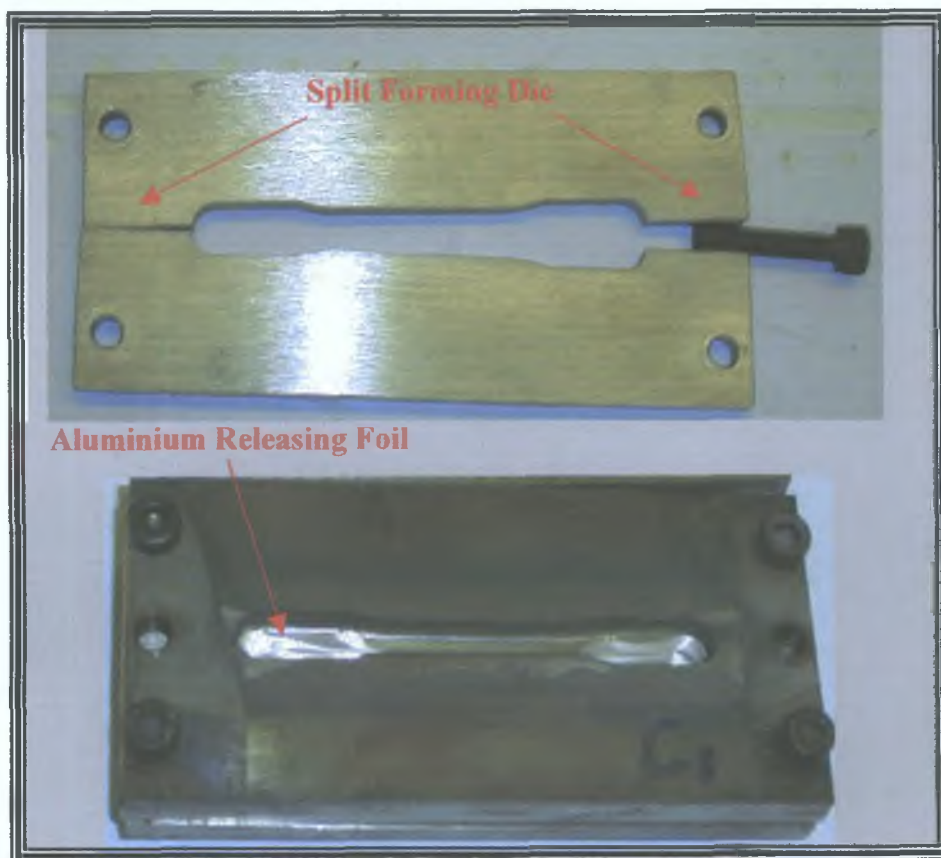


Figure 123, Split tensile forming die and the location of the releasing layer.

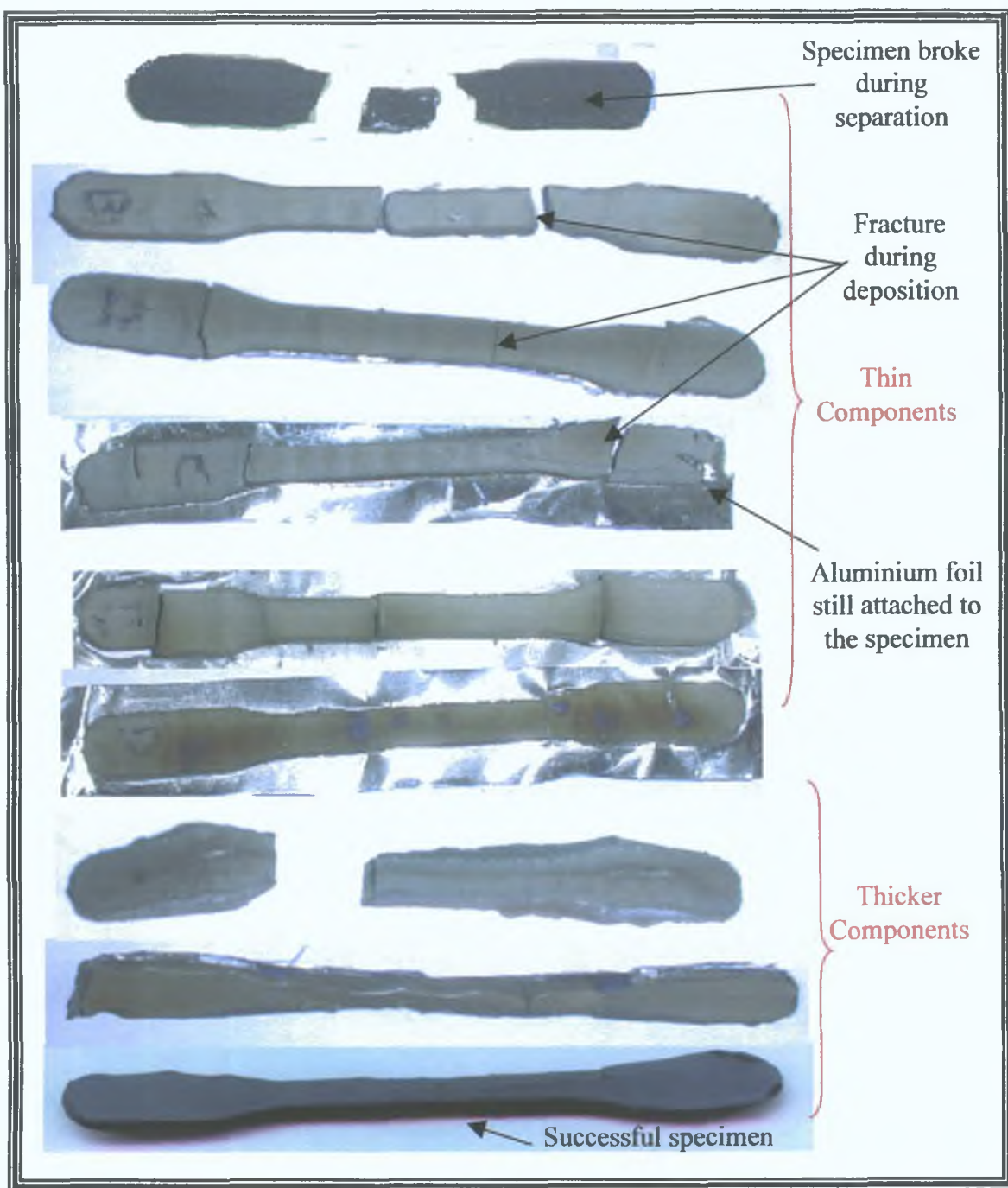


Figure 124, Thermally sprayed tensile specimens.

## (2) Finite Element Analysis

The residual stress within the tensile deposit (1.2mm thick) was simulated using the generated moment finite element technique only, as the thermal load required the system to be a bimetallic beam. The contact with the sides of the forming die effect was taken into account, as this proved to be a difficulty in the fabrication process. The centre of the tensile specimen was displaced by 3mm (deflection measured from the experimental data). Figure 125 shows the finite element solution, where the maximum residual stress was found at the centre due to bending, and at the grip locations, as the edges were restricted by the sides of the forming die. Figure 103 shows that deposits below a residual stress of 80MPa were produced before failure. According to the analysis, the maximum tensile stress was given as 55.786MPa at the components centre (top surface), and similarly the minimum compressive stress was 7.969MPa at the centre (bottom surface). The stress change through the centre of the finite element component was calculated as -63.755MPa, suggesting that this component could avoid failure. In previous tests where the finite element analysis was compared to the experimental data, the generated moment system underestimated the stresses in the deposit by on average 5%. Hence the maximum residual stress in the tensile specimen could be estimated as 58.58MPa.

## (3) Tensile Test

The two successful tensile specimens were post heat-treated to remove the releasing layer and to reduce the residual stress within the deposit. The deflection reduced to approximately 1.5mm, hence care was taken not to fracture the sample during testing. The samples were then tensile tested using the Houndsfield tensile tester at the lowest rate of  $0.54\text{mm}\cdot\text{min}^{-1}$  using a 20kN load cell. The applied force and displacement during the test was imported into a Microsoft Excel file. The stress-strain relationships was found by manipulating the data, including the cross-sectional area of the sample and the gauge length. The results are shown in figure 126. A linear fit was made and the Young's moduli found for each sample were 190.42 and 187.92GPa. The average stiffness of the material was calculated as approximately 189GPa, which is in good

agreement with the result reported by Tucker [134], where a stiffness of 190GPa was measured for a tungsten carbide-cobalt free standing ring tested under tension. The stiffness differs from the result found using the cantilever test (184.9GPa), however the stiffness found in the current section was post-heat treated before testing, whereas the cantilever stiffness result was a tested as-sprayed. The yield strength of the material was measured as 65MPa. Errors in the results are in the order of  $\pm 3$ MPa, however the samples initial had a slight deflection, which would cause undesirable stresses to be applied to the sample during clamping. Slippage in the clamps may also have occurred.

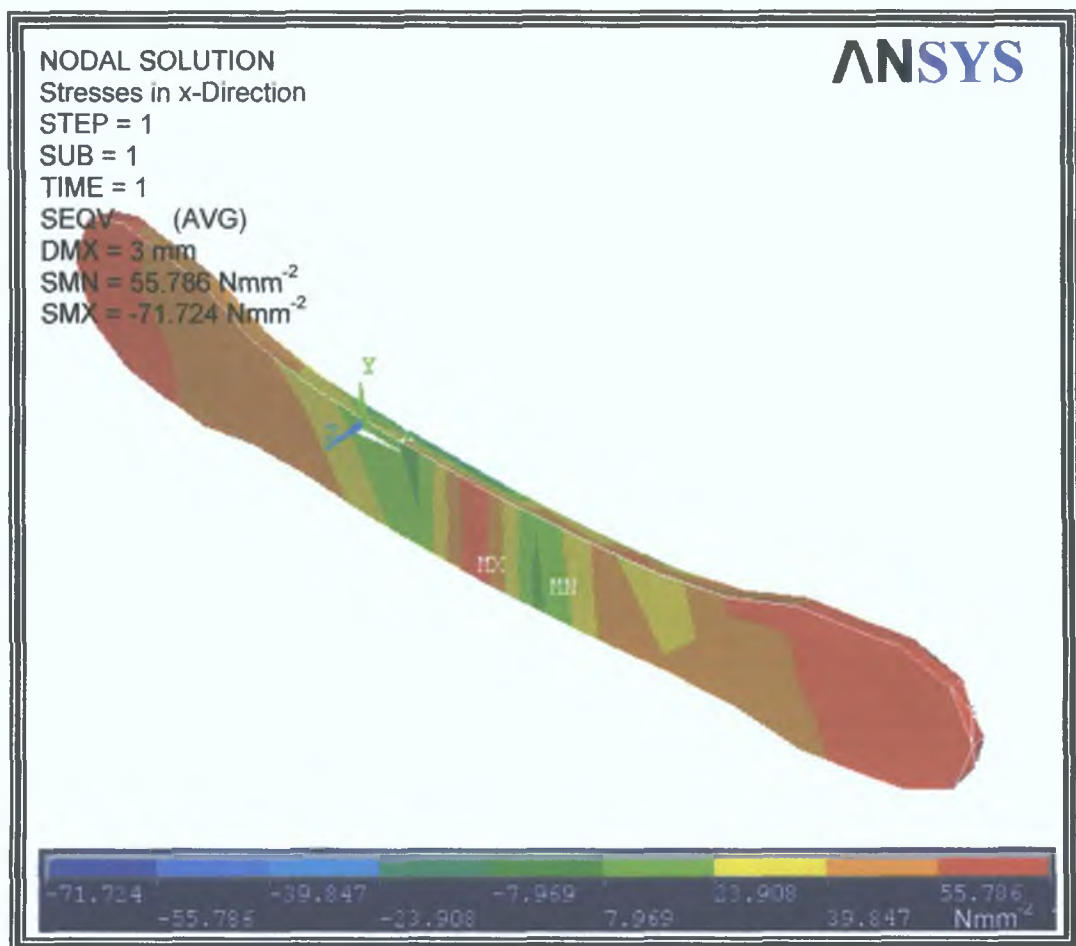


Figure 125, Finite element result for the tensile specimen.

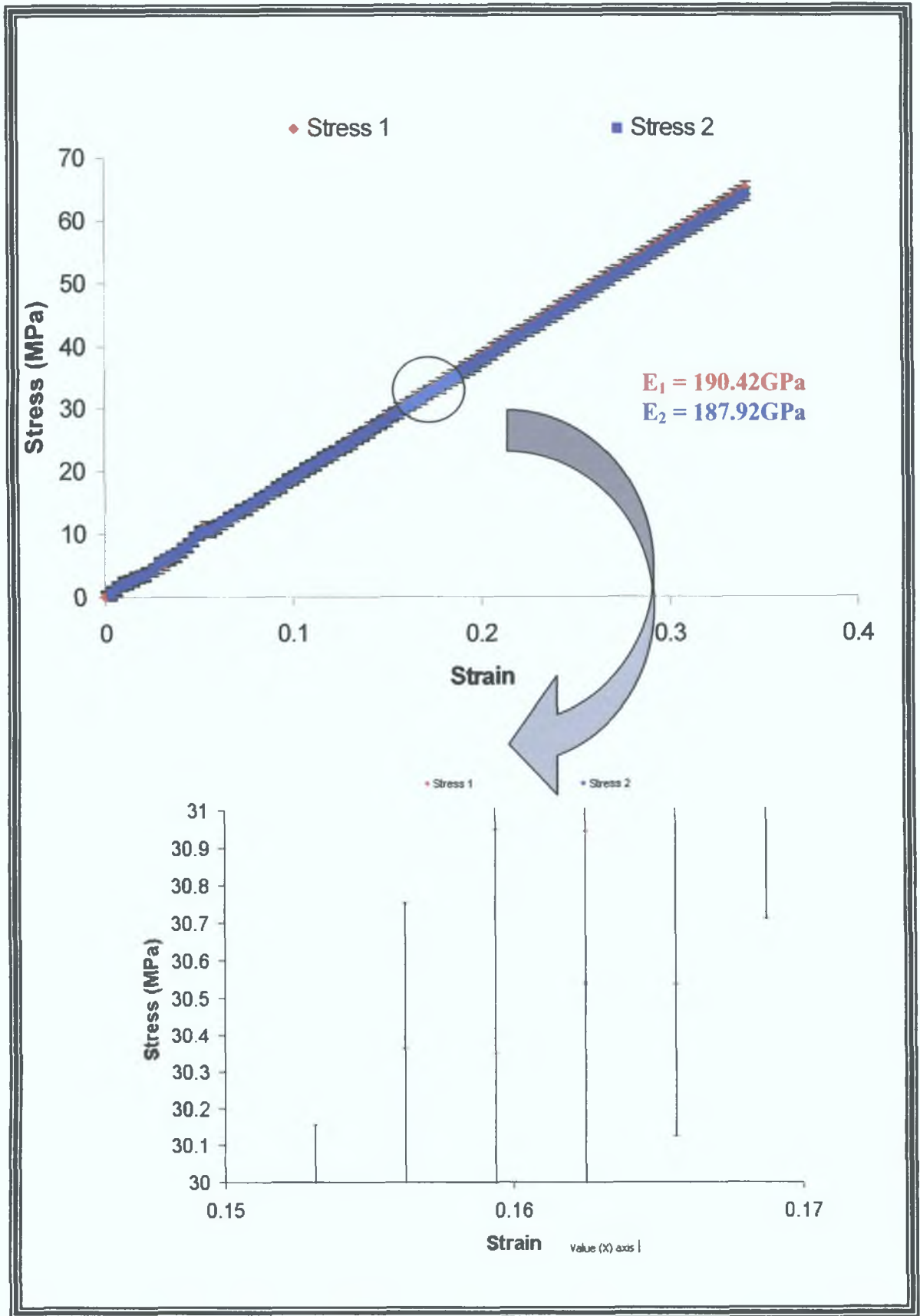


Figure 126, Tensile stress strain curve for the sprayed WC-Co material.

### 5.13 COST ANALYSIS

The cost of producing the components formed within the research is just as an important assessment as measuring various mechanical and chemical properties. Capital costs are usually the initial concern of the manufacturer and sometimes the dominant concern. Production volume may prove worthy assessments, however operating and material costs often prove to be the major contributor of the overall cost of a production process [135,136]. An analysis of the cost involved in producing the 12mm diameter, 9mm thick free-standing engineering components using the HVOF process is addressed in this section.

The cost of forming a component using the HVOF thermal spraying process includes the following items:

- I. Cost of forming die material.
- II. Machining of the forming die.
- III. Cost of the releasing layer material.
- IV. Cost of using the HVOF process.
  - (a) Cost of pre-heating the forming die.
  - (b) Cost of the tungsten carbide-cobalt powder material.
  - (c) Cost of spraying the component.
- V. Cost of post-heat treating.
- VI. Cost of final finishing.
- VII. Labour and overheads.

#### Cost of items I and II:

The material for the stainless steel forming die was bought for 15 Euro (cost includes VAT), and two hours of machining (grinding and milling) would accumulate to approximately 10 Euro (excluding labour). The die was used repeatedly, therefore the cost of the forming die is not a significant factor compared to other costs. Labour costs vary from worker to worker (and country to country), however even if the cost of labour

is a contributing factor to the cost in producing the die, the cost has been excluded in this survey.

Cost of item III:

The amount of material used as a releasing layer was approximately 0.35 grams (volume of 130mm<sup>3</sup>), costing 5.12 Euro (cost includes VAT).

Cost of item IV:

The cost of using the HVOF process is broken into the cost of the various gases (oxygen, propylene, nitrogen, compressed air and the carbon dioxide liquid cooling).

The purchasing cost of four oxygen tanks is approximately 150 Euro. Each tank holds 50 litres and the maximum oxygen flow rate for the HVOF process is approximately 32 litres per hour [137,138]. Therefore the cost of using oxygen is approximately 24 Euro per hour.

The purchasing cost of three propylene tanks is approximately 530 Euro. Each tank holds 40 litres and the maximum propylene flow rate is approximately 7 litres per hour [137,138]. The cost of using propylene is approximately 31 Euro per hour.

The purchasing cost of a single tank of nitrogen is approximately 40 Euro. The tank holds 50 litres and the maximum nitrogen flow rate is approximately 4 litres per hour [137,138]. The cost of using nitrogen is approximately 3.2 Euro per hour.

The cost of producing the compressed air is mainly attributed to electricity costs. The total electricity cost is assumed to be 2 Euro per hour.

The purchasing cost of a single tank of CO<sub>2</sub> is approximately 155 Euro. The tank holds 200 litres and the maximum flow rate is approximately 40 litres per hour [137,138]. Therefore the cost of using propylene is approximately 31 Euro per hour.

The total cost (excluding powder material costs) for the HVOF is therefore 91.2 Euro per hour (cost includes VAT).

Cost of item (a):

For pre-heating, the HVOF spray gun was used and the time taken to raise the forming die to the pre-heating temperature took approximately four minutes. The cost based on the last section would then be 8 Euro.

Cost of item (b):

After fabrication, the weight of the component should be approximately 12.7 grams. Assuming a target efficiency of about 60% (as some of the powder material is lost during spraying, due to over spray) and a deposition efficiency of 70% [31] (some of the powder material fails to deposit), the powder material required to form this component is approximately 40 grams. The cost of 1kg of tungsten carbide - 12%wt cobalt (Diamalloy 2003) powder material is 165 Euro. Therefore the cost of material is 6.6 Euro (cost includes VAT).

Cost of item (c):

The spraying of the component took fifteen minutes, therefore the cost of spraying is a total of the HVOF (91.2 Euro per hour) and material (6.6 Euro) costs. The total cost of spraying for fifteen minutes is 29.4 Euro.

Cost of item V:

The cost of post-heating the component for 80 minutes in a 3kW furnace is approximately 0.5 Euro (electricity 12 cent per 1 kW hour).

Cost of item VI:

The final finishing (grinding) costs are approximately 5 Euro (electricity and grinding paper) excluding labour

Cost of item VII:

Labour and overheads are ignored in the study, as they vary depending on where the component production takes place.

Total Cost

The total cost (excluding labour) to produce the cylindrical component is therefore 73.02 Euro. The forming die contributes to the highest cost, however this is not a recurring cost as the die is used repeatedly once manufactured. Figure 127 shows the distribution of costs over the life of a forming die. The spray and pre-heating costs are two of the highest process costs, however low batch volumes of components may be produce at each stage. In the present study, two components were produce at a time. An important point is the efficiency of the process, in terms of loss of powder material. Material losses are quite high, hence a system of recycling the powder would be essential to reduce material costs.

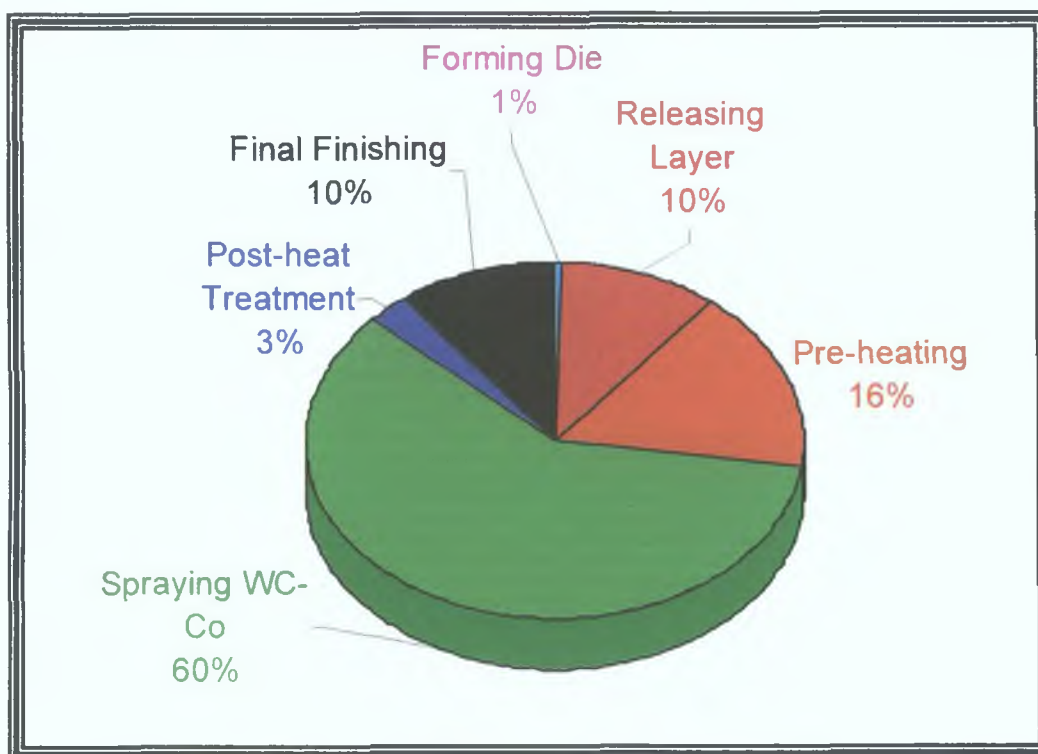


Figure 127, The distribution of costs in the production of a cylindrical component.

To produce a thermally spray-formed cutting tool, modification of the forming die would be required. The production time of a single thermally deposited component is approximately 30% of that taken to produce a single sintered component, as shown in table 16, however increasing the batch number in each process varies this difference in favour of the sinter-forming. Unfortunately, the thermally spray-formed component mechanical properties such as stiffness and hardness fall below those found for sinter-formed components.

Table 16, HVOF spray-forming versus sinter-forming of a WC-Co component.

Characteristic	HVOF Spray-Forming (from present research)	Sinter-Forming
Production Time (Hours)	2.75	9 [54]
Young's Modulus (GPa)	189.17	580 [139, 55]
Poisson's ratio	0.278	0.26 [55]
Hardness (kgmm <sup>-2</sup> )	1175	1500 [55]
Porosity (%)	0.5	<1 [55]

---

# CONCLUSIONS AND RECOMMENDATIONS

---

## 6.1 CONCLUSION

In this study, the optimisation of the High Velocity Oxy-Fuel thermal spray process for coating and the spray-forming of tungsten carbide-cobalt was analysed. The component material used in the forming process was tungsten carbide with 12% cobalt. The success of the spray-forming technique depends on many parameters, which influence residual stress development. The conclusions resulting from the investigation are summarised as follows:

- A remote method of spray surface temperature measurement has been developed and calibrated. It is based on thermocouple readings taken at the back of the substrate / die. This was validated by finite element analysis. The model slightly over estimated the back temperature due to the fact that the system ignored lateral and radiated heat loss.
- A linear traverse unit was utilised to improve spraying repeatability by controlling spraying distance, traverse speed and acceleration. Optimisation of this unit found that, speed and acceleration of  $200\text{mms}^{-1}$  and  $4.9\text{ms}^{-2}$  respectively were satisfactory for depositing WC-Co. A third-axis unit was used to produce wider deposits. A shift of 5mm vertically from one pass of the gun to the next produced a relatively flat deposit surface finish.
- Elastic properties of sprayed WC-Co were measured using the Cantilever test. Young's modulus and Poisson's ratio were found to be  $184.9\text{Nmm}^{-2}$  and 0.268 respectively.

- Comparison between the Modified Almen Test Method and Clyne's Analytical Method, used to produce residual stress distribution results in a thermally sprayed sample. The latter method provided the most accurate results as this method accounted for misfit strain within the sample, especially at the deposit / substrate interface.
- It has been established that manual spraying, and the resulting spray temperature fluctuations is unlikely to allow the build up of thick coatings or components. This is because the temperature variations increase residual stress. Use of an automated unit controlling spraying distance, reduced stress range across a sprayed sample by almost 34%.
- A carbon dioxide system reduces tungsten carbide-cobalt spraying temperature by 160°C at a spraying distance of 200mm. The cooling system together with the automotive unit has an extremely significant effect on the residual stress in resulting specimens, reducing the residual stress range by 58% compared to that when manual un-cooled spraying is used.
- Optimisation of spraying distance and powder feed rate for WC-12%wt Co was carried out based on residual stress measurements. The optimum spraying distance and feed rate found were 200mm and 38gmm<sup>-1</sup> respectively.
- The near-zero stress deposit thickness was increased to 1.2mm for a previously reported maximum deposit thickness of 0.6mm. Results were compared numerically to finite element analysis techniques.
- Residual stress results found using Clyne's Analytical Method compared reasonably to other residual stress measurement techniques such as the X-ray Diffraction and Hole Drilling method. Results show that Clyne's Analytical Method produced stress values approximately 30% of that found using the Hole Drilling and XRD methods respectively.

- Post-heat treatment at 675°C for 80 minutes reduces the residual stress generated during the spraying process, to produce relatively stress free deposits, whether the tungsten carbide-cobalt material is a coating or a spray-formed component. The effect of post-heat treatment on the resulting microstructure, such as phase transformation was observed. Heat-treating above the recrystallization temperature encouraged the formation carbide phases, benefit hardness and wear properties.
- Mechanical properties such as Vickers hardness and porosity were measured with varying deposit thickness. The hardness showed an increased of 2.6% as the deposit thickness increased from 1 to 8mm, whereas the porosity reduced by 36%.
- The reduction of residual stress enabled the deposition of high thickness spray-formed WC-Co components using the HVOF thermal spray technique. The maximum thickness achieved when forming a 12mm diameter billet was 9mm, however forming-die design is an important factor. Higher thicknesses were not achieved as the components fractured. Nevertheless, two successful specimens were produced at a thickness of 1.2mm and were used to determine the stiffness of the material. The Young's modulus for the specimen was measured as 189GPa, which was slightly higher than that found using the Cantilever test. Various sized components were fabricated and results showed that a deposit thickness of 1.2mm produced relatively stress-free components (without the involvement of the post-heat treatment cycle).
- Finally, the cost of producing the 12mm diameter, 9mm thick free-standing WC-Co cylindrical engineering components using the HVOF process was analysed. The total cost (excluding labour) to produce the cylindrical component was found to cost 73.02 Euro.

## 6.2 RECOMMENDATIONS FOR FUTURE WORK

The results documented in the present research are significant, however further recommendations are as follows

- **Instrumentation**

Using instrumentation to measurement of residual stress during deposition could be used to lower the quenching stresses

- **Investigation**

Future work could extend to other spray materials and other manufacturing applications (such as Bioengineering) An evaluation of the effect of different releasing layer materials to ease component production

- **Modelling**

Modelling of various aspects associated with the HVOF system, would provide a cheap and reliable method of optimising the process

---

# PUBLICATIONS ARISING FROM THIS WORK

---

- J Stokes and L Looney “HVOF System Definition to Maximise the Thickness of Formed Components”, Proceedings of Advances in Materials and Processing Technologies (AMPT’99), Dublin, Ireland (1999), Vol 2, pp 775 – 784
- J Stokes and L Looney, “Properties of WC-Co Components Produced using the HVOF Thermal Spray Process”, Proceedings of the first International Thermal Spray Conference, Montreal, Canada, (2000), pp 263-271
- J Stokes and L Looney “HVOF System Definition to Maximise the Thickness of Formed Components”, Journal of Surface and Coatings Technology, Vol 148, (2001), pp 18-24

---

# REFERENCES

---

- 1 Marceau, J A , and Adjorlolo, A A , “Commercial Aircraft”, in ASTM, “Corrosion Tests and Standards Application and Interpretation”, American Society for Testing and Materials Society, (1995), pp 574-578
- 2 Groshart, E C , “Military Aircraft and Aerospace”, in ASTM, “Corrosion Tests and Standards Manual Application and Interpretation”, American Society for Testing and Materials Society, (1995), pp 579-581
- 3 Ishikawa, K , Seki, M , and Tobe, S , “Application of Thermal Spray Coatings to Prevent Corrosion of Construction in Japan”, Proceedings of the 5<sup>th</sup> National Thermal Spraying Conference, Anaheim, CA, USA, (1993), pp 679-684
- 4 Ohmori, A , “Thermal Spraying Current Status and Future Trends”, Proceedings of the 14<sup>th</sup> International Thermal Spray Conference, Kobe, Japan, (1995), ISSN 1241-3074
- 5 Herman, H , “Advances in Thermal-Spray Technology”, Journal of Advanced Materials and Processes, (1990), Vol 137 (4)
- 6 Greving, D J , and Shadley, J R , “Experimental Evaluations of Thermal Spray Coatings for Oilfield Equipment Applications”, Proceedings of Thirteenth International Thermal Spray Conference, Florida, USA, (1992), pp 605-610
- 7 Nakagawa, P M , Kawakami, F , and Kudoh, T , “Trends in Automotive Applications of Thermal Spray Technology in Japan”, Proceedings of the 7<sup>th</sup> National Thermal Spray Conference, Boston, (1994), pp 1-6

8. Nicoll, A. R., "Production Plasma Spraying in the Automotive Industry: A European Viewpoint", Proceedings of the 7<sup>th</sup> National Thermal Spray Conference, Boston, (1994), pp. 7-17
9. Nguyentat, T., Dommer, K. T., and Bowen, K. T., "Metallurgical Evaluation of Plasma Sprayed Structural Materials for Rocket Engines", Proceedings of Thirteenth International Thermal Spray Conference, Florida, USA, (1992), pp. 321-326
10. Varacalle, D. J. Jr., Couch, K. W., and Budinger, V. S., "Studies of the Flame Spraying of Polymers", Proceedings of the 9<sup>th</sup> National Thermal Spray Conference, Cincinnati, Ohio, (1996), pp. 251-255
11. Kawase, R., and Nakano, A., "Production of Heat and Corrosion-Resistant Plastic Coatings", Proceedings of the 9<sup>th</sup> National Thermal Spray Conference, Cincinnati, Ohio, (1996), pp. 257-262
12. Parker, D. W., Kutner, G. L., "HVOF-Spray Technology-Poised for Growth", Journal of Advanced Materials and Processes, (1991), Vol. 139 (4)
13. Parker, D. W., Kutner, G. L., "HVOF Moves into the Industrial Mainstream", Journal of Advanced Materials and Processes, (1994), Vol. 146 (1)
14. Moore, D., "Protective Finishing Systems for Navy Aircraft", Journal of Advanced Materials and Processes, (1999), Vol. 155 (4)
15. Mingotaud, P., Bertoli, A. and Fauchais, P., "Thick Coatings (>1.5mm) of CoNiCrAlY Sprayed by HVOF", Proceedings of the 9<sup>th</sup> National Thermal Spray Conference, Ohio, USA, (1996), pp. 457-462
16. Moskowitz, L. N., "Application of HVOF Thermal Spraying to Solve Corrosion Problems in the Petroleum Industry", Proceedings of 13<sup>th</sup> International Thermal Spray Conference, Florida, USA, (1992), pp. 611-618

- 17 Matsubara, Y , and Tomiguchi, A , “Surface Texture and Adhesive Strength of High Velocity Oxy-Fuel Sprayed Coatings for Rolls of Steel Mills”, Proceedings of 13<sup>th</sup> International Thermal Spray Conference, Florida, USA, (1992), pp 637-645
- 18 Byrnes, L , and Kramer, M , “Method and Apparatus for the Application of Thermal Spray Coatings onto Aluminium Engine Cylinder Bores”, Proceedings of the 7<sup>th</sup> National Thermal Spray Conference, Boston, (1994), pp 39-48
- 19 Fukutome, H , Shimizu, H , Yasmashita, N , and Shimizu, Y , “The Application of Cermet Coating on Piston Ring by HVOF”, Proceedings of the 14<sup>th</sup> International Thermal Spray Conference, Kobe, Japan, (1995), pp 21-26
- 20 METCO / Perkin Elmer, “Diamond Jet Process Manual”, (1989)
- 21 Karthikeyan, J , DeFalco, J , and Dorfman, M , “Tungsten Carbide-Cobalt Coatings for Industrial Applications”, Sulzer METCO Technical Papers, [www.sulzermetco.com](http://www.sulzermetco.com), (2001)
- 22 Bull, S J , Davidson, R I , Fisher, E H , McCabe, A R , and Jones, A M , “A Simulation Test for the Selection of Coatings and Surface Treatments for Plastic Injection Moulding Machines”, Journal of Surface and Coatings Technology, (2000), Vol 130, pp 257-265
- 23 Karthikeyan, J and Sreekumar, K P , “Metal Pin Reinforced Thick Ceramic Coatings Prepared by Plasma Spraying”, Proceedings of the 4<sup>th</sup> National Thermal Spray Conference, Pittsburgh, USA, (1991), pp 371-373
- 24 Montavon, G , Coddet, C , Sampath, S , Herman, H , and Berndt, C C , “Vacuum Plasma Spray Forming of Astroloy An Investigation of Processing Parameters”, Proceedings of the 7<sup>th</sup> National Thermal Spray Conference, Boston, (1994), pp, 469-475

- 
- 25 Sampath, S and Herman, H , "Plasma Spray Forming of Metals, Intermetallics, and Composites" (1993), Vol 45 (7), pp 42-49
- 26 McKechnie, T , Krotz, P , Liaw, Y , Zimmerman, F and Holmes, R , "Near-Net Shape Forming of Ceramic Refractory Composite High Temperature Cartridges by VPS", Proceedings of the 7<sup>th</sup> National Thermal Spray Conference, Boston, (1994), pp 457-460
- 27 METCO / Perkin Elmer, "METCO Thermal Spraying General Overview", (1989)
- 28 Kumer, D , and Modi, S C , "Near Net Shape Processing of Metal Ceramic Composites Through Thermal Spraying", Proceedings of the 14<sup>th</sup> International Thermal Spray Conference, Kobe, Japan, (1995), pp 1169-1172
- 29 Jager, D A , Stover, D , and Schutz, H G , "Plasma Spraying of Graded Composites" Proceedings of the 4<sup>th</sup> National Thermal Spray Conference, Pittsburgh, USA, (1991), pp 323-327
- 30 Helali, M M , Looney, L and Hashmi, M S J , "A Technique for Fabricating Complex Shaped Thin Walled Components in Hard Materials Using a High Velocity Oxy-Fuel (HVOF) Thermal Spray Process", Proceedings of Advances in Powder Metallurgy and Particulate Materials, Washington D C , (1996), Vol 5, pp 18 41 – 18 54
- 31 METCO / Perkin Elmer, "Diamond Jet Application Data", (1989)
- 32 Halling, J , "Introduction Recent Developments in Surface Coating and Modification Processes", MEP, London, (1985)
- 33 Bhushan, B , and Gupta, B K , "Handbook of Tribology Material Coating and Surface Treatments", McGraw-Hill, New York, (1991)

34. Stokes, J., "The Theory and Application of the HVOF Thermal Spray Process", In Print, (2003)
35. Ando, Y., Tobe, S., Tahara, H., and Yoshikawa, T., "Application of Supersonic Expanding Plasma Jets to Nitriding of Steel Materials", Proceedings of the 1<sup>st</sup> International Thermal Spray Conference, Montreal, Canada, (2000), pp. 99-104
36. METCO / Perkin Elmer, "Diamond Jet System and Gun Manual", (1989)
37. De Villiers Lovelock, H. L., Richter, P.W., Benson, J. M., and Young, P. M., "Parameter Study of HP/HVOF Deposited WC-Co Coatings", Journal of Thermal Spray Technology, (1998), Vol. 7 (1)
38. Jacobs, L., Hyland, M. M., and De Bonte, M., "Comparative Study of WC-Cermet Coatings Sprayed Via the HVOF and HVAF Process", Journal of Thermal Spray Technology, (1998), Vol. 7 (2)
39. Lesage, J. and Chicot, D., "How to Deduce Absolute Hardness of Coatings from Indentation Standard Tests", Proceedings of the International Thermal Spray Conference, Kobe, Japan, (1995), pp. 951-956
40. ASTM B578-87, "Standard Test Method for Microstructure-Hardness of Electroplated Coatings", American Society for Testing and Materials Standards, Philadelphia, (1987)
41. ASTM B18-94, "Standard Test Method for Rockwell Hardness and Rockwell Superficial Hardness of Metallic Materials", American Society for Testing and Materials Standards, Philadelphia, (1994)
42. ISO 4516, "Metallic and Related Coatings – Vickers and Knoop Micro-hardness Tests", International Standards, (1980)

- 
- 43 Pawlowski, L , “The Science and Engineering of Thermal Spray Coatings”, Wiley and Sons, London, (1995)
- 44 McGrann, R T R , Greving, D J , Shadley, J R , Rybicki, E F , Bodger, B E , and Somerville, D A , “The Effect of Residual Stress in HVOF Tungsten Carbide Coatings on the Fatigue Life in Bending of Thermal Coatings”, *Journal of Thermal Spray Technology*, (1998), Vol 7 (4)
- 45 Kroupa, F , Knesel, Z , and Valach, J , “Residual Stresses in Graded Thick Coatings”, Report from Institute of Electrical Engineering of Academy of Science, Czech Republic, (1993), Vol 38, pp 29-74
- 46 Kroupa, F , “Stresses in Coatings on Cylindrical Surfaces”, Report from Institute of Electrical Engineering of Academy of Science, Czech Republic, (1994), Vol 39, pp 243-274
- 47 Kowalsky, K A , Marantz, D R , et al “HVOF Particle, Flame Diagnostics and Coating Characteristics”, *Proceedings of the 3<sup>rd</sup> National Thermal Spray Conference*, CA, USA, (1990), pp 587-596
- 48 Zukas, J A , Nicholas, T , et al “Impact Dynamics”, John Wiley and Sons Inc , New York, (1982)
- 49 Helali, M D , “Spray Forming of Thin Walled Net-Shaped Components of Hard Materials by the HVOF Thermal Spraying Process”, Ph D Thesis, Materials Processing Research Centre, Dublin City University, Ireland, (1994)
- 50 Itoh, A , Clyne, T W , “Initiation and Propagation of Interfacial Cracks During Spontaneous Debonding of Thermally sprayed coatings” *Proceedings of the 8<sup>th</sup> National Thermal Spray Conference*, Texas, USA, (1995), pp 425-432
- 51 Greving, D J , Shadley, J R , and Rybicki, E F , “Effects of Coating Thickness and Residual Stress on Bond Strength of C633-79 Thermal Spray Coating Test

- Specimens”, Proceedings of the 7th National Thermal Spray Conference, Boston, (1994), pp 639-645
- 52 Rybicki, E F , Schmuesser, D W , and Fox, J , “An Energy Release Rate Approach for Stable Crack Growth in the Free-Edge Delamination Problem”, Journal of Composite Materials, (1977), Vol 11, pp 470-487
- 53 METCO / Perkin Elmer, “Materials Guide”, (2001)
- 54 German, R M , “Sintering Theory and Practice”, Wiley and Sons, New York, (1996)
- 55 Hosford, W F , Caddell, R M , “Metal Forming Mechanics and Metallurgy”, Prentice Hall, New Jersey, 2<sup>nd</sup> Edition, (1993)
- 56 Voggenreiter, H H , Beyer, S , and Spies, H J , “Influence of Particle Velocity and Molten Phase on the Chemical and Mechanical Properties of HVOF-Sprayed Structural Coatings of Alloy 316L”, Proceedings of the Eight National Thermal Spray Conference, Houston, Texas, (1995), pp 303-308
- 57 Geibel, A , Verstreken, P , Delaey, L , and Froyen, L , “Production of Free Standing Plasma Sprayed NiAl Components”, Proceedings of 13<sup>th</sup> International Thermal Spray Conference, Florida, USA, (1992), pp 363-368
- 58 Munjone, F W , and Irons, G , “The Evolution of Thermal Spray Automation”, Proceedings of the 5<sup>th</sup> National Thermal Spraying Conference, Anaheim, CA, USA, (1993), pp 263-273
- 59 Irons, G , “Thermal Spray Applications Speeds”, Proceedings of the 14<sup>th</sup> International Thermal Spray Conference, Kobe, Japan, (1995), pp 1165-1168
- 60 Lyons, P , “Automation of HVOF Thermal Spraying Equipment”, Final Year Project, Dublin City University, Ireland, (2000)

- 
- 61 Tan, J C , “Optimisation of the HVOF Thermal Spraying Process For Coating, Forming and Repair of Components”, Ph D Thesis, Materials Processing Research Centre, Dublin City University, Ireland, (1997)
- 62 Creffield, G K , Chapman, I F , Cole, M A , Page, W J , and McDonough, T “Process Gases for High Velocity Oxy-Fuel Thermal Spraying”, Proceedings of the 7<sup>th</sup> National Thermal Spray Conference, Boston, USA, (1994), pp 233-238
- 63 Cole, M A , and Walker, R , “High Temperature Erosion Properties of Thermal Barrier Coatings Produced by Acetylene Sprayed High Velocity Oxygen Fuel Process”, Proceedings of the 1<sup>st</sup> International Thermal Spray Conference, Montreal, Canada, (2000), pp 1191-1200
- 64 Mellali, M , Grimaud, A , and Frauchais, P , “Parameters Controlling The Sand Blasting of Substrates for Plasma Spraying”, Proceedings of the 7<sup>th</sup> National Thermal Spray Conference, Boston (1994), pp 227-232
- 65 L’Anson, K , Riggs, W L , et al , “Use of the Shot Peening Process for Surface Modification of Thermally Sprayed Coatings”, Proceedings of the 4<sup>th</sup> National Thermal Spray Conference, Pittsburgh, USA, (1991), pp 139-145
- 66 AWS, “Thermal Spraying Practice, Theory and Application”, American Welding Society, (1985)
- 67 Pollack, H W , “Material Science and Metallurgy”, 4th Edition, Prentice-Hall, New Jersey, (1988)
- 68 Richerson, D W , “Modern Ceramic Engineering Properties, Processing and Use in Design”, Marcel Dekker, New York, (1982)
- 69 Thorpe, M L , and Richter, H J , “A Pragmatic Analysis and Comparison of HVOF Processes”, Journal of Thermal Spray Technology, (1992), pp 161-170

- 70 Smith, M F , McGuffin, D T , Henfling, J A , and Lenling, W B , “A Comparison of Techniques for the Metallographic Preparation of Thermal Sprayed Samples”, Proceedings of the 4<sup>th</sup> National Thermal Spray Conference, Pittsburgh, USA, (1991), pp 97-104
- 71 Glancy, S D , “How Metallographic Preparation Affects the Microstructure of WC/Co Thermal Spray Coatings”, Proceedings of the 7<sup>th</sup> National Thermal Spray Conference, Boston (1994), pp 771-777
- 72 Rybicki, E F , Shadley, J R , Xiong, Y , and Greving, D J , “A Cantilever Beam Method for Evaluation of Young’s Modulus and Poisson’s Ratio of Thermal Spray Coatings”, Journal of Thermal Spray Technology, (1995), Vol 4 (4), pp 377-383
- 73 Shadley, J R , Rybicki, E F , Xiong, Y , McGrann, R T R , and Savarimuthu, A C , “An ASM Recommended Practice for Evaluation of Young’s Modulus and Poisson’s Ratio of Thermal Spray Coatings Bonded to a Substrate”, Proceedings of the 1<sup>st</sup> International Thermal Spray Conference, Montreal, Canada, (2000), pp 1291-1295
- 74 ASTM E8M-96, “Standard Test Methods for Tension Testing of Metallic Materials [Metric]”, American Society for Testing and Materials Society, Philadelphia, (1996)
- 75 Richard, C S , Beranger, G , Lu, J , Flavenot, J F , and Gregoire, T , “Four-Point Bending Tests of Thermally Produced WC-Co Coatings”, Journal of Surface and Coatings Technology, (1996), Vol 78, pp 284-294
- 76 Nakahira, H , Tam, K , Miyajima, K , and Harada, Y , “Anisotropy of Thermally Sprayed Coatings”, Proceedings of the 13<sup>th</sup> International Thermal Spray Conference, Florida, USA, (1992), pp 1011-1017

- 77 SAE J433, "Procedures for Using Standard Shot Penning Test Strip SAE J443", Engineering Society for Advancing Mobility Land, Sea, Air and Space, PA, USA (1984)
- 78 Tan, J C , Looney, L , and Hashmi, M S J , "Residual Stress Analysis of WC-Co Solid Components Formed by the HVOF Thermal Spraying Process", Proceedings of Advances in Powder Metallurgy and Particulate Materials - Washington D C , (1996), Vol 3, pp 9 41-9 52
- 79 Brandt, O C , "Measuring of Residual Stresses in Thermal Sprayed Coatings", Proceedings of the 8<sup>th</sup> National Thermal Spray Conference, Texas, USA, (1995), pp 451-455
- 80 Benham, P P , Crawford, R J , and Armstrong, C G , "Mechanics of Engineering Materials", Longman, London, UK , 2<sup>nd</sup> Edition, (1999), ISBN 0-582-25164-8
- 81 Gere, J M , and Timoshenko, S P , "Mechanics of Materials", Chapman and Hall, London, UK , 3<sup>rd</sup> Edition, (1991), ISBN 0-07-Y85805-5
- 82 Tsui, Y C , and Clyne, T W , "An Analytical Model for Predicting Residual Stresses in Progressively Deposited Coatings, Part 1 Planar Geometry", Journal of Thin Solid Films, (1997), Vol 306, pp 23-33
- 83 Clyne, T W , "Modelling of Residual Stress Development in Plasma Sprayed Coatings", [http //www msm cam uk/mmc/research/plasmaspray/num model detail html](http://www.msm.cam.ac.uk/mmc/research/plasmaspray/num_model_detail.html), (2002)
- 84 Knight, R , and Smith, R W , "Residual Stress in Thermally Sprayed Coatings", Proceedings of the 6<sup>th</sup> National Thermal Spray Conference, CA, USA, (1993), pp 607-612
- 85 Cullity, B D , "Elements of X-Ray Diffraction", Addison-Wesley, (1978)

86. ASM Handbook, "Material Characterization", American Society for Metals, 9<sup>th</sup> Ed., (1992), Vol. 10
87. Barrett, C. J., Massalski, T. B., "Structure of Metals", New York, McGraw-Hill, (1966), pp. 475
88. Timoshenko, S. P., and Goodier, J. N., "Theory of Elasticity", McGraw-Hill, New York, USA, 3<sup>rd</sup> Edition, (1985), ISBN 0-07-Y85805-5
89. ASTM E1561 – 93, "Analysis of Strain Gage Rosette Data", American Society For Testing And Materials Standards, Philadelphia, (1993)
90. Hashmi, M. S. J., Pappalettere, C., and Ventola, F., "Residual Stresses in Structures Coated by a High Velocity Oxy-Fuel Technique", Journal of Materials Processing Technology, (1998), Vol. 75, pp. 81-86
91. Rendler, N. J., et. al "The Hole Drilling Strain Gauge Method of Measuring Residual Stresses", Experimental Mechanics, (1966), Vol. 6, pp. 577-586
92. ASTM E837-95, "Determining Residual Stresses by the Hole-Drilling Strain-Gauge Method", American Society For Testing And Materials Standards, Philadelphia, (1995)
93. Figueroa, H., and Diaz, O., "Thermal Spray Modeling of Flat Surfaces and Cylinders", Proceedings of the 4<sup>th</sup> National Thermal Spray Conference, Pittsburgh, USA, (1991), pp. 549-556
94. Fasching, M. M., Weiss, L. E., and Prinz, F. B., "Optimization of Robotic Trajectories for Thermal Spray Shape Deposition", Proceedings of 13<sup>th</sup> International Thermal Spray Conference, Florida, USA, (1992), pp. 221-226

- 
- 95 Brundle, C R , Evans, C A Jr , and Wilson, S , "Encyclopaedia of Materials Characterization Surfaces, Interfaces and Thin Films", Butterworth-Heinemann, Boston, USA, (1992)
- 96 ISO 4516-1980, "Metallic and Related Coatings – Vickers and Knoop Microhardness Tests", International Standards, (1980)
- 97 Yost, F G , "On The Definition Of Microhardness", Metallurgical Transaction, Vol 14A, (1983), pp 947-952
- 98 Lesage, J , and Chicot, D , "How to Deduce Absolute Hardness of Coatings from Indentation Standard Tests", Proceedings of the 14<sup>th</sup> International Thermal Spray Conference, Kobe, Japan, (1995), pp 951-956
- 99 ASTM B823-93, "Standard Specification for Materials for Nonferrous Powder Metallurgy (P/M) Structural Parts", American Society for Testing and Materials Society, Philadelphia, (1993)
- 100 MPIF Standard 10, "Preparing and Evaluating Tensile Specimens of Powder Metallurgy Materials", Metal Powder Industries Federation, (1993)
- 101 Fukanuma, H , and Ohmori, A , "Behavior of Molten Droplets Impinging on Flat Surfaces", Proceedings of the 7<sup>th</sup> National Thermal Spray Conference, Boston, (1994), pp 563-568
- 102 Steffens, H D and Gramlich, M , "FEM-Analysis of Plasma Sprayed Thermal Barrier Coatings", Proceedings of 13<sup>th</sup> International Thermal Spray Conference, Florida, USA, (1992), pp 531-536
- 103 Wright, J K , Fincke, J R , Wright, R N , Swank, W D , and Haggard, D C , "Experimental and Finite Element Investigation of Residual Stress Resulting from the Thermal Spray Process", Proceedings of the 8<sup>th</sup> National Thermal Spray Conference, Houston, Texas, (1995), pp 187-192

104. "ANSYS User's Manual: Introduction to ANSYS", ANSYS Release 5.6, <http://www.ANSYS.com>, (1999)
105. Fagan, M. J., "Finite Element Analysis: Theory and Practice", John Wiley and Sons, New York, (1992), ISBN 0-582-02247-9
106. Moaveni, S., "Finite Element Analysis: Theory and Application with ANSYS", Prentice Hall, New Jersey, (1999), ISBN 0-13-785098-0
107. Boley, B. A., and Weiner, J. H., "Theory of Thermal Stresses", Dover Publications, New York, (1997), ISBN 0-486-69579-4
108. Holman, J. P., "Heat Transfer", McGraw-Hill, New York, 5<sup>th</sup> Ed., (1981), ISBN 0-07-029618-9
109. Hunt, M. W., "Guide to Engineering Materials 2001", Advanced Materials and Processing, (2000), Vol. 158 (6)
110. "ANSYS User's Manual: Procedures", ANSYS Release 5.7, <http://www.ANSYS.com>, (2002)
111. "ANSYS User's Manual: Elements", ANSYS Release 5.7, <http://www.ANSYS.com>, (2002)
112. "ANSYS User's Manual: Commands", ANSYS Release 5.7, <http://www.ANSYS.com>, (2002)
113. Helali, M. M., and Hashmi, M. S. J., "Production Of Free Standing Objects By High Velocity Oxy-Fuel (HVOF) Thermal Spray Process", Proceedings of Advances in Materials and Processing Technologies, Dublin, Ireland, (1993), pp. 1315-1322

114. Swank, W. D., Fincke, J. R., and Haggard, D. C., "A Particle Temperature Sensor for Monitoring and Control of the Thermal Spray Process", Proceedings of the 8<sup>th</sup> National Thermal Spray Conference, (1995), pp. 111-116
115. Compumotor Division, "LX Indexer/Driver User Guide", Parker-Hannifin Corporation, (1997)
116. Kuroda, S., Tashiro, Y., Yumoto, H., Taira, S., Fukanuma, H., and Tobe, S., "Peening Action And Residual Stresses in High-Velocity Oxygen Fuel Thermal Spraying of 316L Stainless Steel", Journal of Thermal Spray Technology, Vol. 10(2), (2001), pp. 367-374
117. McGrann, R. T. R., Kim, J., Shadley, J. R., Rybicki, E. F., and Ingesten, N. G., "Characterisation of Thermal Spray Coatings Used in Dimensional Restoration", First International Thermal Spray Conference (ITSC'00), Montreal, Canada, (2000), pp. 341-349
118. Bianchi, L., Baradel, N., Liorca-Isern, N., and Bertran-Vidal, G., "Influence of Plasma Spraying Parameters on Coating Damage", Proceedings from the First International Thermal Spray Conference (ITSC'00), Montreal, Canada, (2000), pp. 29 – 36
119. Vijgen, R. O. E., and Dautzenberg, J. H., "Mechanical Measurement of the Residual Stress in thin PVD Films", Journal of Thin Solid Films, Vol. 270, (1995) pp. 264 – 269
120. Senderoff, S., and Brenner, A., Journal of Research, National Bureau of Standards, Vol. 42 (2), (1949), pp. 105-123
121. Tipton, A. A., "The Effect of HVOF Sprayed Coatings on the Elevated Temperature High Cycle Fatigue Behaviour of a Martensitic Stainless Steel", Proceedings of the 8<sup>th</sup> National Thermal Spray Conference, Houston, Texas, (1995), pp. 463 – 468

122. Fincke, J. R., Swank, W. D., and Haggard, D. C., "Comparison of the Characteristics of HVOF and Plasma Thermal Spray", Proceedings of the 7<sup>th</sup> National Thermal Spray Conference, Boston (1994), pp. 325-330
123. Girish, D. V., Mayuram, M. M., and Krishnamurthy, S., "Influence of Shot Peening on the Surface Durability of Thermomechanically Treated EN24 Steel Spur Gears", International Journal of Tribology, Vol. 30(12), (1998), pp. 865-870
124. Pron, H., Henry, J. F., Flan, B., Lu, J., Offermann, S., and Beaudoin, J. L., "Estimation of Residual Stresses Induced by Shot-Peening. Measurement of the Thermal Dissipation with an Infrared Camera", International Journal of Thermal Sciences, Vol. 41(4), (2002), pp. 369-375
125. Nerz, J. E., Kushner, Jr. B. A. and Rotolico, A. J., "Microstructural Evaluation of Tungsten Carbide-Cobalt Coatings", Proceedings of the 4<sup>th</sup> National Thermal Spraying Conference, Pittsburgh, PA, USA, (1991) pp. 115-120
126. Stewart, D. A., Shipway, P. H., McCartney, D. G., "Influence of Heat Treatment on the Abrasive Wear Behaviour of HVOF Sprayed WC-Co Coatings", Journal of Surface and coatings Technology, Vol. 105, (1998), pp. 13-24
127. Stewart, D. A., Shipway, P. H., McCartney, D. G., "Microstructural Evolution in Thermally Sprayed WC-Co Coatings: Comparison Between Nanocomposite and Conventional Starting Powders", Acta Materialia, Vol. 48, (2000), pp. 1593-1604
128. Stewart, D. A., Shipway, P. H., McCartney, D. G., "Abrasive Wear Behaviour of Conventional and Nanocomposite HVOF-Sprayed WC-Co Coatings", Journal of Wear, Vol. 225-229, (1999), pp. 789-798

- 129 Berndt, C C , Karthikeyan, J , et al, "Material Property Variation in Thermally Sprayed Coatings", Proceedings of the 4<sup>th</sup> National Thermal Spray Conference, Pittsburgh, USA, (1991), pp 199-204
- 130 Factor, M , and Roman, I , "A Critical Evaluation of the Employment of Microhardness Techniques for Characterizing and Optimizing Thermal spray Coatings", Proceedings of the 1<sup>st</sup> International Thermal Spray Conference, Montréal, Canada, (2000), pp 1345-1354
- 131 Factor, M , and Roman, I , "Vickers Microindentation of WC-12%Co Thermal Spray Coating Part 2 The Between-Operator Reproducibility Limits of Microhardness Measurement and Alternative Approaches to Qualifying Hardness of Cemented-Carbide Thermal Spray Coatings", Journal of Surface and Coatings Technology, (2000), Vol 132, pp 65-75
- 132 Weimer, A W , "Carbide, Nitride and Boride Materials Synthesis and Processing", Chapman and Hall, London, (1997)
- 133 Hwang, S Y , Seong, B G , and Kim, M C , "Characterization of WC-Co Coatings Using HP/HVOF Process", Proceedings of the 9<sup>th</sup> National Thermal Spraying Conference, Ohio, USA, (1996), pp 107-112
- 134 Tucker, Jr R C , "Structure Property Relationship in Deposits Produced by Plasma Sprayed and Detonation Gun Techniques", Journal of Vacuum Science and Technology, (1974), Vol 11, pp 725 – 734
- 135 Dieter, G E , "Engineering Design A Materials and Processing Approach", McGraw-Hill, New York, 2<sup>nd</sup> Edition, ISBN 0-07-016906-3
- 136 Ertas, A , and Jones, J C , "The Engineering Design Process", Wiley and Sons, New York, 2<sup>nd</sup> Edition, ISBN 0-471-13699-9

- 137 Creffield, G K, Cole, M A, and White, G R, "The Effect of as Gas Parameters on HVOF Coatings", Proceedings of the 8<sup>th</sup> National Thermal Spray Conference, Houston, Texas, (1995), pp 291-295
- 138 Kreye, H, Zimmermann, S, and Heinrich, P, "The Role of the Fuel Gas in the HVOF Process", Proceedings of the 14<sup>th</sup> International Thermal Spray Conference, Kobe, Japan, (1995), pp 393-398
- 139 Berger, L M, Hermel, W, et al, "Structure, Properties and Potentials of WC-Co, Cr<sub>3</sub>C<sub>2</sub>-NiCr and TiC-Ni-Based Hardmetal-Like Coatings", Proceedings of the 9<sup>th</sup> National Thermal Spray Conference, Cincinnati, Ohio, (1996), pp 89-96

---

# APPENDIX 1

---

Thermal spray conferences have been held since 1987, and have been on going almost every year since Previous to 1987 thermal spraying research was published at International Metal Spraying Conferences, of which they were twelve in all dating from 1956 The International Metal Spraying Society was renamed, the International Thermal Spraying Society, therefore the international conference held in 1992, was known as the thirteenth, 1995 the fourteenth and similarly in 1998 the fifteenth

The International Thermal Spray Conference 2000 (ITSC 2000), held in Montreal, Canada, represented the first full collaboration between three world-class societies, to develop 'the premier' international conference series on thermal spraying ITSC is now formally a joint initiative between the Thermal Spray Society (TSS), an affiliate society of ASM International, the German Welding Society (DVS- Deutscher Verband für Schweisstechnik), and the International Institute of Welding (IIW)

Presented is a list of the relevant conferences

1<sup>st</sup> National Thermal Spray Conference (1987), Orlando, Florida

Reference Houck, D L, "Thermal Spray Advances in Coatings Technology", ASM International, Materials Park, Ohio, USA,  
ISBN 0-87170-320-3

2<sup>nd</sup> National Thermal Spray Conference (1988), Cincinnati, Ohio

Reference Houck, D L, "Thermal Spray Technology- New Ideas and Processes", ASM International, Materials Park, Ohio, USA,  
ISBN 0-87170-335-1

3<sup>rd</sup> National Thermal Spray Conference: (1990), Long Beach, California

Reference: Bernecki, T. F., "Thermal Spray Research and Applications", ASM International, Materials Park, Ohio, USA,  
ISBN 0-87170-392-0

4<sup>th</sup> National Thermal Spray Conference: (1991), Pittsburgh, Pennsylvania

Reference: Bernecki, T. F., "Thermal Spray Coatings: Properties, Processes and Applications", ASM International, Materials Park, Ohio, USA,  
ISBN 0-87170-437-4

13<sup>th</sup> International Thermal Spray Conference: (1992), (5<sup>th</sup> National Thermal Spray Conference: (1992)), Orlando, Florida

Reference: Berndt, C. C., "Thermal Spray: International Advances in Coating Technology", ASM International, Materials Park, Ohio, USA,  
ISBN 0-87170-443-9

6<sup>th</sup> National Thermal Spray Conference: (1993), Anaheim, California

Reference: Berndt, C. C., "Thermal Spray: Research Design and Application", ASM International, Materials Park, Ohio, USA,  
ISBN 0-87170-470-6

7<sup>th</sup> National Thermal Spray Conference: (1994), Boston, Massachusetts

Reference: Berndt, C. C. and Sampath, S., "Thermal Spray Industrial Applications", ASM International, Materials Park, Ohio, USA,  
ISBN 0-87170-509-5

8<sup>th</sup> National Thermal Spray Conference: (1995), Houston, Texas

Reference: Berndt, C. C. and Sampath, S., "Thermal Spray Science and Technology", ASM International, Materials Park, Ohio, USA,  
ISBN 0-87170-541-9

9<sup>th</sup> National Thermal Spray Conference (1996), Cincinnati, Ohio

Reference Berndt, C C , “Thermal Spray Practical Solutions for Engineering Problems”, ASM International, Materials Park, Ohio, USA,  
ISBN 0-87170-583-4

10<sup>th</sup> National Thermal Spray Conference (1997), Indianapolis, Indiana

Reference Berndt, C C , “Thermal Spray A United Forum for Scientific and Technological Advances”, ASM International, Materials Park, Ohio, USA,  
ISBN 0-87170-618-0

15<sup>th</sup> International Thermal Spray Conference (1998), Nice, France

Reference Coddet, C , “Thermal Spray Meeting the Challenges of the 21<sup>st</sup> Century”, ASM International, Materials Park, Ohio, USA,  
ISBN 0-87170-659-8

1<sup>st</sup> International Thermal Spray Conference (2000), Montreal, Quebec, Canada

Reference Berndt, C C , “Thermal Spray Surface Engineering via Applied Research”, ASM International, Materials Park, Ohio, USA,  
ISBN 0-87170-680-6

2<sup>nd</sup> International Thermal Spray Conference (2001), Singapore, 28-30 May 2001

Reference Berndt, C C

3<sup>rd</sup> International Thermal Spray Conference (2002), Essen, Germany, 4-6

March Reference Berndt, C C

Papers arising from these conferences are produced in journals format, one of the most used being the Journal of Thermal Spray Technology

## APPENDIX 2

### TRAVERSE UNIT AND SINGLE AXIS UNIT

#### (1) Traverse Unit

To traverse the spray gun back and forth, a LX-L20 Series Linear Stepper Motor (LX stands for Linear X-direction), developed by the Parker-Hannifin Compumotor Division, which operates using electrical magnetic principles was utilised. The stationary element is referred to as the platen, and the moving element on which the gun is mounted, is called the forcer, figure A1. The frame was designed to mount the linear motor and Diamond Jet HVOF gun.

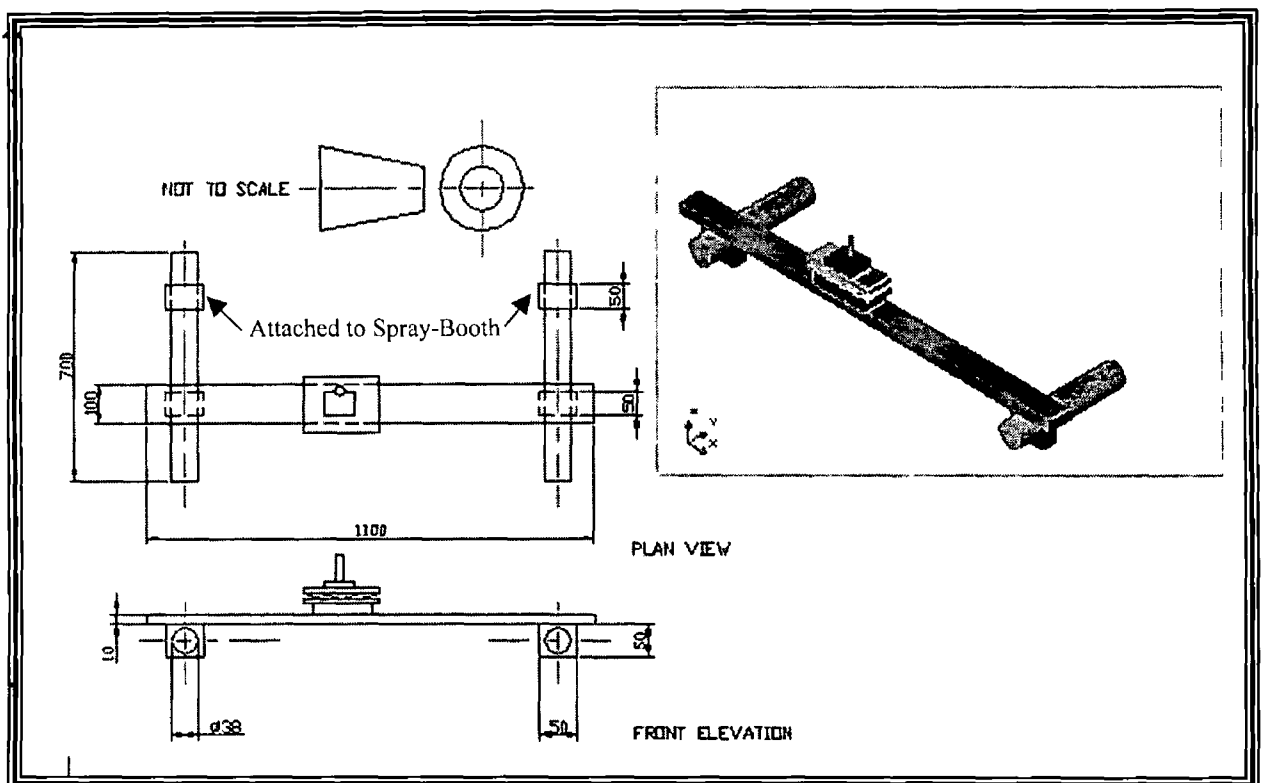


Figure A1, Computer aided drawing of the traverse unit framework

### The Forcer

The forcers' armature incorporates permanent magnets, electromagnets and bearings shown in figure A2 and figure A3. Its motion along the platen is governed by the state of the currents in the field windings. It consists of two electromagnets (A1, A2 and B1, B2) and a strong rare earth permanent magnet as shown in figure A3. The two pole faces of each electromagnet are toothed to concentrate the magnetic flux. The forcer contains four sets of teeth, which are spaced in quadrature, so that only one set of teeth are aligned with the platen teeth at any given time. Magnetic flux passing between the forcer and the platen induces a very strong normal attractive force between them. This attractive force can be up to ten times the peak holding force of the motor, thus requiring a bearing arrangement to maintain precise clearance between the teeth arrangement of the platen and the forcer. Air bearings provided the necessary clearance in this case. Air pressure of 34Bar (50psi) is required to give adequate clearance between the platen and forcer.

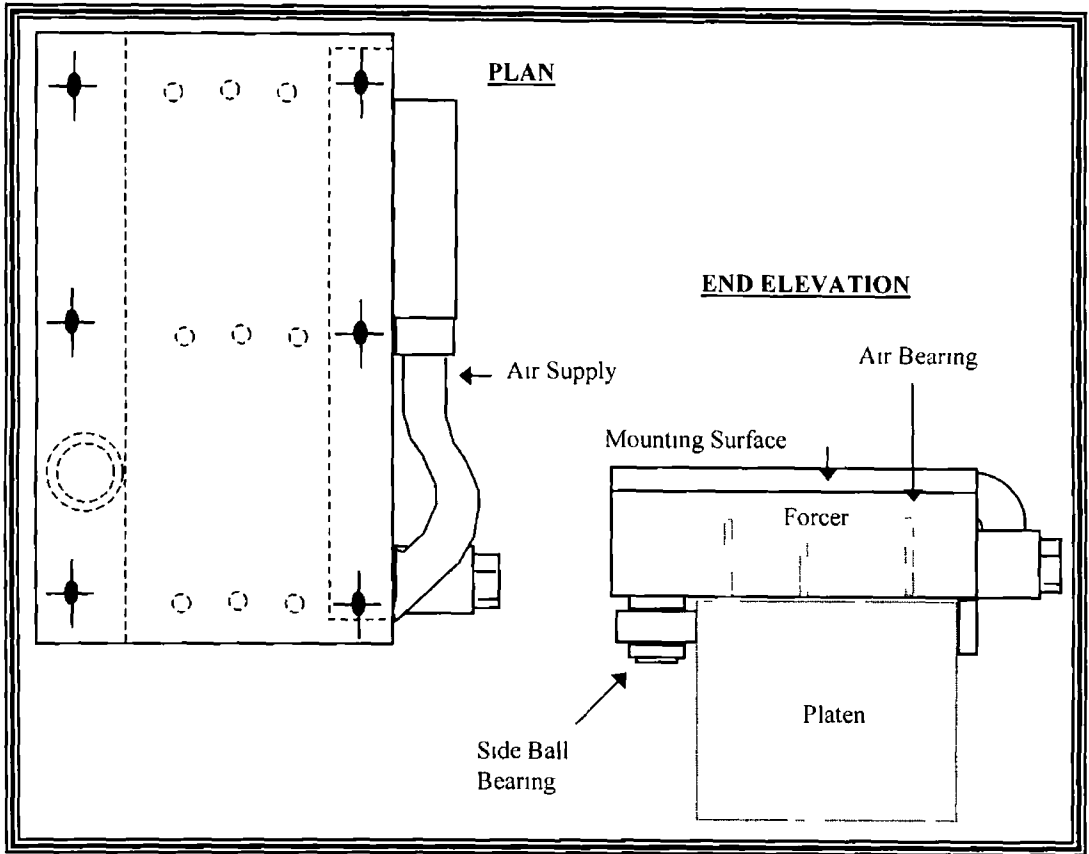


Figure A2, Schematic diagram of the forcer of the linear motor

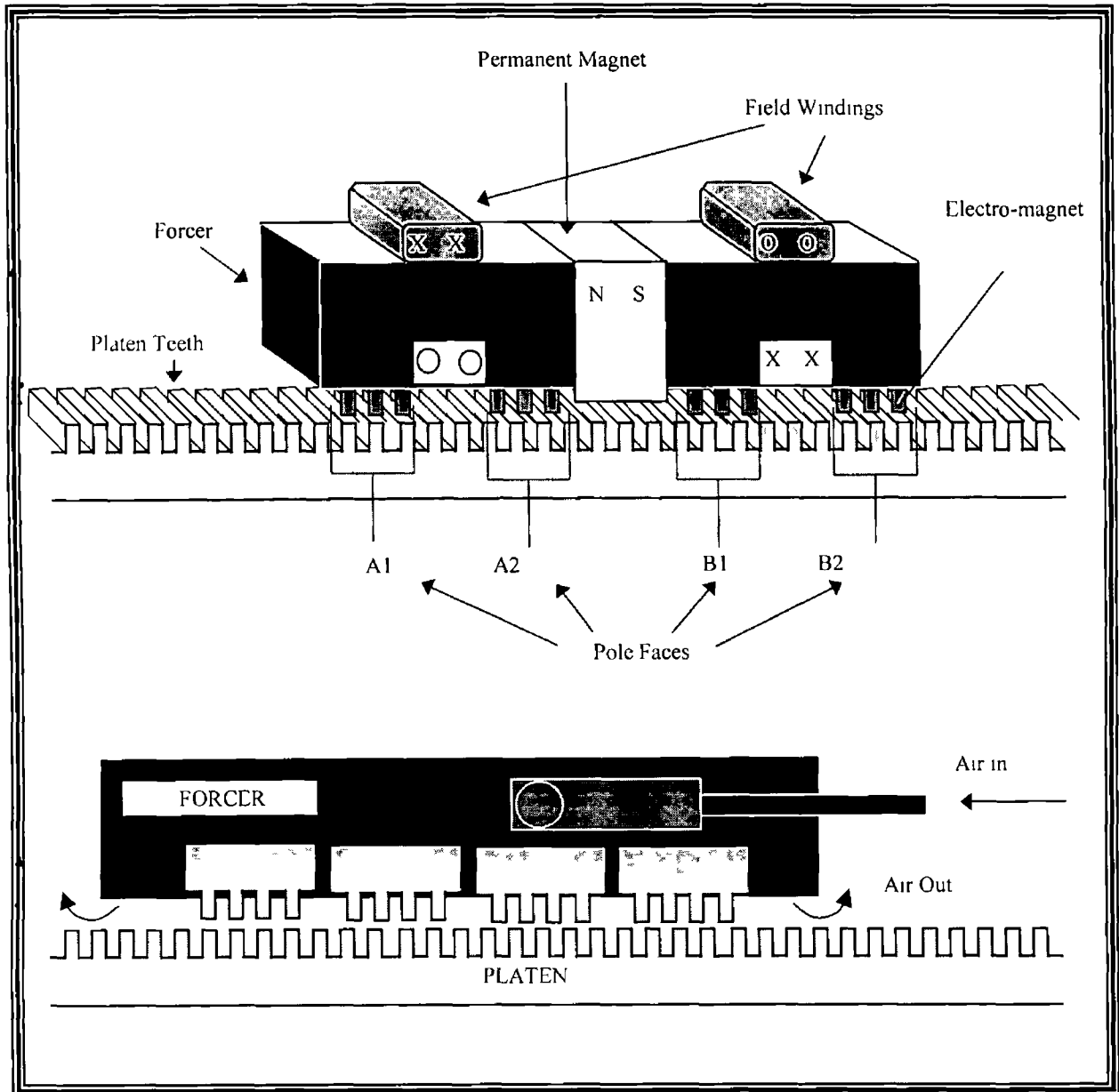


Figure A3, Schematic of the forcer and its interaction with the platen

When current is located in the field winding, the resulting magnetic field tends to reinforce the permanent magnetic flux at one face and cancel it at the other. Inverting the current, exchanges the order of reinforcement, and cancellation in the poles. When the current is removed, the permanent magnetic flux is divided equally between the pole faces. By selectively applying current to phase A and B, it is possible to concentrate the magnetic flux at any of the forcer's four pole faces. The face with the highest flux concentration will align its teeth with corresponding teeth of the platen.

Figures A4 and A5, depict the four cardinal states or full steps of the forcer. The four steps demonstrates the motion of one tooth interval to the right. 'X' and 'O' describe the direction of the current in the field windings, 'X' being the current moving into the page, while 'O' being out of the page. Reversing the sequence moves the forcer to the left. Repeating the sequence will induce the forcer to continue movement in a certain direction depending on the currents' direction. At rest, the forcer acquires a restoring force, which opposes any attempt to displace it from its position (equilibrium).

The linear motor is controlled by a motor driver and a LX indexer drive package system. The LX indexer drive consists of a microprocessor, a digital-analog converter, a ROM (Read-Only Memory) indexer memory, an EEPROM (Electrically Erasable Programmable Read-Only Memory) program storage memory, a force angle modifier, power amplifiers and a power supply. The LX drive contains a RS-323C interface, to communicate with a micro computer and an input/output (I/O) interface to control the external sensors.

The LX drive configuration consists of two sets of dip switches as shown in figure A6. The first set, control the motor (numbered 1 to 12), and the second control the indexer (numbered 1 to 6). Within each set are independent controls. For example, drive settings 1 to 5 control the motor current, 8 to 10 control the motor resolution. The automatic run feature is controlled by number 6 and the automatic stand-by is controlled by number 7, which drops the current of the forcer by 50% when pulses are not received. The motors waveform (which is a pure sine-wave), is controlled by

numbers 11 and 12. As with the indexer, numbers 1 to 3 control the profile selection (an example of this would be a triangular profile, which depends on acceleration and velocity values). The predefined acceleration profiles are stored in the ROM and are designed to maximise the force and minimise the time movement. Numbers 4 to 6 are used to address the indexer with commands.

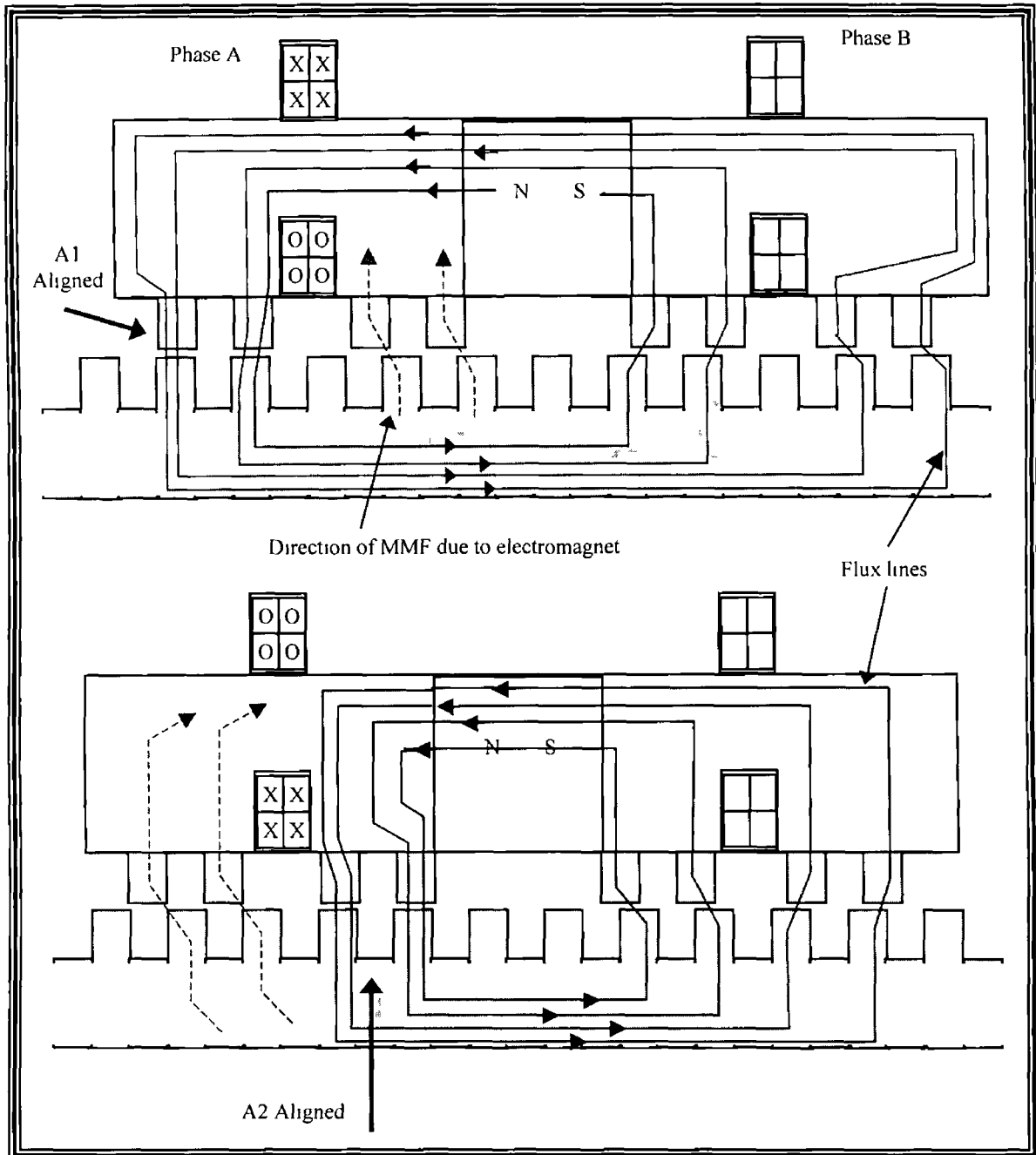


Figure A4, Schematic of flux paths and teeth (pole face) position, steps 1 and 2 of a linear step motor

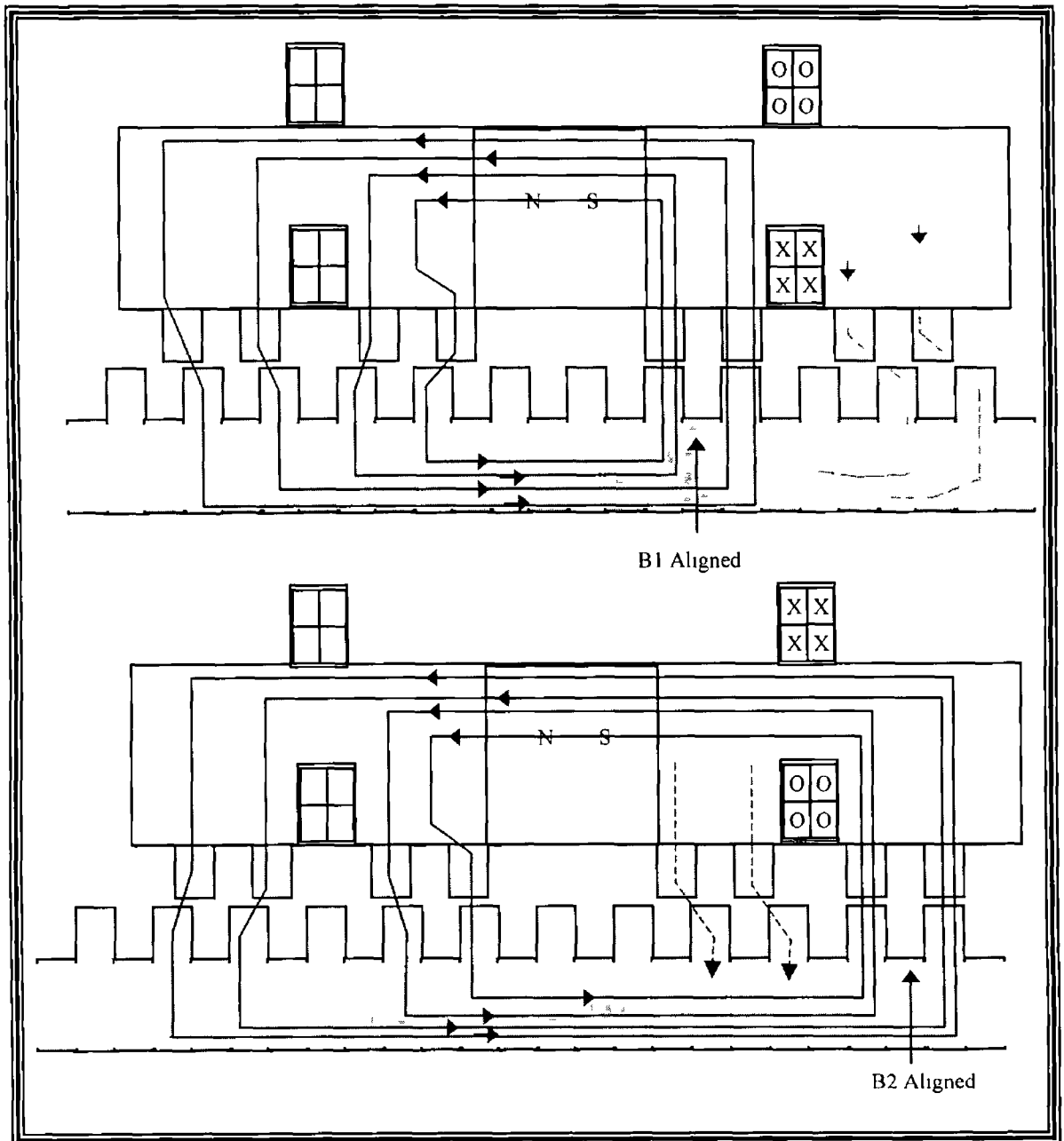


Figure A5, Schematic of flux paths and teeth position, steps 3 and 4 of a linear step motor

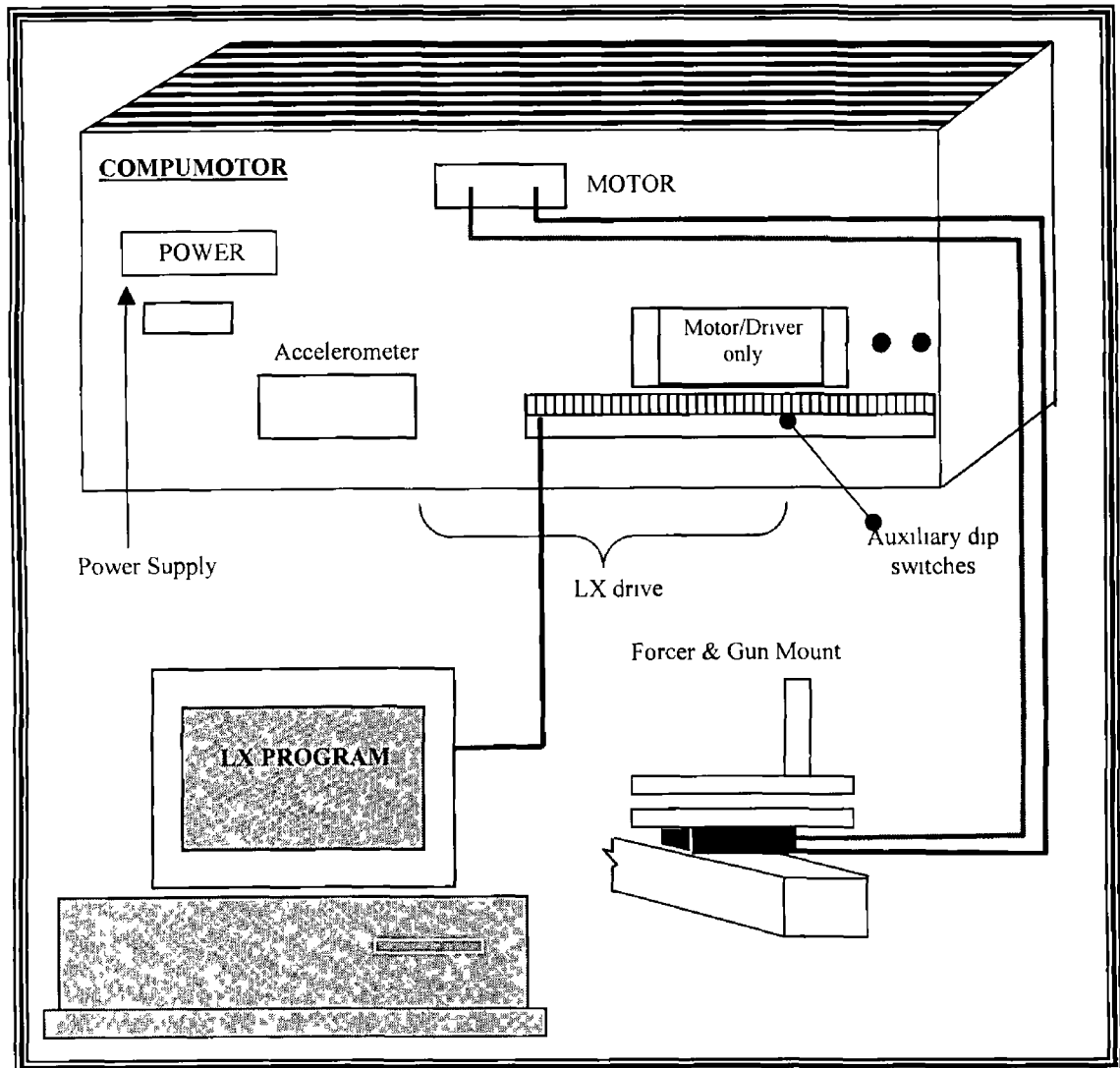


Figure A6, Schematic of the LX drive

### The Platen Mount

The platen is a passive toothed steel bar, extending a length of one meter. Spraying distance control is an advantageous feature of this device, as the platen is fixed between two supports at a set distance from the forming die. The framework consists

of two cylindrical aluminium beams, positioned perpendicular to the substrate face. The platen is attached between these aluminium beams, in such a way as the platen can be moved in towards or out from the substrate as shown in figure A7. Bolts fix the platen in place once the required spray distance has been determined.

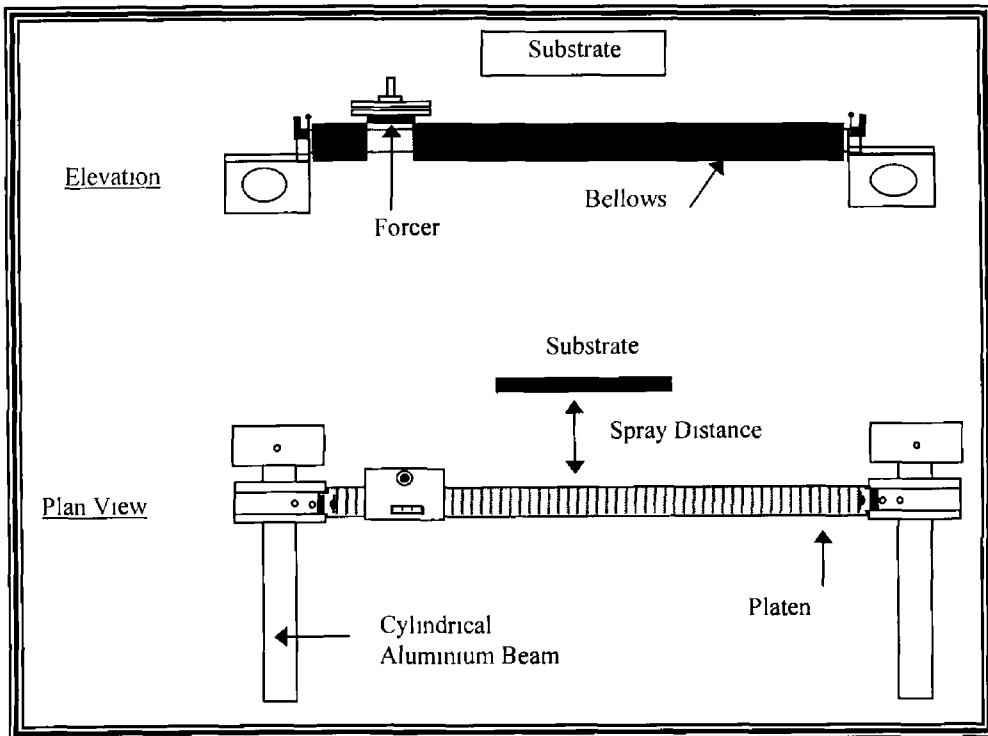


Figure A7, Platen arrangement for spraying distance control

The platen has to be flat and horizontally level, so that the air gap between the forcer and the platen remains constant throughout the travel of the forcer. If the air gap varied, the forcer would run unevenly, or would stall. Referencing a dial gauge and checking at various points along the platen ensures that it is level. A bellows covers the exposed platen track, to protect it from hot powder particles which otherwise would effect the travel of the forcer.

### Programming the Linear Traverse Unit

The operation of the linear unit is to traverse the Diamond Jet gun at various speeds and accelerations according to the operators' desires. The unit was used both during the pre-heat treatment (use of the Diamond Jet HVOF guns flame was used to pre-heat the substrate) and the deposition cycles.

Programs are made up of procedures, such as in this case, the pre-heat treatment of the substrate, followed by the spraying procedure. There are a number of sequences (blocks) of programs, which build up these procedures. Within these sequences are sub-sequences or commands that give the necessary instructions to allow the sequence to be performed.

The commands are given in a LX language, developed by the Compumotor Division for the use of their equipment. The procedure for pre-heat treatment and spraying are essentially the same except for the number of passes each require. The following procedure was used to run the traverse unit.

MPI	Sets unit to incremental position mode*	
MF1	Define Move-Form 1	
A0 3	Sets acceleration to 0.3g (2.943ms <sup>-2</sup> )	
V10	Sets velocity to 10ips (0.254ms <sup>-1</sup> )**	
L5	Loops following code five times for pre-spray treatment	} Pre-heat treatment loop
D12000	Sets distance to 12,000 steps***	
G	Execute the move (Go)	
H	Reverses the direction	
G	Execute the move (Go)	
N	Ends loop	
T3	Waits 3 seconds before carrying out next operation****	
L20	Loops twenty times	} Spray loop
D12000	Sets distance to 12,000 steps	
G	Execute the move (Go)	
H	Reverses the direction	
G	Execute the move (Go)	
N	Ends loop	
C	Initiates command execution to resume	

\* The moves that follow will be carried out in incremental moves

\*\* ips = inches per second

\*\*\* 1000 steps = 1 inch (0.0254m)

\*\*\*\* Allows three second of a delay before running the next procedure (During these three seconds the powder feed is turned on)

### *Selection of Traverse Speed*

According to Irons [59] the appropriate selection of traverse speed depends on the material been deposited. High traverse speeds lead to lower thickness per pass, however the torch returns more rapidly to the same spot, thus reducing temperature

variation of the sprayed piece. However, should a spiral effect appear on the component during deposition, the traverse rate should be reduced until it disappears. Similarly, lower traverse speeds exhibit higher pass thicknesses, hence lead to a difference in temperature between the bottom and upper parts of each layer, thus generating residual stress, causing spalling (adhesion loss between the deposit and the substrate/previously deposited material). If local hot spots appear whilst spraying, traverse rate should be increased, to avoid surface oxidation [59].

### Travel Limits

As the forcer is allowed to travel, there is a possibility that the forcer may travel beyond the end of the platen, caused by an over-estimated travel distance. Thus two limit switches were installed at each end of the platen. The limit switches stop and reverse the forcer in the opposite direction to avoid damage to the assembly.

## (2) Single Axis Unit

In order to produce larger coatings/components an added feature was required along with the gun traverse unit. A third-axis directional unit was designed. A stepper motor run by a Data Acquisition (DAQ) card attached to a PC, is connected to a lead screw at one end, while the component clamp and adjoining structure is connected at the other end of the screw thread.

The stepper motor is wired to a Data Acquisition (DAQ) card, which in turn is integrated to a control program LabVIEW (provided by National Instruments) run by a personal computer. The DAQ card has two inputs and output types, digital and analogue. The digital inputs and outputs run the stepper motor and travel limit switches, where the analogue inputs maybe used for temperature measurement during deposition.

LabVIEW can be described as a graphical programming language, where traditional code written as text is replaced with operating symbols connected together by wire symbols. The code looks like an electrical circuit, however the language behind the circuit resembles the C language program. The stepper motor receives a clock pulse signal (a current is sent to the stepper motor for a set amount of time), controlled by the LabView program, sent through the digital output of the DAQ card. This pulse causes the stepper motor to rotate by a certain amount, resulting in the component clamp moving up or down by a certain height, one revolution (which requiring 200 motor steps) of the lead screw produces a 5mm height change [60].

After lengthy testing, a user friendly control panel was designed in LabVIEW, as shown in figure A8, to allow interaction between the HVOF thermal spraying operator and the movement of the deposit. The panel is made up of two sections, a manual and an automated movement control.

The manual movement control is used to align the component with the DJ gun, for example to line the lowest point of the component with the gun for the first pass, then

the component can be dropped by a desired distance to deposit the second pass. To operate this function, the *Manual/Auto* switch would be set to *M* (manual). Depending on the position of the component relative to the DJ gun nozzle opening, the *Up* or *Down Direction* switch is selected. If the alignment distance is small then a *Half Step* would be used, together with a slow *Speed Control* value. If the alignment distance is large then a *Full Step* would be used, together with a fast *Speed Control* value. Pushing the *Operate* button moves the component clamp into the position required. Pushing the *Operate* button again stops the move.

The automated movement control is used to displace the component during deposition after a set number of passes of the HVOF gun. To operate this function, the *Manual/Auto* switch is set to *A* (Automated). The *Vertical Increment* (distance between the centre point of the initial pass to the centre point of the next pass) is then set (5mm shown in figure A8). Changing the *Counter Control* to a certain value (shown as 4 in figure A8) signifies the number of passes the gun must make before the increment height begins. The *Axis Wait Time* (in milliseconds, so 1000ms is equivalent to 1 second) suggests the time the gun traverse unit should pause, to allow the increment stage to occur. According to Lyons [60], a high *Speed Control* at a *Half Step* yields the lowest incremental operation time, however the operator has the ability to vary these if required. The program counts the total *Number of Passes* at any given point during deposition. The *Count Switch Pause* button prevents the situation, where the limit switch may be double depressed at the end of a pass (due to momentum of the gun traverse unit or vibrational effects). A time space (in milliseconds) is entered, so once the limit switch has been depressed, the count (pass number) will pause for a set amount of time before the next count is reported.

The use of this component third-axis traverse (vertical) unit together with the gun traverse (horizontal) unit, allows accurate control of the HVOF deposition process, offering more repeatable results compared to the manual spraying carried out previously [61].

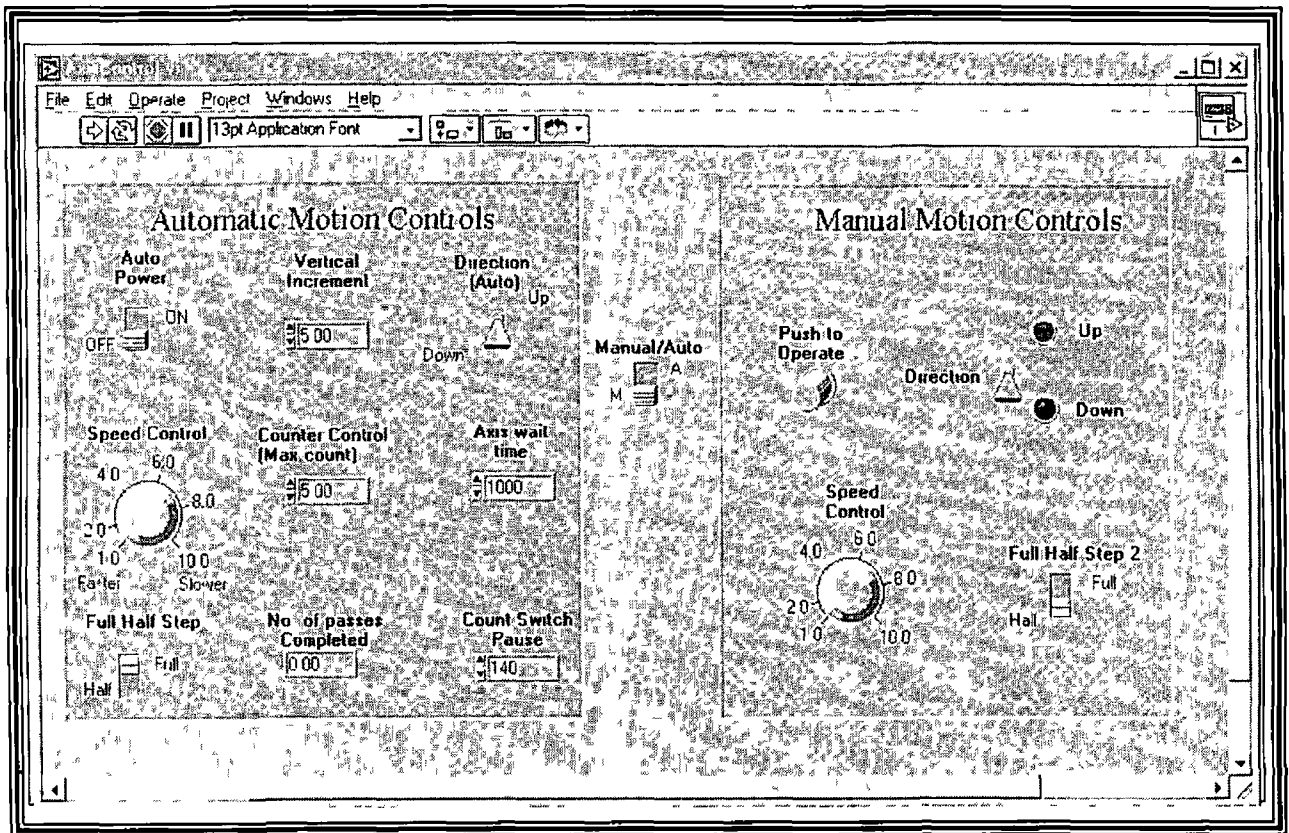


Figure A8, Control panel for the operation of the third-axis unit

---

## APPENDIX 3

---

### The Derivation Of Residual Stress Equations Using Modified Almen Test

The free body diagram in figure 24, demonstrates the bending theory used to determine the residual stress of the coating. The forces acting on the coating and the substrate, denoted by  $F_c$  and  $F_s$  respectively,  $M_c$  and  $M_s$  are the corresponding bending moments.  $E_s$ ,  $A_s$  and  $h_s$  are the properties Young's modulus, area and height of the substrate respectively, and similarly  $E_c$ ,  $A_c$  and  $h_c$  are the properties for the coating. The coefficient of expansion for the coating and substrate are given as  $\alpha_c$  and  $\alpha_s$ .  $R_c$  and  $R_s$  are the resulting bending radius values for the coating and the substrate respectively.

The bending theory is based on statical equilibrium of forces and moments

$$\Sigma F = 0 \quad \text{Equation A1}$$

$$\Rightarrow F_c = F_s = F \quad \text{Equation A2}$$

and

$$\Sigma M = 0 \quad \text{Equation A3}$$

$$\Rightarrow F h = M_c + M_s \quad \text{Equation A4}$$

The overall force ( $F$ ) times the overall thickness of the sample ( $h$ ) is equated to the sum of the moments acting on the coating ( $M_c$ ) and substrate ( $M_s$ ) respectively.

The same elongation occurs between the coating and the substrate, therefore

$$\frac{F_c}{E_c A_c} + \alpha_c \Delta T + \frac{h_c/2}{R_c} = -\frac{F_s}{E_s A_s} + \alpha_s \Delta T - \frac{h_s/2}{R_s} \quad \text{Equation A5}$$

$$\frac{F_c}{E_c A_c} + \frac{F_s}{E_s A_s} = -\frac{h_c/2}{R_c} - \frac{h_s/2}{R_s} + (\alpha_s - \alpha_c) \Delta T \quad \text{Equation A6}$$

and, by equation A2

$$F \left[ \frac{1}{E_c A_c} + \frac{1}{E_s A_s} \right] = -\frac{h_c/2}{R_c} - \frac{h_s/2}{R_s} + (\alpha_s - \alpha_c) \Delta T \quad \text{Equation A7}$$

$$\Rightarrow F = \left[ -\frac{h_c/2}{R_c} - \frac{h_s/2}{R_s} + (\alpha_s - \alpha_c) \Delta T \right] \left[ \frac{E_c E_s A_c A_s}{E_c A_c + E_s A_s} \right] \quad \text{Equation A8}$$

The average stress in the coating is the force divided by the coating area

$$\sigma_{\text{Average}} = \frac{F}{A_c} = \left\{ \frac{\left[ -\frac{h_c/2}{R_c} - \frac{h_s/2}{R_s} + (\alpha_s - \alpha_c) \Delta T \right] \left[ \frac{E_c E_s A_c A_s}{E_c A_c + E_s A_s} \right]}{A_c} \right\} \quad \text{Equation A9}$$

$$\therefore \sigma_{\text{Average}} = \frac{F}{A_c} = \left[ \frac{\left[ -\frac{h_c/2}{R_c} - \frac{h_s/2}{R_s} + (\alpha_s - \alpha_c)\Delta T \right] \left[ \frac{E_c E_s w_c h_c w_s h_s}{E_c w_c h_c + E_s w_s h_s} \right]}{A_c} \right] \quad \text{Equation A10}$$

However the width of substrate and coating is the same;

$$\therefore \sigma_{\text{Average}} = \frac{F}{A_c} = \left[ \frac{\left[ -\frac{h_c/2}{R_c} - \frac{h_s/2}{R_s} + (\alpha_s - \alpha_c)\Delta T \right] \left[ \frac{E_c E_s h_c A_s}{E_c h_c + E_s h_s} \right]}{A_c} \right] \quad \text{Equation A11}$$

Once all of the dimensions and parameters are known, the average stress in a coating may be found using equation A11. However one may be interested in the stress distribution across the coating and substrate.

Beams that are fabricated of more than one material are called composite beams, hence thermally sprayed substrates are among this family. Composite beams may be analysed by the same bending theory used for ordinary beams [80]. The position of the neutral axis can be found by using the condition that the resultant axial force acting on the cross section is zero, therefore:

$$\int_S \sigma_{xs} dA + \int_C \sigma_{xc} dA = 0 \quad \text{Equation A12}$$

Where the  $\sigma_{xs}$  the stress in the substrate,  $\sigma_{xc}$  the stress in the coating, and where it is understood that the first integral is evaluated over the cross-sectional area of the substrate and the second integral is evaluated over the cross-sectional area of the

coating. Replacing  $\sigma_{xs}$  and  $\sigma_{xc}$  by their equivalent stiffness and strain notation, where  $y$  is the distance from the neutral axis [81]:

$$E_s \int_s y \, dA + E_c \int_c y \, dA = 0 \quad \text{Equation A13}$$

This equation will now yield the position of the neutral axis for a beam with two materials. Separating these two integrals out, the assumption will be that the neutral axis lies within the substrate material and the distances from this axis to the bottom and the top of the beam will be  $h_1$  and  $h_2$  (both in millimetres) respectively, as shown in figure 25. The integrals may be evaluated by taking first moments of cross-sectional areas of the substrate and coating about the z-axis, as follows:

$$\int_s y \, dA = -\frac{h_1}{2} (h_1)(w) + \frac{(h_s - h_1)}{2} (h_s - h_1)(w) \quad \text{Equation A14}$$

Expressing this equation as a function of  $h_1$ :

$$\int_c y \, dA = [(h_s + \frac{h_c}{2}) - h_1] (h_c)(w) \quad \text{Equation A15}$$

Substituting both equation A14 and A15 into equation A13, reveals the value of  $h_1$  and in then in turn  $h_2$ , hence the position of the neutral axis ( $y$ ) is found (figure A9).

$$h_1 = \frac{1}{2} \frac{[E_s h_s^2 + E_c h_c^2 + 2E_c h_s h_c]}{[E_s h_s + E_c h_c]} \quad \text{Equation A16}$$

$$h_2 = (h_s + h_c) - h_1 \quad \text{Equation A17}$$

$$y = h_2 \quad \text{Equation A18}$$

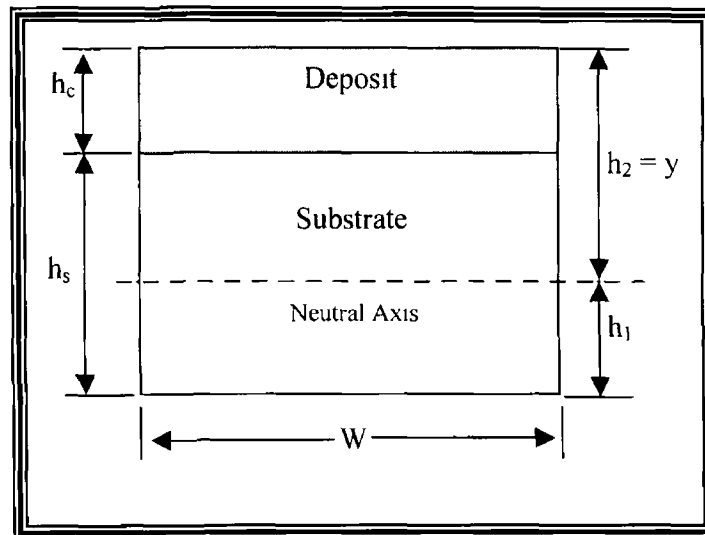


Figure A9, Position of neutral axis

Based on the bending relationship [80]

$$\frac{\sigma}{y} = \frac{M}{I} = \frac{E}{R} \quad \text{Equation A19}$$

Where  $M$  is the bending moment,  $I$  the moment of inertia about the neutral axis and  $R$  the bending radius for a beam, in this case, the stress in the substrate at any point is as follows

$$\sigma_{xs} = -\frac{E_s y}{R} \quad \text{Equation A20}$$

Similarly, the stress at any point in the coating may be found by the expression, which supports findings by Brandt [79]

$$\sigma_{xc} = -\frac{E_c y}{R} \quad \text{Equation A21}$$

The negative sign indicates that a positive bending moment produces a negative curvature. The position relative to the neutral axis (that is  $y$ ), is positive if working above the neutral axis and negative if below, with reference to figure A9

The radius of curvature is measured using the 'Sagital Method'. Referring to figure A10, the radius of curvature is obtained from the relationship:

$$h(2R - h) = a^2 \quad \text{Equation A22}$$

$$\Rightarrow 2Rh - h^2 = a^2 \quad \text{Equation A23}$$

Therefore:

$$R = \frac{a^2 + h^2}{2h} \quad \text{Equation A24}$$

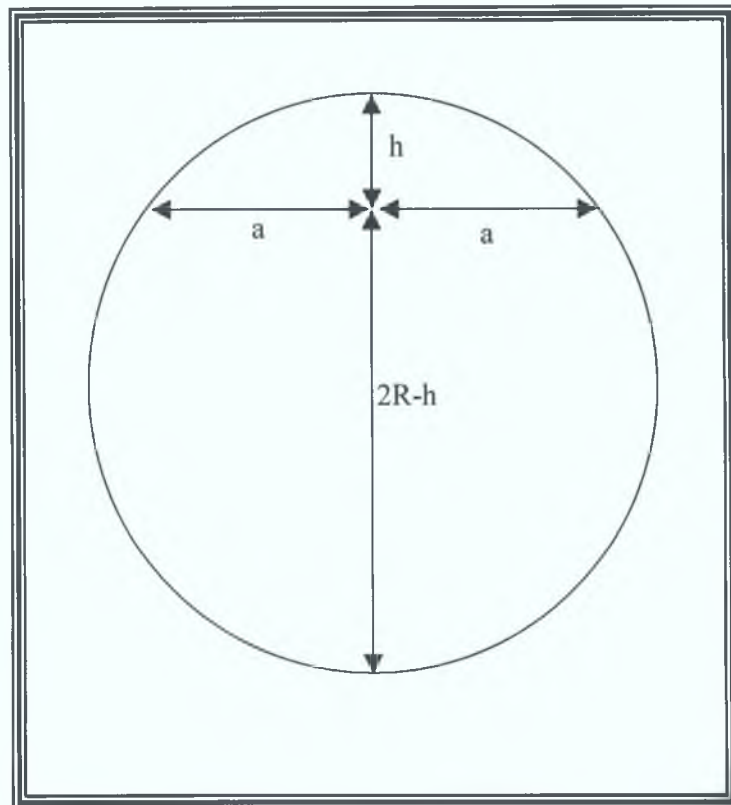


Figure A10, Sagital Method.

---

## APPENDIX 4

---

### The Derivation Of Residual Stress Equations Using X-Ray Diffraction Technique

X-ray Diffraction uses the principle of Bragg's Law given as

$$n\lambda = 2d \sin\theta \quad \text{Equation A25}$$

where  $n$  is an integer value,  $\lambda$  is the wavelength of the X-ray beam (typically of the range 0.7 to 2 Å) and  $\theta$  is the angle between the atomic planes and the incident (and diffracted) X-ray beam. A change in the plane spacing ( $d$ ), causes a shift in the diffraction angle ( $2\theta$ ). For example, figure A11 (A) shows a specimen surface set at two angles to the impinging X-ray,  $\psi = 0$  and  $\psi = \psi$  respectively. According to the ASM Handbook [86] and Barrett et al [87] at  $\psi = 0$ , tensile stresses which may be present, result in a Poisson's ratio contraction and therefore a reduction the lattice spacing and slight increase in diffraction angle  $2\theta$ . If the sample is then rotated through some known angle  $\psi$  (figure A11 (B)), the tensile stress present in the surface increases the lattice spacing ( $d\psi$ ) over the stress free state, and decreases  $2\theta$ . Measuring the change in angular position of the diffraction peak for at least two orientations (such as  $\psi = 0$  and  $\psi = \psi$ ) of the sample, enables the calculation of the residual stress present in the sample surface lying in the plane of diffraction.

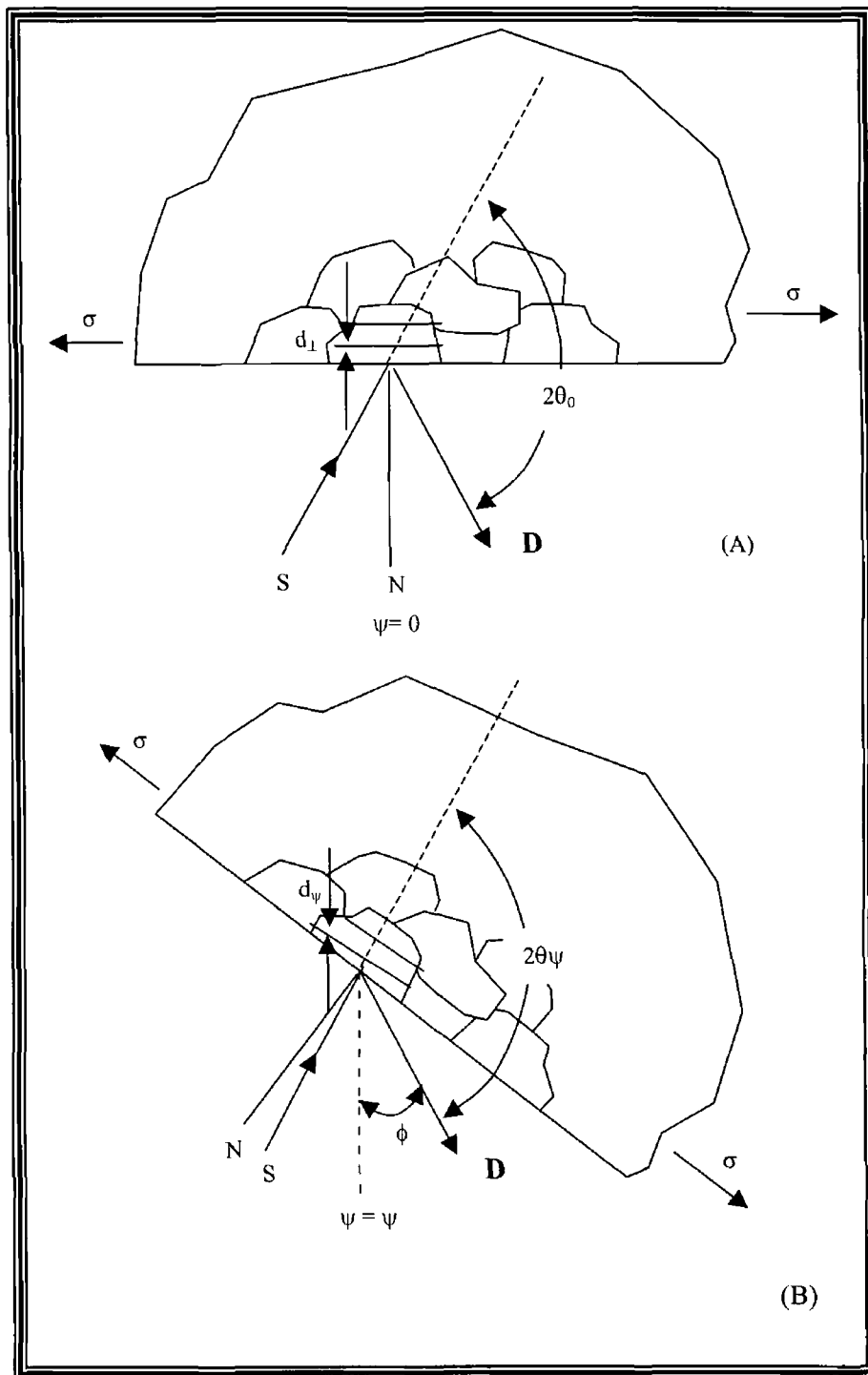


Figure A11, schematic diagram of the orientation of the measured lattice planes with respect to specimen structure A Measuring planes parallel to the surface ( $\psi = 0$ ), B Measuring planes at an angle  $\psi$  to the surface D = X-ray detected, S = X-ray source, N = Normal to surface [86]

Figure A12 shows a plane stress elastic model of a flat specimen. As X-ray diffraction stress measurement is confined to the surface of a sample, in the exposed surface layer, a condition of plane stress is assumed to exist. That is, a stress distribution described by principal stresses  $\sigma_1$  and  $\sigma_2$  exist in the plane of the surface, and no stress is assumed perpendicular to the surface ( $\sigma_3 = 0$ ). The stress distribution is defined as the following [88]

$$\sigma_\phi = \sigma_1 \cos^2\phi + \sigma_2 \sin^2\phi \quad \text{Equation A26}$$

However a strain component ( $\epsilon_3$ ) perpendicular to the surface exists as a result of Poisson's ratio contraction, caused by the two principal stresses. In general the strain is given as [81]

$$\epsilon_3 = \frac{\sigma_3}{E} - \frac{\nu}{E}(\sigma_1 + \sigma_2) \quad \text{Equation A27}$$

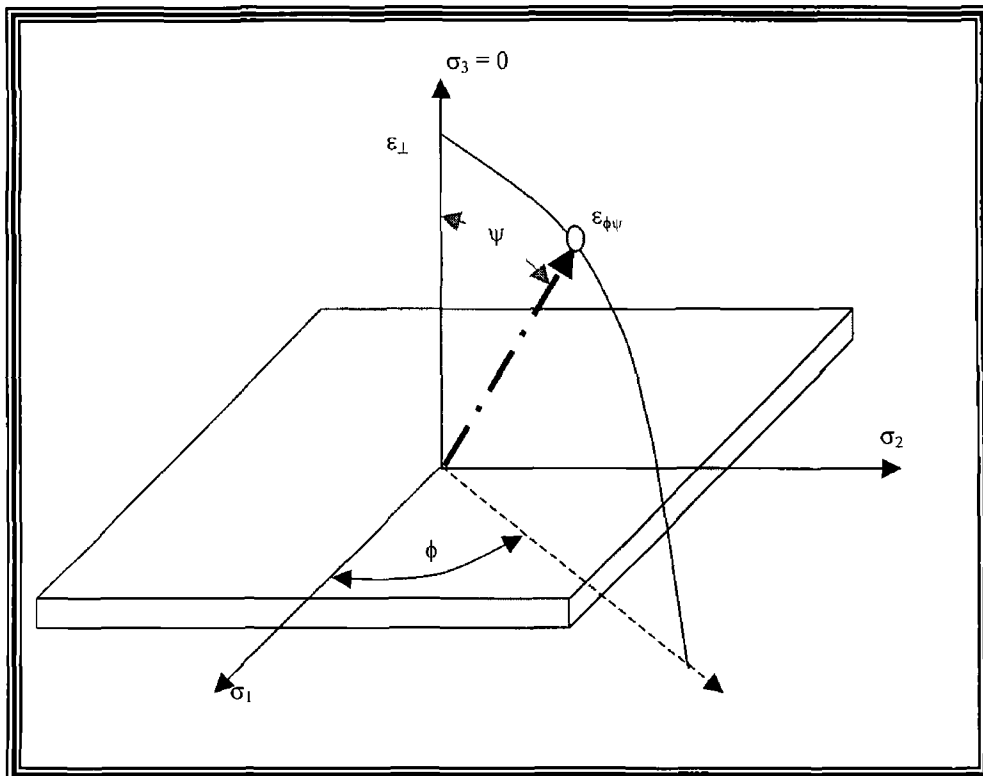


Figure A12, Plane stress elastic model of a flat specimen

In the situation described by figure A11, the strain is as follows:

$$\epsilon_{\phi\psi} = \frac{1+\nu}{E}(\sigma_1 \cos^2\phi + \sigma_2 \sin^2\phi)\sin^2\psi - \frac{\nu}{E}(\sigma_1 + \sigma_2) \quad \text{Equation A28}$$

Substituting equation A26 into equation A28, yields the strain ( $\epsilon_{\phi\psi}$ ) in the sample surface at an angle  $\phi$  from the principal stress  $\sigma_1$ :

$$\epsilon_{\phi\psi} = \frac{1+\nu}{E}\sigma_\phi \sin^2\psi - \frac{\nu}{E}(\sigma_1 + \sigma_2) \quad \text{Equation A29}$$

When the  $\psi$  angle is set to 90 degrees, then the strain vector lies in the plane of the surface. Generally the XRD machine is set up according to the parameters detailed with the equipment and initially a broad scan is carried out to find a chosen peak with the highest intensity. The specimen is then tilted at various angles in order to find the shifted peak values and the system displays the result as a line graph ( $\sin^2\psi$  V's  $\epsilon_{\phi\psi}$ ). From the graph, the slope of the line which best fits the measured points is calculated. Equation A29 shows that the slope of this graph is given as:

$$\text{Slope of Graph} = \frac{1+\nu}{E}\sigma_\phi \quad \text{Equation A30}$$

Therefore the stress in the coating is given by measuring the slope for two or more different angles of  $\psi$ , and substituting into the following:

$$\sigma_\phi = \frac{E}{1+\nu} (\text{Slope of Graph}) \quad \text{Equation A31}$$

---

## APPENDIX 5

---

### Hole Drilling Method

The hole-drilling strain-gage method measures residual stresses near the surface of a material. The method involves attaching strain gages to the surface, drilling a hole in the vicinity of the gages and measuring the relieved strains. The measured strains are then related to relieved principal stresses through a series of equations.

The RS-200 milling guide (figure A13) is a high-precision instrument for analysing residual stresses by the hole-drilling method. Its flexibility makes it equally suitable for laboratory and field application. This apparatus is used to relieve residual stresses near the surface of an isotropic linearly-elastic material. Although the concept is quite general, the test method described is applicable in those cases where the stresses do not vary significantly with depth and do not exceed one half of the yield strength. The method is "semi-destructive" as localised damage is done to the coating surface and it does not significantly affect the usefulness of the specimen. A three-element strain gage of the general type was placed in the area under consideration (figure A14) and the strain gages are numbered with the clockwise convention. A hole is milled at the geometric centre of the strain gage rosette and the residual stresses in the surrounding area relax. Within the close vicinity of the hole, the relief is nearly complete when the depth of the drilled hole approaches 0.4 of the mean diameter of the strain gage circle,  $D [92]$ .

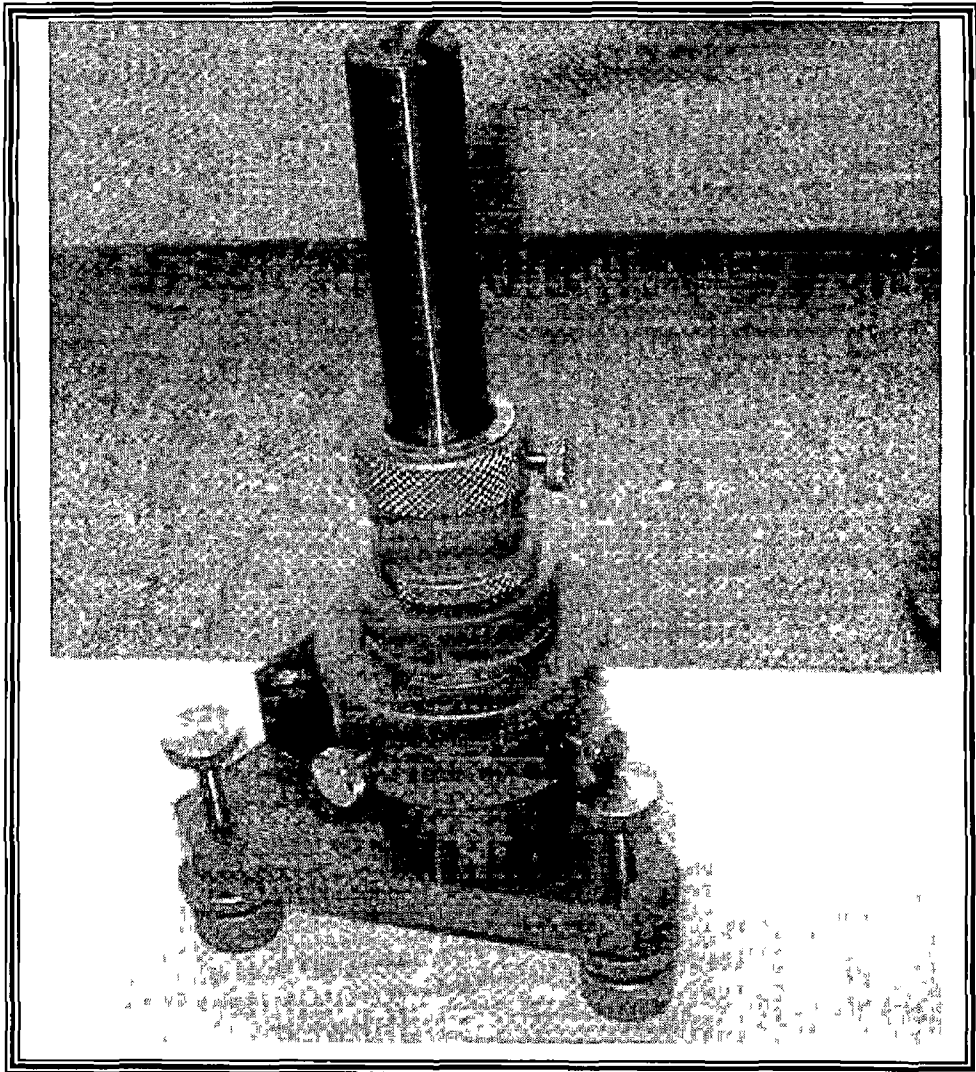


Figure A13, Milling Guide RS-200

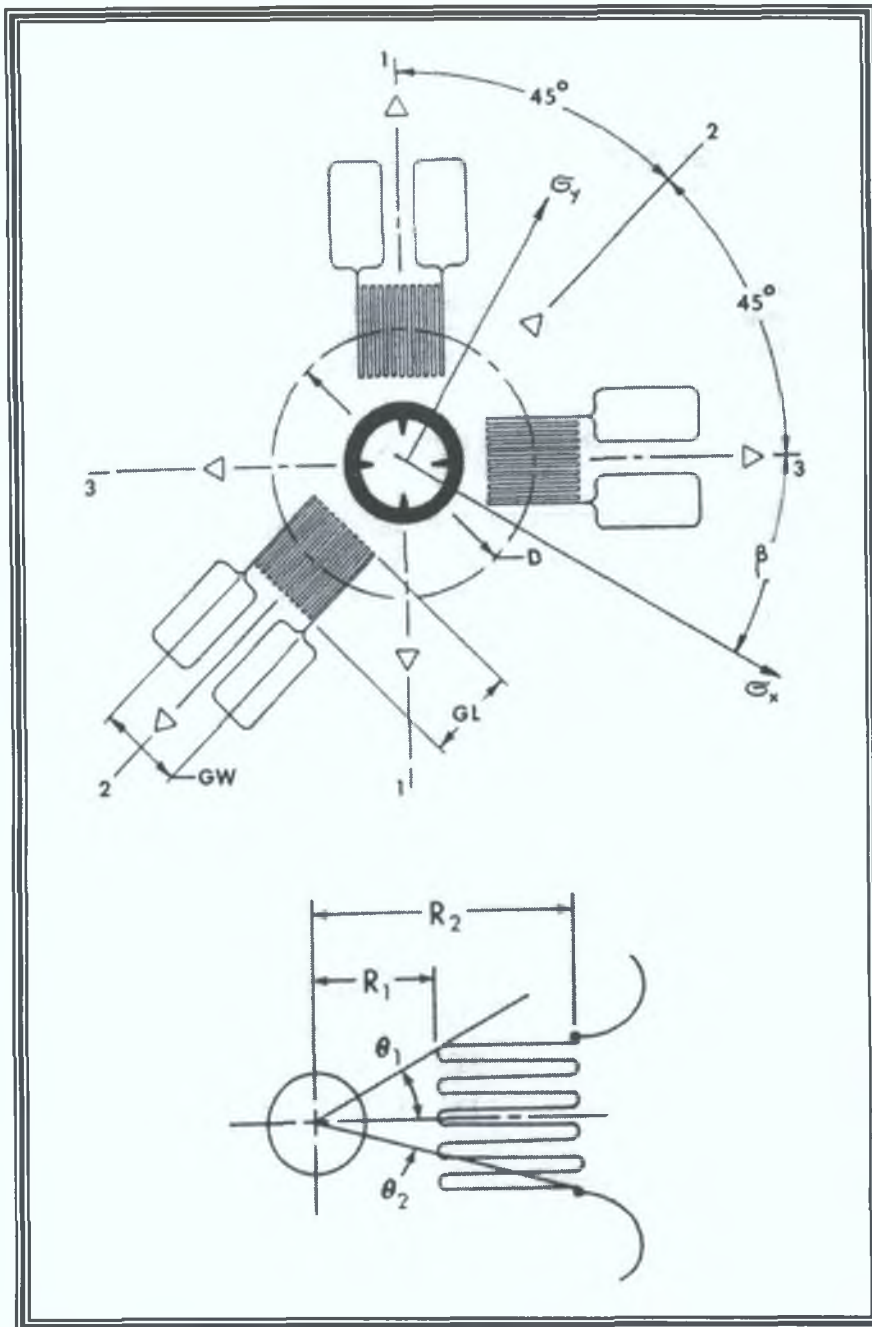


Figure A14, Rosette strain gauge orientation [92]

The strains found using the rosette were measured with a suitable strain-recording instrument (strain indicator) The rosette strain gage measures strain in three directions, 0°C, 45°C, 90°C (or another type at 0°C, 60°C and 120°C), as described in ASTM E1561-93 [89] The residual stress is calculated using Kirsch's Theory [91], which measured the strains located around a circular hole upon an infinite plate, loaded with plane stresses The hypotheses of this theory are

- The coating should be isotropic and a linear elastic material
- The tension perpendicular to the surface is negligible
- The main tension direction is constant along its' depth
- The internal tensions do not exceed one third of the yield strength
- The milled hole must be concentric with the strain gage rosette

Considering a plane plate subjected to the main tensions  $\sigma_1$  and  $\sigma_2$  where  $\sigma_1 \geq \sigma_2$  and a point P on this plate with polar co-ordinates  $r$  and  $\alpha$ , then the tension are

$$\sigma_r = \frac{\sigma_1 + \sigma_2}{2} + \frac{\sigma_1 - \sigma_2}{2} \cos(2\alpha) \quad \text{Equation A32}$$

$$\sigma_t = \frac{\sigma_1 + \sigma_2}{2} - \frac{\sigma_1 - \sigma_2}{2} \cos(2\alpha) \quad \text{Equation A33}$$

$$\tau_{rt} = \frac{\sigma_1 - \sigma_2}{2} \sin(2\alpha) \quad \text{Equation A34}$$

While with the hole (radius  $a$ ) the tensions are

$$\sigma'_r = \frac{\sigma_1 + \sigma_2}{2} \left(1 - \frac{a^2}{r^2}\right) + \frac{\sigma_1 - \sigma_2}{2} \left(1 - \frac{4a^2}{r^2} + \frac{3a^4}{r^4}\right) \cos(2\alpha) \quad \text{Equation A35}$$

$$\sigma'_t = \frac{\sigma_1 + \sigma_2}{2} \left(1 - \frac{a^2}{r^2}\right) - \frac{\sigma_1 - \sigma_2}{2} \left(1 - \frac{3a^4}{r^4}\right) \cos(2\alpha) \quad \text{Equation A36}$$

$$\tau'_{rt} = \frac{\sigma_1 - \sigma_2}{2} \left( 1 - \frac{2a^2}{r^2} + \frac{3a^4}{r^4} \right) \sin(2\alpha) \quad \text{Equation A37}$$

The residual tensions are the difference between the tension before and after the hole

$$\Delta\sigma_r = \sigma'_r - \sigma_r \quad \text{Equation A38}$$

$$\Delta\sigma_t = \sigma'_t - \sigma_t \quad \text{Equation A39}$$

$$\Delta\tau_{rt} = \tau'_{rt} - \tau_{rt} \quad \text{Equation A40}$$

The radial strain produced is

$$\varepsilon_r = \frac{\Delta\sigma_r - \nu\Delta\sigma_t}{E} \quad \text{Equation A41}$$

where E and  $\nu$  are the Young's modulus and Poisson's ratio of the material (tungsten carbide-cobalt in this case)

Substituting the equations A32 to A37 into the equation A41, the radial strain results

$$\varepsilon_r = A(\sigma_1 + \sigma_2) + B(\sigma_1 - \sigma_2)\cos(2\alpha) \quad \text{Equation A42}$$

where

$$A = -\frac{1+\nu}{2E}\bar{a} \quad \text{Equation A43}$$

$$B = -\frac{1}{2E}\bar{b} \quad \text{Equation A44}$$

$\bar{a}$  and  $\bar{b}$  constants supplied by the gage manufacturer

To calculate the main tensions  $\sigma_1$  and  $\sigma_2$  and the angle  $\gamma$ , which is the angle measured clockwise from the location of the reference gauge (gauge 1) to the direction of  $\sigma_{\max}$  =

$\sigma_1$ , the operator needs three strains, thus a rectangular rosette was used

Equation A41 was manipulated for the three strains  $\varepsilon_1$ ,  $\varepsilon_2$  and  $\varepsilon_3$ , to show that

$$\sigma_{\min}, \sigma_{\max} = \frac{\varepsilon_3 + \varepsilon_1}{4A} \pm \frac{\sqrt{(\varepsilon_3 - \varepsilon_1)^2 + (\varepsilon_3 + \varepsilon_1 - 2\varepsilon_2)^2}}{4B} \quad \text{Equation A45}$$

$$\tan(2\gamma) = \frac{\varepsilon_3 + \varepsilon_1 - 2\varepsilon_2}{\varepsilon_3 - \varepsilon_1} = \frac{N}{D} \quad \text{Equation A46}$$

The following table allows giving the right sign to  $\gamma$  by considering the signs of N and D

Table A1, Values and signs for  $\gamma$

$N \geq 0, D > 0$	$0 \leq \gamma < 45^\circ$	$\gamma = \frac{1}{2} \text{tg}^{-1}(N/D)$
$N > 0, D = 0$	$\gamma = 45^\circ$	$\gamma = \frac{1}{2} \text{tg}^{-1}(N/D)$
$N \geq 0, D < 0$	$45^\circ < \gamma < 90^\circ$	$\gamma = \frac{1}{2} \text{tg}^{-1}(N/D) + \pi/2$
$N < 0, D < 0$	$90^\circ < \gamma < 135^\circ$	$\gamma = \frac{1}{2} \text{tg}^{-1}(N/D) + \pi/2$
$N < 0, D \geq 0$	$135^\circ \leq \gamma < 180^\circ$	$\gamma = \frac{1}{2} \text{tg}^{-1}(N/D) + \pi$
$N = 0, D = 0$	$\gamma$ indeterminate, hydrostatic state ( $\sigma_{\min} = \sigma_{\max}$ )	

The diameter  $D_0$  of the drilled hole should be related to the diameter of the gage circle D by the following relation

$$0.3 < \frac{D_0}{D} < 0.5 \quad \text{Equation A47}$$

Moreover, a margin of at least 0.3mm should be allowed between the hole boundary and the strain gauge grid. In general it is suggested to drill as large as possible because this increases the method's sensitivity. Where the material thickness is at least 1.2 D,

the final depth of the hole should be  $0.4 D$ , whereas in the case of a material whose total thickness is less than  $1.2 D$ , a through-hole is drilled through the entire thickness. The centre of the drilled hole should coincide with the centre of the strain gage circle to within either  $\pm 0.004 D$  or  $\pm 0.025$  mm, whichever is greater. Errors due to the misalignment of the strain gage could produce significant errors in the calculated stress [92]. During the first 60% of the total depth, the depth increments should not exceed 10% of the total depth, while, for the remaining 40 % of the hole depth, the depth increments should not exceed 20% of the total depth.

## APPENDIX 6

### The Dimensions Used To Produce The Tensile Specimen

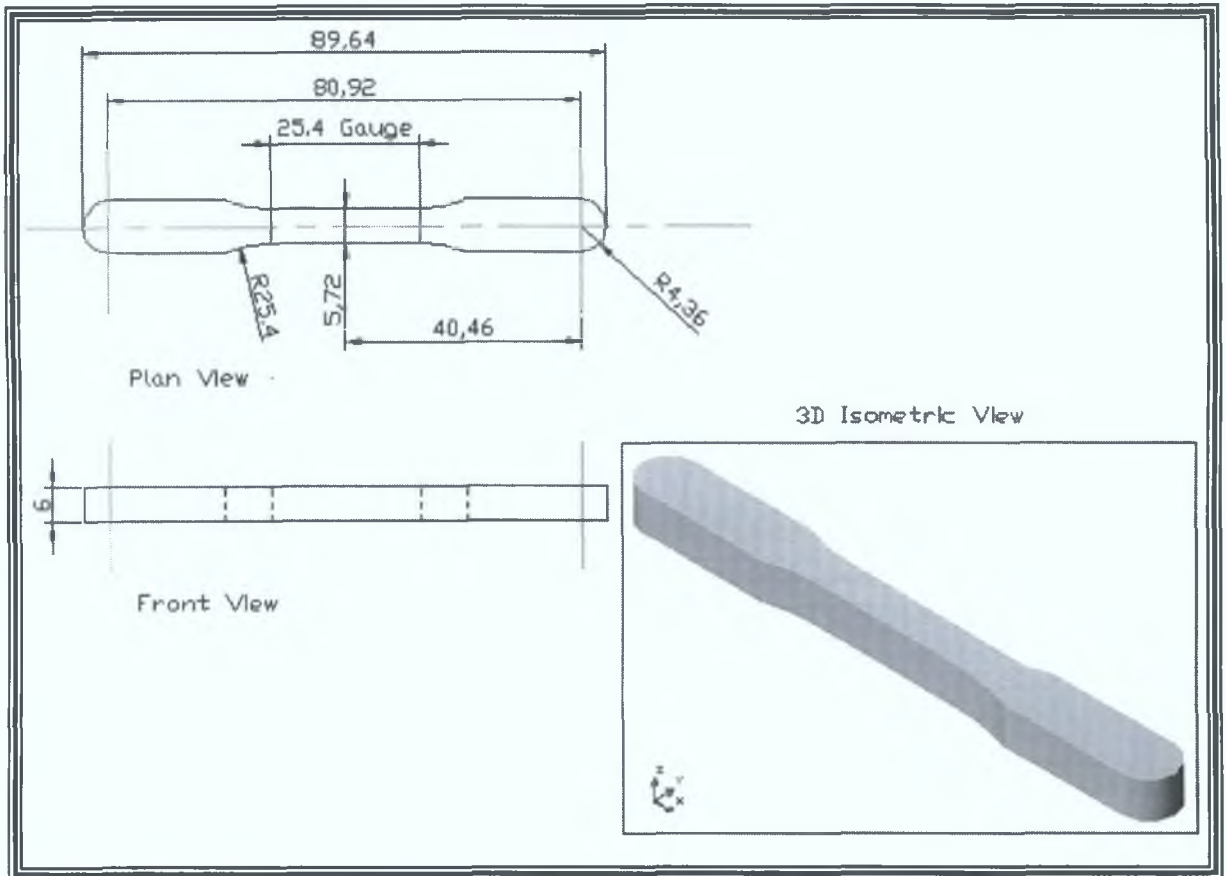


Figure A15, Computer Aided Drawing of the tensile specimen shape used to produce WC-Co samples.

---

## APPENDIX 7

---

### Heat Transfer Through A Thermally Sprayed Sample

#### **Problem Description:**

In the present study, the procedure shown here depicts the simplest approach carried out to analyse the steady-state heat transfer of the Diamond Jet flame acting on the coating (Tungsten Carbide Cobalt), releasing layer (Aluminium) and substrate (Stainless steel) during deposition. Numerous other more complex three-dimensional approaches were used to gain the results presented later in the report. Radiation effects are ignored. The two-dimensional steady-state heat transfer analysis of the coating and substrate is shown in figure A16. The dimensions and boundary conditions of the sample, are shown in the accompanying figure. On the coating side of the sample, a flame temperature surrounded by the carbon dioxide (CO<sub>2</sub>) cooling jet stream, causes a temperature distribution across the sample. This is simulated, by placing a temperature value at each node along the right most edge (front). The left most edge (back of the substrate), was given a convection load (film coefficient), representing the air temperature behind the sample. The selected thermal conductivities (k) were 90 [33], 125 [109], and 25 W(mK)<sup>-1</sup> [109], for Tungsten Carbide Cobalt, Aluminium and Stainless steel respectively. The air film coefficient was taken to be equal to 0.03 W(mK)<sup>-1</sup> and the flame coefficient was taken to be equal to 0.058 W(mK)<sup>-1</sup> [108].

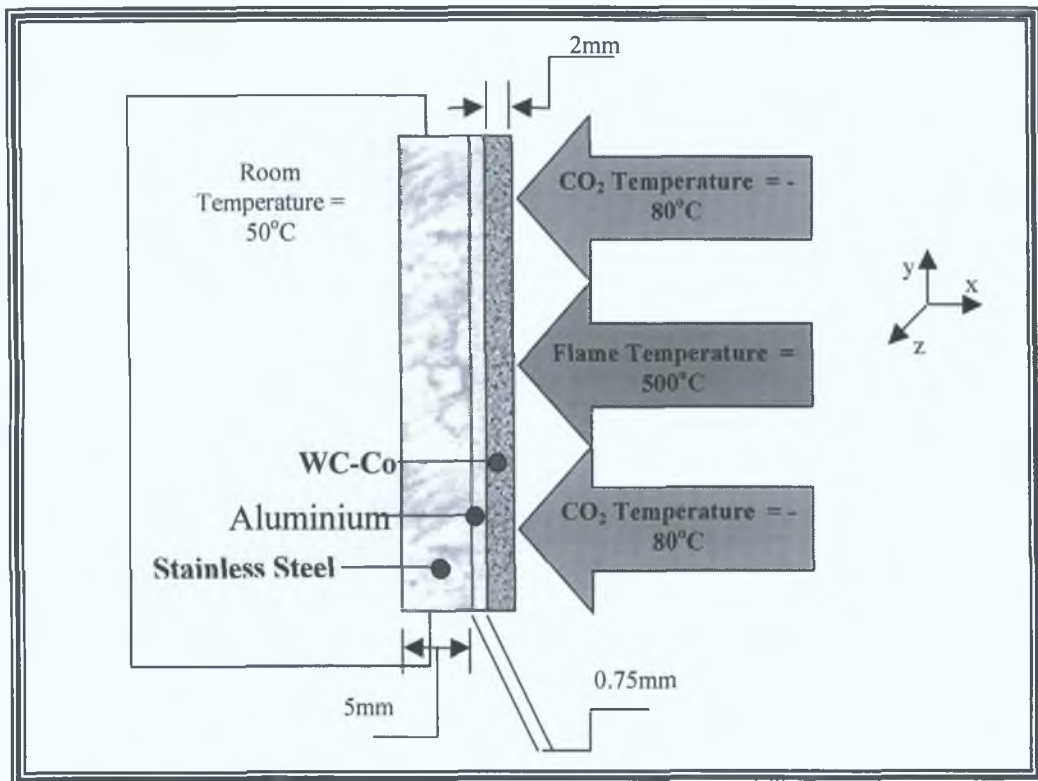


Figure A16, Schematic of the steady-state heat transfer problem to be analysed.

### This is the beginning of Preprocessing

#### *Build Geometry:*

There are several ways to create the model geometry within ANSYS, some more convenient than others. For simplicity the analysis shown is of one unit thick slice of the sample. The first step was to recognize that the problem could be created by rectangular primitives.

*Firstly it was decided where the origin would be located and then define the three rectangle primitives (substrate, releasing layer and coating) relative to that origin, all in metres. The location of the origin is arbitrary. In ANSYS, this origin is called the global origin.*

- 1 **Main Menu Preprocessor**  
     **-Modeling-Create**  
         **-Areas- By Dimensions**
- 2 **Enter X1 = 0 (Note Press the Tab key between entries), X2 = 0 005, Y1 = 0, Y2 = 0 02 -> (substrate)**
- 3 **Apply to create the first rectangle ->**
- 4 **Enter X1 = 0 005, X2 = 0 00575, Y1 = 0 02, Y2 = 0 -> (releasing layer)**
- 5 **Apply to create the second rectangle ->**
- 6 **Enter X1 = 0 00575, X2 = 0 00775, Y1 = 0, Y2 = 0 02 -> (coating)**
- 7 **OK to create the third rectangle and close the dialog box ->**

#### ***Change Plot Controls and Replot***

The area plot shows three rectangles, which are *areas*, in the same color. To more clearly distinguish between the areas, turn on area numbers and colours.

- 1 **Utility Menu PlotCtrls**  
     **Numbering**
- 2 **Turn on Area numbers ->**
- 3 **OK to change controls, close the dialog box, and replot ->**
- 4 **Toolbar SAVE\_DB**

#### ***Glue Areas***

Now that the appropriate pieces of the model are defined (areas), the substrate, releasing layer and coating must be glued together (using a Boolean operation) to act as a solid piece.

1. **Main Menu: Preprocessor**  
    **-Modeling-Operate**  
        **-Booleans-Glue**  
            **Areas**
2. **Pick All for all three areas to be glued ->**
3. **Toolbar: SAVE\_DB**

***Define Material Properties:***

For this analysis, there is one material properties, thermal conductivity  $k$  to be entered for each of the three materials.

1. **Main Menu: Preprocessor**  
    **Material Props**  
        **-Constant-Isotropic**
2. **OK since defining material 1 -> (substrate)**
3. **Enter 25 for KXX -> (keeping units in  $W(mK)^{-1}$ )**
4. **APPLY to define material property set ->**
5. **Define as material 2 and enter OK -> (releasing layer)**
6. **Enter 125 for KXX ->**
7. **APPLY to define material property set ->**
8. **Define as material 3 and enter OK -> (coating)**
9. **Enter 90 for KXX ->**
10. **OK to define material property set and close the dialog box ->**

***Define Material Attributes***

The three materials must be defined as having different material properties

- 1 Main Menu Preprocessor  
Define Attributes  
-Areas-Picked Areas ->**
- 2 Pick the left most rectangle and OK to defining the material ->**
- 3 Select the material number as 1 -> (substrate)**
- 4 OK to define material property set and close the dialog box ->**
- 5 Main Menu Preprocessor  
Define Attributes  
-Areas-Picked Areas ->**
- 6 Pick the middle rectangle and OK to defining the material ->**
- 7 Select the material number as 2 -> (releasing layer)**
- 8 OK to define material property set and close the dialog box ->**
- 9 Main Menu Preprocessor  
Define Attributes  
-Areas-Picked Areas ->**
- 10 Pick the left most rectangle and OK to defining the material ->**
- 11 Select the material number as 3 -> (coating)**
- 12 OK to define material property set and close the dialog box ->**

***Save the Database***

At this point, the model was save to the database as a named file (a name that represents the model before meshing) If the user decides to go back and remesh, then all the user needs to do is resume this database file The model was saved as *model db*

**1 Utility Menu File****Save As****2 Enter *model db* for the database file name ->****3 OK to save and close dialog box ->*****Generate Mesh***

The preference (thermal analysis) type, must be selected to state the type of analysis, the ANSYS program should carry out

**1 Main Menu Preferences****2 Turn on Thermal->****3 OK to apply filtering and close the dialog box ->*****Define Element Types***

The choice of element for this simple test was a 4 – node quadratic (PLANE55)

**1 Main Menu Preprocessor****Element Type****Add/Edit/Delete****2 Add an element type ->****3 Choose Thermal Solid family of elements ->****4 Choose the 4-noded quad (PLANE55) ->**

- 5 **OK to apply the element type and close the dialog box ->>**

### *Mesh the Area*

- 1 **Main Menu Preprocessor  
Mesh Tool**
- 2 **Set Global Size control ->>**
- 3 **Type in 0 0005 ->> (every element edge will be no longer than 0 0005m or  
0 5mm)**
- 4 **OK ->>**

### *Save the Database*

Here again, the database is saved as another named file (*mesh db*)

- 1 **Utility Menu File  
Save as**
- 2 **Enter *mesh db* for database file name ->>**
- 3 **OK to save file and close dialog box ->>**

### **The Beginning of the Solution Phase**

#### *Apply Convection Loads*

Apply the convection to the back line (back of substrate), loads applied to solid modeling entities are automatically transferred to the finite element model during solution. On the right most edge the cooling and flame temperatures are applied

- 1 **Utilities Menu Plot  
Lines**
- 2 **Main Menu Solution**

**-Loads-Apply**  
**-Thermal-Convection**  
**On Lines ->**

3. **Select the back line of the substrate->**
4. **OK (in the picking menu) ->**
5. **Enter 0.03 for Film Coefficient->**
6. **Enter 50 for Bulk Temperature->**
7. **Utilities Menu: Plot**  
**Elements->**
8. **Main Menu: Solution**  
**-Loads-Apply**  
**- Temperature**  
**On Nodes ->**
9. **Select 8 nodes (out of 40) on the right most edge, starting at the top corner moving down->**
10. **Select 8 nodes (out of 40) on the right most edge, starting at the bottom corner moving upwards->**
11. **OK to apply constraints->**
12. **Enter -80 as the Bulk Temperature-> (position of the CO<sub>2</sub> cooling)**
13. **OK to apply constraints and close dialog box ->**
14. **Main Menu: Solution**  
**-Loads-Apply**  
**- Temperature**  
**On Nodes ->**
15. **Select 24 nodes (out of 40) on the right most edge, 12 above and below the midpoint of the edge-> (that is the rest of the nodes that were not**

selected for the cooling effect temperature)

16. OK to apply constraints->

17. Enter 500 as the Bulk Temperature-> (position of the DJ Gun flame)

18. OK to apply constraints and close dialog box ->

19. Toolbar: SAVE\_DB

***Obtain Solution:***

Now the solution of the problem was computed by the ANSYS package and sent to a file for view.

1. Main Menu: Solution

-Solve-Current LS ->

2. Review the information in the status window, then choose

File Close (Windows), or Close (X11/Motif), to close the window ->

3. OK to begin the solution ->

4. Close the information window when solution is done ->

**The Beginning of the PostProcessing Phase**

***Review Results:***

Entering the general postprocessor the user will read in the results (in this example, a temperature contour will be obtained through the sample).

1. Main Menu: General Postproc

-Read Results-First Set

2. Main Menu: General Postproc

Plot Results

-Contour Plot-Nodal Solu

- 3 Choose Temperature item to be contoured ->
- 4 OK ->

A coloured temperature contour of the specimen was displayed, along with a legend displaying the temperature values associated with each colour

*Exit the ANSYS Program*

- 1 Toolbar Quit
- 2 Choose Quit - No Save! ->
- 3 OK ->

Following this procedure should yield similar results presented in the research

## Static Analysis of Residual Stress

### Applying A Thermal Load

#### *Problem Description*

The system is considered as a bimetallic beam consists of two materials (substrate and tungsten carbide-cobalt deposit) with different coefficients for thermal expansion,  $\alpha_s$  and  $\alpha_c$ , and is initially at a reference temperature of  $0^\circ\text{C}$ . The beam is simply supported and a uniform temperature is applied to both surfaces. The beam is expected to undergo a large lateral deflection. The residual stress generated as a result of depositing will be determined.

#### *Problem Specifications*

Material properties for each material

- Thermal conductivity of substrate  $k_s = 25\text{W(mK)}^{-1}$
- The stiffness of the substrate  $E_s = 200 \times 10^3 \text{ Nmm}^2$
- The Poisson's ratio for the substrate  $\nu_s = 0.3$
- Thermal expansion coefficient of the substrate  $\alpha_s = 16 \times 10^{-6} \text{ }^\circ\text{C}^{-1}$
- Thermal conductivity of deposit  $k_c = 90\text{W(mK)}^{-1}$
- The stiffness of the deposit  $E_c = 184.9 \times 10^3 \text{ Nmm}^2$
- The Poisson's ratio for the deposit  $\nu_c = 0.268$
- Thermal expansion coefficient of the deposit  $\alpha_c = 8.1 \times 10^{-6} \text{ }^\circ\text{C}^{-1}$

The geometric properties for this problem are

- The length of the sample was 80mm
- The thickness of the substrate  $t_s = 0.075\text{mm}$
- The thickness of the deposit  $t_d = 0.2\text{mm}$
- The total thickness of the sample was 0.275mm

Loading for this problem is

$$T_{\text{top}} = 500^{\circ}\text{C}$$

$$T_{\text{bottom}} = 487^{\circ}\text{C}$$

Since the problem is symmetric, only one-half of the beam was modelled. A convergence criteria force is specified with a tight tolerance to converge the large deflection behaviour.

### ***Procedure***

#### **Step 1 Specify the Title and Set Preferences**

- 1 Choose menu path

**Utility Menu>**

**File>**

**Change Title**

- 2 Enter the text "Residual stress sample"
- 3 Click on OK

#### **Step 2 Define Element Types**

- 1 Choose menu path

**Main Menu>**

**Preprocessor>**

**Element Type>**

**Add/Edit/Delete**

- The Element Types dialog box appears
- 2 Click on Add The Library of Element Types dialog box appears
  - 3 In the left scroll box, scroll to Coupled Field and select it
  - 4 In the right scroll box, click once on Vector Quad 13
  - 5 Click on OK
  - 6 Click on Options The PLANE13 element type options dialog box appears
  - 7 In the scroll box for Element degrees of freedom, scroll to UX UY TEMP AZ and select it
  - 8 In the scroll box for Element behavior, scroll to Plane stress and select it
  - 9 Click on OK, then click on Close

### Step 3 Define Material Properties

- 1 Choose menu path

**Main Menu>**

**Preprocessor>**

**Material Props>**

**Material Models**

- The Define Material Model Behaviour dialog box appears
- 2 In the Material Models Available window, double-click on the following options Structural, Linear, Elastic, Isotropic A dialog box appears
  - 3 Enter 200e3 for EX (Elastic modulus) Click on OK Material Model Number 1 appears in the Material Models Defined window
  - 4 Enter 0.3 for NUXY (Poisson's ratio) Click on OK
  - 5 In the Material Models Available window, double-click on the following

- 
- options Thermal Expansion Coef, Isotropic A dialog box appears
  - 6 Enter 16e-6 for ALPX (Thermal expansion coefficient) Click on OK
  - 7 In the Material Models Available window, double-click on the following options Thermal, Conductivity, Isotropic A dialog box appears
  - 8 Enter 25 for KXX (Thermal conductivity) Click on OK
  - 9 Choose menu path Edit>Copy Click on OK to copy Material Model Number 1 to Material Model Number 2 Material Model Number 2 appears in the Material Models Defined window on the left
  - 10 In the Material Models Defined window, double-click on Material Model Number 2, in the Material Models Available window, double-click on the following options Structural, Linear, Elastic, Isotropic A dialog box appears
  - 11 Enter 184 9e3 for EX (Elastic modulus) Click on OK Material Model Number 2 appears in the Material Models Defined window
  - 12 Enter 0 268 for NUXY (Poisson's ratio) Click on OK
  - 13 In the Material Models Available window, double-click on the following options Thermal Expansion Coef, Isotropic A dialog box appears
  - 14 Enter 8 1e-6 for ALPX (Thermal expansion coefficient) Click on OK
  - 15 In the Material Models Available window, double-click on the following options Thermal, Conductivity, Isotropic A dialog box appears
  - 16 Enter 90 for KXX (Thermal conductivity) Click on OK
  - 17 Click on menu path Material>Exit to remove the Define Material Model Behaviour dialog box

**Step 4 Create and Glue Rectangles**

- 1 Choose menu path

**Main Menu>**

**Preprocessor>**

**Modeling-Create>**

**Areas-Rectangle>**

**By Dimensions**

The Create Rectangle by Dimensions dialog box appears

- 2 Enter **0,0** and **40,-0.075** (half the substrate) for the X and Y co-ordinates Use the TAB key to move between fields
- 3 Click on Apply
- 4 Enter **0,0** and **40,0.2** (half the deposit) for the X and Y co-ordinates and click on OK
- 5 Choose menu path

**Main Menu>**

**Preprocessor>**

**Modeling-Operate>**

**Booleans-Glue>Areas**

The Glue Areas picking menu appears

- 6 Click on Pick All
- 7 Choose menu path

**Main Menu>**

**Preprocessor>**

**Attributes-Define>**

**Picked Areas**

8 In the graphics window, click on the top rectangle (Area 3 after the glue operation) and click on OK in the picking menu. The Area Attributes dialog box appears.

9 Enter 2 for material number and click on OK.

10

### **Step 5 Set Element Density and Mesh**

1 Choose menu path

**Main Menu>**

**Preprocessor>**

**Meshing-Size Cntrls>**

**ManualSize-Global-Size**

The Global Element Sizes dialog box appears.

2 Enter 1 for the edge length of the element and click on OK.

3 Choose menu path

**Main Menu>**

**Preprocessor>**

**Meshing-Mesh>**

**Areas-Free**

The Mesh Areas picking menu appears.

- 4 Click on Pick All
- 5 Click on SAVE\_DB on the ANSYS Toolbar

### **Step 6 Set Boundary Conditions and Initial Temperatures**

- 1 Choose menu path

**Utility Menu>**

**Select>**

**Entities**

- 2 In the top scroll box, select Nodes
- 3 In the second scroll box, select By Location
- 4 Click on X co-ordinates to select it, and enter 0 for Min,Max
- 5 Click on Apply
- 6 Click on Y co-ordinates, then Reselect
- 7 Enter 0 for Min, Max, and click on OK
- 8 Choose menu path

**Main Menu>**

**Solution>**

**Loads-Apply>**

**Structural- Displacement>**

**On Nodes**

The Apply U,ROT on Nodes picking menu appears

- 9 Click on Pick All The Apply U,ROT on Nodes dialog box appears

10. Click on UY for DOFs to be constrained and click on OK.

11. Choose menu path

**Utility Menu>**

**Select>**

**Entities**

12. Click on X co-ordinates to select it, click on From Full, enter **40** for Min,Max and click on OK.

13. Choose menu path

**Main Menu>**

**Solution>**

**Loads-Apply>**

**Structural-Displacement>**

**SymmetryB.C.-On**

**Nodes**

The Apply SYMM on Nodes dialog box appears.

14. Click on OK to accept the default of Symm surface is normal to X-axis.

15. Choose menu path

**Main Menu>**

**Solution>**

**Loads-Apply>**

**Structural-Displacement>**

**On Lines**

The Apply U,ROT on Nodes picking menu appears

- 16 Click on top Line of sample The Apply U,ROT on lines dialog box appears
- 17 Unselect UY and select Temp
- 18 Enter **500** for displacement value and click on OK
- 19 Choose menu path

**Main Menu>**

**Solution>**

**Loads-Apply>**

**Structural-Displacement>**

**On Lines**

The Apply U,ROT on Nodes picking menu appears

- 20 Click on bottom Line of sample The Apply U,ROT on lines dialog box appears
- 21 Unselect UY and select Temp
- 22 Enter **487** for displacement value and click on OK

**Step 7 Set Analysis Type and Large Deformation Option**

- 1 Choose menu path

**Main Menu>**

**Solution>**

**Analysis Type>**

**New Analysis**

- 2 Click on OK to accept the default of Static
- 3 Choose menu path

**Main Menu>**

**Solution>**

**Analysis Options**

The Static or Steady-State Analysis dialog box appears

- 4 Click Large deform effects option on and click on OK

**Step 8 Set Convergence Based on Force Only**

- 1 Choose menu path

**Main Menu>**

**Solution>**

**Load Step Opts-Nonlinear>**

**Convergence Crit>**

**Static**

The Default Nonlinear Convergence Criteria dialog box appears

- 2 Click on F to select it and click on Replace
- 3 Enter **0.1** for Minimum reference value and click on OK
- 4 Close the warning message box
- 5 Click on Close

**Step 9 Solve the Model**

- 1 Choose menu path

**Main Menu>**

**Solution>**

**Solve>**

**Current LS**

- 2 Review the information in the status window, and click on Close when finished
- 3 Click on OK in the Solve Current Load Step dialog box to begin the solution
- 4 Close the warning box and choose Yes to the question "Should solve be executed?"
- 5 Click on Close when the solution is done
- 6

**Step 10 Look at the Deformed Shape**

- 1 Choose menu path

**Utility Menu>**

**PlotCtrls>**

**Style>**

**Displacement Scaling**

- 2 Click on 1 0 (true scale) for Displacement scale factor and click on OK
- 3 Choose menu path

**Main Menu>**

**General Postproc>**

**Plot Results>****Deformed Shape**

The Plot Deformed Shape dialog box appears

- 4 Click on Def + undeformed, and click on OK. The deformed shape appears on the ANSYS Graphics window
- 5 Choose menu path

**Main Menu>****General Postproc>****Plot Results>****Contour Plot>****Nodal Solu**

The Plot Deformed Shape dialog box appears

- 6 Choose Stress item to be contoured
- 7 Scroll down and choose x-dir and click OK

**Step 11 List Nodal Solution**

- 1 Choose menu path

**Main Menu>****General Postproc>****List Results>****Nodal Solution**

The List Nodal Solution dialog box appears

2. In the right scroll box, click on All U's UCOMP to select it, and click on OK.
3. Review the results in the PRNSOL Command window, and click on Close.

**Step 12: Exit Ansys**

1. Choose QUIT from the ANSYS Toolbar.
2. Choose the save option you want and click on OK.

## Residual Stress Due to Moment

### *Problem Description*

The three-dimensional generated moment static analysis of the coating and substrate is shown in figure A17. The dimensions and boundary conditions of the sample, are shown in the accompanying figure. One end of the sample are constrained in the upward direction, while the other end under goes an applied load  $P$  (positive for the deposit and negative for the substrate), which generates a moment. Various loads are applied until the required deflection at the center of the sample is the same as that found in the experimental results. The selected Young's modulus and Poisson's ratio was 200GPa and 0.3 for the substrate, and 184.5GPa and 0.278, for the coating respectively. The objective of the problem is to demonstrate the typical ANSYS analysis procedure, which was carried out in the research to yield the results shown later.

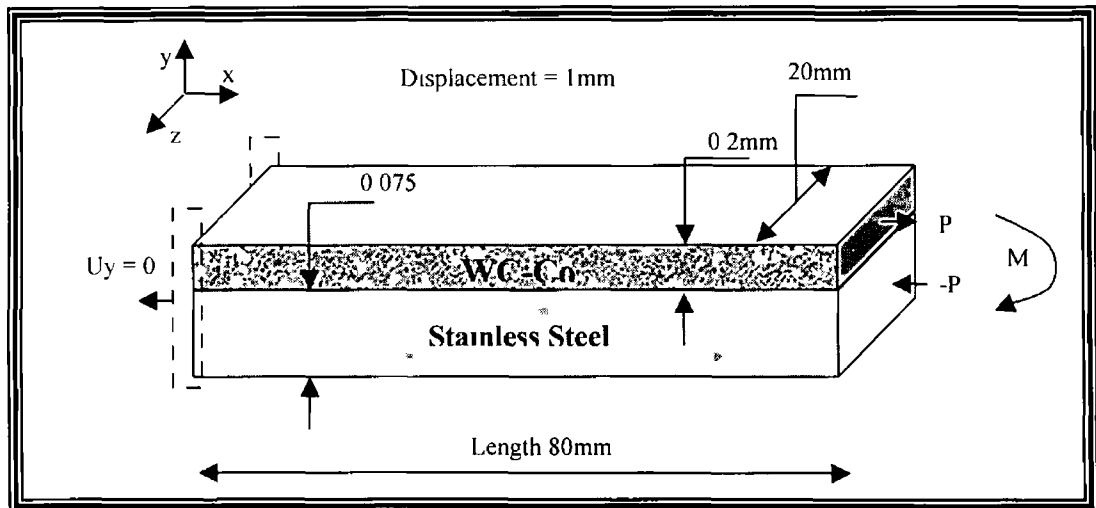


Figure A17, Schematic of the residual stress problem to be analysed

## *Preprocessing*

### *Build Geometry:*

- 1 Main Menu Preprocessor
  - Modeling-Create
  - Volumes-Block
  - By Dimensions
- 2 Enter  $X1 = 0$  (*Note Press the Tab key between entries*),  $X2 = 20$ ,  $Y1 = 0$ ,  
 $Y2 = 0.075$ ,  $Z1 = 0$ ,  $Z = 80$  -> (substrate)
- 3 Apply to create the first block ->
- 4 Enter  $X1 = 0$ ,  $X2 = 20$ ,  $Y1 = 0.075$ ,  $Y2 = 0.275$ ,  $Z1 = 0$ ,  $Z = 80$  -> (coating)
- 5 OK to create the second block and close the dialog box ->

### *Change Plot Controls and Replot*

- 1 Utility Menu PlotCtrls
  - Numbering
- 2 Turn on Volume numbers ->
- 3 OK to change controls, close the dialog box, and replot ->
- 4 Toolbar SAVE\_DB

### *Glue Areas:*

- 1 Main Menu Preprocessor
  - Modeling-Operate
  - Booleans-Glue
  - Volumes
- 2 Pick All for all both volumes to be glued ->

**3. Toolbar: SAVE\_DB*****Define Material Properties:***

For this analysis, there are two materials properties to be entered, namely Young's modulus of elasticity and Poisson's ratio.

**1. Main Menu: Preprocessor****Material Props****-Constant-Isotropic**

- 2. OK since defining material 1 -> (substrate)**
- 3. Enter 200e3 for EX -> (keeping units in N/mm<sup>2</sup>)**
- 4. Tab or click on NUXY field and enter 0.3 ->**
- 5. APPLY to define material property set ->**
- 6. Define as material 2 and enter OK -> (coating)**
- 7. Enter 184.5e3 for EX -> (keeping units in N/mm<sup>2</sup>)**
- 8. Tab or click on NUXY field and enter 0.278 ->**
- 9. OK to define material property set and close the dialog box ->**

***Define Material Attributes:***

The two materials must be defined as having different material properties.

**1. Main Menu: Preprocessor****Define Attributes****-Volumes-Picked Volumes ->**

- 2. Pick the lower block and OK to defining the material ->**
- 3. Select the material number as 1 -> (substrate)**
- 4. OK to define material property set and close the dialog box ->**

- 5 **Main Menu Preprocessor**  
**Define Attributes**  
**-Volumes-Picked Volumes ->**
- 6 **Pick the Upper block and OK to defining the material ->**
- 7 **Select the material number as 2 -> (coating)**
- 8 **OK to define material property set and close the dialog box ->**

### ***Changing the View***

At this point, the model is in a two dimensional shape, to change the view to an isometric view, carry out the following

- 1 **Utility Menu PlotCtrls**  
**PanView**
- 2 **Select Iso ->**
- 3 **OK to close dialog box ->**

### ***Generate Mesh:***

The preference (structural or thermal analysis and so on) type, must be selected to state the type of analysis, the ANSYS program should carry out

- 1 **Main Menu Preferences**
- 2 **Turn on Structural filtering ->**
- 3 **OK to apply filtering and close the dialog box ->**

### ***Define Element Types***

In any analysis, the user needs to select from a library of element types and define the appropriate ones for an analysis. For this analysis, only one element type, SOLID186, which is a 3-D, quadratic, structural, high-order brick. The choice of a higher-order

brick element here allows the user to have a coarser mesh, rather than with lower-order elements while still maintaining solution accuracy. Also, ANSYS will generate some triangle shaped elements in the mesh that would otherwise be inaccurate if lower-order elements (for example PLANE42) were used.

**1 Main Menu Preprocessor**

**Element Type**

**Add/Edit/Delete**

**2 Add an element type ->**

**3 Structural Solid family of elements ->**

**4 Choose the 20-noded quad (SOLID186) ->**

**5 OK to apply the element type and close the dialog box ->**

***Mesh the Area.***

One nice feature of the ANSYS program is that the user can automatically mesh the model without specifying any mesh size controls. This is using what is called a *default mesh*, otherwise the user may specify a global element size to control overall mesh density, as shown.

**1 Main Menu Preprocessor**

**Mesh Tool**

**2 Set Global Size control ->**

**3 Type in 0.1 -> (every element edge will be no longer than 0.1mm)**

**4 OK ->**

## The Beginning of the Solution Phase

### *Apply Loads:*

A new, static analysis is the default, so the user will not need to specify analysis type for this problem. Firstly, displacement constraints ( $U_y = 0$ ) are applied directly to nodes at each end of the specimen. To do this, the node entities at either end must be selected.

#### 1 Utilities Menu Edit

-Select Entities-Nodes

-By Location-Z

0-From Full

Apply-»(selects all nodes at  $Z = 0$ )

#### 2 Main Menu Solution

-Loads-Apply

-Structural-Displacement

On Nodes- Select All-»

3 Select  $U_y$  and enter 0 for zero displacement-» (all of these nodes are free to move in any direction except Y-direction)

4 OK to apply constraints and close dialog box -»

***Apply Force Load***

Now apply the force load to the end of the sample. The ANSYS convention for any loading force, pressure or in this case displacement, is that a *positive* displacement value represents displacement into the sample.

- 1 **Main Menu Solution**  
     **-Loads-Apply**  
         **-Structural-Force**  
             **On Nodes- Pick the Deposit End Face ->**
- 2 **Select  $F_y$  and enter 1 for Load->** (all of these nodes will move in a tensile manner in the Y-direction)
- 3 **OK to apply constraints and close dialog box ->**
- 4 **Main Menu Solution**  
     **-Loads-Apply**  
         **-Structural-Force**  
             **On Nodes- Pick the Substrate End Face ->**
- 5 **Select  $F_y$  and enter -1 for Load->** (all of these nodes will move in a compressive manner in the Y-direction)
- 6 **OK to apply constraints and close dialog box ->**
- 7 **Toolbar SAVE\_DB**

***Obtain Solution***

Now the solution of the problem will be computed by the ANSYS package and sent to a file for view.

- 1 **Main Menu Solution**  
     **-Solve-Current LS**

- 2 **Review the information in the status window, then choose File Close (Windows), or Close (X11/Motif), to close the window ->**
- 3 **OK to begin the solution ->**
- 4 **Close the information window when solution is done ->**

## **PostProcessing Phase**

### ***Review Results***

Entering the general postprocessor the user will read in the results (in this example, the x-directional stress result will be obtained)

- 1 **Main Menu General Postproc  
-Read Results-First Set**
- 2 **Main Menu General Postproc  
Plot Results  
-Contour Plot-Nodal Solu**
- 3 **Choose Stress item to be contoured ->**
- 4 **Scroll down and choose X-dir ->**
- 5 **OK ->**

A coloured deformed contour of the specimen after a deflection of 1mm about its centre is displayed, along with a legend displaying the stress values associated with each colour

### ***Exit the ANSYS Program***

- 1 **Toolbar Quit**
- 2 **Choose Quit - No Save! ->**
- 3 **OK ->**

Various loads were applied to achieve the desired displacement Following this procedure should yield similar results presented in the research